2014

MAGNESIUM-TITANIUM ALLOYS FOR BIOMEDICAL APPLICATIONS

Ilona Hoffmann
University of Kentucky, iho222@g.uky.edu

STUDENT AGREEMENT:

I represent that my thesis or dissertation and abstract are my original work. Proper attribution has been given to all outside sources. I understand that I am solely responsible for obtaining any needed copyright permissions. I have obtained needed written permission statement(s) from the owner(s) of each third-party copyrighted matter to be included in my work, allowing electronic distribution (if such use is not permitted by the fair use doctrine) which will be submitted to UKnowledge as Additional File.

I hereby grant to The University of Kentucky and its agents the irrevocable, non-exclusive, and royalty-free license to archive and make accessible my work in whole or in part in all forms of media, now or hereafter known. I agree that the document mentioned above may be made available immediately for worldwide access unless an embargo applies.

I retain all other ownership rights to the copyright of my work. I also retain the right to use in future works (such as articles or books) all or part of my work. I understand that I am free to register the copyright to my work.

REVIEW, APPROVAL AND ACCEPTANCE

The document mentioned above has been reviewed and accepted by the student's advisor, on behalf of the advisory committee, and by the Director of Graduate Studies (DGS), on behalf of the program; we verify that this is the final, approved version of the student's thesis including all changes required by the advisory committee. The undersigned agree to abide by the statements above.

Ilona Hoffmann, Student

Dr. Yang-Tse Cheng, Major Professor

Dr. Thomas D. Dziubla, Director of Graduate Studies

MAGNESIUM-TITANIUM ALLOYS FOR BIOMEDICAL APPLICATIONS

DISSERTATION

A dissertation submitted in partial fulfillment of the requirements for the degree of Doctor of Philosophy in the College of Engineering at the University of Kentucky

By

Ilona Hoffmann

Lexington, KY

Co-Directors: Dr. Yang-Tse Cheng, Professor of Materials Engineering

and Dr. David A. Puleo, Professor of Biomedical Engineering

Lexington, KY

2014

ABSTRACT OF DISSERTATION

MAGNESIUM-TITANIUM ALLOYS FOR BIOMEDICAL APPLICATIONS

Magnesium has been identified as a promising biodegradable implant material because it does not cause systemic toxicity and can reduce stress shielding. However, it corrodes too quickly in the body. Titanium, which is already used ubiquitously for implants, was chosen as the alloying element because of its proven biocompatibility and corrosion resistance in physiological environments. Thus, alloying magnesium with titanium is expected to improve the corrosion resistance of magnesium.

Mg-Ti alloys with a titanium content ranging from 5 to 35 at.-% were successfully synthesized by mechanical alloying. Spark plasma sintering was identified as a processing route to consolidate the alloy powders made by ball-milling into bulk material without destroying the alloy structure. This is an important finding as this metastable Mg-Ti alloy can only be heated up to max. 200C° for a limited time without reaching the stable state of separated magnesium and titanium. The superior corrosion behavior of Mg_{80}-Ti_{20} alloy in a simulated physiological environment was shown through hydrogen evolution tests, where the corrosion rate was drastically reduced compared to pure magnesium and electrochemical measurements revealed an increased potential and resistance compared to pure magnesium. Cytotoxicity tests on murine pre-osteoblastic cells in vitro confirmed that supernatants made from Mg-Ti alloy were no more cytotoxic than supernatants prepared with pure magnesium. Mg and Mg-Ti alloys can also be used to make novel polymer-metal composites, e.g., with poly(lactic-co-glycolic acid) (PLGA) to avoid the polymer's detrimental pH drop during degradation and alter its degradation pattern.

Thus, Mg-Ti alloys can be fabricated and consolidated while achieving improved corrosion resistance and maintaining cytocompatibility. This work opens up the possibility of using Mg-Ti alloys for fracture fixation implants and other biomedical applications.

KEYWORDS: Magnesium, titanium, corrosion, biodegradable implants, PLGA

Ilona Hoffmann

08-27-2014

MAGNESIUM-TITANIUM ALLOYS FOR BIOMEDICAL APPLICATIONS

By

Ilona Hoffmann

Dr. Yang-Tse Cheng
Director of Dissertation

Dr. David A. Puleo
Co-Director of Dissertation

Dr. Thomas D. Dziubla
Director of Graduate Studies

08-27-2014
Date

ACKNOWLEDGEMENTS

This dissertation, while an individual work, benefited from insight, guidance, and technical support of several people. First and foremost, I would like to thank my advisor Dr. Y.-T. Cheng, for accepting me as his student and giving me a challenging, but interesting research topic. He has been very helpful, supportive, and encouraging during this time. I highly appreciate the guidance he has provided me in designing experiments, analyzing results, and writing. Especially his teaching to thrive for simple solutions and think differently has influenced my work.

I thank my co-advisor Dr. David A. Puleo for expertise guidance, resourceful insights and patient discussions, as well as teaching me the biomedical aspects that were crucial for my research. He always provided timely and instructive comments.

I also thank my committee members Dr. Christine Trinkle and Dr. John Balk for their time and insights on my work and Dr. Larry L. Cunningham for kindly agreeing to serve as the outside examiner and for feedback from a physician's view. Special thanks go to Dr. Guangling Song from Oak Ridge National Laboratory for unhesitatingly sharing his profound knowledge with me and guiding me in many problems of magnesium corrosion experiments. Each individual provided insights that guided and challenged my thinking.

Jerry Rogeux helped me many times with skillful equipment repairs. Nancy Miller kindly taught me how to use shared equipment.

Dr. Jung Young Cho, from the GM R&D Center, has taught me how to do spark plasma sintering, which I am very grateful for. His group leader, Dr. Jan Herbst, has kindly allowed me to use their spark plasma sintering machine several times.

I'd like to thanks to Tricia Coakley from the Environmental Research and Training Laboratory (ERTL) for running ICP measurements for me. I thank Dr. Kim Anderson for letting me use her well plate reader and cell lab during the lab move and her student Anastasia Kruse for showing me how their equipment works. Thank you to Dr. Nihar Shah and Dr. Vijay Raghunathan for helpful discussions about cell staining methods.

I'm thankful to Paul Fisher for sharing his cells with me. Amanda Clark, Bryan Orellana, and Dr. Yuan Zou taught me how to run μCT. I am very grateful for their support. I thank Theodora Asafo-Adjei for instructions on how to prepare samples for gel permeation chromatography and Erin Bellhorn for running the tests for me as well as Dr. Thomas Dziubla for allowing me to use his instrument. Thank you to Yan Jin for running the compression tests for me. I acknowledge the undergraduate students who worked with me, Michaelah Wilburn, Leonard Franke, Yue Yu, and Noah Kratzer for the experience of teaching others. I'd also like to thank all the faculty, staff, and students, especially the students in my research group, who helped me in any way during my studies for their help and support.

I am very grateful to have received the Halcomb fellowship that provided funding for me for two years.

TABLE OF CONTENTS

LIST OF TABLES

LIST OF FIGURES

1. INTRODUCTION: The concept of this work

At present, there is a huge demand for implants: 1.8 to 2.0 million cases of artificial articulation replacements alone have been reported in the world each year[3]. Orthopedic biomaterials have to face the following challenges: corrosion, fatigue and erosion, and their combined interactions[3]. For optimal osseointegration the biomaterial properties are important[4,5]. For temporary and permanent implants biocompatibility and mechanical endurance are the most important properties[4]. Corrosion resistance is especially important when different implants are combined, as in the case of plates and screws for internal fracture fixation[4]. For a biodegradable implant it is of paramount importance to have an appropriate degradation rate[6]. To facilitate motion implant materials should be lightweight[4]. Implant materials should also exhibit characteristics similar to bone, i.e., stiff yet flexible, light yet strong[4]. In addition to suitable mechanical properties the material must be biologically stable as it interacts with soft and hard tissues, blood, intra- and extracellular fluids in the human body[4]. In summary, an implant should possess matching mechanical properties, biocompatibility, high corrosion and wear resistance, and enable osseointegration[4].

Today, four major types of materials are in use as biomaterials: metals, ceramics, polymers, and their composites[3]. Currently approved and commonly used metallic biomaterials include stainless steels, titanium, and cobalt-chromium-based alloys[3,7]. Metallic materials continue to play an essential role as biomaterials to assist healing or replace bone tissue that are diseased or damaged[7], because they are more suitable for load-bearing applications due to their combination of high mechanical strength and fracture toughness[3,7] compared to ceramics or polymers. Therefore, metal implant materials have found a wide range of deployment[3].

Materials that can be gradually dissolved and then excreted by the human body may be used as temporary implants.[8,9] The main advantage of such biodegradable implants is that they do not require a second surgery to remove the implant after the healing process is complete.[9,10] The challenge is to design and tune the degradation rate to fit specific applications. Furthermore, the degradation byproducts must not elicit chronic inflammation or other undesirable host responses. Materials that corrode or degrade in biological environments are interesting for temporary implants[10], which are at high demand[11]. This feature would not only abrogate the

need for a second surgery to remove the implant once it has served its purpose[10], but also avoid the potential long-term complications of permanent implants[10,11]. The ideal degradable implant material would offer better physiologic repair, reconstruction of local compliance, a temporary support of the harmed tissue, and the possibility for growth and late positive remodeling[11]. It should further be compatible with follow-up procedures and not restrict surgical revascularization[11]. The possibility of drug delivery and genetic transfer should also be provided, especially for stent materials[11]. Because an implant needs to fully function for a certain period of time until the region which underwent surgery starts healing, a delayed degradation process is critical to a biodegradable implant[9]. Today, researchers are working on the development of an adequate biodegradable material, which at the same time must also be biocompatible and may not provoke a significant inflammatory response[11].

Biocompatibility can be restricted by the technical aspects of the implant[11]: Design, material composition, physicochemical characteristics, including surface energy, electrical surface charge, surface texture, and surface chemistry have a significant influence on implant-host interaction phenomena[11]. First studies on the feasibility of magnesium implants for bone fixation were conducted as early as the 1930s, revealing excellent resorbability and high biocompatibility[10]. However, the formation of hydrogen gas pockets is harmful[10]. Although hydrogen formation does not play a major role in small-scale implants like stents, it is problematic when dealing with large bulk parts needed for the support of osteosynthesis[10]. The accumulation of hydrogen and poor transport mechanisms for gas bubbles in the human
flesh lead to the occurrence of gas pockets around magnesium implants[10]. These subcutaneous gas bubbles can be removed by puncturing to avoid a high risk for patients in the field of osteosynthesis[10]. But it would be much better to inhibit gas bubble formation.

The research emphasis for biodegradable implant materials has been on polymers and metals[10]. Metallic materials possess greater mechanical strength and their corrosion products provoke less drastic inflammation[10]. In the metals group iron and magnesium can be taken into consideration for utilization in cardiovascular intervention and osteosynthesis[10]. Iron has the virtue of very slow corrosion rates[10]. Magnesium alloys have been shown to be very biocompatiable for use in orthopaedic implants[3].

In addition to biocompatibility and biodegradability, the low modulus of Mg and its alloys can help minimize stress shielding, which is a common problem with implants made of steel and titanium: When a material with a much higher modulus than that of bone is implanted into bones, the stiffer material will carry the majority of the load placed on the bone and implant. When the bone does not experience stimulation by external loads it will not form new bone structure and grow[7]. Even worse, the existing bone might even be resorbed and weaken because the body is signaled that the bone is not needed as there is no load for it to carry. Obviously, this stress shielding effect creates complications in bone fracture treatment. If the implants used for fracture fixation is made of magnesium, which has a modulus much closer to bone than the traditionally used implant materials, this stress shielding effect can be minimized. Therefore, magnesium has been identified as an appropriate base material for osteosynthesis purposes[10].

The objective of this work was to find a suitable method for increasing the corrosion resistance of magnesium without compromising its biocompatibility. Since both magnesium and titanium are known to have excellent biocompatibility[4,12,13] titanium was chosen as an alloying element to slow down the corrosion. As titanium has proven to withstand corrosion in the human body very well, it was hypothesized that alloying magnesium with it could possibly yield an alloy with better corrosion resistance than that of pure magnesium. Therefore, the goal of this work is to evaluate whether alloying of magnesium with titanium slows down the corrosion rate in simulated body fluid and preserves the biocompatibility of the two elements they possess in their pure forms. This work covers synthesis, characterization, compaction, corrosion, and biocompatibility studies of Mg-Ti alloys. A major part of the study is on the corrosion behavior of magnesium and Mg-Ti in simulated body fluid, because fast corrosion is the main obstacle preventing successful applications of magnesium alloys, which otherwise possess favorable properties for use as temporary implants in physiological surroundings. Pure magnesium served as a reference in the experiments to evaluate the improvements through alloying with titanium.

2. STATE OF KNOWLEDGE

Implants

Advances in medical technology are fast-paced and currently undergoing profound changes [14]. Many implants are available that restore mechanical/physical functions of diseased or damaged tissues or aid regenerate traumatized tissues with synthetic materials, for example artificial hips or plates to repair broken bones[14]. These materials have to stay in the body for a defined time (temporary or a lifetime) and need to meet not only the requirements to fulfill their function physically, but also must not cause harmful effects on the body[14]. This latter requirement is usually called biocompatibility[14]. Although not all mechanisms with which biomaterials interact with the body being completely understood, there's a good level of understanding what biocompatibility needs to encompass[14]: Materials to be placed inside the body should not be toxic or cause irritation to tissues or organs[14].

The first generation biomaterials were designed to only match the physical properties of the replaced tissue and have a minimal toxic response to the host[4]. The second generation could interact with biological environments to enhance tissue bonding and progressively degrade while new tissue forms[4]. Today, the third generation focuses on stimulation specific cell responses at the molecular level[4]. In the past the approach was to use stable, solid, macroscopic, and biologically 'inert' metals, polymers, ceramics, and composites[14]. Even though these materials are able to physically perform their function they are limited to being dead materials in a living body as they cannot serve any biological function[14]. Currently the understanding is that the best solution would be replacing diseased and damaged body parts with living tissues, but it is still too challenging to source a sufficient amount of them[14], so this 'perfect' alternative will remain without reach until further breakthrough discoveries are made. But the key focus on biomaterial development nowadays is to develop replacements that are closer to 'living' than the traditionally completely inert synthetic materials[14]. This does not mean that the new biomaterials need to be of biological origin, but that the materials are able to interact with the cells because the cells are the key to any regenerative process[14]. Communication with cells involves molecular and mechanical signals[14]. Certain mechanical stresses are needed to initiate or maintain cell functions and affect the attachment of the integrins that cells have on their surfaces to the material[14]. The method with which cells convert stresses into biological signals inside them is called mechanotransduction[14]. It can be initiated by

fluid shear stresses or structural stresses in the material, so this stress transfer can be controlled by the Young's modulus of the material the cell is in contact with. Since this is the way the cells 'sense' and experience the presence of all materials placed into the body this communication interface is of utmost importance[14]. To ensure the cells can get in touch with the material's surface to pick up the signals they need to have a fitting hydrophilicity and molecular mobility[14]. Newly developed biomaterials will thus involve nanoscale features, manipulated at the molecular level and derived from natural sources to incorporate biological events[14].

The requirements for materials for regenerative medicine are competing and complex and include intrinsic material characteristics like structural and chemical parameters, functional properties, and biological functionality[14]. Examples of the above mentioned are pore size, shape, and distribution, elastic modulus and time-dependent deformation, hydrophobicity/hydrophilicity, molecular mobility, chemical functionality, response to pH, stress, and temperature, surface topography at the micro- and nano-scale, and biodegradation mechanisms and rates[14]. Metabolism of degradation byproducts plays an important role, too[14].

Implants today

Implanting artificial biomaterials serves to reduce pain and restore function to otherwise functionally compromised body parts[4]. Current clinically established therapeutic approaches use autografts and allografts, metallic and ceramic implants to assist in the repair of bone defects and they all have inherent disadvantages[15]. The orthopedic, dental, and reconstructive surgery problems facing society are increasing, some of them are difficult to solve[15]. The long-term effects of any form of therapy, including the placement of fracture fixation devices are unknown[12]. The most critical consideration for placement of fracture fixation devices in children is that the devices should not adversely affect children's growth and development[12].

The majority of internal fixation devices are made of stainless steel because it is comparatively cheap, easily available, biocompatible, great strength, and excellent fabrication properties[4]. These include wires, pins, screws, plates, and intramedullary nails or rods[4]. Stainless steels, however, can release their alloying elements, e.g., nickel and chromium, which are toxic. The high nickel content has been a special concern, so that nickel-free stainless steels were developed that show good cell viability[4].

There is an active research endeavor in the field of orthopedic and craniofacial implants[4]. Metallic implants continue to be used despite their shortcomings, primarily due to their mechanical properties[4]. Modifications are being made to minimize the harmful side effects of metal implants and their by-products[4]. Nickel leaching out from alloys is toxic, so it has been replaced by less harmful alternatives[4]. Metallic implant materials with lower moduli are developed[4] to reduce the stress shielding effect[4]. Efforts in cost reduction include replacing rare elements with less expensive ones[4]. New alloy systems are attracting increase attention due to their mechanical and biological properties, for example tantalum, niobium, zirconium, and magnesium[4]. The implant family is expanding to include polymer/magnesium composites to improve the polymer's mechanical and degradation properties[4].

The most commonly used implants for pediatric craniomaxillofacial fractures are either resorbable or nonresorbable materials[12]. The former are all co-polymers based on glycolic acid, lactic acid, and cyclic lactones (polydioxanone, polyglyconate, and polyglycolic acid), while the latter are exclusively metals (titanium and titanium alloys, stainless steel alloys, cobalt-chromium alloys)[12]. Nonresorbable implants are usually removed after three months[12].

The most frequently fractured bone is the mandible, which is subjected to compression and torsion with functional forces ranging from 0.5 to 40 kg [12]. In adults functional loads of the jaw range from 0.5 to 26.7 kg for chewing, 1.8-30.2 kg for swallowing, and 15.5-443 kg for maximum bite force[12]. When implanted into the growing body of children, implants will migrate, or rather become translocated because the bone about them will grow by apposition, deposition, and interstitial growth[12]. Therefore, bioabsorbable fracture fixation systems have been developed for children because titanium plates and screws were never considered to be ideal solution for children[12]. The requirements for those implants are that they must resist compression and torsion and only resorb after the fracture has healed[12]. Although polymeric implants have the advantage of being bioresorbable, there are other disadvantages to them[12]: After implanting the fracture fixation device an initial inflammatory response is elicited, just as in the case of titanium implants[12]. However, after this step the implant is encapsulated[12]. Initially, implant degradation occurs through hydrolysis, i.e. water molecules hydrolize the polymer´s bonds[12]. The broken down polymer building blocks are then phagocytized by macrophages into water and carbon dioxide[12]. Some biodegradable implants have an impact even after they disappear in the body[12]. The greater the inflammatory response, the more fibrous scar tissue grows, which can restrict

growth and development just like permanent implants[12]. Currently available resorbable implants are too large for some applications, e.g., frontal sinus injuries or naso-orbital-ethmoid fractures in children[12].

Tibia fractures are the second most common reason for children being admitted to hospitals for orthopaedic inpatient care[16]. In the age group infancy to18 years tibial shaft fracture has an incidence rate of 190 per 10,000 boys and 110 per 10,000 for girls annually[16]. The yearly incidence of hospitalization for a child sustaining a tibia or tibula fracture is 27 per 10,000 [16]. In early childhood tibial shaft fractures have excellent healing potential and mostly heal without complications[16].

Historically external fixation played a major role in managing highly unstable or severely open fractures, but it has disadvantages, such as physeal injury, pick-track infection, and delayed union[16]. Most tibial fractures can be successfully managed by traditional casting methods, but in certain cases surgical stabilization is warranted[16]: Closed tibial shaft fractures that have failed appropriate efforts at cast management, pediatric open tibial fractures can be treated analogous to adult settings[16]. Up to date surgical options for skeletally immature patients are intramedullary, internal, transcutaneous, and external fixation[16]. The elastic stable intermedullary nailing (ESIN) system works by inserting two nails with opposing curves into the broken bone to achieve a stable construct held in place by the flexibility of the nails (Figure 1)[17]. The nail is pre-bent and restrained by the intramedullary canal in the bone, resulting in a three-point pressure on the bone[17]. ESIN is an attractive minimally invasive approach to fracture fixation[16] because it has advantages over the traditional plating method:[18] The technique takes less time to perform, the implant is easier to remove later, and, most importantly, the wounds are small and less conspicuous than with plating.[18] An increasing number of reports show the effectiveness of surgical treatment of pediatric tibial fractures[16]. The ideal implant for internal fixation for tibial fractures is a simple load sharing device that can maintain alignment, but allows mobilization until a bridging callus forms[16]. It should not cross the physes and insertion/removal ought to be easy[16]. Intramedullary nails satisfy most of the above mentioned criteria, so an increasing number of surgeons adopted this technique to treat a variety of pediatric long bone fractures[16].

Figure 1: Radiograph of titanium elastic nails in a femur in an eight-year-old[1]. Reprinted from JOHN M. FLYNN, MD, LAEL M. LUEDTKE, MD, THEODORE J. GANLEY, MD, JUDY DAWSON, RN, RICHARD S. DAVIDSON, MD, JOHN P. DORMANS, MD, MALCOLM L. ECKER, MD, JOHN R. GREGG, MD, B. DAVID HORN, MD, AND DENIS S. DRUMMOND, MD , Comparison of Titanium Elastic Nails with Traction and a Spica Cast to Treat Femoral Fractures in Children, The Journal of Bone and Joint Surgergy, Volume 86-A, Number 4, p. 770-777, April 2004, The Journal of Bone and Joint Surgery, Inc. with permission by the publisher.

In general, tibial fractures heal within six months, but open fractures can take longer to heal and are at an increased risk of incection[16]. Srivastava et al. found that the average union time for pediatric fibia fractures was 20.7 weeks in their study[16].

In orthopedic procedures performed by Furlan et al. the implants were removed after a median of six months after implantation.[18] Humeral fractures were healed according to radiographs in a range of 5 to 11 weeks.[18] Tibial fractures healed in a comparable time frame.[18] Femoral fractures took the longest, with healing times ranging from 5 to 15 weeks.[18] The patients with diaphyseal forearm fractures achieved complete healing within 4 to 9 weeks.[18]

Bone-implant interactions

Nature has created bone as a composite of collagen, non-collagenous proteins, and hydroxyapatite to be able to carry large biomechanical loads[15]. Bone has a complex structure and is a composite material in many ways: porous, polymer-ceramic mixture, lamellar, fiber-matrix material[15]. Its mechanical properties are hence linked to each of those structural and compositional aspects[15]. Bone has an intrinsically high capacity for regeneration after trauma or disease and thus most bone defects, including fractures, can heal without surgical

intervention.[15] Complex fractures caused by high-impact trauma, disease, developmental deformity, revision surgery, and tumor resection often need surgery, implants, and postoperative care[15]. Extensive soft tissue damage, insufficient surgical techniques, biomechanical instability, and infections can lead to the formation of large defects that cannot heal by themselves[15]. Those large defects are challenging and expensive to treat, and have a severe impact on the patients' quality of life[15].

Children's bones have an astonishing healing capacity and high potential for remodeling, but their bones can be damaged irreversibly if the growth plate is injured, therefore special attention has to be paid to selecting a material that will not harm an immature body still in growth[19]. The growth plate is unique to children's bones[19]. It sits at the end of bone bones and is responsible for longitudinal bone growth[19].
Right after implantation the implant must carry load to allow the injury to heal slowly[20]. As the damaged tissue heals, the implant should gradually dissolve and transfer an increasing, but appropriate, amount of load to the body, until the injury is fully recovered[20]. The corrosion rate has to be slow enough for the implant to not deform or fracture under the load and the concentration of corrosion by-products to not exceed tolerable levels[20].
Stress shielding is a major issue with metallic implants because of the big difference in the elastic modulus of the implants and bone. Stress shielding leads to bone absorption, which in turn results in lossening of the implant or refracture after the implant has been removed[4]. It is thus of paramount importance to lower the modulus of metallic implants to match the modulus of bone[4].

Biodegradable implant materials

After fulfilling an only temporarily needed function the material should ideally be removed from the implantation site to make space for newly formed tissue[21], for example through degradation[14]. In this process degradation products form and are released[14]. Many degradation products can elicit inflammation and aggressive cells can destroy the freshly formed tissue that just grew in the attempt to remove the hazardous material[14].

Developing biodegradable metallic implants is a complex problem because it requires engineering and medical knowledge[20]. Nowadays many different biodegradable materials are

used and researched[21]. Biodegradable implants were predicted and have been proven to be beneficial for the regeneration of tissue[20]. They were also found to have other advantages for different biomedical applications[20]. There is a great need for biodegradable devices, making the development of biodegradable implants an area open for innovation[20]. The materials research community is taking on the challenge by researching suitable metallic, glass, and nano materials to revolutionize the field of biomaterials[20].

In specific applications biodegradable systems offer advantages over implants used today[20]. New implants on the basis of biodegradable metals are expected to adapt to the human body and eventually dissolve in the human body when they have served their purpose and are no longer needed[20]. Biodegradable implants would be beneficial for patients with cleft palate, fracture, angular deformities of long bones, and limb length discrepancies because it would spare them the pain and expense of the second surgery necessary to remove the implant after healing[20]. Another application is metallic wire stents used treat blockages in the circulatory system in millions of patients[20]. In some cases the stent elicits an immune response, which triggers scar tissue to grow and the formation of blood clots[20]. When blockages form again it's difficult to remove the stents so that additional stents have to be inserted[20]. The use of biodegradable stents would circumvent this problem and minimize invasive procedures[20]. Currently proposed biodegradable implants have their main target and market in younger patients, but adult patients would also greatly benefit from them[20].

Magnesium-based implant materials

There has been a lot of research on magnesium and its alloys for fracture fixation hardware[19] due to a great interest in magnesium-based biodegradable alloys as biomaterials for bone and cardiovascular applications[22]. Magnesium is regarded as a promising material for these applications because it shows good cytocompatibility and mechanical properties similar to bone[4,22]. Magnesium based implants have the potential to initially provide stability and bear loads before eventually degrading in vivo, eliminating the extra surgery for implant removal[22]. During corrosion magnesium and the alloying elements are released as ions[21]. Magnesium ions released due to corrosion did not show allergic potential in animal tests[21]. Direct contact between corroding magnesium alloys and bone has been observed[21] suggesting that a good

bond between magnesium-based implants and bone can be achieved. It is important that the implant is integrated into the bone because the tissue-implant interface determines the performance of the device[23]. Stable fixation between bone and implant permits earlier loading of the implant[23]. Degraded magnesium can either be stored in the callus that forms around a bone fracture site or in newly formed bone or eliminated into blood to be excreted by urine without causing hyper-magnesium[4]. Due to their rapid degradation magnesium alloys tend to form gaps at the interface of bone and implant[4]. Significant effort is put into the development of methods that prevent fast in vivo degradation of magnesium[4]. Alloying is one of the approaches, but the usable elements are very restricted[4]. However, alternatives are being sought[4].

Magnesium

Magnesium alloys have played an important role in automotive and aerospace industries for decades. They have also been considered as promising materials for biodegradable implants. The setback of magnesium for nearly all applications is its low corrosion resistance, especially in salty aqueous solutions.

Magnesium is a very attractive element for light alloys due to its low density and affordable price[24]. In fact, it is the most lightweight material for load-bearing applications[25] because of its combination of mechanical strength and fracture toughness[26]

Magnesium can absorb large quantities of hydrogen, which has sparked interest in using it for hydrogen storage for fuel cells and as the negative electrode in nickel - metal hydride batteries in the form of magnesium hydrides [24]. However, the application of Mg and its alloys is limited by their high sensitivity to oxidation and their comparatively low corrosion resistance[24].

The features that make magnesium an attractive candidate material for biodegradable orthopedic implants is its low Young's modulus, biocompatibility, and the lowest density among structural metals[6]. Magnesium and its alloys have a Young's modulus (40-45 GPa) close to that of femur bone[27,19], making it particularly appropriate for osteosynthesis purposes[10], because it will significantly reduce, if not eliminate, the stress shielding effect[6]. Compared to other commonly used metallic implants[7], ceramics and polymers, the modulus and strength of Mg are much closer to those of bone[28]. The specific density of magnesium and its alloys is 1.74 g/cm^3, which is very close to that of human calvarium bone (1.75 g/cm^3)[3]. The fracture toughness of magnesium is greater than that of ceramic biomaterials such as hydroxyapatite[29]. Thus, in terms of physical and mechanical properties magnesium alloys are superior to any other metallic or polymer implants for orthopedic, bone repairing, and bone replacement applications[9]. The mechanical properties of Mg alloys are affected by their poor corrosion resistance in physiological environments through loss of mass and structural integrity[6]. Pure magnesium has been reported to have antibacterial properties[22].

Magnesium as a biodegradable metal for biomedical applications is a topic of ongoing research[22] and biomedical application of Mg alloys have been steadily increasing in the past years[28]. The aging population is one market factor[28]. By 2030 it is estimated that 20% of the US population

will be 65 or older[28]. In this age group 80% will suffer from at least one chronic disease, which creates a large demand for orthopedic and cardiovascular devices[28]. As life expectancy increases, the lifespan of implants has to be prolonged to avoid patients needing multiple surgeries to exchange failed medical devices[28]. On the other hand, temporary implants, capable of being absorbed into the body after fulfilling their tasks are being actively researched[28]. There is, therefore, a great interest in magnesium due to its therapeutic potential in orthopedic and cardiovascular temporary implants[28].

In vivo degraded Mg can be replaced by newly formed bone when implanted in a fracture site[6]. Commonly used stainless steel implants need to be removed after 15-20 years[6], or earlier if complications arise or if used in children who are still in the growth phase. Eliminating the need for the second surgery for implant removal would greatly reduce medical cost, complications, and stress to the patients[6].

Magnesium alloys are expected to satisfy most mechanical, biocompatibility, and degradation performance requirements[11], as long as mechanical properties and corrosion of magnesium alloys are reasonably controllable under physiologic conditions[11]. Magnesium alloys have proven to be very biocompatible and show promise as possible orthopaedic implant materials[3]. The main disadvantage of Mg for the application as an implant material is its fast corrosion rate in salty aqueous solutions[6]. Rapid corrosion of Mg alloys leads to detrimental effects on the biological environment[6]. The corrosion of Mg raises the pH in the vicinity and produces hydrogen bubbles[27]. In the body those hydrogen bubbles can cause complications in the healing process because they separate the surrounding tissue[27]. First, a reduction of the corrosion rate of magnesium-based alloys in the physiological environment must be accomplished[7]. The possible toxicity of more corrosion resistant magnesium materials also has to be evaluated thoroughly[7].

Recently, a bioabsorbable coronary stent became the first magnesium implant, demonstrating a significant progress of magnesium alloys as biomaterials[3]. In tests from animal experiments to preliminary clinical applications these magnesium stents have not only demonstrated that magnesium stents are safe for the human body, but also shown that they carry the potential to overcome the shortcomings of permanent metallic stents, namely chronic inflammation, late stent thrombosis, prolonged antiplatelet therapy, and artifacts when images are taken by

multislice-computed tomography (CT) or magnetic resonance[3]. Magnesium cardiovascular stents typically get absorbed within 2-4 months[28].

Magnesium is non-toxic[30] and shows good biocompatibility without systemic inflammation reactions or affecting the cellular blood composition[19]. Mg^{2+} is present in the human body in large amounts; in fact, it is the fourth most abundant cation[2728] and the second most abundant intracellular cation[29]. The majority of magnesium exists in muscles and bones[3] (Table 1). Approximately half of the magnesium in the body is present intracellularly in soft tissue, while the other half is incorporated in bones.[7,29]. Less than 1% of the total body magnesium is present in blood[29]. On average, the human body contains approximately one mole of magnesium[29].

Table 1: Distribution of magnesium in the adult human[29] :

	Body magnesium content [% of total]
Serum	0.3
Red blood cell	0.5
Soft tissue	19.3
Muscle	27
Bone	52.9

Mg as an important factor for bone metabolism directly influences osteoclasts[27]. The presence of Mg is beneficial to bone strength and growth[27,30]. Magnesium binds strongly to phosphates[3] and thus influences the mineralisation of bony tissue through its control of hydroxyapatite (HA) (calcium phosphate) formation[3]. Mg is one of the most important 2+ ions for the formation of biological apatite[27]. High mineral apposition and increased bone mass were observed during the corrosion of magnesium by several researchers[19]. Osseointegration and bone-implant interface strength are reported to be higher for magnesium than even conventional titanium implant materials[19]. Although the large amounts of hydrogen gas produced during the degradation of magnesium do not harm the bone, they still make rapidly corroding magnesium unsuitable for implants because the hydrogen bubbles could disturb the bone healing process[19].

Magnesium is essential to the human metabolism[31] and the recommended daily intake of Mg for an adult is 300-400 mg [27]. The absorption of magnesium by the gastrointestinal tract is inversely related to intake and total body magnesium status. Studies indicate that the majority of magnesium is absorbed in the ilium and colon. The kidney is the main organ for magnesium excretion[30] and thus primarily responsible for the control of serum magnesium concentration. Approximately 70 - 80% of magnesium present in the plasma is filtered through the glomerular membrane. More than 50% of magnesium is reabsorbed along the thick ascending limb of the Loop of Henle. Just 6% of the filtered magnesium (equaling 120 - 150 mg/24h) appears in urine because of tubular reabsorption by the kidney[29]. Hyper-magnesium is very rare because excess Mg ions can be harmlessly and efficiently excreted with urine[7,27]. The biologic half-life for the majority of magnesium in the body is between 41 and 181 days[29].

Magnesium may be a factor in the treatment of acute myocardial infarction and the rate of atherosclerosis, although opinions vary concerning the importance of magnesium in health and disease[3]. Changes in the total amount of magnesium in red blood cells have been linked to hypertension, premenstrual syndrome, and chronic fatigue syndrome[3]. Disorder of magnesium metabolism has also been linked to cardiovascular disorders (acute myocardinal infarction, atherosclerosis, and arrhythmias), diabetes mellitus, alcoholism, aldosteronism, hperthyroidism, and renal tubular disorders[3].

Deficiency in Mg can lead to a variety of chronic illnesses[28]. Dietary magnesium deficiency has even been implicated as a risk factor for osteoporosis and is affiliated with various other health problems[3]: Magnesium depletion leads to cardiac arrhythmias, development of atherosclerosis, vasoconstriction of coronary arteries and is attributed to high blood pressure in the cardiovascular system[3]. Magnesium reduces the vascular resistance subsequently increasing the cardiac index[11]. A high extracellular magnesium concentration not only reduces the vascular tone in the systemic, coronary, and pulmonary vasculature but also lowers the systemic blood pressure[11]. Sufficient evidence exists that magnesium acts as a systemic and coronary vasodilator[11].

Mg-Ti materials

Synthesis of metastable Mg-Ti alloys

The phase diagram of the Mg-Ti system[32] shows that the equilibrium mutual solubility of magnesium and titanium is very low[33,34]: Equilibrium mutual solid solubility of the binary magnesium-titanium system is less than 2% [35]. The theoretical enthalpy of formation of a magnesium alloy containing 20 at.-% titanium is about 10 kJ/mol[25]. As magnesium and titanium have positive heats of mixing, they do not form intermetallic compounds[32].

Because of the limited solubility of titanium in magnesium and a large difference in melting points (Ti (1668°C) vs. Mg (1091°C)), it´s impossible to fabricate Mg-Ti alloys by conventional powder metallurgy, e.g., arc-melting[36], rapid solidification[25], and solid-state processing of Mg-Ti alloys[33].

However, it has been demonstrated that Mg-Ti alloys can be synthesized by non-equilibrium processes such as vapor quenching[34], physical vapor deposition[37,38], magnetron sputtering[39] and high-energy ball milling[25,34,40-42]. When using a non-equilibrium fabrication technique the large difference in melting points between Ti and Mg is no longer an issue and the solubility of titanium in magnesium can be substantially extended[39]. Mechanical alloying and physical vapor deposition are the most frequently used fabrication methods for metastable supersaturated Mg-Ti alloys[33]. Mg-Ti alloys produced by physical vapor deposition have a low density and exhibit attractive mechanical properties[33]. XRD data from Mg-Ti alloys show broad peaks, which have been attributed to a high dislocation density, small grain sizes, and high residual stresses[33]. Annealing or hot pressing of metastable Mg-Ti alloys at 500°C or above led to a precipitation of Mg or Ti from the solid solution[33]. With vapor quenching complete solid solutions were achieved with up to 27 wt.-% magnesium without formation of compounds[34].

Thermal annealing above 200°C decomposed the supersaturated solid solution Mg-Ti alloy[25]. Annealing at temperatures below 200°C for up to 1 h does not obviously change the diffraction pattern[25]. Ti peaks emerge when annealing at 300°C and become very obvious at 350°C [25]. However, even at 350°C remain broad, which means that the grain growth is slow below this temperature[25]. Below 500°C there is not much grain growth at all[25]. The nanocrystalline alloy's high stability could be due to the fine titanium particles, which might pin grain boundaries and

so retard grain growth[25]. The same mechanism could be responsible for the slow release of strain below 300°C through pinning effects of dislocations on Ti solutes[25], especially since the strain release is very fast at 200°C for pure Mg.

Synthesis of Mg-Ti composites

A group from Spain investigated the influence of the titanium volume fraction of the mechanical properties of magnesium-titanium composites in the temperature range of 25 - 400 °C prepared by powder metallurgy from titanium particles smaller than 25 µm and magnesium particles of less than 45 µm [43]. The titanium content was varied from 5 to 15 % [43]. A slight decrease in the yield strength was found with increasing titanium volume fraction, but the ductility of all composites was significantly enhanced by titanium addition[43]. The change in the mechanical properties was linked to a change in texture with increasing titanium content with which the basal texture along the extrusion direction decreases[43].

Esen et al. fabricated bioinert and biodegradable Ti-Mg two phase composites by hot rotary swaging in compositions of 50 - 80 vol.-% magnesium[44]. Their vision for the material is that new bone formation could be improved by delivering magnesium to the wound site through corrosion and then creating a mechanical interlock between the then porous titanium surface and bone that grows into the voids left behind by the dissolved magnesium[44]. XRD scans of their composites clearly show both sets of peaks for magnesium and titanium in the range of 30 - 42° 2θ.[44]

Passivation was observed in potentiodynamic polarization (PDP) scans after immersion in Ringer's Solution[44]. The open circuit potential observed in PDP scans changes with Mg content[44], but the changes are rather small (14 mV between the samples with the largest and smallest Mg content). The group observed a smaller increase in magnesium corrosion than expected from galvanic coupling with titanium[44]. Their explanation is a thin oxide layer covers the surface of the Mg particles and thus the Mg-Ti interface is separated by an insulating MgO layer[44]. In an early state of corrosion TiO formed on the titanium regions of the samples[44]. On the magnesium particles in the titanium matrix the formation and cracking of MgO_2 was observed by EDS[44]. Corrosion started at the interface between magnesium and titanium[44]. Magnesium was selectively dissolved, leaving behind craters inside the remaining Ti matrix[44]. Corrosion was

especially severe where magnesium was in contact with titanium[44], as expected from galvanic coupling. The authors think that the volume ratio of Ti to Mg together with a continuous MgO layer are the most important parameters in designing Mg-Ti composites with an appropriate corrosion rate as a biodegradable implant material[44].

Young's modulus and ultimate strength decreased with increasing Mg content in the Mg-Ti composite[44]. At the same time ductility increases[44]. Overall the mechanical properties are close to those of bone[44]. Cracks were observed to form along titanium boundaries through magnesium particles[44].

A group at Wuhan University of Technology used magnesium and titanium in different weight ratios to fabricate functionally graded materials with density gradients[45]. These materials are potentially useful as flier-plates to create quasi-isotropic compression waves in dynamic high-pressure technology[45]. The Mg-Ti composites the group fabricated by spark plasma sintering are targeting the demand for low density at the front of the flier-plates[45]. Full density was achieved with a sintering temperature of 560°C up to 75 wt.-% titanium[45]. During the sintering process a small amount of Mg-Ti solid solution was formed through diffusion of magnesium into the titanium lattice[45]. X-ray diffraction graphs reveal that the materials are physical mixtures of magnesium and titanium[45]. The aforementioned solid solution phase is not detectable in the presented x-ray diffractograms. Both Mg and Ti are distributed uniformly[45]. Magnesium acts as a bonding agent for the titanium grains[45].

Structure of Mg-Ti alloys

Structure of Mg-Ti films by vapor deposition:

Zheng et al. made a titanium alloy with 45 at.-% Mg by vapor quenching[33]. The resulting alloy is a highly supersaturated solid solution[33]. Its microstructure is made up of columnar units that grew parallel to the deposition growth direction with axes almost parallel to said direction, columnar grains and subgrains, resulting in Herring-bone patterns and parallel stripes[33].

A slight misorientation between subgrains of their [0001] direction within each grain up to 5° was observed by TEM[33]. Bright and dark contrast regions on a scale of 5-100 nm within the subgrains are caused by compositional variations: Some regions are rich in Mg, others in Ti[33].

The thickness of subgrains varied between 8 and 40 nm. [33] Within the subgrains' herringbone bands are even finer structures, ~2 nm wide, caused by variations in the composition. A series of solid solutions with different lattice parameters, but same hcp crystal structure are present[33]. The ratios of the lattice parameters for Mg and Ti rich phases were determined to be 1.06 and 1.08, both slightly smaller than the ratio (1.09) for the pure metals[33]. The ratios change from region to region, according to compositional variations on the nanometer scale[33]. Additionally, twin boundaries appeared in both Mg and Ti rich bands, parallel to the $\{10\bar{1}1\}$ planes.

Different factors could be responsible for the change in composition: periodic changes at the Ti target during evaporation could have caused the 0.5 µm bands because the electron beam is not perfectly stable[33]. Ti and Mg atoms could move locally just beneath the growth surface during crystal growth and so form lamellar Ti and Mg rich regions, which would explain the orientation approximately parallel to the growth surfaces[33].

Their explanation of the broad XRD peaks is that the XRD diffraction pattern is an average result from probed regions that are several µm in size[33]. The dislocation density of the material is not very high, therefore the strain and the variation in composition are likely to be the main factors that contribute to the peak broadening[33]. The strain of 6-8% could be due to difference in lattice parameters between magnesium- and titanium-rich areas[33]. The mis-orientation of neighboring regions and the thermal stress during manufacturing could also contribute to the strain[33]. Compositional changes with a periodicity of 0.5 µm also make a significant contribution since the lattice parameters in Mg-Ti solid solutions are proportional to their composition[33]. The slight differences in lattice parameters leads to diffraction peaks that simultaneously appear at different positions, but so close to each other that they cannot be resolved as individual peaks, but rather form a single broad peak corresponding to the probe crystallographic plane[33]. Although the presence of twin boundaries can further broaden XRD peaks, it is not expected that they play a major role in this case due to their low density[33].

Mitchell et al. investigated vapor deposited Mg-Ti alloys containing up to 25.3 % titanium by x-ray photoelectron spectroscopy[46]. The group reported lattice parameters for compositions between 1.7 and 21.8 % titanium[46]. Vermeulen et al. determined the lattice parameters of dc/rf sputtered Mg-Ti alloys with 10, 20, and 30 at.-% titanium by x-ray diffraction[46]. The samples all had a hexagonal structure, but when hydrogenated, the crystal structure changed to fcc for $Mg_{70}Ti_{30}$ and $Mg_{80}Ti_{20}$ compounds, while $Mg_{90}Ti_{10}$ formed body-centered tetragonals[46].

The microstructure of Mg-Ti solid solutions depends on several factors due to the complexity of the process.[46] That different fabrication techniques lead to different titanium distribution patterns might also explain the differences in lattice parameters between dc/rf sputtering, physical vapor deposition, and ball milling with various parameters.[46] Both experimental and calculated lattice parameters deviate from Vegard's law.[46] The variation in experimental lattice parameters paired with the calculated deviation was interpreted as the occurrence of nanoclusters in Mg-Ti alloys.[46] If titanium is allowed to segregate the volume increases relative to the quasirandom distribution in all compositions.[46]

Structure of ball-milled Mg-Ti alloys:

Liang and Schulz fabricated binary Mg-Ti alloys with a Ti content of 20 at.-% by mechanical alloying of a mixture of elemental powders in a SPEX steel milling vial and balls made of stainless steel with a ball-to-powder weight ratio 10:1 under argon. [25]. The result was a nanocrystalline Mg-Ti alloy with extended solubility of Ti in Mg compared to the phase diagram[25]. The extended solubility is credited to the isomorphous structure of Mg and Ti as well as a favorable size factor[25]. The dissolution of Ti in Mg caused the unit cell to contract from 0.0464 to 0.0442 nm^3.[25]The hexagonal crystal structure was retained, but the c/a ratio decreased from 1.624 to 1.612.[25]

The diffraction peaks of the Mg and Ti phases were observed to broaden with increasing milling time[25]. At the same time the diffraction intensities decrease and the Mg phase peaks shift[25]. No Ti peaks were visible any more after 25 h of milling, which indicates that alloying has occurred and the Ti atoms have been incorporated into the Mg lattice[25]. After a milling time of only 1 h the Ti particles are merely kneaded into the Mg matrix, but most of the Ti is dissolved after 31 h of milling[25]. However, fine Ti particles of 50 - 150 nm size are still left even at the longer milling time[25]. As Ti is incorporated into the Mg lattice the lattice parameters a and c of the hexagonal crystal structure decrease with increasing milling time[25]. For a content of 10 at.-% of Ti stable values are reached after 15 h of milling[25]. Prolonging the milling time to 40 h does not change the lattice parameters[25]. In the case of a 20 at.-% Ti alloy the a and c values stabilize after 12 h of milling[25]. For both samples the milling process has reached a stable state after 15-25 h[25]. Based on the lattice parameters it is estimated that only 8 and 12.5 at.-% Ti are dissolved in Mg when

the milling process reaches a stable state, although the nominal composition is 10 and 20 at.-% Ti respectively[25]. In XRD spectra there is a small, broad Ti peak observable around 40° in the Mg80Ti20 alloy milled for 12 h[25]. After increasing the milling time to 25 h this peak is buried in the background.[25] Conventional XRD is not sensitive to crystals under several nanometers in size embedded into a matrix[25].

The micro strain in the ball-milled Mg-Ti alloys is a function of milling time[25]. It increases to 0.7% after 25 of mechanical alloying[25]. The crystallite size decreases with milling time and reaches 35 nm after 25 h[25]. Further increasing the milling time changes neither the microstrain nor the crystallite size significantly[25].

The Mg-Ti alloys Kalisvaart and Notten synthesized with compositions between 65 and 85 at.-% magnesium by ball milling consisted of two FCC phases by using powdered reactants and a process control agent[41]. With a coarse magnesium precursor the process control agents is unnecessary and milling resulted in a hexagonal solid solution magnesium-titanium alloy[41]. The authors found in previous research that complete conversion of a binary magnesium-titanium mixture in stainless steel vials was not possible due to excessive cold-welding, but partial conversion into at least one FCC phase was proven[41]. For other studies, they doubled the ball-to-powder mass ratio to 16:1 and used tungsten carbide balls to obtain a complete conversion of a Mg65-Ti 35 mixture[41]. The reaction time for conversion of HCP magnesium and titanium into cubic structures was found to be only 5h when using stainless steel balls and a ball-to-powder ratio of 16:1[41]. In experiments without process control agents, the lattice parameter changes showed only 10 at.-% of titanium in magnesium alloys that nominally should contain 25 - 35 at.-% [41]. No pure titanium peaks were observed, though, but a considerable amount of titanium was converted into other compounds[41]. For example, a trace of FCC phase was found that contained some titanium, but this still left a discrepancy between the actually dissolved element and the starting composition[41]. It was concluded that the use of stearic acid might prevent mutual dissolution of the HCP phases, but has negligible effect on the HCP-to-cubic transition, which is more significantly influenced by impurities already present in the starting reactants[41].

The team at AIST fabricated binary Mg-Ti alloys with three different crystal structures by ball-milling[40]. The group used a planetary type ball mill[40]. The compositions ranged from 35 to 80 at.-% magnesium[40]. By varying the composition and the materials of the milling tools hexagonal close packed (HCP), face centered cubic (FCC), and body centered cubic (BCC) structures were

obtained[40]. Since different materials for milling pots and balls provide a different amount of impact on the milled powders, the milling products are determined by the dynamic energy provided by the milling setup[40]. During ball milling, magnesium deforms mainly by the basal plane slip and titanium through twinning[40].

The lattice parameters increased with increasing magnesium content for all crystal structures because magnesium has a larger atomic radius than titanium[40]. Ball milling of magnesium with titanium shifted diffraction peaks of magnesium to a higher angle and the peaks characteristic for titanium disappeared, which indicates that titanium is randomly dissolved into the magnesium lattice without changing the crystal structure[40]. The crystallite size of the HCP phase of $Mg_{80}Ti_{20}$ alloy was estimated to be 15 nm based on the width of the diffraction peaks[40].

The BCC alloy was formed in compositions with 30 and 50 at.-% magnesium and HCP structure with 80 at.-% magnesium, when using stainless steel milling tools[40]. A combination of BCC and HCP phases evolved with a composition of 65 at.-% magnesium[40]. When switching to zirconia milling pots and balls, the group achieved FCC alloys with 35 and 50 at.-% magnesium and with 65 and 80 at.-% a mixture of FCC and HCP phases evolved[40]. Thus it was concluded that the crystal structure of the milled powders was determined by the milling parameters, mainly the materials of the milling tools and composition[40]. The stress on the milled materials is affected by the dynamic energy input of the milling balls, which is determined by the mass of the milling tools[40]. The lattice parameter depends on the composition, meaning the phases with smaller lattice parameters are rich in titanium, while the phases with larger lattice parameters are magnesium-rich[40]. The lattice parameters of HCP and BCC Mg-Ti alloys followed Vegard's law[40].

It is assumed that various stacking faults are introduced to the material during ball milling, as stacking faults are formed by dislocation gliding on the basal and prismatic plans of the HCP lattice[40]. Asano et al. assume that the FCC phase was formed through the introduction of stacking faults into the HCP structure of the starting powders[40]. The stacking fault energy is comparable to the twin boundary energy in magnesium and titanium[40]. The stability of the stacking faults that are associated with dissociation of the dislocations is similar to that of twin boundaries in both magnesium and titanium[40]. The density of stacking faults introduced by using stainless steel milling tools is assumed to be higher than that in case of using zirconia, because the dynamic energy input is higher when using stainless steel balls[40]. The researchers hypothesized that the FCC structure tansformed into BCC through strain-induced nucleation due

to the introduction of stacking faults when switching to stainless steel milling tools[40]. It has been shown that titanium transformed from the ambient temperature HCP phase to the high temperature BCC phase by dissolving magnesium into the lattice during ball milling[40]. The difference in crystal structures is probably related to the stacking fault density because the crystallite size, which is sensitive to the stacking fault density, was lower in the BCC phase than in the FCC phase with the same magnesium content[40].

Wilkes' group made a Mg-Ti alloy with 9 wt.-% magnesium completely dissolved in titanium by mechanical alloying in an inert atmosphere[34]. It was found that eliminating any form of contamination is crucial for a high level of magnesium in solid solution with titanium[34]. The temperature on the outside of the vial was monitored during milling and never exceeded 60°C[34].

In the early stages of mechanical alloying magnesium and titanium are welded together, then sheared and fractured[34]. This leads to the formation of a lamellar structure, which consists of layers of either metal, each containing varying amounts of the other element in solid solution[34]. Upon prolonged milling the spacing between the lamellae decreases and the variations in composition are reduced[34]. Eventually, no lamellar structure can be observed any more and the resulting material is homogeneous on an atomic scale[34].

After 6 h of milling the authors observed a clear lamellar structure in the powder particles[34]. The layers were made up of magnesium- and titanium-rich phases, both already containing the other element in appreciable amounts[34]. The lamellae were no longer visible after 48 h of milling and a homogeneous structure with the same composition as the starting powders was obtained[34]. At this point the compositional variations between individual particles or within a single particle were negligible[34]. After 48 h of milling the oxygen content was around 3000 ppm by mass, or 0.9 at.-% [34]. Although the titanium peaks in XRD graphs were found to be shifted after 12 h of milling, the shift is much larger after milling for 48 h[34]. After milling for 48 h all magnesium was in solid solution[34].

Lattice parameter measurements are an accurate indication of solid solution formation[34]. According to the change in lattice parameters all the magnesium was in solid solution after 48 h of milling[34]. The lattice parameter change cannot be attributed to a high oxygen concentration as 15-20 at.-% of oxygen would be required for a shift of that magnitude, which is much higher than the measured oxygen content of 0.9 at.-% [34]. As a side effect such a high oxygen content

would significantly increase the hardness to over 700 H_V, whereas the measured hardness is around 400[34].

The microstructure of the alloys shows extremely fine titanium grains of about 30 nm with magnesium homogeneously distributed in them[34]. No precipitation or clustering of magnesium was observed[34]. The grains were severely strained[34].

Controlled precipitation of magnesium particles from Mg-Ti solid solutions increase the hardness significantly[34]. The precipitates are thermally stable because there is no driving force for diffusion back into the Mg-Ti solid solution[34]. The precipitated magnesium could also be oxidized in situ to fabricate a dispersion strengthened material with magnesium oxide, which has the benefit of a higher melting point [34]. Magnesium precipitates were observed to be stable in heat treated vapor quenched Mg-Ti alloys[34]. It is expected that these magnesium precipitates will allow consolidation of the mechanically alloyed powder by hot working without noticeable degradation of the properties of the material[34].

A solid solution of magnesium and titanium with composition ranging from Ti56:Mg44 toTi50:Mg50 has been achieved by Maweja et al. by high-energy ball milling[42]. To avoid contamination by the stainless steel vial, the vials were milled with pure titanium powder to form a titanium layer on the vial and ball surfaces before milling the sample material[42]. The structure obtained was FCC and BCC titanium-magnesium solid solution matrix with small amounts of a titanium-rich HCP-phase[42]. After half of the milling time (24 h) an intermediate FCC solid solution of titanium in magnesium was observed, in which the titanium-rich crystallites were twinned[42]. Release of the lattice strain energy seems to trigger the formation of solid solution of magnesium and titanium by ball milling[42]. The twinning might also indicate a strain-induced martensitic transformation of the metastable ω-FCC into BCC lattice[42]. Preferential sites for the heterogeneous nucleation of twins were crystallite boundaries, which also served to release strain energy and thus form a solid solution[42].

Properties of Mg-Ti alloys

Corrosion behavior of Mg-Ti alloys:

A group from Kansai University developed a Ti-Mg alloy that shows resistance to a weak acid solution with fluoride ions for dental implants[36]. Ti tends to dissolve in the presence of fluoride

ions, which causes problems with dental implants because toothpaste contains fluoride ions[36]. Their approach to improving the corrosion resistance of Ti is to identify a metal fluoride that is difficult to dissolve in water, and then alloy Ti with this metal[36]. This is expected to improve the corrosion resistance because a thin, insoluble film of metal fluoride will form on the alloy surface and passivate it[36].

Alloying was carried out by placing 2 mm thick Ti plates into a graphite crucible with Mg granules and heating it up to 950°C[36]. At this temperature the Mg was present as liquid and vapor, so that the samples could be dipped into the liquid Mg or hang in the vapor[36]. Both methods allowed Mg to diffuse into the Ti samples to form Ti-Mg alloys[36]. A homogeneous distribution of Mg throughout the samples was achieved by exposing the samples to Mg vapor for 430 h, which resulted in a Mg concentration of 0.22 at.-%[36]. Hardness increased close to linearly with increasing Mg concentration from the edge towards the inside of the samples[36]. As hardness and Mg content correlated linearly, it was concluded that the Mg presence increases the hardness through solid-solution hardening[36]. With 0.2 at.-% of Mg the hardness increased to 1.2 times the value for pure Ti[36]. The same sample exhibited the highest improvement in corrosion resistance in a test solution containing fluoride ions at the concentration of toothpaste with a pH of 4 at 25°C, approximately 80 times higher compared to Ti[36]. This went along a shift in the transitional potential and a drop of peak current density, which both increased with exposure of the Ti samples to Mg during fabrication[36]. XPS confirmed the presence of passive MgF_2 on the surface of the alloyed samples, which prevented dissolution in the weak acid fluoride solution that is common for pure Ti[36].

Corrosion studies of binary Mg-Ti alloys fabricated in a wide range of compositions (0 - 100 % Ti) by magnetron sputtering deposited on glass slides have been published by Xu et al.[39]. Their idea was that Ti as a strong passivating element might improve the passivity of Mg[39] and reduce its fast anodic dissolution in NaCl solutions. While many conventional Mg alloys developed for structural applications (e.g., the Al containing ones) have intermetallic phases with a positive free corrosion potential compared to the Mg matrix resulting in micro-galvanic corrosion that reduces the corrosion resistance of the alloy, it is expected that a single-phase solid solution of Mg and Ti will be more corrosion resistant[39]. The research group found that alloying Mg with Ti made the alloy more corrosion resistant than pure Mg in saturated $Mg(OH)_2$ solutions with and without 0.1 M NaCl added[39]. The higher the Ti content the more corrosion resistant were the

alloys in polarization experiments. $Mg_{20}Ti_{80}$ alloy was found to not show any signs of corrosion damage after the tests.

Corrosion products on pure Mg appeared white, on Ti they appeared black, and on Mg-Ti alloys black or black and white[39]. The group furthermore found from XPS analyses that Mg80Ti20 contains $Mg(OH)_2$ and MgO on the surface after corrosion, whereas an alloy containing 80 at.-% of Ti only forms MgO. Both materials form TiO_2, too. TiO_2 and MgO mixed form a passive film that protects the underlying material from Cl^- ions and thus improve the corrosion resistance of Mg-Ti alloys. $Mg(OH)_2$ can hardly protect against corrosion because it forms a mechanically weak layer[39].

The passivity determined from the electrochemical experiments is only half of the contribution to the corrosion behavior[39]. The material has different mechanical properties depending on the composition, so cracks and layers peeling off were observed for some samples, but not for others[39]. This occurrence changed the corrosion protection ability measured by immersion tests with respect to the polarization measurements in some cases[39]. A passive regime was only found for alloys with at least 40 at.-% Ti[39].

This improved corrosion resistance was linked to the presence of a strong oxide layer, which could be TiO_2[39]. XPS spectra revealed that samples with lower titanium content had magnesium oxide and magnesium hydroxide on their surfaces, which is not very protective[39]. Magnesium can corrode easily in areas where it is covered by a mechanically weak and unstable $Mg(OH)_2$ film, but a mixture of the stable TiO_2 and MgO can form a passive film, which was credited with preventing corrosion attacks, and thus improving the corrosion resistance of Mg-Ti alloys[39].

Mechanical and hydrogen storage properties:

After compaction the powders milled for 48 h has a Vickers microhardness of around 400 kg/mm², compared to values between 210 and 250 for vapor-deposited Mg-Ti alloys with the same composition[34]. Mg was homogeneously distributed on the nm scale, so that the material is homogeneous chemically and microstructurally[34]. The investigated Ti-Mg alloy showed appreciable deviation from Vegard's law, which is common among hexagonal binary alloys[34].

It was concluded that the nanostructure, higher Ti content, and reduced c/a ratio of the Mg-Ti alloys lead to altered mechanical properties and enhanced hydrogen storage capabilities[25].

Unexplored opportunities

To the author´s knowledge there has not been any investigation of the electrochemical response of binary Mg-Ti alloys in simulated physiological conditions yet. In the Mg-Ti-Si work samples were tested in solutions with clorine and sulphate ions because they react differently to those two kinds of ions[38], which are both found in the human body and are commonly used in in vitro experiments, e. g., Hanks´ Solution.

Ball milling and mechanical alloying

Introduction

Mechanical alloying is an effective far-from-equilibrium method that can change the thermodynamic, mechanical, and chemical properties of materials[47]. The technique was developed in 1966 by The International Nickel Company in an effort to combine oxide dispersion strengthening with gamma prime precipitation hardened superalloys for gas turbines[2].

Mechanical alloying is an alternative alloying approach at room temperature for the fabrication of alloys and advanced materials[2]. Originally, the term milling referred only to breaking down particles to smaller sizes[2]. However, its great potential for synthesizing new phases, new materials, or enhancing the physical and mechanical properties of materials was recognized[2,40]. High-energy ball milling gained a lot of attention as a non-equilibrium process for materials with nanoscale microstructures[47] . Mechanical alloying beyond the thermodynamic equilibrium solubility limit can lead to the formation of amorphous metals in a vast range of alloys[47]. Amorphization is considered to be a result of both mechanical alloying and the incorporation of lattice defects into the crystal lattice [47] . It occurs by intermixing atoms on the atomic scale, hereby softening and destabilizing the crystalline lattice and driving the crystalline solid solution outside its range of stability[47].

Ball milling has been used to make a wide range of materials, including[2]:

- Oxide dispersion strengthened alloys
    - Ni-base superalloys
    - Ti-base alloys
- Equilibrium phases
    - Solid solution alloys
    - Intermetallic compounds
- Non-equilibrium
    - Amorphous alloys
    - Quasicrystalline materials
    - Nanocrystalline materials
- Composites

- Metal-matrix composites
- Ceramic-matrix composites

It is also a powerful tool for processes that involve inducing a chemical reaction, for example, reducing metallic oxides in the presence of reducing agents (Mechanical Solid State Reduction) and other gas- or liquid-solid reactions, e.g., producing nitrides by milling an elemental powder in nitrogen[2].

Mechanical alloying starts by mixing the individual powder constituents[2]. At the beginning of the ball milling process the starting powders agglomerate and then continuously disintegrate until the particle size reaches its final state[2]. Their morphology is changed once they get crushed between colliding balls and the vial walls[2]. The effect of being subjected to colliding balls depends on the type of powder material[2]. Initial collisions flatten the ductile component[2]. Over time they are cold-worked through cold welding and mechanical deformation[2] (Figure 2). Freshly created surface of the constituents are brought into immediate contact and cold weld together to form layered structures of composite particles with various stoichiometry. Continued milling refines the microstructure through deformation and cold welding[2]. The hardness increases with progressing milling so that the agglomerated particles fracture into smaller and smaller pieces[2]. During ball milling repeated mechanical deformations caused by the collision of balls on powder particles introduce strain in the powder and fracture the crystals into smaller pieces, which can be as low as the nanometer range[48].

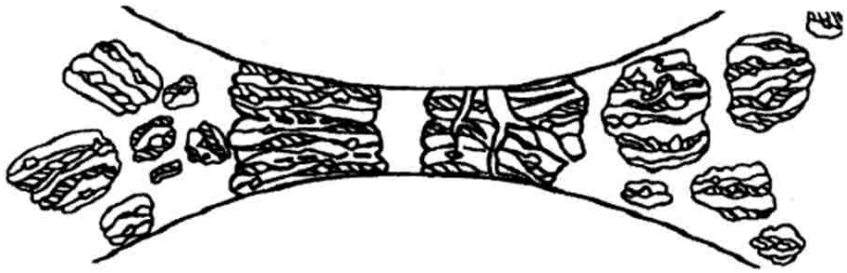

Figure 2: Crushing and cold-welding of particles upon the impact of the milling balls[2]. Reprinted from M. Sherif El-Eskandarany, Mechanical alloying for fabrication of advanced engineering materials, Introduction, p. 17, Noyes Publications/William Andrew Publishing, Norwich NY, Copyright ©2001, with permission from Elsevier.

What makes mechanical alloying unique is the solid state reaction that takes place between the freshly formed surfaces of the broken down material at room temperature[2]. This technique is a powerful tool to produce alloys and compounds that are difficult or impossible to make with conventional processes that involve melting, for example due to poor wettability[2]. This pioneer process that is often turned to when trying to fabricate materials that are impossible to yield through conventional powder metallurgy methods, such as coating hard phases with soft ones or the formation of several binary aluminum-based amorphous alloys[2].

Mechanical alloying is a synthesis route that can produce super saturated solid solutions and very fine grained microsctructures[34], with a possible refinement of the internal structure of the powder particles down to nanometer scales[47]. High energy ball milling is capable of achieving alloying on an atomic scale by repeated cold welding, fracturing, and deformation[49] to yield a material with chemical and microstructural homogeneity[34]. Mechanical alloying can be used to produce large volumes of material[34]. In mechanical alloying the alloy composition is directly controlled[34] by filling the milling jar with the starting materials in the desired composition. Asano et al. showed that by varying the milling parameters, especially the materials of the milling pots and balls, the crystal structure of ball-milled powders can be altered[40].

Aside from reducing particle size milling has also been used as a means of mixing/blending and particle shaping[2]. Mechanical alloying can be carried out in high-energy ball mills (e.g., planetary type, centrifugal type, and vibratory type) as well as low-energy tumbling mills with balls or rods[2]. One of the components should be fairly ductile to act as a binder, the others can be ductile or brittle metals, intermetallic compounds, nonmetals, or refractory compounds[2].

The following factors play an important role in fabricating homogeneous materials and determine particle size distribution, degree of disorder, amorphization, and final stoichiometry[2]:

- Type of mill (high or low energy)
- Material of the milling tools (e.g., stainless steel, tungsten carbide)
- Types of milling media (balls or rods)
- Milling atmosphere (e.g., reactive gasses, inert)
- Milling environment (dry vs. wet milling)
- Milling media to powder mass ratio
- Milling temperature (e.g., uncooled or cryo-milling)
- Milling time

The milling time is influenced by the particle size of starting powders. If they are too coarse it can take significantly longer to obtain the desired end product.

The most commonly used mill types in research are the planetary and vibratory ball mills[2]. In the planetary ball mill the balls and milling stock fly off the inner walls of the milling pots while the centrifugal force can reach up to twenty times gravity with speeds of 360 rpm[2]. The milling vials and the supporting disc onto which the vials are mounted turn in opposite directions so that the centrifugal forces alternate between synchronized and opposite[2]. Milling vial sizes vary from 45 to 500 mL so that different amounts can be synthesized[2]. By design at least two milling vials are processed at the same time, further increasing the milling load that can be handled per run. Vibratory type ball mills by design have much smaller capacities (around 10 mL volume)[2]. In vibratory type ball mills the milling vials are shaken back and forth or in a figure 8-motion (Figure 3).

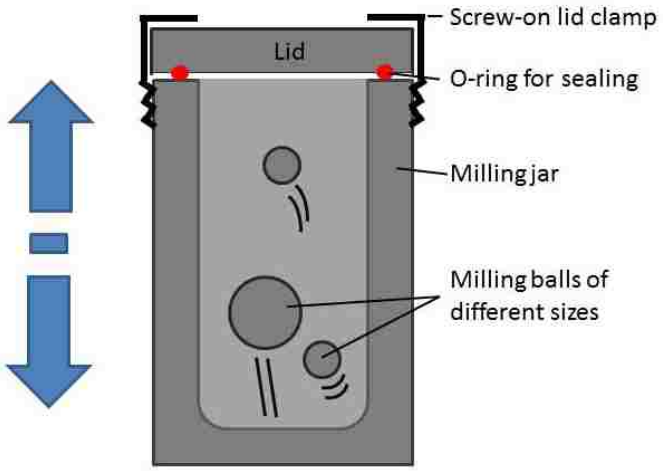

Figure 3: Schematic cross section through a milling jar during milling in a vibratory type mill.

To ensure an inert atmosphere and avoid oxidation of the powder during ball milling the vials have to be filled and sealed in a glove box under inert gas[2]. The milling atmosphere is a crucial factor because fine powders have a high surface-to-volume ratio and thus readily react with oxygen, nitrogen, and hydrogen[2]. This effect can be exploited for reactive milling, but is an undesired effect when making metallic alloys.

High-energy milling forces result from high frequencies and small amplitudes of vibration[47]. Ball mills are preferable for small batches of powders (e.g., up to 10 mL) as they are highly energetic

and reactions take place faster than in other types of mills[47]. Because the kinetic energy of the balls is a function of their mass and velocity, dense materials (e.g., steel) are preferred over ceramics[47] . The collision time of the balls is generally about 2 μs [47]. The required milling time in low-energy ball mills is usually much longer than with high-energy ball mills, typically around a factor of 10, depending on the ball-to-powder mass ratio.

Although ball-milling is said to be a room temperature process the milling vials can heat up to significantly higher temperatures than room temperature from the kinetic energy transferred from the balls to the vial upon impact. The temperature rise during this process can be as high as 100 to 200°C[47].

Due to the high impact speeds of the balls there is a concern for contamination from the milling tools. However, it was found that the concentration of iron contamination decreases significantly from the first run with unused tools to the second and even more to the third run[2]. During the first milling cycle the tools get coated with the milled ductile material so that in subsequent runs the milled powders are no longer exposed to the bare surfaces of the tools, but the same material, which greatly reduces contamination[2]. Contamination-free processing is the key to success in mechanical alloying because it guarantees that solid solutions form without chemical reactions to nitrides or oxides[34]. It is now possible to virtually eliminate contamination during milling[34]. The clean processing technique allows making solid solutions with high purity[34].

The rate of alloying or amorphization strongly depends on the kinetic energy input[2]. Alloying or amorphization is also affected by the collision frequency of the powder particles inbetween balls and walls[2]. Therefore, increasing the ball-to-powder mass ratio accelerates the formation of amorphous/alloyed phases[2]. There is an optimal ratio and increasing the ball-to-powder mass ratio beyond this threshold transforms the metastable material back to its crystalline state or de-alloys it, probably due to the high kinetic energy being transformed into heat[2]. A high ball-to-powder mass ratio also yields finer particles at the end of the milling process, but leads to increased contamination from the milling tools[2].

It is important to strike a balance between the cold welding and fracturing events during ball milling to successfully alloy[2]. To reduce particles joining and promote fracturing a processing control agent can be added that inhibits clean metal surfaces from welding together[2]. This process is called wet milling[2]. Cooling can also be helpful[2], for example by switching to cryo-

milling where the milling vial is immersed in liquid nitrogen during milling. This works best for materials that become brittle at low temperatures (e.g., bcc metals).

Effects of ball-milling on pure magnesium

High-energy ball milling or mechanical alloying of nanostructured magnesium compounds has sparked interest in the research community working on hydrogen storage materials[50]. During ball milling the native oxide layer on magnesium is broken up, thus exposing fresh active surfaces for hydrogen absorption[50]. The formation of numerous defects during milling can act as hydride nucleation sites[50]. A high concentration of grain boundaries in nanostructured materials facilitate hydrogen diffusion into the material[51].

Grosjean et al. investigated the influence of ball-milling with milling times varying from 30 min to 40 h on the morphology, structure, chemical composition, and electrochemical corrosion behavior of magnesium and found that milling affects the morphology of magnesium powders.[24] After 40 h of milling the particles become irregular and the grain size distribution varies from few µm to several tens of µm.[24] The larger particles are formed through cold welding that occurs concomitantly to the repeated fracturing of particles during milling.[24] In general, the particle sized decreases with increasing milling time.[24] A steady state is reached after 40 h of milling with a mean particle size of 20 µm, compared to 40 µm of unmilled magnesium powder, which increases the specific surface area of the milled powders.[24] Milled magnesium powder is not constituted of very small particles despite the long milling time due to cold-welding[48].

In x-ray diffraction graphs the diffraction peak position does not change from milling, i.e., the lattice parameters remain constant.[24] This indicates that there is no alloy formation or contamination from the milling tools.[24] However, MgO peaks appear in the milled powder and their intensities increase slightly with milling time.[24] Texture is largely unmodified by milling, except for an increase in the (002) peak intensity after 30 min. of milling.[24] The same texture evolution was observed when running x-ray diffraction scans on compressed magnesium powder which has been linked to a preferential orientation along the c-axis being induced in the initial stage of milling through cold welding of the powder particles.[24] This observation could be explained by the low energy needed to carry out a deformation by slip perpendicular to the c-axis. At the beginning of milling or during cold pressing of untreated magnesium powder, when

low deformation energy is involved, the main deformation is caused by dislocations through slip perpendicular to the c-axis, resulting in (002) texture.[24] During prolonged milling (over 3 h) large amounts of energy accumulate in the powder, enabling dislocations to move in all directions so that the deformation is randomized.[24]

The diffraction peaks of milled magnesium are broadened, indicating a substantial decrease in crystallite size during milling[50]. The authors observed that the crystallite size was reduced to 34 nm after 10 h of milling, from over 100 nm of the unmilled state[24,50]. The crystallite size does not significantly decrease when extending the milling time[24], indicating that a stable state was reached. This finding is consistent with other reports of 40 nm crystallite size in magnesium after 6-7 h of milling.[24] Thus, nanocrystalline magnesium can be synthesized by ball milling.[24] The crystallite size for magnesium after ball milling is high compared to other metals processed in the same way because its melting temperature is relatively low, facilitating the recovery process rather than plastic deformation during milling[24]. The decrease in crystallite size goes along with an increase of internal strain, which is linked to lattice distortion at grain boundaries and higher dislocation density after prolonged milling[50]. Strain measured after 10 h of milling is about 0.04% [50]. The maximum strain after milling for 40 h is low with 0.056%, which confirms magnesium's high potential for recovery during milling.[24] No MgO enrichment was detected on the surface of milled magnesium, which confirms that the oxide is homogeneously distributed throughout the bulk of the material rather than segregating on the surface[50].

Iron contamination from erosion of the milling vials was found to linearly increase with milling time, yet is very low (only about 0.05 wt.-% after 10 h milling[50] and 0.09 wt.-% after 40 h of milling[4], compared to 0.04 wt.-% before milling[50]), much lower than the contamination found for other metallic powders milled with steel grinding tools, which are typically in the range of 1-4 wt.-% of iron[24]. The low contamination can be attributed to the low strength and hardness of magnesium compared to steel.[24] The nitrogen content is less than 0.2 wt.-% after 40 h of milling, but the oxygen concentration is much higher than expected considering that milling was performed under argon.[24] This could be due to the larger affinity of magnesium to oxygen.[24] The oxygen content does not increase linearly as the nitrogen content, but shoots up abruptly after the first milling step, saturating at around 2.6 wt.-% after 10 h of milling.[24] This oxygen concentration is caused by the presence of 6.5 wt.-% MgO for powders filled for 10-40 h, compared to 1.0 wt.-% for unmilled magnesium powder.[24] The oxygen contamination is too

large to be attributed solely to the exposure of fresh magnesium on the surface of the milled particles to air when opening the vials after milling, so that it is hypothesized that the oxidation occurs during milling.[24] Oxygen could be in contact with magnesium during milling from oxides on the surface of the milling tools, residual air in the milling container, or air leaks.[24] The increase of the oxygen content with milling time indicates an increasing sensitivity of magnesium to oxidation through the fracturing processes occurring during milling, which exposes fresh and highly reactive magnesium surfaces before subsequent cold welding.[24] The initial oxygen layer on the particles is incorporated into the bulk of the material during fracturing and cold-welding.[24]

Spark Plasma Sintering (SPS)

This technique is a fairly recent invention to facilitate fabrication of bulk material from powders[1]. The process is also called Electric Field Assisted Sintering (EFAS), a term that hints at the electric field applied during sintering which brings advantages over conventional sintering techniques because it allows for increased densification rates while requiring lower temperatures and shorter holding times than conventional sintering methods[52]. Alternative names for the same technique are field-activated (or assisted) sintering (FAST), Plasma Activated Sintering (PAS)[53], electric pulse assisted consolidation (EPAC)[54] and pulsed electric current sintering(PECS)[55,56].

SPS works for both conductive and non-conductive samples[57] and can consolidate a large variety of advanced materials, both traditional and new[56]: Metals (e.g., titanium alloys[58] and hard alloys[59]), semiconductors[60], ceramics (e.g., bioceramics[61]), and composites have been successfully sintered by SPS, but the technique is also capable of consolidating polymers (e.g., thermosetting polyimide[60]), joining metals, promoting crystal growth, and even triggering chemical reactions[60,62]. It has also been used for nanostructured[63,62] and amorphous materials, intermetallic compounds, highly refractory metals, functional graded materials[64], porous materials[65], diamonds[66] as well as metal and ceramic matrix composites, all of which are difficult or impossisble to sinter with conventional sintering methods [55,60]. SPS has thus contributed to the development of innovative materials that cannot be prepared by any other technique[2]. The versatility of SPS has been proven in the past two decades on thousands of materials in a variety of compositions and structures by hundreds of laboratories around the world[54].

Using electric current discharge for acceleration of the densification of metal and ceramic powders is an idea that dates back to the early 1900s, when patents on this issue were filed[54]. Commercial machines using the technique became available in the late 1980s[54]. A pulsed electric field is applied to powders for very quick consolidation while preserving the particle sizes in the densified material[54].

SPS is a highly effective way of producing bulk samples with pre-determined shapes while retaining the nanostructure[54]. In many cases SPS treatment has positive effects on the properties[54]. SPS can produce net and near net shapes of symmetrical and relatively simple parts, meaning that the powder is directly turned into a finished part in one processing step[57].

Operational expenses for SPS are only 20 to 50 % of those for conventional sintering methods, primarily because it is up to twenty times faster: while most conventional systems take hours, SPS sintering is done in mere minutes[57].

The main characteristics of SPS are the spark plasma created by a pulsed direct current[60] , as well as a fast heating rate of up to 1000°C/min [56]and short holding times (0 - 10 min. in most cases)[55]. Sintering is achieved at low temperatures, about 200-300°C lower than most conventional techniques[55]. Due to these advantages SPS is the most popular ultrarapid sintering technique[55]. At the same time it has been found to suppress grain growth[52], possibly due to the short processing time and comparatively low temperatures.

The powder is loaded into a graphite die [56]and pre-pressed before sintering. The sintering chamber is kept under vacuum or filled with inert gas to avoid oxidation[57,67]. During the sintering an even higher load is applied uniaxially. In addition, a pulsed DC current passes through the electrically conducting die and the sample throughout the whole sintering process. Due to this configuration the die itself acts as a heat source and the powder is heated from outside and inside[62]. As there are no heating elements with large heat capacity involved, very fast heating and cooling rates can be achieved thanks to the efficient transmittance of heat to the sample[60,62]. The holding times can be shortened significantly compared to conventional hot pressing techniques and comparable densities can be obtained at much lower sintering temperatures [62].

Sintering retardation is proportional to the surface oxide thickness and caused by the stability of oxides up to high temperatures and limited solubility for oxides in the metals[52], thus it is important that the surface of the particles at to be sintered are cleaned from oxides and other contaminants at the beginning of the process[52]. SPS can compact metallic nanoparticles covered with insulating surface oxides because surface effects have an important influence on inter-particle neck formation[52]. At the onset of the sintering process dynamic surface cleaning of metallic particles through electric field-induced dielectric breakdown (loss of capacitance in insulating thin films) takes place[52]:

The applied electric field polarizes the metal oxide layer, which causes the formation of oxygen vacancies with a formal positive charge, which trap electrons[52]. If the field is applied for a long time an increasing number of those oxygen vacancies form until a critical number is reached[52].

Finally, this leads to a local electrostatic field across the dielectric equivalent to the breakdown voltage of oxide[52]. This local field is greater than the externally applied field[52]. This local field enhancement drives the electrothermal depletion of the surface areas of oxygen[52]. In oxides the electric field generates spark plasma discharges in voids and pores between the particles[68]. Oxide migration is further fueled by Joule heating[52]. When the oxygen moves away from the inter-particle contacts small filaments of metal can form to connect two metal particles[52]. With conventional sintering techniques powders covered with oxides cannot be sintered because the oxide layers cannot be removed by heat[2]. Omori describes how aluminum particles covered with an oxide film cannot be sintered by conventional sintering methods because the oxide film cannot be broken up or removed by heat[60]. Although even in SPS the oxide layer cannot be removed completely and persists in the sintered product, during SPS processing the plasma can make holes into the oxide film[60,55] so that the thermal diffusion ability of the material to be sintered is enhanced[55]. The interval of plasma generation corresponds to the current pulse frequency[60]. The high frequencies of the cycles transfer and distribute the heating due to sparks and Joule phenomena (locally high temperature) uniformly throughout the sample, resulting in a rapid and thorough heat distribution[57,69].

Particle and grain growth are restricted[55] due to the rapid cooling rates, by the speed of the process and because only the surface temperature of the particles rises quickly[57]. The rapid processing together with low sintering temperatures allows a tight control over grain growth and the microstructure, retaining the particles' characteristics and ensuring high uniformity[57]. Although as in all sintering processes, grain growth occurs during SPS[67]. As a results the samples show a high homogeneity and consistent densities[57]. The energy of the spark plasma is only weak at the particle contact points, but in combination with the applied stress small holes are created in the oxide films[60], allowing the particles to fuse through diffusion of atoms. The spark discharge also removes adsorptive gasses and other organic impurities present on the particle surfaces[55]. As oxide layers and contaminates are vaporized from the particle surfaces during SPS, stronger bonding is achieved between particles because material of higher purity is exposed[57]. SPS can even sinter dissimilar materials without the necessity of producing a liquid phase on the materials with lower melting points[57]. When fabricating composites, even at low densities the homogeneity is high[57].

Fine impurities and gasses on and between the surfaces of the particles aid the initiation of the spark discharges in the gaps between particles[57]. The spark discharges momentarily create local high temperatures of up to 10,000°C, which vaporizes the impurities and the surface of the particles in the area of the spark[57]. The underlying material melts and via electron draw during the on time of the current and the vacuum in the following off phase the liquidized surfaces are drawn together and create necks[57]. Joule heating and pressure gradually let those necks develop and grow[57]. Radiant heat additionally allows for plastic deformation on the surface of the particles, a necessity for achieving high densities[57]. During the process heat is concentrated on the surfaces of the particles[57].

The operational temperatures, as monitored, vary between 200 and 2,400°C, which is commonly 200-500°C lower than conventional sintering methods[57]. SPS has therefore been classified as a low-temperature sintering method[57]. The pressure and temperature ramp-up and holding times at the sintering temperature are short, approximately 5-25 min.[5768]. The temperature measured inside the die can be very different from the temperature experienced by the sample: Zhang et al. report that they measured the temperature in the center of the discharge location was 2088°C, whereas the temperature measured at the die only rose to 992°C[55].

Plasma is created during the sintering process, which is created by the high DC pulsed current applied to the electrodes[55]. Zhang et al. report evidence for spark discharge during spark plasma sintering based on visual observations and the microstructure of their sintered samples[55]. The group's hypothesis is that spark plasma is generated in the microgaps between particles from the electric discharge[55]. The spark plasma is generated in the gaps due to the electrical discharge between powder particles at the beginning of the DC pulse energizing[55]. The electric discharge results in spark plasma formation and local spark impact pressure. Spark plasma impact is due to the mechanical pressure caused by the spark plasma, but does not greatly influence the process[60].

Zhang et al. explain that the microdischarge between two powder particles stops as soon as a connection is formed between them[55]. The local temperature then decreases rapidly, resulting in a unique microstructure due to the fast cooling rate[55]. No insulators or heating elements with large heat capacity are used, but the graphite die is heated directly by electric current, which

results in rapid heating and cooling[60]. Cooling is usually achieved by letting the die cool off by itself or with argon gas flooding[56].

Joule heating, resulting from the electric pulses[68], and plastic deformation during the process contribute to the densification[55]. Through a combination of these effects the sintering efficiency is improved significantly[55]. Pressing the powders is also a requirement to achieve plasma, because loose particles have too high a resistance and would not allow current to pass through[60]. The external pressure enhances contact between the electrodes and the sintered sample[68]. Pressure also plays an important role in curbing particulate growth and it influences the overall density[57]. In SPS accurate manipulation of the applied force can enhance the process[57]. Higher forces multiply the spark initiation throughout the sample because the material moves under pressure, which is especially important during out-gassing[57]. Too much and too little pressure can have negative influences on the sample quality[57]. In large samples requiring high densities the force is often applied in stages to enhance out-gassing and electrical diffusion[57]. The physical compression during SPS can be up to 300 t [57].

SPS offers improvements over conventional sintering methods, such as hot pressing and hot isostatic pressing[57]. The advantage of SPS when sintering materials that are by nature covered with a layer of oxide is that the pulsed current in conjunction with the applied pressure breaks the oxide layer locally, allowing diffusion and thus bonding between particles through the holes in the oxide layer, enabling even materials that are challenging to process with conventional sintering methods to sinter to full density[70]. Another benefit is its high sintering speed[56] and thus short processing time[68]. Several characteristics of SPS make it a very fast densification process: rapid heat transfer, higher mechanical pressure than in hot pressing, fast heating and cooling, and the pulsed current, exposing the sample to an electric field. The mechanical pressure helps remove pores and to facilitate diffusion. The pulsed current passing through the sample has the greatest effect on higher densification. A disadvantage is that the sample sizes need to be kept small[68].

SPS involves a complexity of thermal, electrical, and mechanical processes[55]. The combination of spark discharge, Joule heating, electrical diffusion, and plastic deformation during the SPS process achieves fast and efficient sintering[55]. No one single mechanism can explain the efficienccy of SPS[71]. Each of the active mechanisms contributes in a different way to different stages of sintering[71]. It was found that heating rate through thermal processes alone, i.e., in the

absence of an applied field, does not usefully contribute to the densification of nano-sized powders[71]. Electric fields contribute significantly to the densification of same powders[71]. With non-contact fields, there is an opportunity for applying the electric fields to even more operations than just uniaxial pressing[71]. However, the exact SPS mechanism is still under debate[55] and it is still not completely understood why SPS works so well[54].

Due to the rapid spark diffusion and the consistent heat throughout the sample, the sintered parts experience very little internal stress when fabricated with SPS[57]. The heat is consistent on the outside and center of the part[57]. Together with the high speed of processing this eliminates much of the internal stress experienced by conventionally sintered samples[57].

SPS can achieve nearly 100% theoretical density with any material, be it metallic, ceramics, or composites[57]. True seamless bonding can be created through SPS as dry and liquid phase bonding[57]. Even dissimilar metals can be liked in this way[57]. When bonding rough surfaces loose powder can be applied between the surfaces to ensure a solid bond[57]. No binders are needed when using SPS[57].

As SPS is gaining in polularity, modifications to the technique have been proposed, for example a modification of the die material and set-up to allow for high pressures of up to 1 GPa by Anselmi-Tamburini et al. [72]. Morsi et al. modified SPS into an extrusion process[73]. A research group from Rostock, Germany, suggests integrating a gas quenching system into SPS to turn it into rapid cooling SPS, so that it could be used for sinter hardening[56]. Sinter hardening is a method used in powder metallurgy in which the fabricated parts are quenched right after sintering[56]. This saves energy and thus costs compared to conventional hardening where the parts are re-heated to the hardening temperature[74]. Sinter quenching is performed with gas instead of oil, resulting in better dimensional stability and cleanliness of the parts[56]. Although SPS has been successfully applied in research, industrial applications have been comparatively limited[71]. The biggest issue with translation from laboratory to production is the problem of scalability, which is problematic technically and practically[71]. From a technical perspective maintaining a minimal sample temperature distribution, the essential contribution of currents and fields to sintering, uneven pressure distribution, and the understanding of the mechanisms of SPS all need to be solved for scaling up[71]. On the practical side, extremely high currents are needed to achieve a given hold temperature or high heating rates, which has inherent implications for the efficiency of SPS compared to other sintering techniques[71]. With the current

technology SPS faces real limitations when increasing the sample sizes and is related to the power requirements to achieve high temperatures and heating rates of the dies, plungers, and parts themselves[71]. When the part diameter exceeds a few centimeters the amount of current necessary to maintain the typical heating rates of SPS (> 100°C/min) become impractical[71]. The difficulty of maintaining a sufficiently even temperature distribution across the sample also increases with larger diameters[71]. Thus, the nature of SPS in its current form does not readily lend itself to scaling up beyond sample diameters of around 1 cm[71].

An alternative to SPS could be electric pulse sintering (EPS), which is a sintering method utilizing high electric discharges of several kilovolts, which is much higher than the low voltage used in SPS, and electric current densities of over 10 kA/cm² [75]. In this technique pressures of up to 10 GPa can be applied[75]. Usually the powders are consolidated through a short (less than 0.1 s in duration) single electric pulse[75].

Corrosion behavior of magnesium and titanium in physiological environments

Magnesium alloys are attractive materials for their low densities and high strength-to-weight ratios, but their low corrosion resistance limits their applications[76]. With the lowest standard potential (-2.38 V vs. standard hydrogen electrode (SHE)) of all engineering metals (Only Na, Ca, K, and Li have lower potentials), magnesium is prone to corrosion in physiological environments[6]. Due to its extremely low potential magnesium is widely used for sacrificial anodes to protect cathodic metals.[20] The actual corrosion potential, however, is influenced by a number of other factors, including the surface state and the environment[6]. For example, in a diluted chloride solution the corrosion potential of Mg is -1.7 V vs. SHE [6].

The pH value is a crucial factor as well[6] because corrosion is greatly reduced at higher pH[38]. Because magnesium corrosion is so sensitive, an increase in the pH in in vitro experiments due to magnesium corrosion falsifies the results because it changes the environment drastically and in an unrealistic way[6]. With increasing pH the corrosion rate of magnesium decreases monotonically and full passivation is reached at a pH of 12 [77].Above a pH of 11.5 the protective layer of $Mg(OH)_2$ forming on the surface of Mg in aqueous environments becomes stable, which leads to low corrosion rates in alkaline solutions[27]. If a saline test solution is poorly buffered the same effect arises[27].

It has been suggested to buffer corrosion test solutions with 2-(4-(2-hydroxyethyl)-1-piperazinyl) ethanesulfonic acid (HEPES) to avoid any changes in pH [77], but it has been shown that alkalization occurs in vivo, so preventing any pH change might lead to unrealistic environments that do not accurately reflect physiological environments. On the other hand, it is easier to compare quantitative results. Fixing the pH will also prevent some naturally occurring effects, such as deposition of salts with increasing pH. During corrosion the degrading material might interact with the corrosion test solution. Even if the pH stays the same, the solution might become depleted of the constituents that react with the sample during corrosion and should be replaced at certain intervals.

The low corrosion resistance of magnesium in aqueous media is caused by a high dissolution tendency of magnesium at a pH of less than 11, the permeability and low stability of the magnesium hydroxide film formed on the surface, and the sensitivity of magnesium to impurities and alloying elements that promote galvanic corrosion[24]. The corrosion behavior of

Mg alloys mainly depends on their alloying elements[27]. Mg alloys with two phases tend to have an accelerated corrosion rate due to the formation of microgalvanic coupling between the matrix and the secondary phase[27]. Iron impurities have a big influence on Mg corrosion, unless they are below 40 ppm[77]. Microstructural features, such as grain size, grain boundary and phase distribution, influence the corrosion behavior of Mg alloys[6]. Grain refinement, changing the density and distribution of grain boundaries, not only influences the mechanical properties, but the corrosion rate as well[6]. The influence of environmental, structural, and chemical factors on the corrosion behavior of magnesium and its alloys is well known[24].

Magnesium corrosion reactions

The review of corrosion mechanisms of magnesium alloys has mainly been motivated by their use in the transportation industry[38]. Magnesium corrodes slowly in air, but very quickly in aqueous solutions, especially in the presence of chloride and sulphate ions[20]. The degradation processes of magnesium are complex[20]. In aqueous solutions the corrosion of magnesium is coupled with a reduction of water molecules, resulting in the production of magnesium hydroxide and hydrogen gas from combining protons[24]:

$2\ H_2O + 2\ e^- \rightarrow 2\ OH^- + H_2$ (cathodic reaction) (1)

$Mg \rightarrow Mg2^+ + 2\ e^-$ (anodic reaction) (2)

$Mg + 2\ H_2O \rightarrow H_2 + Mg(OH)_2$ (overall reaction)[76] (3)

The following chemical precipitation reaction produces the surface film[76]:

$Mg2^+ + 2\ OH- \rightarrow Mg(OH)_2$ (4)

Initially magnesium dissolves, producing Mg cations[27]. This process might involve intermediate steps with monovalent Mg ions[27]. The corrosion on Mg in aqueous solutions is accompanied by the formation of hydrogen bubbles, because the potential of Mg in below the region of water stability when the pH is neutral or acidic[27]. The pH rises due to the byproduct of hydroxide ions[27]. The presence of the hydroxide ions favors the formation of $Mg(OH)_2$ (brucite), which becomes stable at high pH values, as can be seen from the Pourbaix diagram[27]. The magnesium hydroxide film forming on the surface determines the corrosion kinetics[6]. The formation of

insoluble corrosion products on the surface, e.g., Mg hydroxide in the case of Mg alloys, hinders the charge transfer process[27]. These corrosion products precipitate from the test solution while Mg corrodes due to saturation and localized alkalization[27].

Magnesium hydroxide has a low solubility in water.[20] However, this mineral's hexagonal structure is easily penetrated by chlorine ions which convert it to MgCl [27].

$$Mg(OH)_2 + 2\ Cl^- \longrightarrow MgCl_2 + 2\ OH^- \quad (5)$$

Magnesium chloride dissolves easily, so that the presence of Cl ions accelerates the dissolution of the surface layer[27]. In saline solutions Mg forms chlorides, oxides, and hydroxides [27].

According to thermodynamics and the Pourbaix diagram there should be no surface film on magnesium in solutions with pH values below 10 because the film would be unstable under those conditions[76]. Despite the instability of the surface layer at low pH values, a surface layer exists of the dissolution kinetics are slower than the formation kinetics[76]. Moreover, the pH in the vicinity of degrading magnesium can be much higher than 10 even if the bulk pH is below 10 [76]. This significant alkalization near the surface due to self-dissolution of magnesium leads to the formation of a MgO/Mg(OH)2 surface layer[76]. The surface film formed in water consists of three layers: the inner layer is hydrated, the intermediate layer is apparently dense, and the outer layer shows a platelet-like morphology[24].

It has been proposed that monovalent magnesium ions are involved in the corrosion reaction as intermediate species during anodic dissolution because the calculated valence of dissolved magnesium is in the range of 1.33 to 1.66 [76].

$$Mg \rightarrow Mg^+ + e^- \quad (6)$$

Mg^+ is believed to be very short lived, undetectable by ring-disk electrode experiments[76]. The monovalent magnesium ion reacts chemically to produce hydrogen through the following reaction:

$$Mg^+ + 2\ H^+ \rightarrow 2\ Mg^{2+} + H_2 \quad (7)$$

Another proposed mechanism was the formation of magnesium hydride:

$$Mg + 2\ H^+ + 2\ e^- \rightarrow MgH_2 \quad (8)$$

Magnesium hydride is not stable in contact with water. According to thermodynamic data it further reacts to be released as hydrogen gas[76]:

$$MgH_2 + 2\ H_2O \rightarrow Mg^{2+} + 2\ OH^- + 2\ H_2 \quad (9)$$

$Mg(OH)_2$ and MgO were detected on the surface of corroded magnesium by ex-situ techniques[76]. XRD of the material scraped from the surface of a magnesium electrode provides strong evidence for the presence of MgH_2[76]. Hydrogen embrittlement along grain boundaries and dislocations can cause strain and brittle fracture, prompting Chen et al. to suggest that magnesium hydride may be responsible for brittle fracture in magnesium.[20]

Pitting, filiform, and granular corrosion have been observed on magnesium and its alloys[38]. Corrosion can be induced by fatigue[38]. The corrosion mechanisms include de-alloying and particle undermining (secondary phase particles released from sample)[77].It is also called the chunk effect, because portions are physically detached from the anodic metal.[20] While magnesium dissociates to form a thin film of magnesium hydroxide and hydrogen on the surface during corrosion in water magnesium particles mechanically detach by hydrogen stress cracking.[20] Kruger[76] showed an SEM picture showing a partially undermined particle to support the suggested mechanism of undermining and falling away of second phase particles during corrosion, especially during higher anodic currents or potentials[76].

The oxide layer that forms on magnesium in air changes to $Mg(OH)_2$ over time in contact with water[76]. Subsequently the potential decreases, caused by an increase in thickness of the magnesium hydroxide layer, which makes the film more protective[76]. When the current density exceeds -0.4 mA/cm^2, the surface coverage decreases with time[76]. Therefore, magnesium dissolution and hydrogen evolution rate increase[76]. Through the accumulation of magnesium ions within the layer at the electrode surface the anodic current at rest potential decreases with time[76].

Under free corrosion conditions (no external potential or current applied) magnesium corrosion occurs through the interaction of local anodes and cathodes[76]. Below the current threshold of -0.5 mA/cm^2 magnesium is covered with a protective film, so that very little magnesium dissolves[76]. In that case there is not enough magnesium corrosion to protect the cathodic

phases containing impurities, making them subject to chemical dissolution[76]. Above the critical current density both magnesium and the impurities are exposed to the electrolyte because the protective film is damaged[76]. The electrochemical behavior of magnesium is similar over a pH range of 3 - 11 [76]. With moderate anodic currents applied, the surface film covers only parts of the underlying magnesium[76].

In acidic solutions the film free area is larger than in alkaline solutions under these conditions because the dissolution rate of the film is higher at lower pH values[76] . It is furthermore easier for magnesium ions to deposit and accumulate on the surface layer at the unprotected area in alkaline solutions, which lowers the rest potential in acidic solutions[76]. When the applied current or potential are high, the covered area diminishes towards zero and high concentrations of magnesium and hydroxide ions are reached in the surface electrolyte layer independent of the bulk pH[76]. Therefore, the magnesium potentials are similar in different pH solutions when the same external high anodic current density is applied[76]. If the applied current or potential is sufficiently negative almost all of the magnesium surface becomes covered in a protective film and the resistance of the surface mainly determines the potential of magnesium[76]. But even if magnesium is covered with a protective film, that surface film itself is subject to dissolution in aqueous solutions[76].

The amount of magnesium dissolved can be predicted with Faraday's Law[76]. It was experimentally observed that the anodic magnesium dissolution current can increase faster than expected based on polarization curves [76]. The anodic magnesium dissolution rate is a product of the unprotected area fraction, which increases with higher applied potentials, and Tafel behavior, i.e., increasing magnitude with higher applied potential (Eq. 10 and11)[76]. Consequently, the dissolution always increases with an increase in applied potential or external anodic current[76]. However, the second term has a negative sign in its exponential part, so that the hydrogen evolution rate initially increases with an increase in potential/anodic current and then decreases at higher potentials[76].

The anodic magnesium dissolution rate can be expressed as:

$$I_a = \theta(E, pH) I_{a_0} \exp\left[\frac{E-E_{ae}}{b_{a0}}\right] \qquad (10)$$

The corresponding cathodic hydrogen evolution rate is:

$$I_c = \theta(E, pH) I_{c_0} \exp\left[-\frac{E-E_{ae}}{b_{c_0}}\right] \quad (11)$$

Where

I_{a_0} and I_{c_0} are reaction rates for magnesium dissolution/hydrogen evolution at the equilibrium potential, b_{a_0} and b_{c_0} are Tafel slopes corresponding to the magnesium dissolution and hydrogen evolution, θ is the fraction of the surface that is not protected by a surface layer, and E_{ae} and E_{ce} are equilibrium potentials of the anodic and cathodic reactions.

Negative difference effect

Compared to other conventionally used metals, magnesium and its alloys have an unusual corrosion behavior[20]: Song described magnesium's different corrosion mechanisms called negative difference effect (NDE)[20]. The name stems from the phenomenon that the rate of hydrogen evolution increases with increasing anodic polarization in magnesium[20,76]. For most elements the opposite would be expected[76]. A common definition of NDE is through the applied galvanostatic current I_{appl} and the difference in hydrogen evolution as:

$\Delta = I_S - I_{H,m}$

I_S spontaneous hydrogen evolution rate

$I_{H,m}$ measured hydrogen evolution rate

$I_{appl} = I_{Mg,m} - I_{H,m}$

Song et al. proposed a new definition for the negative difference effect to extend the definition to work for both anodic and cathodic regions because magnesium starts its NDE from a cathodic external current density or potential lower than its rest potential[76]:

$\Delta = (I_S - I_C)\, I / |I|$

I_C hydrogen evolution rate

I_a anodic magnesium dissolution rate

I external current density at an electrode potential E. $I = I_a - I_c$

Several mechanisms have been proposed to explain the NDE, but the partially protective film model was found to provide the best fitting explanation as it can explain all experimental observations[76]. Although the model of a partially protective film has been identified as the most reasonable, it cannot be assumed that the other proposed mechanisms do not play a role in the corrosion process of magnesium[76]. Some aspects of magnesium corrosion remain unclear, including the exact composition of the surface film, detailed reactions, and the important controlling steps[76].

Biocorrosion

Metal implants are prone to corrosion when in contact with biological systems[78]. Corrosion occurs through redox reductions in tissue fluids, wherein metal is oxidized[78]. Proteins can influence the electrochemical behavior of implants, but the exact effect on corrosion is still being debated[78]. Pure titanium readily reacts with water and quickly forms a thin surface oxide layer that protects the metal from further corrosion[78].

All metals corrode in physiological environments by electrochemical redox reactions[78], even titanium that is considered “bioinert”. Human osteoclast precursors were shown to grow and differentiate to mature osteoclasts on titanium surfaces[78]. Mature cells directly corroded the titanium surface and took up metal ions that were released during the corrosion process[78]. The metal ions might be released and thus induce osteolytic lesions in the bone they are in contact with[78]. These processes oftentimes lead to implant loosening[78].

In the body Mg is exposed to blood, proteins, organic substances with low molecular weight, high molecular weight polymers, dissolved oxygen, and ions (e.g., Na^+, K^+, Ca^{2+}, Mg^{2+})[6]. This is a very complex corrosive environment[6]. The pH can vary from 2 to 8 in the human body, depending on the location[6]. Injury, surgery, and diseases may shift the pH at a given site in the body[6]. Magnesium corrosion is commonly tested in vitro first through electrochemistry and biocompatibility assets in simulated body fluids before running in vivo tests[6]. The corrosion behavior of Mg changes in simulated body fluids with different compositions[6]. Adding albumin to simulated body fluids changes the corrosion rate of Mg alloys immersed into it because the protein forms a layer on the material surface and thus shields the material from the corrosive

environment[6]. Proteins themselves contain metal cations, which have the potential to accelerate the corrosion rate[6]. The degradation rate of the magnesium particles in Di Virgilio et al.'s experiment was different with and without cells, showing that cell metabolism affects the corrosion rate[31].

Hydrogen bubbles evolve from corrosion sites[20]. In the body hydrogen gas can cause problems as it is toxic to tissue[20].The local rise in pH from the hydroxyl groups is also a concern.[20] The pH can rise up to 10 in a static solution[20]. Elevated pH values inhibit cell proliferation and tissue formation[20]. However, these effects may be more severe in static laboratory experiments than in the body where fluids are moving past the implants[20]. The increasing pH on the corroding surface can be neutralized by the buffers present in body fluids as well as through sheer flow[20]. The increased flow rate, however, also increases the corrosion rate of biodegradable materials[20]. Together with the mechanical stimulus from by flowing liquids this can lead to stress-corrosion cracking, pit growth, and fatigue corrosion[20]. Design of implant hardware must therefore evaluate the strength of the part as it corrodes and develop corrosion control mechanisms that will adjust the corrosion rate and reduction in strength over time to desired values[20].

Traditionally, there have been many different test solutions mimicking physiological environments and methods to monitor the corrosion behavior recommended to test the corrosion rate of Mg and its alloys. Thus it is not surprising that a wide variety of them has been used by scientists and reported in the literature. However, this diversity makes comparison between tests difficult since not only the test solution may be different but also other important parameters, such as the sample surface area to test solution volume ratio. Unfortunately, no standardized test methods have been established for investigating the corrosion behavior of magnesium and its alloys under physiological conditions, but it would be very beneficial if at least the most basic variables (body temperature, pH, appropriate buffer systems etc.) were standardized to ensure the quality and comparability of data[77]. There is, however, an ongoing effort to persuade and educate the international research community of useful practices to make sure published results are useful and readily comparable through review articles about good testing practices, but there are still no strict guidelines in terms of established, proven testing procedures in testing standards. Modification of existing standards oftentimes falls short

of taking into account the vast differences in the environment the implants experience compared to, e.g., biodegradable polymeric materials or permanent metallic implant materials[6].

Kirkland, Birbilis, and Staiger reviewed the currently available literature and suggested test standards to make testing of corrosion of Mg alloys for biodegradable implants more comparable and guide researchers in identifying suitable test methods for their applications[77]. All those test methods are based on immersion of a sample into a test solution, but the way to assess the corrosion behavior is different. In vitro tests of Mg alloys for biomedical applications include measurement of the biocorrosion behavior and biocompatibility tests, which mainly focus on checking the sample for possible toxic reactions[77].

Walker et al. investigated how in vitro tests on the corrosion behavior of Mg alloys could be performed to closely predict the corrosion rate in vivo as up to now it has been a huge challenge because the current standards for the degradation of biomaterials have been found to not be appropriate for Mg alloys[79]. The group suggests to use Earle´s balanced salt solution (EBSS) with $NaHCO_3$ as buffer for weight loss experiments over 7-21 days. The physiological environment was further imitated not only by temperature and CO_2 concentration but also by constantly keeping the solution in movement with a shaker and mimicking the exchange of fluids by replacing approximately half of the solution every day[79]. They found that for four investigated Mg alloy sample this procedure was closest to the in vivo corrosion rates observed for the same samples, although the corrosion rate obtained with this method in vitro was still faster than that in vivo[79].

This test method that has a close relationship between in vivo and in vitro tests is extremely important and valuable because it allows an accurate pre-screening of samples in large numbers before animal tests.

Corrosion measurement techniques

A variety of corrosion measurement techniques have been employed to evaluate the complex biodegradation performance of Mg and its alloys[77]. Each one has advantages and shortcomings[77], so only a combination of several methods gives a fairly complete picture of corrosion rates and protection mechanisms. In vitro tests fall either into the category of

biocorrosion resistance or toxicity, but both are closely related[77]. Corrosion assessment usually doesn´t require the presence of living cells and is thus less complex and easier to run, which makes it an important pre-screening method for subsequent in vitro and in vivo biocompatibility tests[77].

The test methods for characterizing the corrosion behavior and rates can be divided into unpolarized and polarized techniques, the difference being the presence of an electrochemical driving force in polarized methods[77]. Unpolarized methods include measurements based on mass loss, hydrogen evolution, and pH changes[77]. The downside to unpolarized methods is that they do not provide information on the corrosion mechanism and cannot be accelerated[77]. On the other hand, they are inexpensive and easy to set up[77].

Weight loss

Mass loss does not provide time-dependent information, so many samples are needed to investigate the corrosion behavior at different time intervals[77]. The most difficult aspect of mass loss measurements is that the corrosion layer forming on the surface affects the results and thus must be removed before weighting[77]. A hydrated corrosion layer on the surface of magnesium results in a net weight gain (7, 27)[77]. This corrosion layer has no mechanical integrity with the underlying substrate[77]. Removing only the corrosion layer and not affecting the underlying uncorroded material is challenging. In order to change the mass sufficiently to be discerned by a balance, a substantial degree of corrosion is needed[77]. This requires multiple samples[77] and potentially long corrosion intervals. Mass loss experiments provide a simple benchmark for determining the amount of corrosion that occurs during a set time frame[77].

Kirkland et al. observed that mass loss did not change any more as a function of surface-to-medium volume above 50 mL/cm^2, so the best practice is to keep the test solution volume as large as possible[77]. Rising pH values cause formation of $Mg(OH)_2$ surface layers and precipitation of CaP on magnesium, which further protect the underlying substrate from the corrosion solution[77]. The American Society for Testing and Materials (ASTM) has set standards for mass loss measurements of metals, however, those are not suitable for magnesium as the recommended solution volumes of 0.2 to 0.4 mL/mm² are too small to avoid the rapid change in pH associated with magnesium corrosion[77].

Hydrogen evolution

Along with the corrosion of magnesium hydrogen is set free, according to Eq. (3), which evolves from the reaction site on the metal's surface as gas bubbles. The amount of hydrogen created is directly related to the amount of magnesium corroded, i.e., 1 mole of corroding magnesium results in 1 mole of hydrogen molecules evolving. 1 mol of hydrogen gas, equivalent to 22.4 L, is coupled to the dissolution of 1 mol or 24.31 g of magnesium[77], which means that roughly 1 mL of H_2 evolves for every 1 mg of magnesium that is dissolved[80]. Thus, measuring the volume of hydrogen gas rising from the sample can be used to determine the amount of corroded magnesium[77]. The gas bubbles can be collected, an experimental setup suggested by Song et al.[81] for determining the corrosion rate through the hydrogen evolution rate .In the hydrogen evolution test setup the hydrogen produced by the corrosion reaction is usually collected by a funnel and then channeled into a burette filled with corrosion medium, so that the gas replaces the test solution inside the burette as the sample corrodes[77]. The hydrogen evolution method is not affected by corrosion products and allows real-time measurement[77]. A single sample can provide many time points. It can be viewed as a continuous pseudo-mass loss experiment[77]. However, n most literature accounts the theoretical 1:1 ratio of hydrogen to actual mass loss is not found[77]. The technique may not always be accurate due to non-Faradaic dissolution that leads to mass loss, but is not detectable through hydrogen evolution[77]. Hydrogen evolution does not reveal the corrosion mechanisms[77]. A drawback to the method is that sufficient hydrogen evolution is needed to monitor the corrosion progress, i.e., in the early stages of corrosion the method is inaccurate and it's unsuitable for monitoring very corrosion resistant alloys that produce little hydrogen[77]. Water itself can dissolve 1.4 mg/kg or 1.04 mL/L hydrogen at 37°C, which introduces an error source[77]. This error becomes significant at short immersion times or when the test solution volume is large compared to the sample surface are[77]. The solubility of gasses in water varies with temperature. When heating water from room temperature to body temperature comparatively large quantities of oxygen and nitrogen could be released[77]. Since hydrogen evolution is due to the cathodic part of the magnesium corrosion reaction[77], i.e., Eq. (1), the method is inaccurate if water reduction is not the major cathodic reaction[77]. Because hydrogen can permeate many polymers, glassware should be used to capture hydrogen in hydrogen evolution experiments to prevent leaks[77]. It is important to keep sufficient space between the funnel and the beaker so that the corrosive medium can circulate and maintain a

uniform composition[77]. All surfaces that are not measured for corrosion studies should be covered to avoid unintended degradation thereof[77].

pH

Similarly, pH monitoring can be performed continuously[77]. However, pH changes will affect corrosion and therefore pH changes are avoided in in vitro tests[77]. The hydroxide ions released during magnesium corrosion first increase the local surface pH, which can rise up to 12, then the bulk solution pH increases[77]. When pH measurements are reported in the magnesium biomaterial literature, they are treated as qualitative measures[77]. The bulk solution pH may be very different from the pH on the sample surface[77].

Electrochemical corrosion measurement techniques can be used to measure specific cases of corrosion, e.g., corrosion rate over time, initiation of crevice corrosion, and stress corrosion cracking.[20] They are also useful for detecting the breakdown of coating layers.[20] Potentiodynamic polarization and electrochemical impedance spectroscopy (EIS) are polarized test methods and require specialized equipment[77]. There are several cases reported in the literature where polarized experiments were run on compressed powders[24,38,82], so a bulk sample is not necessary.

Open-Circuit Potential (OCP)

Monitoring the open-circuit potential (OCP) is the simplest of the electrochemical measurements, but can yield useful insight into the changes that occur over time while a sample is corroding. Without applying any external currents or fields the sample's potential is measured continuously. OCP measurements are oftentimes run while a sample is let to stabilize in contact with the test solution before other electrochemical tests are started. OCP can be used to determine at which time point the sample's potential has stabilized.

Potentiodynamic Polarization (PDP)

PDP is the most commonly employed electrochemical test for studying the corrosion behavior of magnesium[77]. Usually the samples are let to stabilize in contact with the test solution for a specified time prior to running PDP tests until they reach a stable potential[77]. During PDP the voltage is swept at a pre-defined rate between select potentials with current flowing between the working electrode, i.e., the sample, and an inert metal counter electrode[77]. The scans

typically start at voltages below the OCP and proceed to increasingly positive values (Figure 4)[77]. The sample is thus first exposed to cathodic conditions that become more anodic as the scan progresses[77]. From PDP test information on the corrosion potential, relative anodic and cathodic reactions, and kinetics can be gained[77]. The cathodic part of the polarization curves represents the cathodic half of the electrochemical process[27], which is the splitting of water molecules into hydroxide ions and protons. PDP scans can be very fast[77]. PDP has been employed to investigate effects of multi-phase alloys in simulated body fluid (SBF) and for determining the individual contributions of each phase to the overall corrosion mechanisms[77]. The technique can also be used to investigate the effects of organic components on individual phases[77]. As the sample experiences significant perturbation during PDP scans because high currents are passed through it in a short time, only a single scan can be run on each sample[77]. These samples are also not useful for analysis of the corroded surface because the reactions were artificially accelerated[77]. PDP cannot distinguish the individual contributions of the layers formed on the sample surface, but only shows the overall effect on the corrosion current and shifts in the corrosion potential[77]. Most uncoated magnesium alloys do not corrode uniformly, so that PDP measurements cannot be used to calculate an absolute corrosion rate[77]. The conversion of the corrosion current into a corrosion rate is only justified under the assumption of general corrosion[77]. PDP can only indicate the intensity of magnesium corrosion[77]. Expressing the corrosion rate through the current density from PDP experiments is very accurate despite the current coming from local sites on the surface[77]. The dwell time before commencing a PDP scan is very important for the formation of an electrical double layer[77]. It is advisable to monitor the OCP and determine at which timepoint the potential is relatively stable and then start the scan[77]. The disadvantage is that it is unknown how much the sample has already been altered at the start point[77]. As an instantaneous test PDP only represents the corrosion behavior at the time the test is performed[77]. Therefore, characteristics measured at one time point may not be representative of all time points during the corrosion time frame[77].

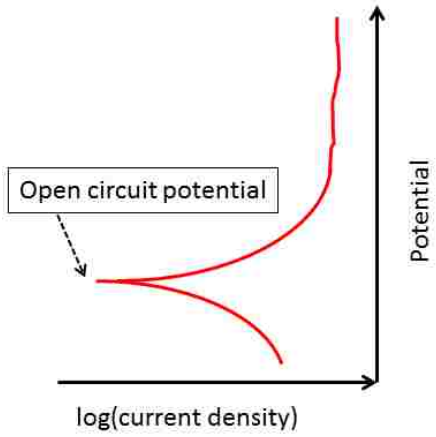

Figure 4: Schematic of potentiodynamic polarization (PDP) plot.

Kirkland et al. suggest limiting the PDP scan range to provide just enough data because polarizing magnesium anodically increases the corrosion rate and impacts the results obtained[77]. Any polarization away from the OCP perturbs the sample[77]. Large cathodic polarizataion alters the local pH, thus changing the surface that is later probed in the scan[77]. The authors found that a range of 150 mV below to 500 mV above OCP was sufficient for analysis and did not affect the corrosion noticeably[77]. It is difficult to perform Tafel analysis on PDP scans because the measurements of the anodic and cathodic slopes can change if the sample corrodes significantly[77], and some people suggest that the method better not be used on magnesium at all[81]. The scan rate affects PDP results because it determines the amount of current that is produced[77]. If the scan rates are too slow, corrosion proceeds to change the surface during the scan and if the sample is scanned too quickly there is not enough time for the system to respond to the change in potential, which makes the current density measurement inaccurate[77]. In fast scan rates the corrosion potential is not clearly defined[77].

PDP is a powerful technique for determining the mechanisms of magnesium corrosion[77]. Information on the kinetic and thermodynamic differences of alloys and test solutions can be derived from PDP[77]. But the measurement only gives one time point[77].

Electrochemical Impedance Spectroscopy (EIS)

In EIS the surface characteristics of a sample are probed using frequency responses to AC polarization[77]. It shows formation of surface layers and their roles in corrosion protection[77]. In

this technique a range of low magnitude polarizing voltages oscillating from the maximum anodic to the maximum cathodic voltage over a spectrum of frequencies are utilized[77]. At each frequency the resistance and capacitance are recorded to visualize the phenomena happening at the surface and investigate the properties of the surface layers formed during corrosion[77]. EIS provides instantaneous data about the impedance of a polarized surface[77]. The impedance is directly proportional to the corrosion resistance and can thus be used to determine the corrosion rate[77]. In contrast to PDP, EIS is non-destructive as the voltage changes are kept very small as to not alter the corrosion behavior of the sample, allowing for multiple recordings on the same sample[77]. Among the most useful features of EIS is the ability to detect individual layers formed on the surface of magnesium[77]. Corrosion or passivation layers, e.g., CaP on the surface can be detected[77]. The technique can even reveal how much each layer contributes to the corrosion protection[77]. CaP layers formed on the surface are the main protection of magnesium in simulated body fluids[77]. EIS is susceptible to corrosion that occurs during the scan, especially in the low frequency range[77]. This phenomenon leads to drifts at low frequencies during active corrosion[77].

EIS data are routinely translated into equivalent circuit models to convert the frequency response to corrosion properties[77]. A purely electronic model can represent an electrochemical cell by applying established AC circuit theory, so the electrochemical system can be characterized with its equivalent circuit consisting of a combination of resistors and capacitors[83]. Oftentimes multiple equivalent circuits can fit one data set, which results in very different values for the resistance during calculation[77]. To select a meaningful equivalent circuit model it is, therefore, important to understand the corrosion mechanisms, including the effects of layers formed on the surface[77]. This is a very challenging task, as magnesium corrosion layers depend on the test parameters (e.g., test solution, presence of buffers)[77]. After identifying an appropriate equivalent circuit chemical and physical properties can be correlated with circuit elements and fitted numerically[83]. Choosing the correct equivalent circuit is thus very difficult[77]. Data can be interpreted with computer problems written for that purpose, but because of their high complexity they still require an initial guess of the circuit parameters[83].

The model representation is the Randles cell (Figure 5), consisting of a polarized resistance(R_P) and a double layer capacitance (C_{DL}) in parallel, which are in series with a resistance (R_Ω)[83]. The ohmic or uncompensated resistance represents the resistance of the test solution[83]. The

polarization resistance stands in for the charge-transfer reaction at the electrode-solution interface, while the capacitance describes the double layer capacitance at the interface[83]. At the high and low frequency limits the Randles cell behaves like a resistor[83]. In order to determine the appropriate equivalent circuit one needs to probe the system´s impedance response over a wide range of frequencies (1 mHz to 10 kHz in most cases)[83]. This is usually done by applying AC voltage or current in different frequencies and measure the resulting current or voltage response[83]. Based on those results the impedance can then be calculated for each applied frequency[83].

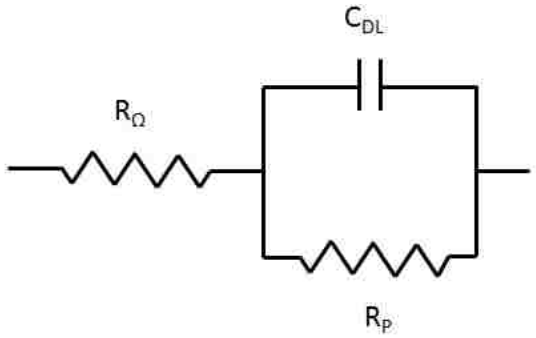

Figure 5: Randles cell as basic equivalent circuit for a single electrochemical cell. After[83].

EIS can give detailed information on the kinetics and mechanisms of corrosion, making it a powerful tool in studying corrosion[83]. It has three advantages over DC techniques[83]: Only small excitation amplitudes are used, typically in the range of 5 - 10 mV[83]. These perturbations are very small and thus reduce errors caused by the measurement technique[83]. EIS gives information on both charge-transfer kinetics and electrode capacitance[83]. By analyzing the EIS spectrum the corrosion mechanism can be identified[27]. It's a steady-state technique that can access relaxation phenomena with relaxation times varying over orders of magnitude with high precision[27]. No potential scan is involved, so it can even be carried out in low conductivity solutions[83].

There are several standard representations for EIS data, each offering advantages for determining specific values[83]. Oftentimes it is useful to work with different representations of the same data set[83]: In the Nyquist Plot/Cole-Cole Plot/complex impedance plane plot the real and imaginary parts of the impedance are plotted against each other (Z´ on the x-axis, Z" on the y-axis) for each frequency (Figure 6)[83]. In the Nyquist plot the polarized and ohmic resistance can be read from the points where the plotted curve touches the x-axis[83]. If the recorded data

doesn´t reach far enough, it can easily be extrapolated[83]. The shape of the curve does not change if the ohmic resistance changes[83].

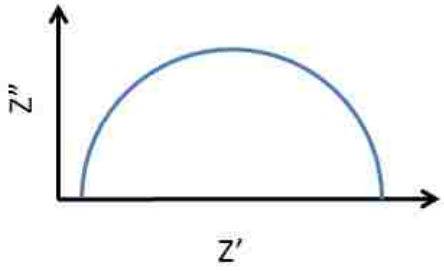

Figure 6: Schematic of a Nyquist plot. This simplest shape with only one semicircle represents the response of the Randles cell (Figure 5).

The Bode plot shows the absolute impedance and the phase shift of the impedance as a function of the frequency (Figure 7)[83]. Combining both into a log(Z)-log(ω) can yield the values of the ohmic and polarized resistances from the two extremes of the frequency spectrum[83]. Extrapolating the slope of the medium frequency part gives the value of the capacitance[83]. When using the Bode plot to determine the parameters one can avoid having to go to the low frequencies the Nyquist plot requires[83]. In case of data scattering it is easier to fit data in the Bode plot than in the Nyquist plot[83].

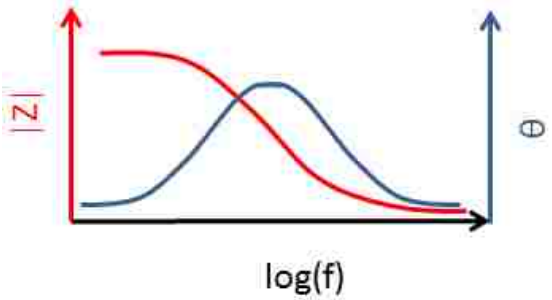

Figure 7: Schematic representation of a Bode plot.

There may be more than one rate-determining step in some electrochemical processes, with each step representing an impedance component of the system and each contributing to the overall reaction rate constant[83]. EIS can often distinguish the individual steps[83]. While they may not always be clearly visible in Nyquist plots, Bode plots clearly reveal their frequency breaks[83].

Under passivating conditions, such as in the KOH solution, it is expected to observe two semi-circles in the Nyquist plots, one at the high frequency range, characteristic of the film resistance

(R_f) and capacity (C_f), and another one at the low frequency range, which is determined by charge-transfer resistance (R_{ct}) and double-layer capacity (C_{dl}) [50].

A distortion of the semi-circles, i.e., not perfectly round, can indicate microscopic roughness or inhomogeneities on the electrode surface [50]. It was determined that the first capacitive loop in the high frequency region is related to the corrosion rate and can be linked to weight loss data[27]. A larger diameter of the loop means better corrosion resistance[27]. An increase in the impedance values over the time of immersion indicates a decrease in the surface film capacitance and has been linked to a proportionally lower adsorbance of Cl ions[27].

Although cyclic voltammetry has been widely used to analyze the formation of surface layers it is unsuitable for magnesium alloy corrosion tests in physiological environments because they corrode too quickly and thus change their surfaces during the experiment[77].

In fact, none of the corrosion measurement techniques mentioned here yields an absolute corrosion rate for magnesium, because that would require uniform corrosion, which is rarely the case for magnesium and its alloys[77]. The described corrosion assessment techniques are complementary to each other and several different measurement methods should be employed to get a more complete picture of magnesium corrosion behavior[77]. No single experiment can provide all the information necessary to completely understand the corrosion of magnesium[77]. To get meaningful and reliable data it is critical to understand the features and limitations of each technique[77]. Rosalbino et al. stress the importance of long-term experiments to assess the longevity of potential implant materials because their rate of corrosion is influenced by the corrosion products forming on the surface[27].

Influence of ball-milling on the corrosion of magnesium

It has been reported that the corrosion potential becomes nobler with increasing milling time at room temperature[24]. Grosjean et al. observed that ball-milling pure magnesium improved the corrosion resistance of in alkaline aqueous media, which they attributed to the formation of a protective magnesium hydroxide layer on the increased number of surface defects and grain boundaries.[38]

When immersing magnesium milled for 10 h in 1 M KOH solution with pH=14, the open circuit potential (OCP) increases drastically over the first 10 min. [24]. After the intial immersion time the slope becomes flatter, but continues to rise until -1.3 V vs. SCE are reached after 1 h exposure[24]. In the case of unmilled magnesium the OCP sharply increases during the first 5 min. of immersion, then flattens out and reaches -1.41 V vs. SCE after 1 h in the solution[24]. The difference between milled and unmilled magnesium is that milled magnesium starts out at a higher potential and has a much higher overall potential increase[24]. This change in OCP is assumed to be due to the formation of a passivating $Mg(OH)_2$ layer on the electrode surface[24]. The larger OCP variation for milled Mg could indicate that it reacts more actively with the electrolyte to form magnesium hydroxide on the surface[24]. The nobler potential indicates the positive effect of ball milling on the corrosion resistance of magnesium[24]. Polarization curves for milled and unmilled magnesium in KOH solution show similar shapes without active-passive transition, confirming that the passive behavior in the high-pH solution is independent of the microstructure[24]. However, the current densities of milled magnesium were much lower in the passive region than those of unmilled magnesium, most likely due to the formation of a more protective surface film. [24] The anodic current, which is associated with oxygen evolution and possible simultaneous breakdown of the passivating film, starts at a lower potential and increases more steeply for milled magnesium and decreases substantially with increased milling time[24]. OCP and polarization resistance increase with prolonged milling time, simultaneously the corrosion current density decreases[24]. An improvement in corrosion resistance is observable after just 30 min. of ball milling, but becomes more pronounced with increasing milling time until a stable state is reached after 10 h of milling, after which no further improvement with prolonged milling time happens any more[24]. In contrast, the apparent breakdown potential becomes more negative with milling, indicating an easier rupture of the passivating film or better electronic transfer through the passive film because it is very thin, facilitating electron tunnelling[24].

In more active corrosion condition (0.3 M borate buffer solution, pH=8.4) unmilled and milled magnesium show an active-passive transition with a pseudo-passive region, but the dissolution current is drastically lower for milled magnesium[24]. In this environment the potential of the milled magnesium is shifted to more positive values as well, confirming the corrosion resistance improvement through milling[24]. However, the corrosion current is almost unchanged by milling in the borate solution and the polarization resistance only changes slightly[24]. This could be

because the cathodic reduction of water is controlling the corrosion of magnesium in borate solution and is not affected by ball milling[24].

XPS surface analysis on the Mg2p spectrum shows that MgO is the major component on the surface in both milled and unmilled magnesium, although there is also a peak corresponding to the metallic state, which means the surface oxide layer must be thin[24]. The intensity ratio between elemental and oxidized states hints at a thinner MgO layer on milled magnesium than before milling[24].After exposure to water oxide and hydroxide peaks emerge, for both unmilled and milled magnesium[24]. Immersing both samples into KOH inceases the MgO peaks[24].The thickness of the oxide layer on unmilled magnesium powder is roughly 50 nm[24]. The higher concentration of elemental magnesium on the surface of milled samples could be due to the exposure of oxide free metal surfaces during milling[24]. Milled magnesium contains more oxygen in the bulk than untreated magnesium, because the oxygen originally present on the surface of the particles is dispersed throughout the sample during the milling process[24].The thickness of the $MgO/Mg(OH)_2$ surface layer after contact with water was 500 nm for unmilled Mg and 350 nm after milling for 10 h[24]. When immersed in KOH solution the layers are about half as thick, as expected considering the higher tendency of magnesium to passivate at a higher pH[24]. More than half of those layers is hydroxide, which is also closer to the surface[24]. The difference in thickness could explain the improved corrosion resistance of the milled sample[24].

EIS investigations revealed that interfacial resistance and capacitance vary with immersion time as a result of charge transfer and film thickness, but are less accentuated and reach a steady state faster in milled magnesium, which suggests a bigger kinetic for the formation of a passive layer[24]. Although MgO reacts to $Mg(OH)_2$ in the presence of water, it could contribute to the improved corrosion resistance of milling magnesium because it is thermodynamically less reactive with water than magnesium[24]. The main contribution to the corrosion resistance of milled magnesium is however contributed to its nanostructure[24]. It has been argued that the grain boundaries and dislocations act as paths that ease diffusion and thus lead to the rapid formation of a protective layer[24]. It was also observed that oxides nucleate more readily in contact with water on open-packed faces with smaller surface coordination numbers[24].

Approaches to increasing the corrosion resistance of magnesium

In the past decades the research efforts have intensified, yet controlling their corrosion rate in physiological environments remains a challenge[6]. Many methods have been proposed to protect magnesium from corrosion, e.g., anodization, chemical treatments, coatings, lime treatment, surface modifications, purification, addition of new components, and the use of new metallurgical methods[76]. Non-equilibrium methods have also been employed to improve the corrosion resistance of magnesium alloys, among them rapid solidification, magnetron sputtering, and mechanical alloying[24]. These synthesis routes change the microstructure in several ways, for example increased homogeneity, extended solid solubility of the alloying elements, formation of new corrosion resistant phases, and amorphization[24]. Surface treatments for corrosion protection include electro or electro-less plating, anodization, inhibitors, and organic coatings.[20]

The corrosion resistance of magnesium has been greatly improved by reducing the impurity content and alloying with other elements[24]. Alloying elements influence the mechanical and physical properties of Mg through changes in the structure or the introduction of new phases[6]. Among the many approaches taken to protect Mg against corrosion, alloying has been among the most effective[6] because it alters all the material and is not limited to surface protection alone that is ineffective once removed, e.g., through corrosion or scratches during implantation. To obtain useful Mg alloys for this purpose it is crucial to look for alloying elements that will enhance the corrosion resistance, mechanical properties, and show excellent biocompatibility[6].

Up to now, the majority of Mg alloys whose behavior under implant conditions were investigated were originally designed for structural engineering, transportation, aerospace, and military applications[6]. But gradually the focus is shifting towards newly developed alloys, designed specifically for implants. Binary, ternary, and quaternary alloys are frequently developed. Alloying is preferably done with elements that form stable oxide layers which inhibit further corrosion. One of those is aluminum, which is used in many commercial magnesium alloys to improve corrosion and mechanical properties. It forms a second phase. Mg alloys in general divided into those with and without Al. The general agreement is that a magnesium-based alloy should ideally be a single-phase, chemically homogeneous system with passivating alloying elements in sufficient concentration to be highly corrosion resistant[24].

AZ91 is one of the most frequently studied Mg alloys, but its main alloying element, Al, is a known neurotoxicant[84]. AZ31(Mg-3Al-1Zn, wt.-%) from the same family of Mg alloys also has moderate strength thanks to the strengthening effect of Al and good corrosion resistance owing to the formation of a protective aluminum oxide film, but it is not as corrosion resistant as AZ91[27].

Peng et al. incorporated silver into their Mg-Zn alloy because it is known to have anti-inflammatory properties with a broad effective spectrum range against microbial activity[26]. This is to replace the drug coatings placed on implants nowadays, which inherently can only offer temporary protection[26]. Silver improves mechanical properties through grain refinement[26].

Rosalbino et al. investigated ternary Mg alloys containing zinc and manganese for biomedical applications because the alloying elements are known for their good biocompatibility[27]. Their samples all have two phases, a Mg-Zn-Mn solid solution matrix and a Mg-Zn binary phase[27]. Corrosion behavior in Ringer's physiological solution improved with increasing Zn and Mn content, which the authors link to a stabilization of the magnesium hydroxide film on the surface by the alloying elements[27]. Among the tested samples Mg-1.5Zn-1Mn alloy showed the highest corrosion resistance along with the highest charge transfer resistance and lowest double-layer capacitance and was thus suggested as a promising candidate for biodegradable implants[27], even though no biocompatibility study was presented.

Spin-coating magnesium with PLGA increases the corrosion potential slightly and decreases the corrosion current in a simulated body fluid[85]. The effect is even stronger when nano hydroxyapaptite particles are mixed into the coating[85]. Although both coatings reduce the degradation rates of both pure magnesium and AZ31 initially, they delaminate with extended immersion time[85].

A fluoride conversion coating on magnesium by a 24 h immersion into 48 % hydrofluoric acid produces a 1.5 µm thick MgF2 coating on the surface[86]. With this conversion coating the polarization resistance is increased 30 times and the corrosion current density decreases 40-fold[86]. The coated magnesium samples show milder and more uniform corrosion compared to uncoated samples[86].

Surface processing by severe plasticity burnishing on AZ31B remarkably improved the corrosion resistance in NaCl solution[87]. The enhanced corrosion behavior was attributed to a dramatical

decrease in grain size and the development of a strong basal-textured grain orientation[87]. Residual stresses introduced during processing might have some positive effect on the corrosion resistance as well[87].

A group from ETH Zurich proposed MgZnCa metallic glasses for biodegradable implants because they did not observe any gas cavities in animal studies, as opposed to crystalline form of the alloy[10]. The solubility of alloying elements can be extended in amorphous metals and they have a homogeneous single-phase structure, improving their corrosion resistance over their crystalline counterparts[10]. Although bulk metallic glasses show promising mechanical properties and corrosion rates, manufacturing them into a tubular stent preform is a major processing challenge[88].

Magnesium/5 wt.-% hydroxyapaptite bio-nanocomposites manufactured by high frequency induction heat sintering have a decreased dissolution of magnesium compared to the pure metal[89]. The composites improve the resistance of magnesium against uniform corrosion, but increase the probability of localized corrosion[89].

Oxygen plasma ion implantation into ZK60 alloy only slightly increases the surface oxide thickness, but does not improve the corrosion resistance much[90]. Plasma immersion ion implantation with carbon dioxide lowers the initial corrosion rate of AZ31 in simulated physiological environments[91]. Titanium ion implantation was explored on the same alloy[92]. With titanium ions implanted by metal vapor vacuum arc implantation, a layer containing titanium ions about 900 nm in thickness formed on the surface of the alloy and enhanced its corrosion resistance[92]. When chromium ions alone are implanted into pure magnesium it induces galvanic coupling, resulting in a much faster corrosion rate[93]. However, implanting oxygen in a second step afterwards produces a thick oxidized layer on the surface containing chromium oxide, which retards corrosion[93].

Yun et al. suggests a cathodic protection technique for magnesium implants, in which an external current is applied via reference electrodes[20]. The external current polarizes the cathodic part to the open circuit potential of the anode, so that the current across both electrodes becomes equal and the corrosion current in effect very small[20]. This technique would circumvent the development of exotic alloys to improve corrosion resistance[20].

Many metal ions are not biocompatible and their presence in the body negatively affects healing, for example causing inflammation[6]. Toxic substances that must be avoided, especially in a child's body[19]. Similarly, many alloying elements utilized in Mg alloys have been found to be hazardous when placed into the body, so current research efforts focus on identifying biocompatible alloying elements and developing new Mg alloys with those non-toxic elements with the goal to improve corrosion protection, mechanical stability, and ideally incorporate additional beneficial functions, such as osteoinductivity[6].

Identifying suitable alloying elements is not trivial: Even elements that are abundant and essential in the body and are thus considered safe (for example, Zn) can show adverse effects: Despite their crucial role as trace elements Mn and Zn can affect the biocompatibility negatively[6]. However, as long as their concentration is limited, it is still possible to achieve acceptable biological responses[6]. The concentration is also a crucial factor in determining biocompatibility.

Although information about the toxicity of various elements is available from the Acency for Toxic Substances and Disease Registry (ATSDR), which is part of the US Department of Health and Human Services, and the UK Food Standards Agency (FSA) with recommended maximum concentrations for commonly used alloying elements for implant materials, for some cases that information is not reliable due to a lack of information[6]. Although large amount of research has been done to assess the compatibility of alloying elements, far more work is needed to reach clear standards[6]. The concept of biodegradable metallic implants has only been pursued in depth in the last 10 years and there are still no testing standards established, making it difficult to ensure comparability of experimental results from different groups[6].

Al, Mn, Zr, rare earth elements improve mechanical and corrosion properties[26]. Mn increases the yield strength[27] and improves the corrosion resistance by binding iron and heavy metals[27]. Except for extreme exposure it's non-toxic[27] and plays an important role in many enzyme systems[27]; excessive amounts cause neurotoxicity and lead to Parkinson's disease[26]. Mn oxide substitutes Mg ions in the layered brucite structure, blocking out chloride ions, which enhances the protection by the surface film and hinders charge transfer[27]. High concentrations of Mn, however, decrease the corrosion resistance of Mg and causes cytotoxicity and even neurotoxicity, therefore it is advised to use no more than 1 wt.-%[6].

Zn strengthens Mg[27] through grain refinement[6] and minimizes the corroding effect of Fe and Ni[27]. It is essential for physiological functions[27], but excessive amounts can be cytotoxic[27]. Similarly, excessive addition of Zn negatively imparts the corrosion behavior[6]. Overdoses can be harmful, so the content should be limited to a maximum of 5 wt.-% in Mg alloys to keep them biocompatible and improve the corrosion behavior[6]. As the main alloying elements Zn and Mn exhibit high cytotoxicity, leading to a suppression of cell viability and genotoxicity[6].

Al, a very common alloying element, has a strengthening effect on magnesium. It provides corrosion protection through the formation of an Al oxide film[27]. Al is suspected to cause nerve toxicity and restrain growth in humans[27]. Accumulation of Al in the body is associated with neurological disorders including dementia, senile dementia, and Alzheimer's disease by causing a lack of phosphate in the body because it binds to inorganic phosphate compounds[26,84]. In addition, Al inhibits phosphorylation and ATP synthesis, which subsequently decreases the intracellular energy reserve [27] and can lead to muscle fiber damage, and decreased osteoclast viability[19]. Aluminum and iron further cause bone pathologies in humans and animals[94].

Zr has been associated with liver, lung, breast and nasopharyngeal cancer [26]but was found to be biocompatible as long as the content is not too high. Alloying magnesium with Zr refines grains[6].

Rare earth elements (REE) often improve the corrosion resistance of Mg, but some have been found to be toxic and should therefore not be used for implant materials[6]. They can enrich in some organs and the critical concentration has been determined in cell culture experiments, but detailed toxic mechanisms are not fully understood yet[26]. The REEs Er, Ce, La, and Nd can exhibit cytotoxicity[6]. Thorium is acutely toxic. REEs influence apoptosis and the expression of inflammatory markers in vitro[19]. It is not clear whether any adverse effects occur in vivo[19]. Ce accumulates in the bone, liver, heart, and lung and has been found to exhibit toxicological effects on the body[6]. Er is moderately to highly toxic and can cause ataxia, labored perspiration, walking on the toes with arched back, and sedation[6]. Yttrium is potentially toxic[19,95], but the influence of Gd and Y on corrosion is still under debate[6]. The primal influencing factor for Gd is its content in Mg alloys[6]. Acceptable biocompatibility can be achieved by keeping the Gd content below 1 wt.-%[6]. A surface layer containing Y was found to decrease the corrosion rate, but when it is present as a secondary phase ($Mg_{24}Y_5$) it accelerates corrosion by forming galvanic couples with the Mg matrix[6]. 2.5 mol-% Y in HA showed good biocompatibility[6].

Sr has been identified as a bio-functional element that accelerates bone healing by triggering the formation of new osteoblasts[6]. This promoted bone cell growth could benefit postmenopausal osteoporosis patients[6].It shows excellent biocompatibility and is osteoinductive[6]. At the same time it improves the mechanical properties.[6] As long as the content does not exceed 2 wt.-% it also improves the corrosion resistance[6]. The effect of Sr on muscles and the heart has been studied as well[6]. Identified as a promising candidate, it has been incorporated into a various alloys for biomedical applications, such as Mg-Sr[6] and Mg-Zr-Sr[6]. Mg alloys with the right combination of Zr and Sr show enhanced corrosion behavior, mechanical properties, and biocompatibility[6].

Vanadium is toxic in elemental and oxidized form[4]. Nickel is very toxic[4].

Alloying magnesium with lithium increases the pH in the vicinity, which stabilizes the magnesium hydroxide film on the surface[20], but lithium is toxic[6].

As the most abundant metal in the human body, Ca is crucial for the growth and maintaining health of bone[6]. Disturbing the balance of Ca in the body can have severe pathological consequences[6]. Calcium is abundant in the human body, especially in bones[84]. It has a low density of 1.55 g/cm, thus Mg-Ca alloys are expected to have densities similar to that of bone [84]. The Mg-Ca system has a beneficial combination of strength, creep resistance, castability, corrosion resistance, and low cost[84]. Han et al. observed a fast degradation of Mg-Ca alloys in vivo when used to fill osteonchondral defects in the subchondral bone of the distal femoral condyle of rat models[84]. No infections or wound healing problems occurred after surgery[84]. High levels of bone formation markers were found[84]. Doubling the Ca content from 5 to 10 wt.-% increased yield strength to 165 MPa (vs. 15 for pure Mg) and the ultimate compression strength to 254 MPa (145 MPa for pure Mg)[84]. Due to the fast degradation hydrogen evolution was so severe in case of the Mg-Ca alloy that it was too much to deal with for the host tissue[84]. It has been suggested that the Ca content in Mg alloys be limited to less than 1 wt.-%[6].

Researchers still debate which elements and at which concentrations they may be used in Mg alloys without compromising biocompatibility[6]. There is no such black-and-white painting as categorizing elements as “toxic” and “biocompatible” as even some of the elements classified as toxic have been successfully applied Mg alloys for biomedical applications[6]. Toxic effects under some conditions should not mean that these alloying elements have to be banned from use for

biomedical magnesium alloys completely as there are no per se harmful or harmless substances, it is all a question of dosage[6]. Reducing the corrosion rate and thriving for good biocompatibility will remain the most important goals in future research on Mg-based biodegradable implant materials[6].

Alternatives to magnesium

Bowen et al. suggest that zinc may be better suited as the base metal for bioabsorbable cardiac stents than magnesium because it combines the favorable properties of iron, namely longevity in vivo, and the harmless degradation of magnesium[88]. Zinc is an essential element for basic biological function and participates in nucleic acid metabolism, signal transduction, apoptosis regulation, and gene expression [88]. Zinc has strong antiatherogenic properties and acts an antioxidant and endothelial membrane stabilizer in its ionic form[88]. The systemic toxic potential of a zinc stent is considered to be negligible[88]. Zinc ions are rapidly transported in living tissue so that no zinc enrichment should occur that might cause cytotoxicity or necrosis in the vicinity of the implant, but cytotoxicity studies have not been carried out yet[88]. Concerns yet remain regarding the systemic toxicity of large zinc implants[88], although Zn-Mg alloys have been considered for orthopedic applications.

Zinc exhibits near-ideal biocorrosion behavior[88]. After implantation of up to six months healthy arterial tissue firmly surrounded the implanted wire samples and the amount of attached tissue increased with prolonged time in vivo[88]. During early implantation stages only a thin layer of zinc oxide formed on the samples, but upon onset of accelerated corrosion through localization a phase rich in calcium and phosphorus appears alongside with the aforementioned oxide interspersed in zinc carbonate on the top[88]. Local akalization is believed to influence the formation of the compact oxide layer[88].

Pure zinc possesses outstanding ductility with an exceptional elongation to failure of 60-80%, but its tensile strength is only around 120 MPa, which is not sufficient for stents[88].

Another candidate for biodegradable metallic stents is iron[96]. In contrast to magnesium, iron's degradation rate needs to be sped up to be appropriate for the application[96]. Alloying with manganese has been identified as a way to increase the corrosion rate of iron[97]. Iron and iron based alloys have the advantages of high strength and medium corrosion rates[98], which enables them to bear high loads in the repair or replacement of bones[99]. Iron foams have been

suggested to reduce the high stiffness of the material to avoid stress shielding[99]. Mueller et al. found limited inflammatory reactions after letting iron degrade in the tails of mice for several months[100]. No cellular responses to excess iron content was observed, which led the investigators to conclude that the degradation products from iron corrosion were metabolically inactive[100].

Corrosion characteristics of titanium

Titanium and its alloys are some of the most corrosion-resistant metals and almost free of galvanic, pitting, crevice, and fretting corrosion[12]. Ti is the material of choice for many dental implants, including crowns and orthodontic wires, because it is corrosion resistant in the mouth, biocompatible, and has fitting mechanical properties[36].

Like aluminum, titanium forms a protective corrosion layer that reforms after being damaged[38]. However, the corrosion layer of titanium is more effective than that of aluminum[38] and its mechanical properties are better than aluminum[38]. In addition, there are concerns that aluminum ions potentially induce Alzheimer's Disease, making it an element that should not be considered for implants until this hypothesis has been proven wrong.

Both magnesium and titanium are biocompatible by themselves, so combining them into an alloy can potentially yield another biocompatible material. As a strong passivating element titanium can improve the passivity of magnesium[39].

Cytotoxicity testing

The first step in investigation the biocompatibility of a potentially new implant material is to test its cytotoxicity, preferably on a cell type similar to the cells found at the wound site that would likely be in contact with the implant. When metal ions are released from implants into surrounding tissues they cause biological responses over short or prolonged times[101]. Therefore, the toxicity of a metal is not only determined by its composition and the toxicity of the individual components, but also by its wear resistance and corrosion rate[27]. Constituents of orthopedic implant alloys can be grossly cytotoxic at concentrations as low as in the ppb range[102]. Cytotoxicity can be reflected in various cell responses, e.g., morphologically indicated cell damage, release of cytosolic compounds, altered prolilferation, and modified metabolism[102]

In vitro tests can be used to determine whether cells will attach to the implant surface[20]. If the cells do not attach to the implant material they will migrate away from it or in the worst case, die by apoptosis or necrosis[20]. In the case of apoptosis the cell stops growing and undergoes controlled cell death, whereas in necrosis it loses the integrity of its membrane and quickly dies as a result of cell lysis[20].

All metals corrode in contact with biological systems[21]. Increased levels of cobalt, chromium, and titanium ions have been measured in serum and urine of patients with metallic implants[21]. Elevated ion concentrations in the vicinity of corroding implants have long been known from animal studies[21]. The released metal ions and particles can accumulate to ion-protein complexes, which have a high immunogenic potential[21]. Degradation can affect the mechanical properties of the implant and weaken it, which in turn leads to the release of more ions or particles[21]. The allergic potential is either due to the ions themselves, debris, organo-metallic complexes, anorganic metallic salts, or oxides[21]. Phagocytosis of metal ions or particles can lead to cell-mediated allergic reactions[21]. Thus, corrosion products can be directly or indirectly immunogenic[21].

Risks associated with metal particles from implant wear include toxicity, chronic inflammation, implant loosening, hypersensitivity reactions, aseptic osteolysis, and carcinogenesis[21]. Even in non-cytotoxic concentrations titanium, chromium, and cobalt have been found to have a negative effect on osteoblasts and can lead to bone resorption by triggering osteoclasts[21]. This way even a non-allergenic substance can disturb the bone metabolism by local irritation[21].

It is speculated that a basic pH that occurs during degradation of some biodegradable implants could be linked to the absence of allergic reactions[21]. In contrast, the acidic pH observed with some polymers, β-TCP, and slowly degrading metallic implants, can stimulate inflammation [21].The release of magnesium ions from corroding magnesium has been shown to not only be nontoxic, but to even have beneficial effects on cells in the surrounding tissue[31]. Although magnesium is generally considered biocompatible and safe to use in the body based on the absence of negative systemic reactions, its effect on the local environment of the implant site has to be examined. pH changes and the presence of magnesium ions in the wound site can have a profound impact that is different from the systemic biocompatibility.

Gao et al. carried out cytotoxicity tests with pure magnesium in direct contact and extracts from the corroded samples[103]. Extracts were made from samples corroded in medium for 24h at 37°C[103]. The preosteoblastic cell line MC3T3-E1 was used for cytocompatibility tests run for 6 days[103]. The authors found that a magnesium ion concentration of 96 - 153 mg/L promotes cell proliferation[103]. The observed growth of osteoblast cells was faster than the control grown in just medium[103]. Magnesium ion concentrations of 505-374 mg/L showed a decrease to 28-73% in viability in comparison to the control[103]. At a conc. of 198 mg/L after 6 days 98% in comparison with the control were still alive[103]. The direct contact measurement showed a decrease of viability to 92 % compared to the control after 6 days, although it was over 100% after 4 days[103].

Pichler et al. studied the viability and metabolic activity of primary human growth plate chondrocytes and MG63 osteoblasts in response to eluates of magnesium alloys WZ21 and ZX50.[19] Of the investigated alloys the slower degrading WZ21 showed superior performance with regard to cell viability, metabolic activity, cell proliferation, and morphology.[19] ZX50 eluate was found to induce an upregulation of osteogenic markers in MG63 cells.[19] This is a desirable effect because elevated alkaline phosphatase levels indicate active bone formation[19]. Both eluates made the chondrocytes express a notably higher amount of the same osteogenic markers[19]. A dose-dependent beneficial effect on the proliferatin, re-differentiation as well as gene and protein expression of articular chondrocytes was reported [19]. Magnesium stimulates proliferation, induces matrix production, and promotes expression of chondrogenic markers in these cells in relation to the ion concentration[19]. It was also discovered that chondrocytes have the ability to compensate for transiently increased concentrations of magnesium ions[19]. Both

cell lines tested tolerated a higher amount of the slower degrading alloy's eluate[19]. After a 2 d exposure to eluate from fast degrading magnesium alloy cell density is decreased, which has been observed before and attributed to the very high pH due to rapid magnesium corrosion rather than Mg ion concentration[19]. The authors concluded from their findings that magnesium alloys are well tolerated by osteoblasts and growth plate chondrocytes and thus suitable for biodegradable implants.[19]

Favorable biocompatibility of magnesium salts and several magnesium alloys on bone cells has been reported several times [19].Magnesium enhances bone cell adhesion onto biomaterials through integrin expression and mitogen-activated protein kinase pathway[19] and successful osseintegration has been observed for a magnesium alloy[31]. The bone mass around the magnesium implant had also increased[31]. Both effects are attributed to bone cell activation induced by the presence of magnesium[31]. Di Virgilio et al. investigated the cytotoxic effect of magnesium particles on rat osteosarcoma UMR106 cells with 325 mesh magnesium powder[31]. The group aimed to simulate the effect of magnesium debris[31]. A significant reduction in living cell numbers was found at concentrations of 500 µg/mL [31]. Magnesium particles up to sizes of 200 nm were taken up by the cells after 2 h of exposure[31]. After 24 h they had dissolved[31]. The corrosion of the magnesium particles along with the changes in pH, hydrogen evolution, and uptake of particles into the cells lead to cyto- and genotoxic effects on the cells[31].

Extracts of pure magnesium showed cytotoxic effects on osteosarcoma U2-OS cells, which are a kind of bone cancer cell[104]. The effect could be linked to an increased pH due to the corrosion of magnesium and was not observed with the increase in magnesium ion concentration alone [104]. Wang et al. found that human osteosarcoma MG63 cells and human oral epithelial KB cells are inhibited when grown on magnesium samples[105]. This opens up a possible way of curing bone cancers by creating an alkaline environment in the vicinity of the cancer cells[105].

Titanium and its alloys are ubiquitously used biomaterials for dental, orthopedic, and trauma applications due to their combination of strength, low inherent toxicity, minimal reactivity with biomolecules compared to other biomaterials, and good fabrication properties[78].

Even when titanium particles left the implant site they did not cause significant complications[12]. Whenever titanium particles were found distant from the implant site this was attributed to mechanical wear during placement of the implant rather than corrosion[12]. Commercially pure

titanium induces neither anaphylaxis nor hypersensitivity[12]. Pure titanium and titanium alloys are non-toxic and compatible with all currently used imaging techniques[12]. In fact, titanium is one of the most biocompatible metals, with a long success history in dental implants[12]. One special feature of titanium implants is that they fuse to the surface of both soft and hard tissues instead of eliciting the formation of a fibrous capsule around the implant, as is the case with many other implant materials[12].

However, titanium wear particles with sizes in the nanometer range play a role in initiating and developing aseptic loosening by eliciting inflammatory responses, which ultimately lead to osteolytic activity[78]. It has been speculated that the release of ions from titanium alloy implants might have an adverse effect on the surrounding tissue or trigger allergic reactions, although it is widely considered to be biocompatible[106]. Li et al. compared the cytotoxicity of titanium and some commonly used alloying elements in titanium alloys of the bulk material with ions[106]. The research team found that osteoblast-like human osteosarcoma cells of the SaOS-2 cell line spread well on bulk titanium, which was taken as a sign of excellent biocompatibility[106]. However, when cultured with extracts made by incubating titanium powder in medium, the cell viability was greatly reduced[106]. The group established that a titanium ion concentration of 15.5 µg/L is non-toxic[106].

It's been shown that titanium ions directly induce differentiation of osteoclast precursors towards mature osteoclasts[78]. Titanium ions are further believed to influence recruitment of precursors of osteoclasts through induction of expression of specific cytokines[78].

Human osteoclast precursors can directly grow on titanium surfaces and mature into osteoclasts[78]. The cultures were found to be long-term viable[78]. The mature cells directly corrode the metal, releasing titanium ions[78]. The osteoclasts take up these ions, but they are subsequently released[78]. It is believed that those ions cause inflammation and activate to osteoclastic differentiation[78]. They have also been linked to the formation of osteolytic lesions in the periprosthetic bone, which contribute to implant loosening[78]. Osteoclasts use a Ca^{2+} receptor in their plasma membrane as a feedback mechanism for bone resorption[107]. The receptor can also bind other di- and trivalent cations[108,109], so that exposure to Mg^{2+} can lead to decreased bone resorption[110]. This could first speed up bone formation during the initial healing stage after a fracture because the bone is resorbed at a slower pace than usual. However,

remodeling of new bone into mature bone might be slowed down, depending on the ion concentrations given off by implant materials at that point.

Nichols and Puleo investigated the effects of titanium ions on the maturation of rat hematopoeietic precursors into osteoclast[110]. The ions didn't affect cell proliferation at the investigated concentration, but the osteoclastic activity was decreased in the presence of titanium ions[110]. The 50 % toxicity level for Ti^{4+} was reported as 4 ppm[110].

Puleo and Huh investigated the acute toxicity of several metal ions commonly used in orthopedic implants on osteogenic cells derived from bone marrow[102]. After 48 h of exposure Ti^{4+} ions were toxic only at the highest concentrations (25 and 50 ppm)[102]. The cytotoxicity was time dependent and irreversible toxic effects were initiated after only 3-6 h of exposure to the ions[102].

Thompson and Puleo also demonstrated that sublethal concentraions of titanium ions affect the formation and function of osteoblastic cells in vitro[111]. Although solutions containing Ti^{4+} ions did not affect cell proliferation and alkaline phosphatase secretion much, they inhibited the cells from secreting osteocalcin and forming a mineralized matrix[111]. This could indicate that titanium ions interfere with the differentiation of osteoblasts[111].

In another study Thompson and Puleo explored the inhibition of osteogenic cell phenotype by ions representing Ti-6Al-4V[112]. In this study rat bone marrow stromal cells were exposed to doses of ions at different time points over the course of four weeks of culturing[112]. The cells treated with the ion solutions showed little differences compared to the control in terms of proliferation, but osteocalcin synthesis was strongly inhibited[112]. When the ions were added before a critical time point for osteoblastic differentiation the calcium levels were reduced, indicating that the ions inhibit the normal differentiation to mature osteoblasts[112]. The ions released from titanium alloy implants may thus impair normal bone deposition[112].

Titanium dioxide is used in sunscreens, toothpaste, and can be used as a color additive for food[113]. As a food additive the quantity of titanium dioxide is limited to a maximum of 1% of the food's weight[113]. Within a 2 week study period nano-sized titania particles with sizes of 25 and 80 nm administered to adult mice at doses of 5g/kg body weight showed no obvious acute toxicity[113]. No abnormal pathology changes were observed in heart, lung, spleen and testicle/ovary tissues, but there were signs of hepatic injury of the liver and nephrotoxicity and

pathology changes of the kidneys as well as myocardial damage[113]. The titanium dioxide nanoparticles were found in the liver, spleen, kidney, and lung tissues, indicating they could be transported to other tissues after uptake through the gastrointestinal tract[113]. It has been reported that the retention halftime of titania particles in vivo is long because they are difficult to excrete[113].

Sayes' team researched the cytotoxic effects of nanoscale titania on human dermal fibroblasts and human lung epithelial cells[114]. They found that the material only elicited cytotoxicity and inflammation at relatively high concentrations of 100 µg/mL [114]. The cellular response is dose-dependent and the effects increase with exposure time[114]. No correlation to the sample surface area was found[114]. Instead, the structure of the titanium dioxide is important[114]: TiO_2 in anatase structure was found to be 100 times more toxic than the rutile form[114]. The damaging effect is closely linked to the material's ability to produce reactive species under UV illumination. Sayes et al. therefore link the disruption of cellular function to oxidative damage[114].

It has been demonstrated by Fischer et al. that MTT, a popular staining technique used for cytotoxicity tests, cannot be used when assessing magnesium alloys because the presence of magnesium ions in the cell culturing medium interferes with the staining mechanism and as a result gives false results[115].

PLGA

PLGA is a co-polymer of poly lactic and poly glycolic acid (Figure 8) that is biodegradable through hydrolysis of the ester backbone without the need for enzymes[116]. The degradation process is bulk erosion, during which lactic acid and glycolic acid, the components of the polymer, are separated[116]. Water and CO_2 are byproducts of this reaction[116]. The by-products of PLGA degradation are easily incorporated into metabolic pathways, so that they are finally excreted and thus PLGA is considered biocompatible[117].

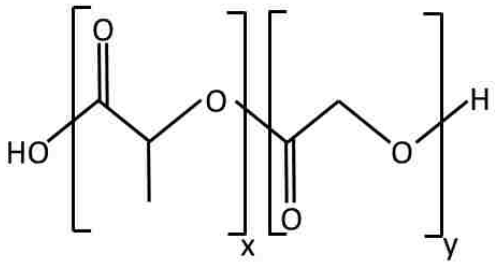

Figure 8: Structure formula of PLGA.

PLGA is approved by the FDA and has been widely used for drug delivery in different medical fields[116]. PLGA can support osteoblast attachment, growth, and function both in vitro and in vivo[117], so it is used to fabricate scaffolds[118]. PLGA has also been investigated as a coating on magnesium to protect it from corrosion[85]. In comparison, PLGA coatings on iron increased the degradation rate of the metal in in vitro studies[119].

The degradation characteristics of PLGA can be altered by choosing hydrophilic end groups for quicker degradation and hydrophobic end groups for slower degradation. Higher molecular weight also slows down degradation[116]. Hydrolysis of poly(α-hydroxyacid)-based polymers is catalyzed by acids and accelerates after having started[117]. Yoo et al. report that PLGA degraded slower in Phosphate Buffered Saline (PBS) with higher pH than in an acidic environment[116]. During degradation of those samples the pH of the test solution dropped continuously over the test period of 30 days[116]. Around degrading polymers the pH can be in the range of 2.0 - 6.0 [117]. In long-term organ culturing experiments on PLGA the culture medium progressively acidified, reaching pH values as low as 4.1 [117]. The pH change led to decreased glycolysis, collagen synthesis, and mineral content[117].

The effect of altered pH on cell functions is important for the field of biodegradable implant materials since biodegradable polymers are known to generate an acidic microenvironment

during degradation[117]. The findings further underline that degrading polymers in the vicinity can influence the biologic activity of cells and affect their behavior[117].

The acidic degradation products from PLGA degradation in the body have been found to cause serious inflammation and tissue damage in animal models[21]. Kohn et al. found that a decrease in extracellular pH has a tremendous effect on bone marrow stromal cells[117]. Collagen gene expression, collagen synthesis, and alkaline phosphatase activity altered due to low pH[117]. In this study human and murine cells were exposed to lowered pH solutions for 48 h and their response was assessed by measuring marker expression[117]. Alkaline phosphate activity and collagen synthesis decreased markedly with lower pH[117]. When decreasing the pH from 7.5 to 6.6 the drop was two- to threefold[117]. Based on this study's results it is expected that degrading polymers likely influence the biologic activity of the cells in the vicinity[117]. Osteocalcin levels were low at superphysiological pH levels, but were undetectable below physiological pH[117]. The magnitude of pH change studied is equivalent to the amount of shift bone cells would be exposed to in the vicinity of a degrading polymer[117]. Foreign body reactions to implanted PLGA fracture fixation devices coupled with bone resorption have been observed[117]. The hypothesis is that the inflammatory response is due to the acidic byproducts of the polymer degradation[117]. The growth and development of several cell types, including osteoblasts, is pH-dependent[117]. Mineralization and thus repair of bones are influenced by the composition of the extracellular fluids[117]. Ca-P salts precipitation depends on the pH[117]. These findings suggest that mineralization and bone repair are dependent on the tissue pH[117]. Even just slightly shifting the extracellular pH to lower values affects osteoblast function in vivo[117]. In studies the activity of osteoblasts decreased with metabolic acidosis, but increased during alkalosis[117]. Proliferation and differentiation of osteoblasts is linked to pH[117]. Similarly, the osteogenic ability of BMSCs also varies with the environment[117]. Small shifts in extracellular pH result in significant changes in the ability of those cells to express osteoblast phenotype markers[117]. Thus, changes in the pH of the local microenvironment by acidic PLGA degradation products could inhibit bone metabolism and impair healing[117]. The magnitude of the pH drop in case of wound healing corresponds to the pH range in which osteoblast function is reduced[117]. During wound healing the pH drops, so that acidity caused by polymer degradation could be perceived as analogous by the body[117].

It has been suggested that the decrease in pH due to PLGA degradation could be neutralized by incorporating basic salts or coating the surface with carbonated apatite minerals to avoid adverse effects[117]. Adding basic salts, e.g., calcium carbonate, to degradable polymers significantly impoved their biocompatibility[21].

A drawback of polymers is that they are not visible in x-rays[21]. Adding inorganic fillers can improve the x-ray visibility and, depending on the filler material chose, can even improve the biocompatibility of the polymers[120].

PLGA has a low modulus, which can potentially be improved by incorporating a material with a higher modulus. If this can be achieved it has the potential to be used in processes associated with bone healing. Hydroxyapatite and polymers have been investigated as reinforcement materials for PLGA[121]. PLGA reinforced with 2 and 4 wt.-% AZ31 alloy fibers was investigated by Wu et al.[122] PLGA had increased ultimate tensile strength (UTS) and elongation with embedded magnesium alloy fibers[122]. The UTS increased with increasing fiber content, but no significant difference between the elongation was found between composite samples with different fiber content[122]. Magnesium has been identified as a promising candidate for biodegradable metallic implants due it is mechanical properties that are closer to that of bone than the traditionally used steel or titanium alloys. As one of the essential metals for metabolism it was also found to be biocompatible. With a Young's modulus closest to that of bone in all metals considered suitable for implants, it has received a lot of attention as a possible candidate for biodegradable structural implants.

It has been observed that PLGA degraded faster when it had magnesium incorporated and a larger amount of added magnesium alloy lead to higher corrosion rates[122], but there is no report through which mechanism it accelerated. In contrast to Yoo´s experiments[116] Wu et al. observed a steady increase in pH when degrading their pure PLGA baseline sample in Hanks´ Solution[122]. Thus, incorporating magnesium into PLGA has the potential to improve the mechanical properties, alter the degradation rate, and neutralize the acids that are set free during the degradation process, which motivates this part of my thesis research.

3. RESULTS

Structure and properties of SPS consolidated Mg-Ti

Introduction:

Mg-Ti alloy synthesis by mechanical alloying through high-energy ball milling yields small particles of the alloy. For structural applications these particles need to be compacted into bulk material. Due to the metastability and low decomposition temperature of the alloy compaction cannot be carried out through standard sintering techniques, which require high temperatures that would destroy the alloy structure.

In this study Spark Plasma Sintering (SPS) was investigated as a possible means of consolidating Mg-Ti alloy particles into bulk form because it allows sintering at lower temperatures than with conventional sintering techniques or hot pressing and because the current flowing through the sample helps break up the oxide layer formed on the surface of the material. The influence of the sintering temperature, sintering pressure, and composition were investigated to find the optimal conditions for successful compaction of Mg-Ti powders.

Experimental details:

Sample fabrication

Magnesium-titanium alloys containing 5, 20, and 35 at.-% of titanium were fabricated by mechanical alloying in a vibratory type high-energy ball mill (SPEX 8000 Mixer/Mill). To achieve a ball-to-powder mass ratio of 16:1, a stainless steel vial and balls (SPEX) were selected. The starting materials were -325 mesh powders (less than 44 μm in size) of 99.8 wt.-% magnesium and 99.5 wt.-% (metals basis) titanium (both AlfaAesar). The milling was performed for 25 h for all samples, except those with 35% titanium, under an inert atmosphere of high purity argon. As a reference pure magnesium was milled under the same condition. The sample with 35% titanium was milled for 50 h as the alloy structure was not well established yet after 25 h of milling.

Spark Plasma Sintering

For SPS a Dr.Sinter SPS-2040 (Sumitomo Heavy Industries, Ltd., 4000 A max. pulse current output) was employed. Several sintering temperatures (350°C, 300°C, 250°C, 235°C, 225°C, and

215°C) were tested on Mg_{80}-Ti_{20} to find the maximum sintering temperature that leaves the alloy structure intact without decomposition and to evaluate the influence of the sintering temperature on the density of the alloy. After establishing the maximum sintering temperature (215°C), samples with 5, 20, and 35 at.-% titanium were sintered at that temperature. The pure Mg samples were sintered at 250°C. The temperature was ramped up at~70°/min. SPS dies made of graphite (C) and tungsten carbide (WC) were used in this study. The dies were closed with graphite stubs on the top and bottom to contain the loose sample particles (Figure 10). A hole is drilled into the die wall on one side to hold a thermocouple during the sintering process. This hole does not reach the sample, so that the measured temperature deviates from the temperature inside the sample. During the sintering process force is applied to the sample by pressing together the graphite stubs. Pulsed DC current is simultaneously passed through the sample via the graphite stubs. The current flowing through the sample helps break down the surface oxide on the particles, thus facilitating particle sintering.

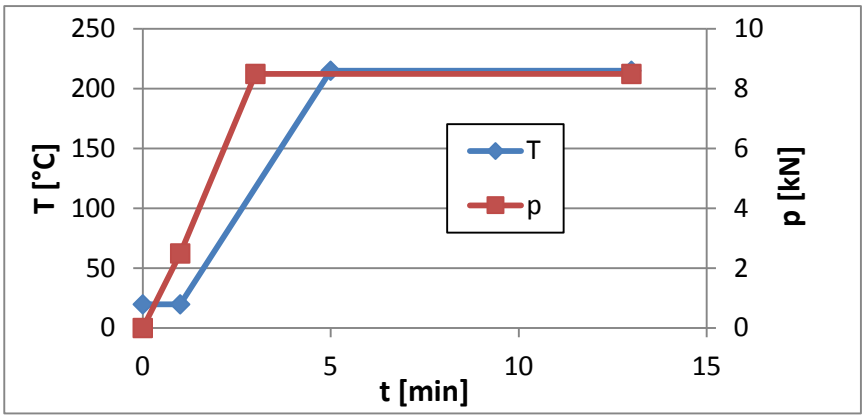

Figure 9: Temperature and pressure control during sintering

The applied sintering pressure varied with the type of die used: 7.5 kN for the graphite die and 8.5 kN for the tungsten carbide die. The pressure was limited by the type of die to prevent damage. Considering that the dies had an inner diameter of 12.7 mm, the applied forces resulted in stresses of 59.2 and 67.1 MPa respectively on the sample. The inserted cylinders in both cases were made of graphite for optimal conduction. A pre-load of 2.5 kN (= 19.7 MPa) was applied after the samples were mounted in the sintering chamber. In order to prevent sticking of the sample particles to the dies, their inside walls were coated with boron nitride spray. The sintering pressure was applied shortly before reaching the sintering temperature. In order to keep consistent comparison the sintering time was constant (12 min.) for all samples. All

sintering parameters were manually applied and controlled until the optimal sintering conditions were found. All subsequent sintering experiments were run with an automated script for repeatability (see Figure 9).

Density measurements

After sintering the thickness of the sintered samples was measured on at least three different points over the whole sample to determine the sample volume. The samples were then weighted to calculate their densities. The obtained values were compared to the theoretical density resulting from a physical mixture of magnesium and titanium at the samples' compositions to determine the achieved density in percent.

Density was also estimated based on optical appearance of metallographic sections taken at 50x magnification. At least three images were analyzed for each sample and the average values of the resulting density are reported. Optical density was determined with ImageJ. First, the original metallographic section photos were cropped to exclude the scale bar and converted to 8 bit black-and-white images. In ImageJ the area to be measured, i.e., the area occupied by material, was selected with the threshold adjustment tool. ImageJ can then calculate which percentage of the image is occupied by the selected area.

Differential Scanning Calorimetry

DSC was performed on a NETZSCH DSC 404 C Pegasus purged with argon at a flow rate of 50 ml/min. Only the ramp-up was recorded from 40°C to 520°C. Pt-Rh sample pans were used. An empty pan served as reference.

X-ray diffraction

The structure, composition, and morphology of powders produced by ball milling were investigated by θ-2θ x-ray diffraction using a Siemens D500 diffractometer with Cu K_α radiation. The step size for these scans was chosen as 0.002° and the scan speed was 0.04°/min for sufficient counts.

Micro computer tomography (µCT)

After SPS the sample were scanned with micro computer tomography (µCT) to see the pore size and distribution. µCT was performed on a SCANOMEDICAL µCT 40 with high resolution settings, which results in a resolution of 20 µm. For analysis the black/white scan data were fitted to

resemble the sample image as closely as possible by changing the lower and upper threshold values determining voids and material present.

Metallographic preparation

Selected sintered samples were embedded into epoxy to expose a well-defined area. One side of the embedded sample was then ground with gradually finer silicon carbide paper up to 4000 grit and subsequently polished with polycrystalline diamond suspensions (METADI Supreme) and pastes (METADI II; all Buehler) with abrasive particle sizes of 6, 3, 1, and 0.25 µm. Grinding was carried out with water as the lubricant and to wash the samples after each grinding step. After the last grinding step the samples were rinsed with ethanol and immediately dried in hot air. For polishing a non-water based lubricant (METADI fluid, Buehler, USA) was used as further exposure to water would have corroded the samples instantaneously. After the individual polishing steps the samples were only washed with ethanol, following by drying in hot air.

Corrosion tests

Samples were corroded in 1 L of Hanks' Solution (appendix) at 37°C. The corrosion progress was monitored via hydrogen evolution, which is a simple, but reliable test method for monitoring the corrosion of Mg and its alloys[77]. To collect the hydrogen a funnel was placed over the sample and an inverted cylinder filled with the test solution fitted over its end to ensure a seal against air. The funnel was held hovering over the sample with a coated wire construction to allow an exchange of solution and not block the sample off from the majority of Hanks' Solution. Half of the test solution was exchanged every week to alleviate the rise in pH and ensure a sufficient amount of corrosive species to be present at all times. One "overheated" Mg-Ti20 alloy sample (sintered at 350°C) was also corroded as a comparison to the intact structure to help identify the corrosion protection mechanism.

Hardness test

Rockwell hardness was tested on a Mitutoyo AR Hardness Testing Machine with settings for the HRH scale (1/8" spherical hardened steel indenter, 60 kgf applied force).

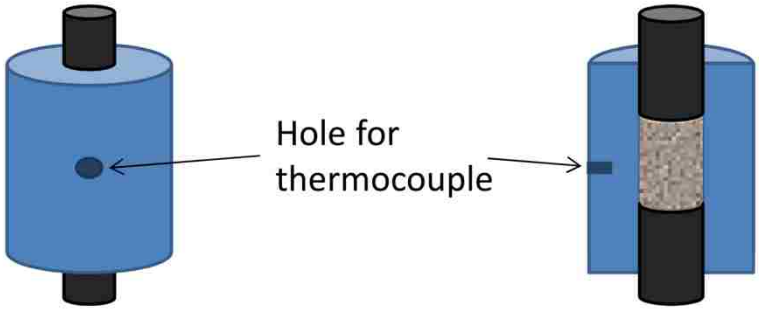

Figure 10: SPS die and thermocouple placement during experiment.

Results & Discussion:

Alloy formation

Upon ball-milling for a sufficiently long time the physical mixture of magnesium and titanium is transformed into an alloy. The change in peaks observed by XRD before and after milling is caused by alloy formation (Figure 11): Before milling, two sets of three peaks, corresponding to the respective pure magnesium and pure titanium, are visible. The titanium peaks are weaker than the magnesium peaks because the mixture contains less titanium than magnesium. After milling, those two sets of peaks merge into one prominent set of peaks that can be indexed by a hcp lattice with a= 3.1662 Å and c= 5.8899Å, thus demonstrating successful alloying. The new peaks are shifted towards higher angles compared to the original magnesium peaks because the titanium atoms have smaller lattice spacing and are incorporated into the magnesium lattice. The new peaks are also much broader and lower in intensity because ball milling introduces large amounts of strain into the lattice. There is a small bump visible at the pure titanium peak position around 40° in the XRD scan of the milled powder. This peak corresponding to the (10·1) set of planes is the most intense titanium peak in the whole spectrum. The presence of the small peak shows that some titanium is still present in its elemental form and has not been incorporated into the alloy.

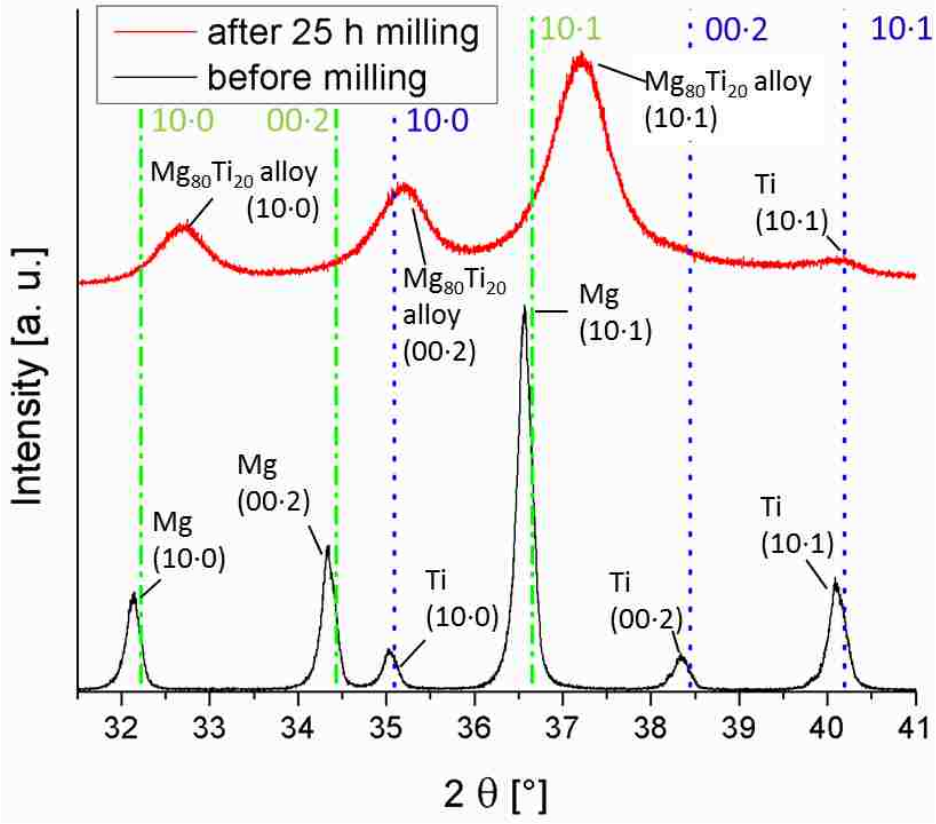

Figure 11: XRD of Mg-Ti mixture with 20 at.-% Ti before ball milling and alloy after 25 h of ball-milling. Green lines indicate the peak positions for pure magnesium and blue dotted lines mark the pure titanium peak positions

When comparing XRD scans of mechanically alloyed Mg-Ti with different titanium contents and ball-milled pure magnesium (Figure 12), it is obvious that the peak shift is correlated to the titanium content: the more titanium, the further the peaks shift.

The XRD scans of Mg-Ti alloys presented here look similar to those reported in the literature[25,40]. With alloying the lattice parameters also change and the values of lattice constant, a, fall between those of pure magnesium (0.32095 nm[123]) and titanium (0.29512 nm[123]) (Figure 13). In contrast, the c values are larger than those of both titanium (0.46845[123]) and magnesium (0.52107 nm[123]). Whereas a follows Vegard's law closely, c does not match by numbers or trend: c for the alloy containing 35% Ti is higher than that of 20 % Ti alloy. This trend mismatch could be due to the broad peaks that make determining the exact peak position difficult and introduces a certain error into the equation. The change in lattice parameters is a strong evidence of alloy formation.

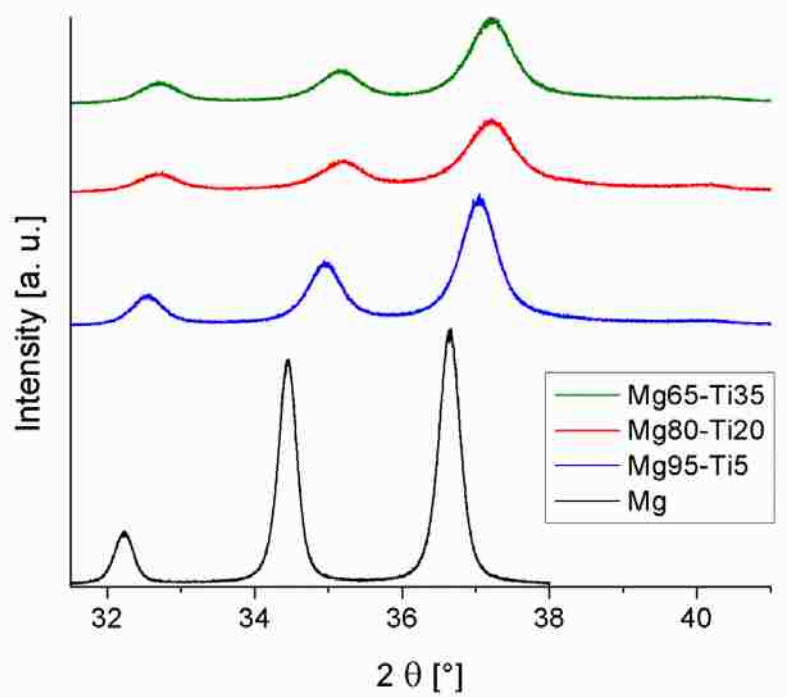

Figure 12: XRD of Mg-Ti alloys with 5, 20, and 35 at.-% Ti and pure Mg ball-milled for 25 h as comparison. 5 and 20% ball-milled for 25 h, 35% for 50h. XRD scans look similar to those reported in the literature.

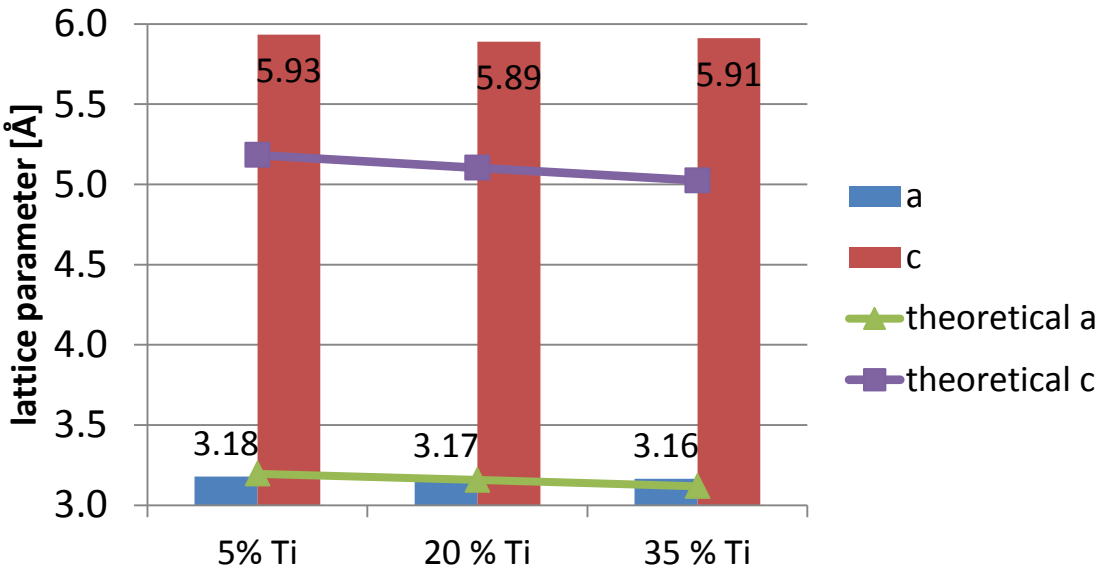

Figure 13: Lattice parameters calculated from 100 and 002 peak positions of the alloys compared to theoretical values based on Vegard's law.

Influence of SPS on alloy structure

Figure 14 shows a compilation of XRD scans of Mg-Ti alloy with 20 at.-% titanium after SPS at different sintering temperatures compared to the original alloy structure after milling. Samples sintered at temperatures of 225°C or above show graphs with distorted features or additional peaks, indicating that the alloy structure was compromised. The structure of the sample sintered at 215°C closely resembles the original alloy structure, so it can be assumed that the material was not noticeably altered in terms of the alloy structure during SPS. Based on this finding 215°C is assumed to be a safe sintering temperature retaining the original alloy structure.

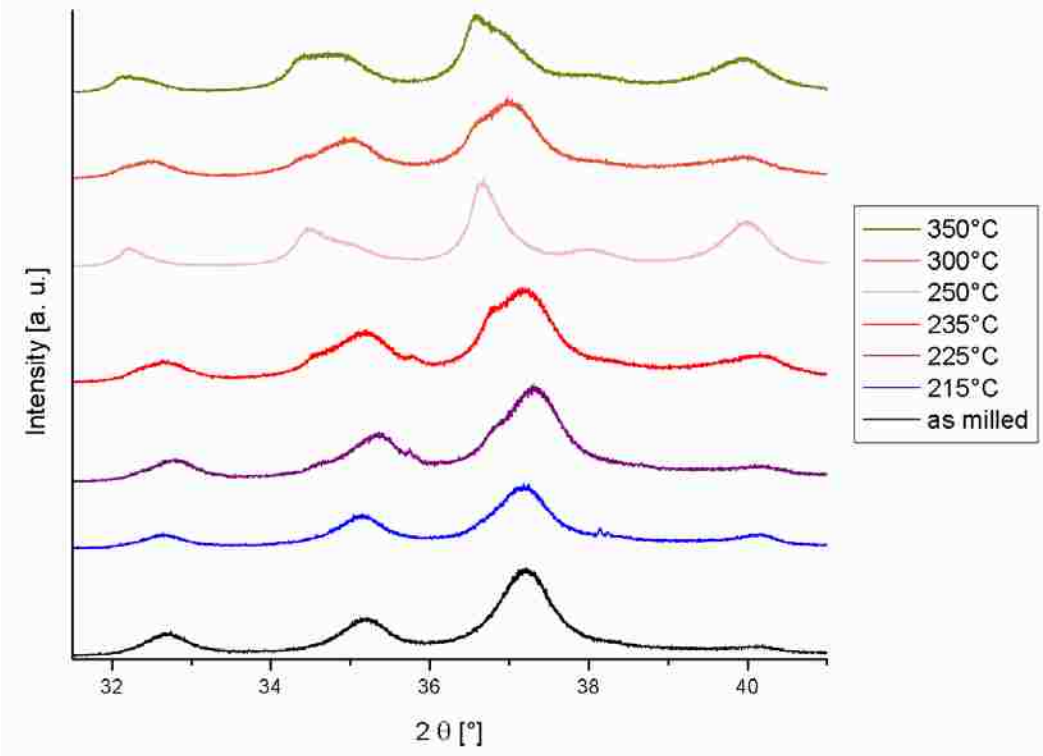

Figure 14: Mg_{80}-Ti_{20} alloy after SPS with different sintering temperatures. The filled curve is unsintered material with the same composition as a reference.

Indeed, when comparing the XRD scans of alloy samples with different compositions after sintering at 215°C (Figure 15), almost all of them retain their original structure very well. The two most intense peaks of the Mg-Ti35 sample sintered in a WC die bulge out on the lower angle sides, indicating slight de-alloying, but other than that all scans retain their original shapes.

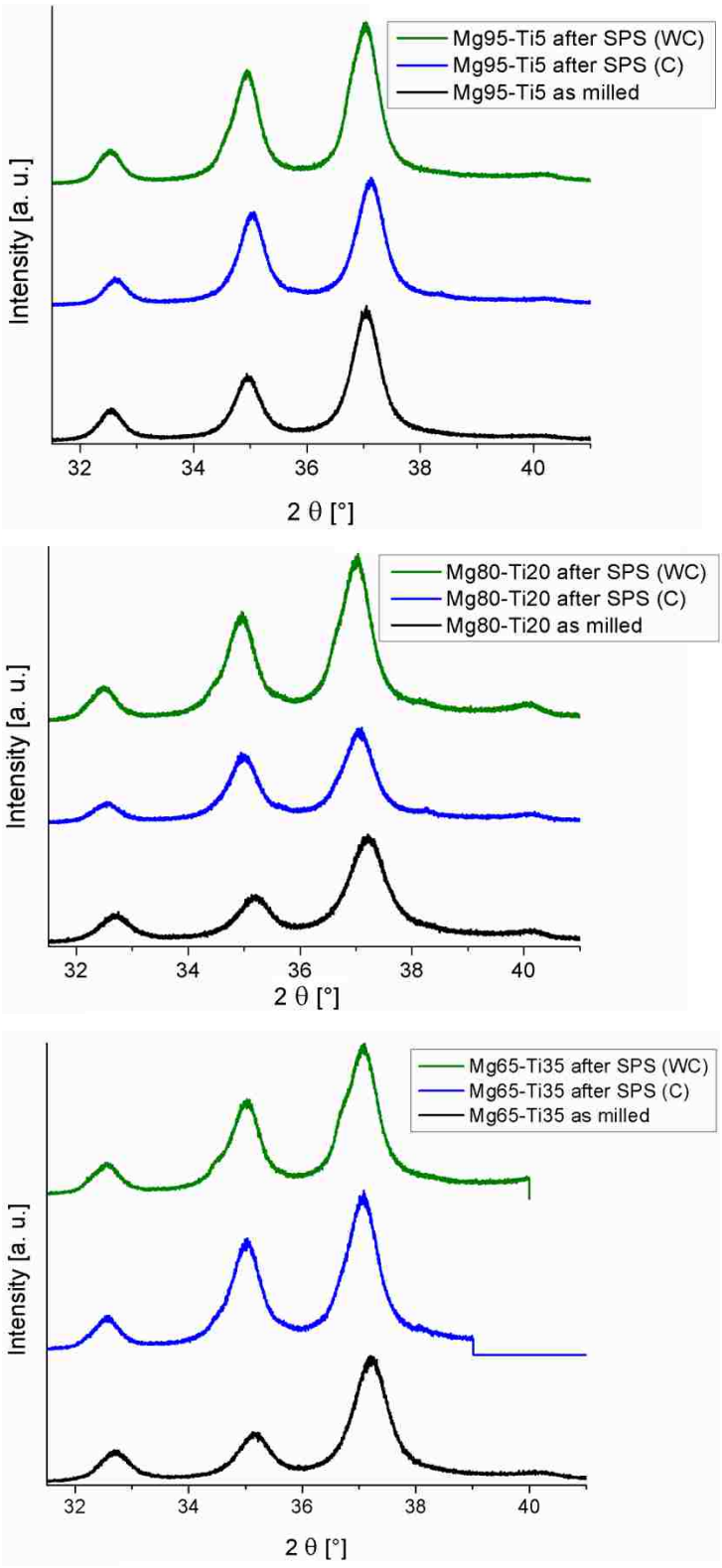

Figure 15: XRD scans of Mg-Ti alloys with different titanium contents before and after SPS at 215°C in both dies.

XRD scans confirm that the alloy structure is preserved during the sintering process with the chosen parameters.

From a comparison of the FWHM values (Table 3) of as-milled and compacted pure magnesium it becomes apparent that the grains grow slightly during SPS, which is expected during a sintering process. Milling pure magnesium increases the FWHM significantly, which indicates that the sample is strained. During sintering some of this strain might be released in addition to grain growth. Since the strain and grain size effects cannot be distinguished in the samples, the real grain size cannot be calculated from the FWHM.

Table 2: Full width at half maximum (FWHM) values of as-milled and compacted pure magnesium.

	FWHM		
Sample	(10·0)	(00·2)	(10·1)
unmilled	0.2014	0.2050	0.2140
as-milled	0.3254	0.3230	0.3526
Compacted by SPS	0.2436	0.2312	0.2592

Metallographic sections

It can be seen from metallographic sections of the sintered samples (Figure 16) that the particle sizes vary greatly within each sample. It is also visible that the density is very low, much lower than the theoretical density calculated based on the assumption that the material has a mixed density of pure magnesium and titanium. Optically it seems that the achieved density decreases with increasing titanium content, which follows the trend observed for the theoretical density calculation.

5% Ti

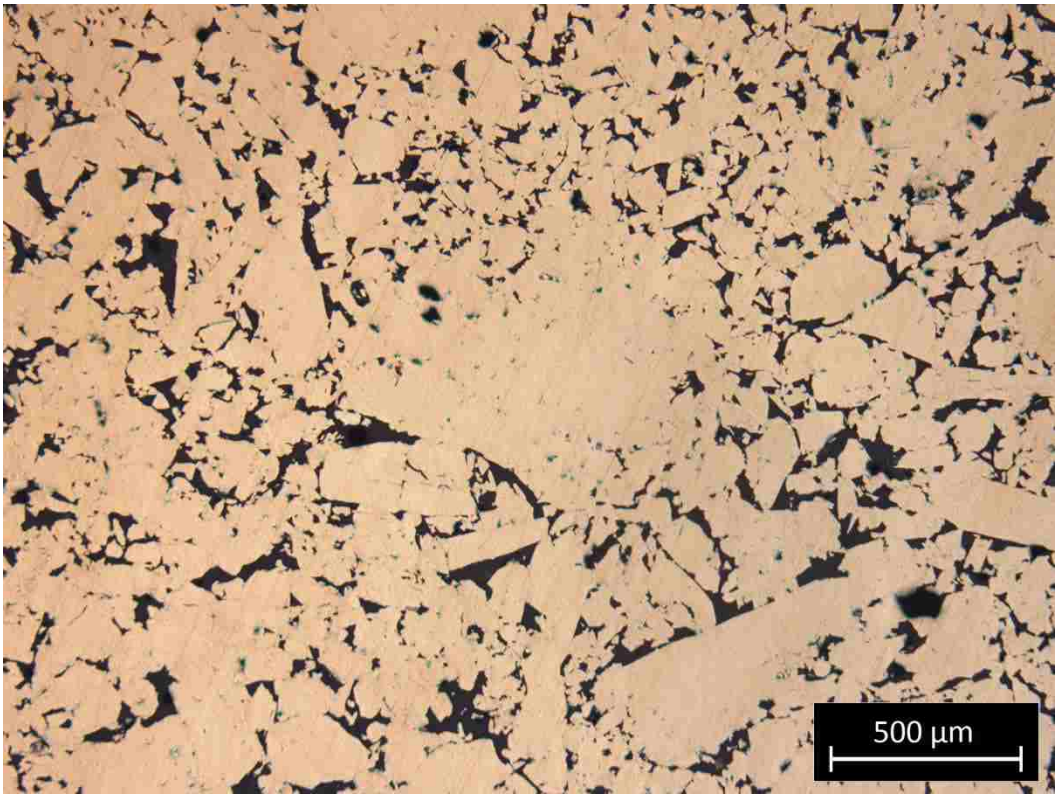

20% Ti

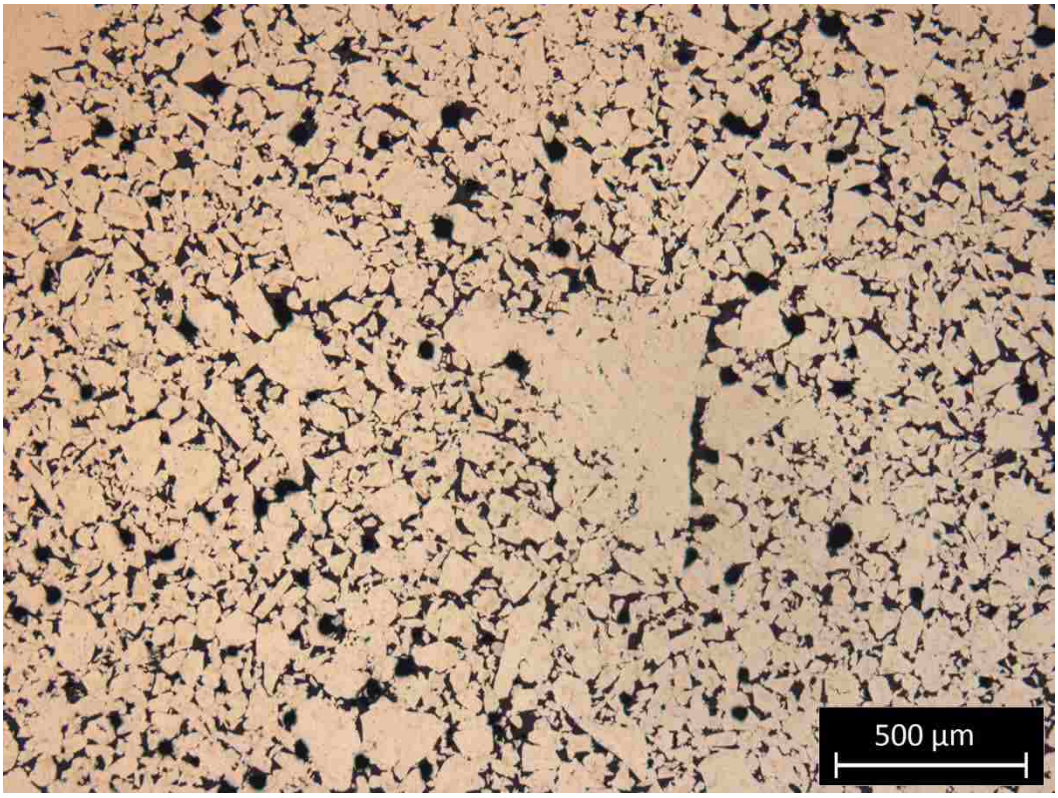

35% Ti

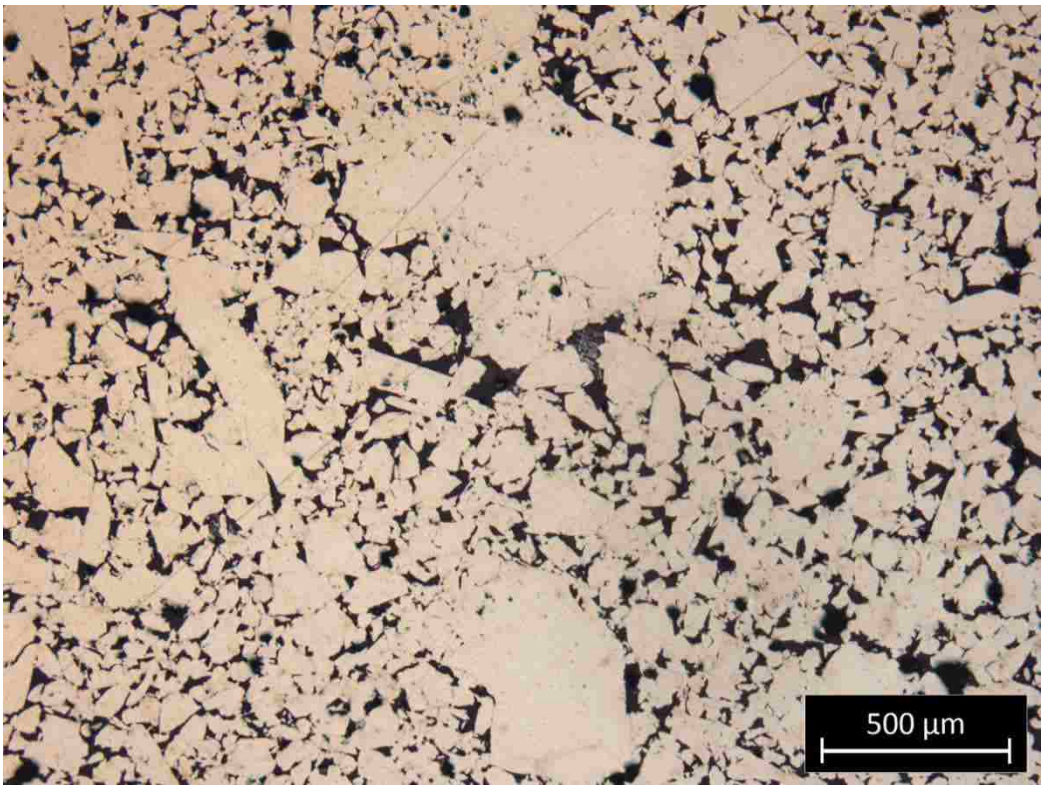

Figure 16: Metallographic sections of the SPS-sintered samples with different titanium contents at 50x magnification.

At 200x magnification the joining boundaries between the particles can be observed in the metallographic sections (Figure 17, Figure 18, Figure 19). Many joints appear seamless, in others a faint line remains, which indicates that they are probably only pressed together, but no chemical bonds are formed between the particles. Especially in the samples with higher titanium content the joints are very narrow, which could explain the brittle fracture during hardness tests. In principle SPS seems to be capable of joining Mg-Ti alloy particles together, but the low pressure limit in this study prevented a higher density. The density could be improved significantly by pre-compressing the powder samples in a uniaxial press prior to the sintering process or using dies for the sintering that can withstand significantly higher pressures. With higher densities the contact area between particles will increase and thus greatly increase the joining areas, resulting in a stronger bulk material.

Within the sample particles small gray speckles can be seen. The amount of gray spots increases with increasing titanium content. They can be linked to the elemental titanium peak observed in XRD scans. It has already been reported by Liang and Schulz[25] that during ball milling not all of

the titanium dissolves in magnesium, but some stays behind in elemental form. In the same study those remaining titanium clusters of 50 - 150 nm in size were too small to be detected by XRD and only show up in TEM investigations[25]. However, it is reasonable to believe that pure titanium particles in varying sizes can remain after milling and that the largest ones are visible under optical microscopes. This hypothesis is further supported by the number of gray speckles increasing with titanium content, which suggests that the solution limit for the parameter set used for synthesis is always below the target composition. The same dispersed gray areas were also observed in the powder particles after milling, before the samples were sintered. Therefore, sintering does not precipitate titanium from the solid solution, but the as-milled state is preserved, as indicated by XRD scans from before and after sintering.

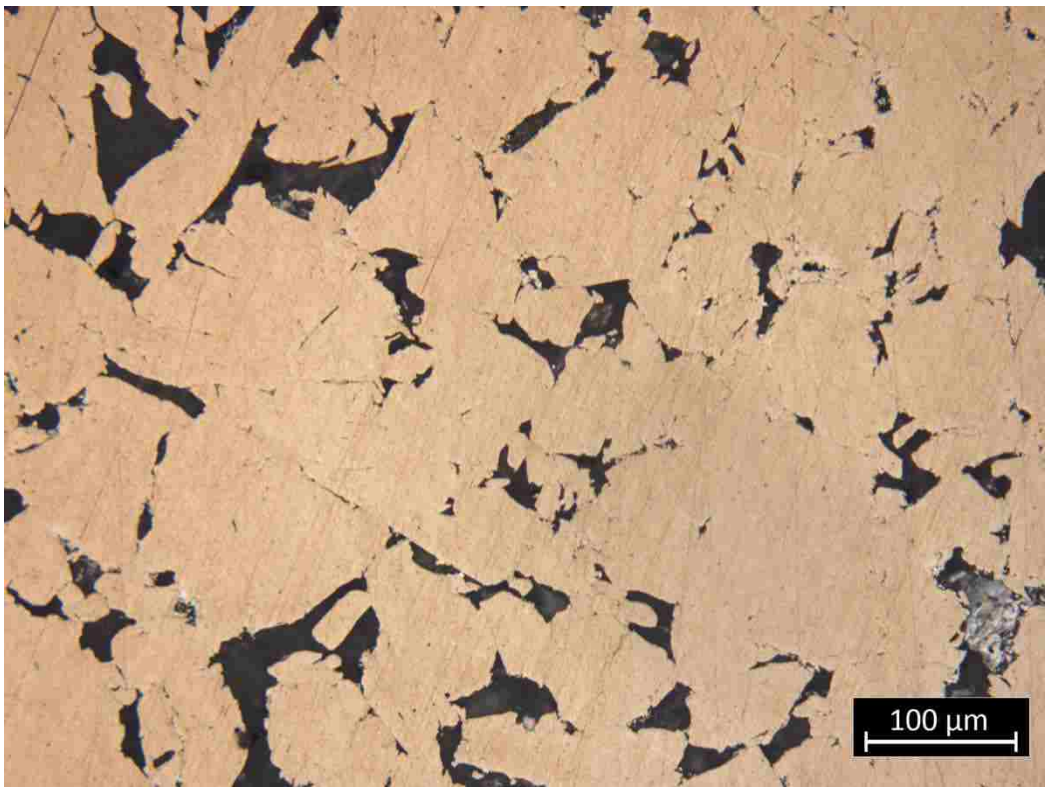

Figure 17: Metallographic section of Mg_{95}-Ti_5 alloy sintered in WC die at 200x magnification.

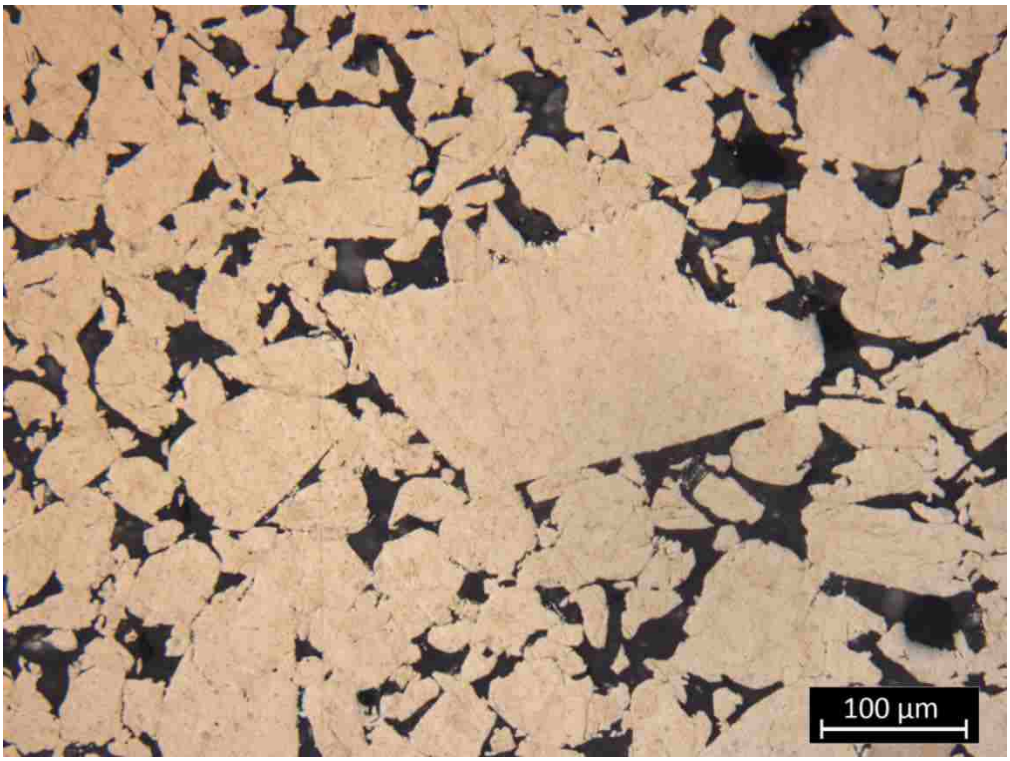

Figure 18: Metallographic section of Mg80-Ti20 alloy sintered in WC die at 200x magnification.

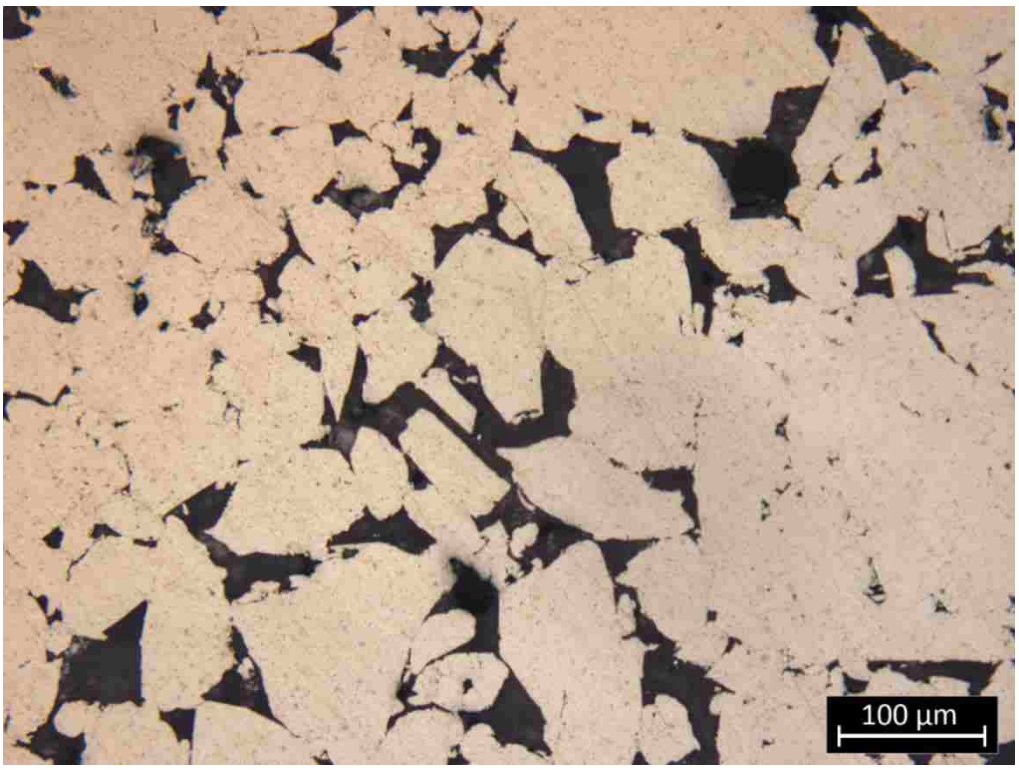

Figure 19: Metallographic section of Mg_{65}-Ti_{35} alloy sintered in WC die at 200x magnification.

Density

To evaluate the influence of the titanium content on the achievable density, powders with different titanium contents were compared. The influence of the dies was also investigated. When comparing pure magnesium and alloys with different titanium content (Figure 20) a clear trends can be seen: The highest density achieved was with pure magnesium. Then the density decreases with increasing titanium content almost linearly.

This is expected because titanium has a higher modulus and higher yield strength than magnesium. Theoretically the modulus of an alloy can be estimated from the rule of mixture, thus the material should become stiffer with the addition of titanium. Moreover, it needs higher temperatures to activate additional slip systems in titanium[124]. All those factors make titanium harder to deform and thus to compress compared to magnesium, resulting in lower densities when the samples contain more titanium.

A factor contributing to the low achieved density is the particle shape. The particles yielded from high-energy ball milling are rather flaky in shape. It might be that the cold welding is more efficient in certain crystallographic directions. Since the particles are not uniform in shape, they cannot be packed as densely without severe deformation, which would require much higher loads.

The low density of the sintered samples can be attributed to the low pressure applied during the sintering process to avoid breaking the dies. The density could be increased by pre-compressing the powders in a uniaxial press with higher loads prior to sintering. Even when the same low pressure is applied during SPS on the pre-compressed samples they should come out with a much higher density. Alternatively, a higher pressure applied during sintering with sufficiently strong dies is expected to increase the density as well.

The achieved density is not very high, but a slightly porous material may also have advantages for biomedical applications. Porosity can (1) further lower the elastic modulus, which is still at least twice as high as that of bone based on theoretical calculations and (2) through tissue ingrowth into the pores lead to mechanical interlocking of the tissue (i.e., bone) with the implant, thus fixing the implant in place. The downside of porosity in physiological environments is the increased corrosion rate due to the higher surface area exposed to the body fluids. Low density also makes samples more brittle, which would pose a problem since hcp materials

inherently are not very ductile. If a higher pressure could be applied before or during sintering by using stronger dies, this would result in even higher density. A higher density was achieved for all compositions with WC dies compared to C dies, which is probably due to the higher pressure applied when using the stronger WC dies.

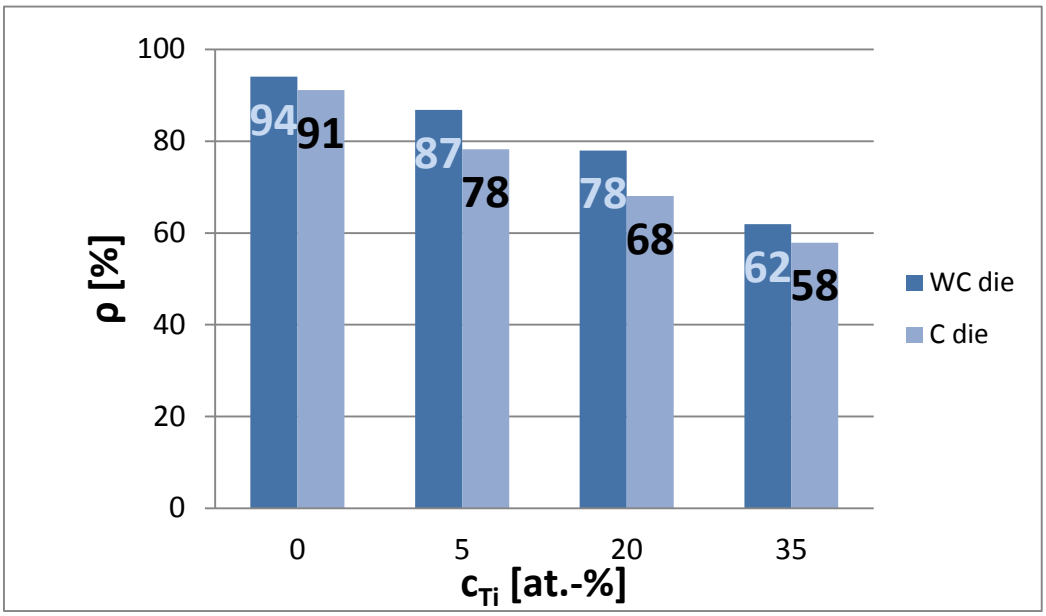

Figure 20: Achieved density in relation to Ti content with both dies as determined from the samples' weights and dimensions. There is a clear correlation between alloy composition and achieved density. To calculate the density the sample geometry was measured and the samples were weighted.

The density values obtained with ImageJ analysis confirm the densities presented above: achieved density decreases with increasing titanium content. When calculating the density from microscope images, though, the gap in density between pure magnesium and the 35 at.-% titanium alloy is not as large. Additionally, no density difference between the two samples with the highest titanium contents were found, although the titanium content of one sample is almost double of the other. Those discrepancies could arise from the way the flaky particles align during compression. The optical density in one orientation may not be accurately representing the overall bulk density.

It is interesting to note that the optical density for the overheated Mg-Ti_{20} alloy was only 70%, compared to 81% of the sample with the same composition that retained its alloy structure. Increasing the sintering temperature in SPS thus may not improve the achieved density.

Table 3: Results from optical density measurement with ImageJ. All alloy samples were sintered in WC dies, the pure Mg sample in a C die.

Sample	Optical density [%]
Mg	92
Mg-Ti5	87
Mg-Ti20	81
Mg-Ti35	81

µCT scans show the three-dimensional morphology of the sintered samples, including outside surfaces and pores. The pores are not interconnected. Pore sizes range from a few hundred µm to a few µm (detection limit of the µCT machine). An example for rough and smooth sides of a rim is shown in Figure 21. Figure 22 shows a representative top surface.

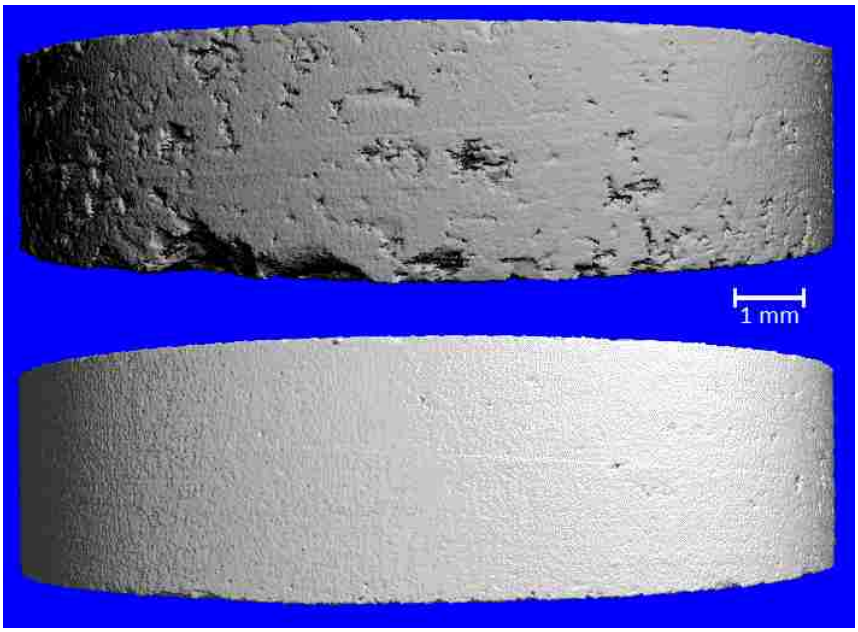

Figure 21: Example of rough (top) and smooth (bottom) rim sides. This sample is pure magnesium sintered in a graphite die.

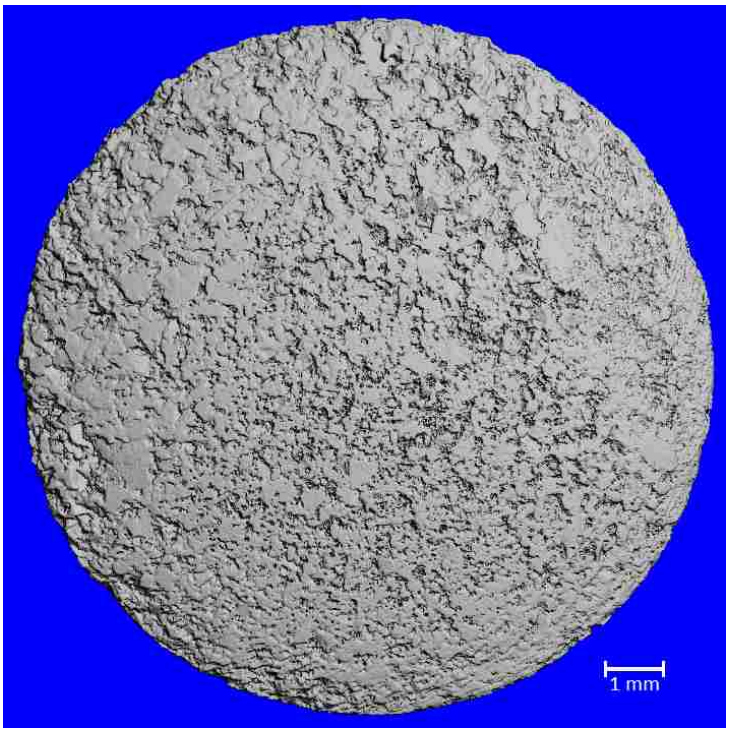

Figure 22: Example of top view on a sample. This is a 5% Ti alloy sample sintered in a graphite die.

Some pits can be seen on the outside surfaces (top, bottom, rim) of the magnesium sample sintered in a graphite die (Figure 23). Large grooves have formed on one side of the rim, the other is very smooth, comparable to the magnesium sample sintered with the WC die. Inside are rather large, irregularly shaped voids, many with sharp, pointy edges. Large and small pores are unevenly distributed throughout the sample, however, the core has more small pores and fewer large ones.

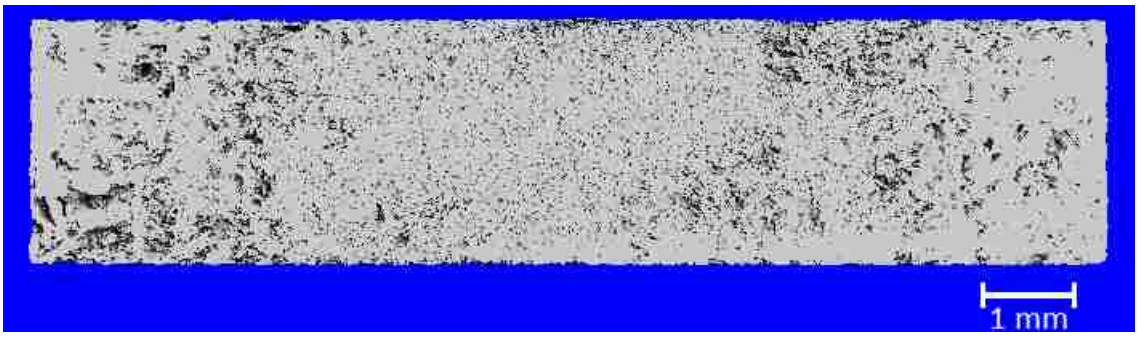

Figure 23: µCT scan of magnesium sintered in C die, cut through the middle of the sample.

The magnesium sample sintered in the WC (Figure 24) has a much smoother rim surface than the one sintered in the C die, with just some small pores visible on the rim. Top and bottom surfaces have pits, similar to the C die sample, but they are smaller. Mostly small pores and a few medium-sized ones are found inside. In the core small pores are uniformly distributed. Around the edge (outer 1 mm of circumference) there are fewer pores, but some are larger than those found in the core.

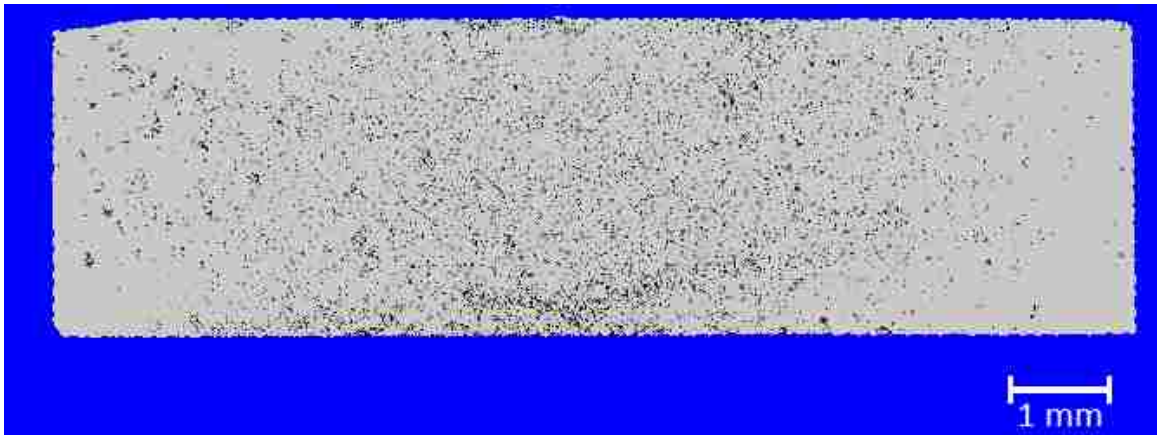

Figure 24: µCT scans of magnesium sintered in WC die.

The 5% titanium alloy sintered in a WC die (Figure 25) has a rougher rim than the pure magnesium sintered in the same die. Its top and bottom surfaces show pits, most of them are interconnected by grooves; overall the surfaces have a rough appearance. Inside the pore distribution is similar to that found in the magnesium sample sintered with a WC die, with the fine pores in the core, but those are larger than in the case of the magnesium sample. The edge area has fewer and smaller pores on one side of the sample, but more of the bigger ones on the other side. There are also bigger pores next to the top and bottom surfaces. Among the larger pores some are randomly shaped with sharp edges, some are oval or round.

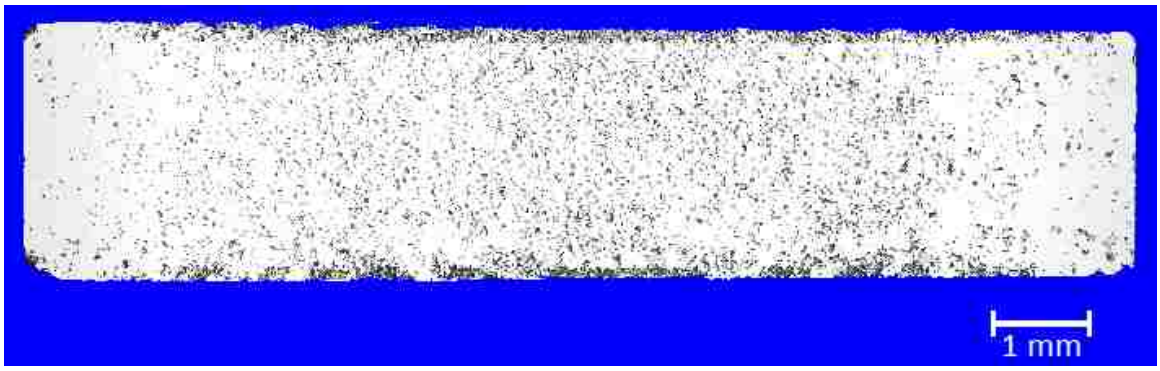

Figure 25: Cut through Mg_{95}-Ti_5 sample sintered in WC die.

When powder of the same batch is sintered in a C die (Figure 26), the rim becomes slightly rougher than with the WC die. Many small pores are located in the core. Fewer pores are seen on the peripheral zone (about 1 - 1.5 mm from the edges). Medium sized pores are distributed uniformly throughout the sample (core and periphery). Small pores are accumulated on the top and bottom of the core region.

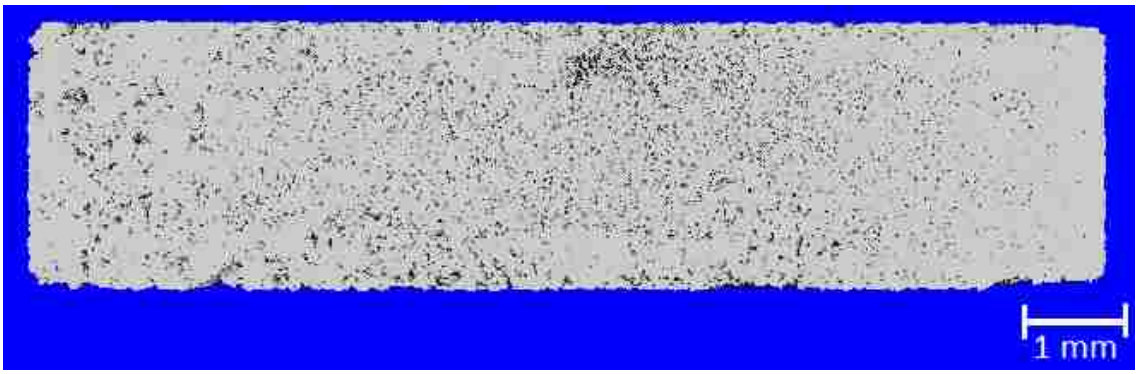

Figure 26: Cut through 5 at.-% titanium sample sintered in graphite die.

The rims of the 20 at.-% titanium containing sample sintered with the WC die (Figure 27) were smoother than those of the 5 % titanium samples. Top and bottom have pits and grooves, but they form larger coherent areas of depressions and flat surface area and appear to be not as deep as those of $Mg_{95}Ti_5$ samples. Small pores penetrate the rim. A lot of small pores are observed in the core, less pores in the periphery. Pore sizes do not vary as much as in the case of pure magnesium and 5% alloy. Medium sized pores appear randomly distributed. Small and medium pores accumulated on the top surface. The gradient between peripheral and core areas is not as pronounced as in pure magnesium and the 5% titanium alloy.

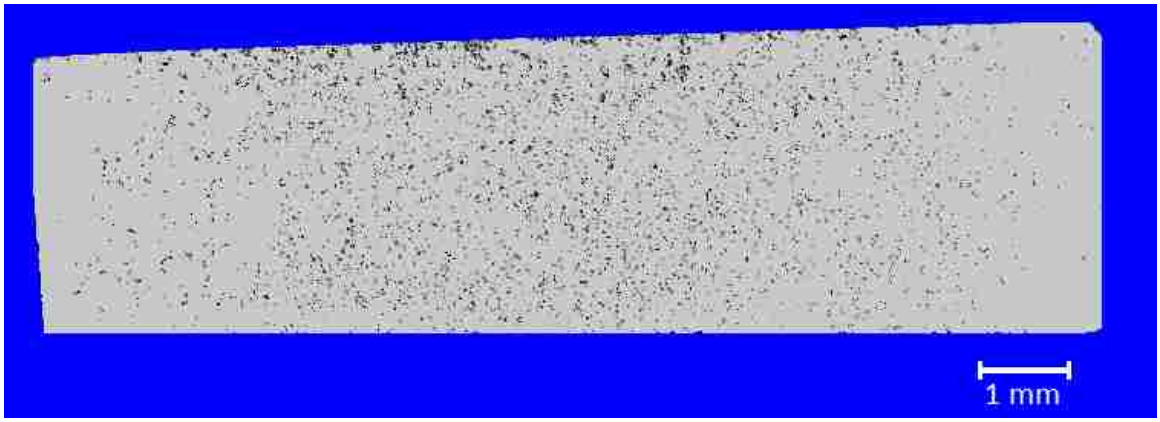

Figure 27: Cut through Mg_{80}-Ti_{20} sample sintered in WC die.

On one side the rim of the $Mg_{80}Ti_{20}$ alloy sample sintered in the graphite die (Figure 28) is very smooth, the other side has one spot with grooves, comparable to the sample sintered in the WC die. The top and bottom roughness are comparable to that of the $Mg_{95}Ti_5$. The pore distribution on the inside is similar to that of the WC-sintered sample.

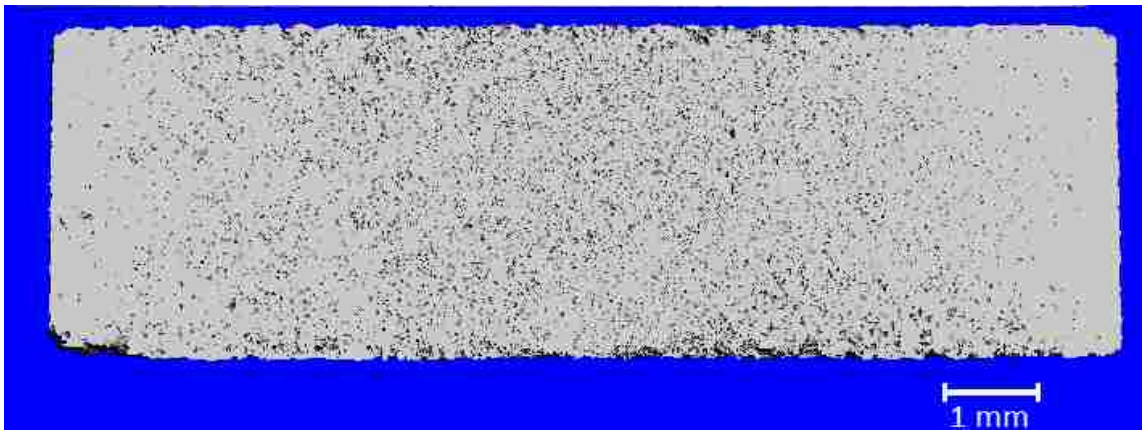

Figure 28: Cut through Mg_{80}-Ti_{20}sample processed with graphite die.

The rim surface, pore distribution on the inside, top and bottom of $Mg_{65}Ti_{35}$ samples (Figure 29 and Figure30) are comparable to the $Mg_{80}Ti_{20}$ samples. Just on the $Mg_{65}Ti_{35}$ sample sintered in a graphite die (Figure 30) the larger pores are accumulated near the top and bottom surfaces.

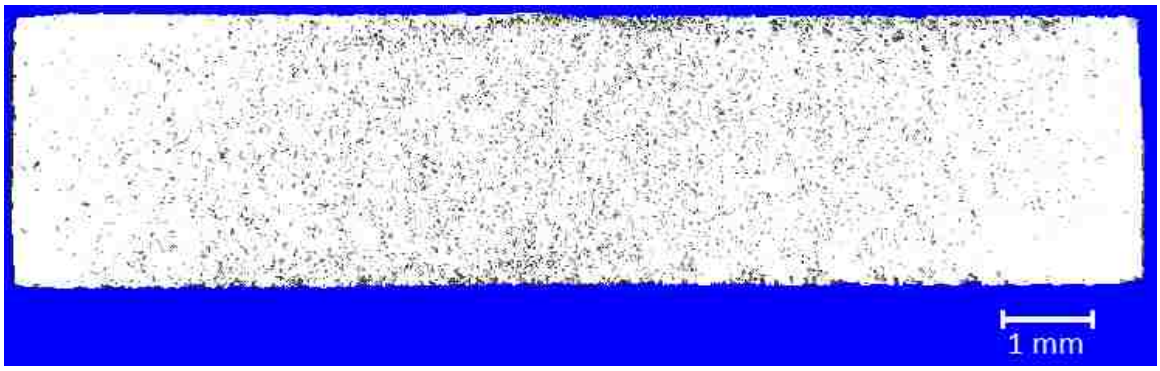

Figure 29: Cut through Mg_{65}-Ti_{35} sample sintered in WC die.

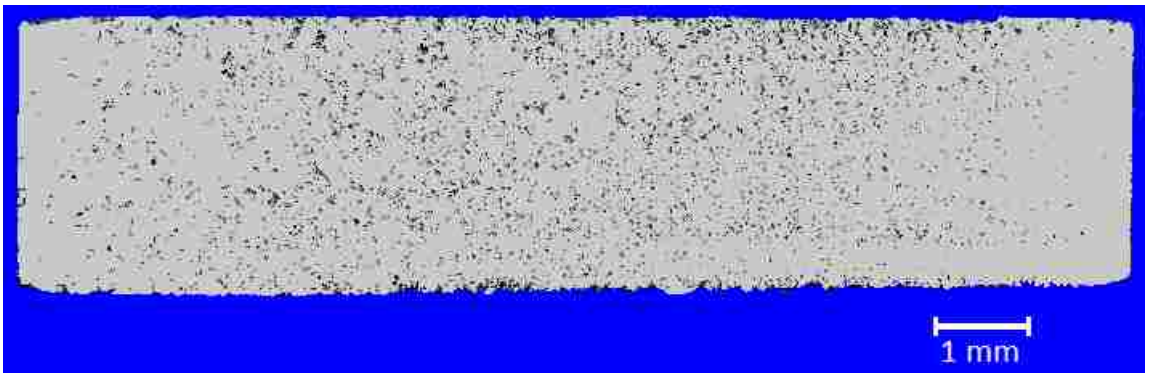

Figure 30: Cut through Mg_{65}-Ti_{35}sample sintered in C die.

DSC

Magnesium-titanium alloy will decompose at elevated temperatures because it is metastable. The decomposition temperature was determined by both DSC and SPS at different sintering temperatures. The decomposition temperature during SPS has to be double-checked, as the recorded temperature is not the actual temperature inside the die because the thermocouple is not touching the sample.

Before the sintering process the 20at.-% titanium alloy´s decomposition temperature was determined by differential scanning calorimetry (DSC). To check how SPS changed the sample another scan was run on the same sample after compaction (Figure 31). The slope changes slightly from 150°C on. From 200°C on the curve rises faster, which means that an exothermic reaction is taking place, i.e., the sample goes into a more stable state, meaning that it loses its non-equilibrium alloying state. From around 330°C on the slope becomes even steeper. From the shape of the DSC curve it can be concluded that the de-alloying sets in at 200°C and is accelerated above 330°C. The curve flattens out after sintering, which indicates that the

material is in a more stable state afterwards. In the case of a metastable material this means that the original alloying state has been altered to a certain degree.

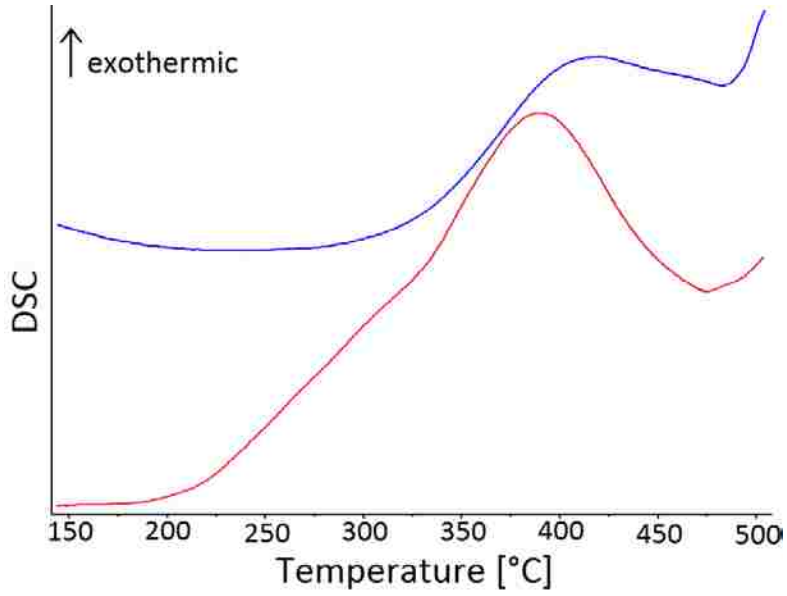

Figure 31: DSC of $Mg_{80}Ti_{20}$ alloy before (red, bottom) and after (blue, top) SPS with a sintering temperature of 250°C.

The obtained DSC plot qualitatively fits with the one presented by Liang and Schulz[25] in that they both exhibit an exothermic phase transition between 350 and 400°C. However, the one presented here exhibits an additional peak around 475°C and the slope of the curve changes at around 330°C. Liang and Schulz on the other hand found some small peaks between 100°C and 150°C, which are missing in this plot. The plots should be very similar because the alloy composition and milling time are the same.

The sintering temperature is limited by the low decomposition temperature of Mg-Ti alloy. Judging from the DSC measurements the temperature should ideally be kept below 200°C. However, due to the hcp structure of magnesium the material does not deform easily. To enhance deformability it needs to be heated up to at least 225°C because above that temperature additional slip systems are activated, leading to increased plasticity[124]. As expected, the alloy processed at 350°C is decomposed (Figure 14).The samples sintered at 300 and 250°C have also decomposed, however, to a lesser extent.

Hardness

Most samples broke during hardness testing, so that only very few hardness values could be obtained. The samples are probably so brittle and weak because the connections formed between the individual particles are small and few due to the low densities. It is noteworthy that the majority of the samples that did survive the hardness test were sintered in WC dies, which also showed the higher densities (Table 1).

Table 4: Hardness values on samples with different compositions and from two kinds of dies.

Sample Ti content [at.-%]	Die material	Sintering temperature [°C]	Average hardness
30	WC	250	73.6 HRH
20	WC	250	89 HRH
20	WC	235	72 HRH
20	WC	225	62.5 - 79.2 HRH
20	C	215	73.3 HRH

Due to the small number of measurements it is hard to evaluate whether the hardness increases with titanium content, but in the samples tested no obvious correlation could be established between hardness and sintering temperature, die material, or composition. Pure magnesium has a hardness of 16-54 HRE or 30-47 HB, depending on the processing method[125]. Pure titanium has a hardness of 70-74 HB[125]. Compared to the highest hardness values of pure magnesium, the hardness of some sintered alloy samples is higher. But compared to the lowest hardness obtained for pure magnesium, all tested samples have a higher hardness. The hardnesss of pure titanium is higher than that of all samples.

Corrosion

The samples are discs with 12.7 mm in diameter and thus a nominal area of 126.7 mm² was exposed to the test solution, 1 L of Hanks´ Solution, resulting in a surface-to-volume ratio of

1.267 cm^2/L. The real surface area is most likely smaller as the samples are porous and the epoxy seemed to have filled in the pores between particles very well from microscopy images.

The hydrogen evolution tests (Figure 32) reveal a significantly slower corrosion rate of the alloys in comparison with pure magnesium, both processed in the same way. The pure Mg sample has an increasing slope at the beginning, meaning its corrosion rate accelerates over time. On the last half of the curve it corrodes at a steady speed throughout the experiment, showing no signs of passivation. In contrast, Mg-Ti shows a rapid corrosion at the beginning, which then gradually slows down, indicating the formation of a passivating layer that protects the underlying material from corrosion and thus slowing down the formation of hydrogen bubbles. Overall, the corrosion rate of all Mg-Ti alloys was significantly lower than that of pure magnesium. It was hypothesized that the passivation is proportional to the titanium content of the alloy. However, within the first week of immersion no differences between the different compositions of the alloys can be found in terms of corrosion rate. After the initial seven days the corrosion rate of the alloy containing 5 at.-% titanium is lower than those of the alloys with 20 and 35 %, which appear to corrode at the same rate at this point. After three weeks the corrosion rates of the 20 and 35 % titanium containing alloys become distinguishable, with the corrosion rate of the alloy with lower titanium content being higher. That alloys with different titanium content would have different corrosion rates is not unexpected, but it is surprising that the alloy with the lowest titanium content has the slowest corrosion rate. This phenomenon needs further investigation to check whether there truly is a difference and what the cause of the lower corrosion rate is, if it is confirmed. The different corrosion rates, especially not being tied to the titanium content in a coherent fashion, could also be side effects of a different amount of material being exposed to the test solution as the top of the sample slowly corrodes away and the density possibly changing towards the center of the sample, leaving a smaller surface area exposed. If it is confirmed that Mg-Ti5 indeed has the lowest corrosion rate of the investigated alloys this could be due to a lower amount of elemental titanium left behind after the mechanical alloying process, which might still cause galvanic coupling. In case Mg-Ti alloys with a low titanium content are more corrosion resistant, or at least as corrosion resistant as those with higher titanium content, implant materials could be made using a low titanium content, minimizing the risks of exposing the body to titanium during degradation and at the same time making implants lighter. The mechanical properties of the material are still unknown, but

hypothetically with lower titanium content the elastic modulus would be lower as well, which is favorable for fracture fixation implants.

From this corrosion experiment a clear connection of alloying state and corrosion pace is visible: The sample compacted at 350°C has a decomposed alloying state, as can be seen from its XRD scan (Figure 14) and corrodes very rapidly, without signs of passivation. It corrodes even faster than pure magnesium. Without an alloy structure the sample resembles a mixture of magnesium and titanium, resulting in galvanic coupling, which speeds up corrosion.

The bumps observed in the graphs of the alloy samples coincide with the solution changes, indicating that changing the solution sped up the corrosion for a short time, probably due to a decrease in pH and a fresh supply of corrosive ions in the solution.

If the reduction in corrosion rate would be brought about simply by only magnesium corroding but titanium staying behind a corrosion rate reduction proportional and equal to the content of titanium in at.-% would be expected. However, this is apparently not the case. There must thus be a different mechanism that alters the corrosion behavior of magnesium in the alloy in comparison to the pure element that is tied to alloying both elements together. The corrosion rates prove that the improved corrosion resistance of Mg-Ti alloys cannot be solely explained by the absence of corroding magnesium that is replaced by corrosion-resistant titanium. If the alloy structure is destroyed by heating the sample up to temperatures at which the alloy structure becomes instable, the sample corrodes faster than pure magnesium. This matches the effect of galvanic coupling, where pure magnesium in contact with a more noble metal serves as a sacrificial anode and electrons are transferred to the material with higher electronegativity values. Mg-Ti alloys with all investigated compositions corroded remarkably slower than pure magnesium and the sample with destroyed alloy structure. This suggests that the process of mechanical alloying is crucial to obtaining these beneficial properties that result from a fundamental change in the material. During alloying of Mg with Ti there is possibly a slight change in the electronic properties of both elements[46], which might alter their reaction to corrosive fluids.

During corrosion pure magnesium forms a white precipitate in Hanks´ Solution that resembles cotton candy in shape and structure. Very small particles came off the alloy samples and their

solution clouded over time as well, but to a lesser extent and it also took longer for this phenomenon to occur compared to pure magnesium.

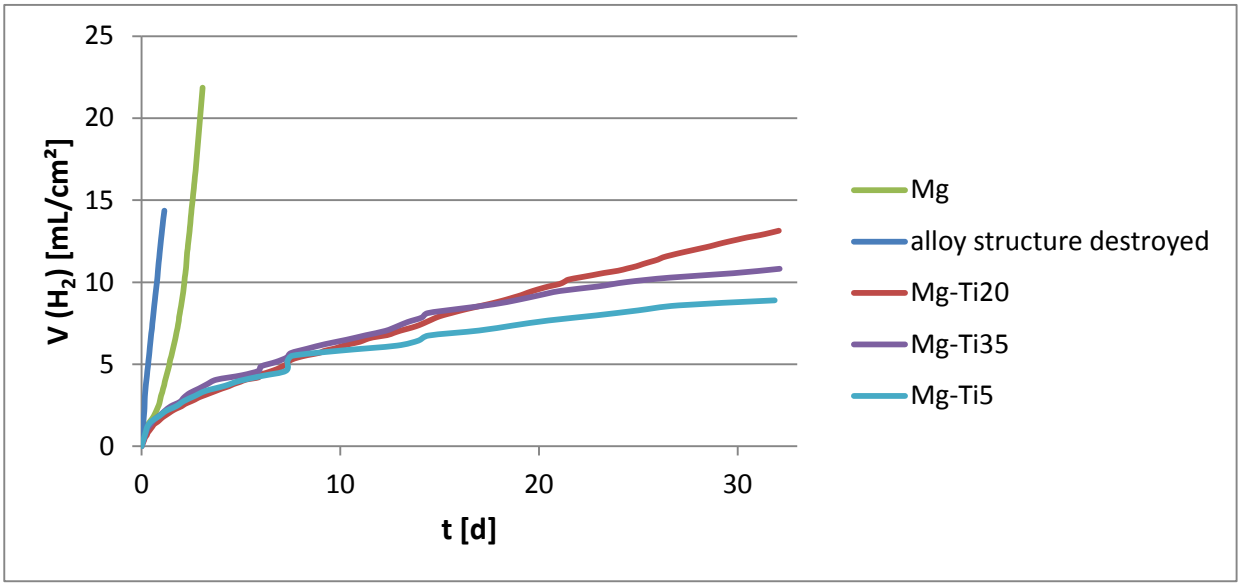

Figure 32: Corrosion rate comparison of pure Mg and various alloys consolidated by spark plasma sintering via hydrogen evolution

The test solution in which the pure magnesium sample degraded reached a pH of 8.51 in the first 24 h of the corrosion experiment. One day later the pH had risen to 8.83. Another day later, at the end of the experiment, the pH was 8.99. The pH in the alloys' solutions rose to 8.65 – 8.7 within a week and then dropped to 8.11-8.29 after the solution change. At the end of the experiment the pH values were 8.68 – 8.71. At all times the pH of the alloy samples' test solution was below that of the pure magnesium sample, further indicating a slower corrosion rate.

As Mg-Ti alloys were first developed for hydrogen storage the question is whether the alloy stores hydrogen that thus cannot evolve into the funnel. In the literature about hydrogen storage in the Mg-Ti system XRD scans[25,40] and DSC[40] are used to determine the formation of hydrides. It is impossible to tell from the XRD scans of corroded pure magnesium and Mg-Ti alloys obtained during this study whether they contain hydrides or not. The counts are very low and there is a high ratio of background noise. In addition, some of the most prominent Mg- and Ti-hydride peaks fall into the region with the main Mg-Ti peaks, so one cannot tell them apart.

However, a DSC scan run on the corroded $Mg_{80}Ti_{20}$ (blue line in Figure 33) shows an endothermic peak at around 400°C on the ramping-up part of the curve. Asano et al. published a DSC scan during which they hydrogenated and dehydrogenated an alloy with the same composition and the peak they designate as dehydrogenation is at about 700 K [40], which corresponds to the same temperature. Thermogravimetric analysis run simultaneously shows a sudden weight loss at the same time the peak occurs (green line in Figure 33), which adds emphasis on the loss of hydrogen. There is no similar peak in the DSC on as-fabricated $Mg_{80}Ti_{20}$ (although there is a peak at around 400°C, but that one points into the opposite direction), so it cannot be an effect of alloy decomposition. This is a strong hint to decomposition of hydrides occurring, which could only have formed during corrosion.

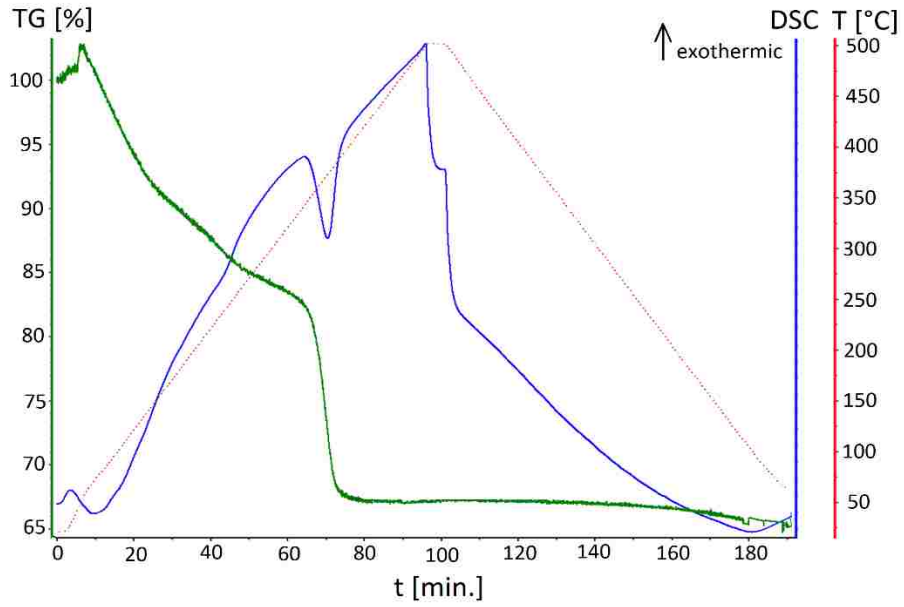

Figure 33: DSC scan of corroded $Mg_{80}Ti_{20}$

Pure magnesium alone can also store hydrogen with a hydrogen storage capacity of 7.6 wt.-% and the hydrogen storage capacity even increases through ball-milling[126]. With the strain imposed on the lattice by incorporation of differently sized atoms, Mg-Ti alloys were found to be superior to magnesium for hydrogen storage and were thus investigated as promising hydrogen storage materials. Electron-beam deposited $Mg_{80}Ti_{20}$ thin films were found to store 6.5 wt.-% hydrogen[127]. Even considering that Mg-Ti alloy has a higher density than pure magnesium, this difference will not explain the big differences in the hydrogen evolution rate observed experimentally. In hydrogen storage research hydrogen has been forced into the materials

either under elevated temperatures and was supplied as pressurized gas[40,128] or electrochemically with an applied palladium top coat on the sample material[127], but DSC suggests that even under very different conditions during corrosion hydrogen is stored inside the material. The differences in hydrogen storage capacity between magnesium and Mg-Ti alloys reduce the accuracy of the hydrogen evolution method when comparing the two materials. It has been reported that there is a discrepancy between mass loss and hydrogen evolution measurements in every comparative study published[77]. Different hydrogen storage capacities of the tested materials could account for that. Only with weight loss experiments can the true corrosion rate of a material be determined reliably. Mass loss experiments would therefore be much better suited to compare the corrosion rates of Mg-Ti alloys to magnesium. However, this test method requires close to 100% dense bulk samples, which have so far not been achieved to make out of Mg-Ti alloy particles. The hydrogen evolution method is thus the only directly comparative corrosion rate measurement technique that can be used. Furthermore, despite its known discrepancy from mass loss experiments hydrogen evolution continues to be used as a standard measurement technique for assessing the corrosion rate of magnesium alloys. Moreover, the difference in produced hydrogen between pure magnesium and the alloys is very large, so even if some hydrogen is stored in the alloy, this is probably not the only effect leading to such a massive difference. Electrochemical measurements will be able to tell whether Mg-Ti alloys exhibit passivation in comparison to pure magnesium and it is therefore to be expected that they corrode slower or not.

Summary:

Mg-Ti alloys with titanium contents between 5 and 35 at.-% were fabricated by high-energy ball milling and successfully consolidated with SPS to densities ranging from 58 to 87 %. It was proven that SPS is a viable low-temperature technique to consolidate metastable Mg-Ti alloys to bulk material while preserving the original alloy structure. The samples consolidated by SPS were not 100% dense, but junctions are formed between samples, i.e., they sintered together. The low density is due to the low force applied during sintering (limited by die selection). This can be improved in the future by either pre-compacting the particles in a uniaxial press at much higher pressures before sintering or by selecting dies that allow higher pressures to be applied during sintering. The proof of concept was demonstrated. This is an important finding since it is

challenging to consolidate Mg-Ti alloy particles due to their metastable nature without altering the alloy structure, thus losing the beneficial properties of the alloys.

Corrosion experiments on the SPS sintered samples showed that Mg-Ti alloys are more corrosion resistant than pure magnesium according to hydrogen evolution measurements. The corrosion protection effect stems not only from the processing by ball-milling alone, nor is it solely due to the titanium content in the sense that easily corroded magnesium is replaced by corrosion-resistant titanium. The material has to be in an alloy structure for the effect to take place.

Electrochemical response of Mg-Ti alloy in Hanks' Solution

Electrochemical characterization methods can be used to measure the corrosion rate and probe protection mechanisms of a given system (i.e., corroding material and test solution). Open circuit potential (OCP) measurement, potentiodynamic polarization (PDP), and electrochemical impedance spectroscopy (EIS) were chosen as complementary techniques that are appropriate for assessing the corrosion behavior of magnesium and Mg-Ti alloy. Although the information obtained from monitoring the OCP is similar to that of PDP, the former shows changes occurring over time, which offer valuable insight. Furthermore, these methods can be used to study corrosion of compacted powder particles, not requiring full consolidation, thus avoiding difficulties with consolidation.

Experimental details

Sample Fabrication:

Mg-Ti alloy (80at.-% Mg + 20 at.-% Ti) was fabricated by high-energy ball milling in a vibratory type ball mill (SPEX Mixer/Mill). The starting materials were -325 mesh Mg (99.8%) and Ti powders (99.5%) from AlfaAesar. All samples were ball-milled for 25 h under argon with a ball-to-powder mass ratio of 16:1 in SPEX stainless steel grinding vial set with six hardened 440C stainless steel milling balls. Two balls were 12.7 mm in diameter and the other two in the set are 6.35 mm. The vial is 2.25" in diameter, 3" high, and holds 65 mL. Pure magnesium was also milled for 25 h to investigate the effect of milling alone separated from the influence of alloying, since an improvement in the corrosion resistance of magnesium through ball-milling had been reported[50]. The alloying process was monitored by powder x-ray diffraction (XRD). The samples were loaded in a side-loader sample holder and scanned from 31 to 41° at 40 kV and 30 mV using a Siemens D5000 x-ray diffractometer with Cu Kα radiation.

Electrochemistry:

The ball-milled powders (pure magnesium and Mg-Ti alloy), untreated Mg powder, and a mixture of 80 at.-% Mg + 20 at.-% Ti were compacted into discs by pressing them uniaxially with over 10 t pressure in a 0.5" diameter die, resulting in pressures of 774 MPa. No lubricating agent was used during pressing to avoid contamination of the samples. Some sample material was deposited onto the die walls during pressing, so that it is unlikely that the samples picked up

iron contamination from the die. The compressed samples were used in the experimental setup without any other processing steps. For comparison, titanium foil (0.89 mm thick, 99.7% (metals basis), AlfaAesar) was used. As titanium forms a well protecting oxide layer when exposed to air, the foil was ground with 1200 grit sandpaper, rinsed with ethanol, and blow-dried with hot air immediately prior to mounting the sample into the flat cell.

Electrochemical experiments were run in a Princeton Applied Research flat cell kit (working- to counter-electrode distance: 80 mm) and a Princeton Applied Research PARSTAT 2273 potentiostat/galvanostat in a three electrode setup. The sample discs served as working electrodes, the counter electrode was a platinum mesh (2.54 cm x 2.54 cm), and a silver/silverchloride electrode in saturated AgCl/KCl solution served as the reference electrode. In the flat cell 1 cm^2 of the sample is exposed to the test solution. For all electrochemical experiments the flat cell was filled with 250 mL naturally aerated Hanks' solution (composition in appendix) as a simulated body fluid prepared with de-ionized water filtered through a Millipore Milli-Q (resistivity = 18 MΩ/cm). To mimic body temperature the test solution was warmed up in a water bath to 37°C (human body temperature) before the experiment and during the experiment the flat cell was kept in a TESTEQUITY 1000 series temperature chamber set to 37°C. The PowerSuite software (Princeton Applied Research) was used to control the experiments, record data, and obtain the resistance from EIS scans.

As a baseline pure Mg and Ti were tested. To show the effects of ball-milling and composition separately, pure Mg was ball-milled with the same parameters as the alloy. Similarly, a physical mixture of Mg and Ti in the same composition as the alloy was prepared and tested, but without prior milling. The main sample was a mechanically alloyed Mg alloy containing 20 at.-%Ti.

Samples were tested at two time points: right after exposure to the solution (designated as "fresh" samples) and after 24 h of immersion in Hanks' Solution to evaluate changes in the corrosion behavior over time. After the 24 h immersion period the solution was exchanged for fresh Hanks' Solution before running the experiment. All samples were run in triplicates. At the beginning of the test the sample was let to stabilize in contact with the test solution for 2 h (fresh samples) or 30 min. for those corroded for 24 h prior to the test. During the stabilization time the open circuit potential (OCP) was recorded to see how quickly the different samples stabilized. After 24 h of exposure the potential was comparatively stable, so OCP was only

recorded for 30 min. Data points were recorded every other second. After OCP Electrochemical Impedance Spectroscopy (EIS) was run with Princeton Applied Research (PAR)´s Galvanostatic Electrochemical Impedance Spectroscopy (GEIS) module. In this module the frequency is applied through current, not voltage, as is commonly reported for conventional potentiostatic EIS in the literature. According to PAR's software manual, in GEIS mode the AC current applied and AC potential are measured to calculate impedance. This gives an advantage when experiencing a shift in OCP, which is a DC phenomenon, for example during corrosion. GEIS eliminates the application of a bias potential that is anodic or cathodic to the true open circuit potential and thus allows the experiment to take place along with the dc drift.

To determine the current range equivalent to a 10 mV amplitude, which is frequently used by researchers, PDP was run on a sacrificial sample with the same composition beforehand. From the PDP scan the current densities at 5 mV above and below OCP were identified and used to calculate the current needed to cause a 10 mV perturbation for the given sample.

For GEIS 140 points were recorded between 2 MHz (the highest possible frequency) and 10 mHz (below that frequency the values became too unstable to be usable) with logarithmic spacing. Only data between 384 kHz and 10 mHz are reported here as the very high frequency responses do not contribute to the understanding of the sample responses. The sample was allowed to stabilize for 10 min. between OCP and GEIS. The sample was kept at OCP during GEIS measurements. The highest data quality (4) was selected and the smallest possible current range was used, i.e., either 200 μA, 2 mA, or 20 mA depending on the amplitude.

The resistance was determined by measuring the diameters of the two loops observed in Nyquist plots. The diameter of the semicircles is directly related to the resistance. To obtain the overall resistance, the resistance values from each of the two loops were added. A minimum of three samples per composition and immersion time combination was analyzed.

After the EIS measurements, potentiodynamic polarization (PDP) was run because it causes big changes in the sample, rendering it unsuitable for following electrochemical investigations. The voltage was swept from 0.25V below OCP to 1.6 V above OCP with a step height of 1 mV at a scan rate of 0.166 mV/s. PDP step time was 6 s. Severe corrosion, which caused gas bubbles to form inside the tube leading to the Luggin well, made measurements unstable at times. When the gas bubbles in the tube became too large, jumps in the scans are observable.

Results &Discussion

The OCP of all samples right after immersion into the test solution (Figure 34) show, as expected, a much higher potential for pure Ti compared to Mg. OCP of pure magnesium (milled and unmilled) become stable after about 50 min, which is comparable to the sample with free magnesium that Brett et al.[38] presented. Titanium containing samples do not reach a stable value in the 2 h window, but the potential keeps steadily increasing. Two different slopes can be distinguished for the Mg-Ti mix and ball-milled Mg and three for the alloy. No significant difference in OCP of untreated and ball-milled Mg was detected. The Mg-Ti mixture had an OCP similar to that of pure Mg, which is in accordance with the data presented by Esen et al.[44], who tested Mg-Ti composites. In contrast, the OCP of Mg-Ti alloy is much higher than that of pure Mg. It should be noted that the potential of the alloy rises to a larger extend during immersion compared to that of Mg and the mixture, indicating that a corrosion protection layer forms on the surface. The same effect can be seen for Ti, which is known to form a very effective corrosion protection layer. After 2 h of immersion in Hanks' Solution the potential difference between the Mg-Ti mixture and alloy is about 300 mV. The change in potential is greatest for the alloy (ca. 200 mV). OCP of pure magnesium samples and the mixture are close together, but the Mg-Ti alloy starts out at a much higher value and reaches an even higher potential at the end of the 2 h period. This effect cannot be due to ball milling alone or the sheer presence of titanium, as it does not appear in the ball-milled pure Mg or the Mg-Ti mixture. As expected, titanium has the highest OCP and its increase in potential during equilibration is similar to that of the alloy, except that it does not exhibit a very steep slope during the first few minutes of immersion.

After 24 h of immersion (Figure 35), the titanium potential has further risen to about -0.2 V. The potential of the alloy continues where it has left off on the equilibration time of the fresh sample and keeps rising during the whole measurement. Pure magnesium samples and the Mg-Ti mixture have not changed markedly in potential compared to the fresh samples. The potential of most samples drops during the equilibration phase on the second day of measurements. This could be due to the fresh supply of corrosive species from the solution change right before the measurement was started, so that the built-up protection layer on the sample surfaces is attacked and its effectiveness reduced. In contrast, the potential of the alloy rises.

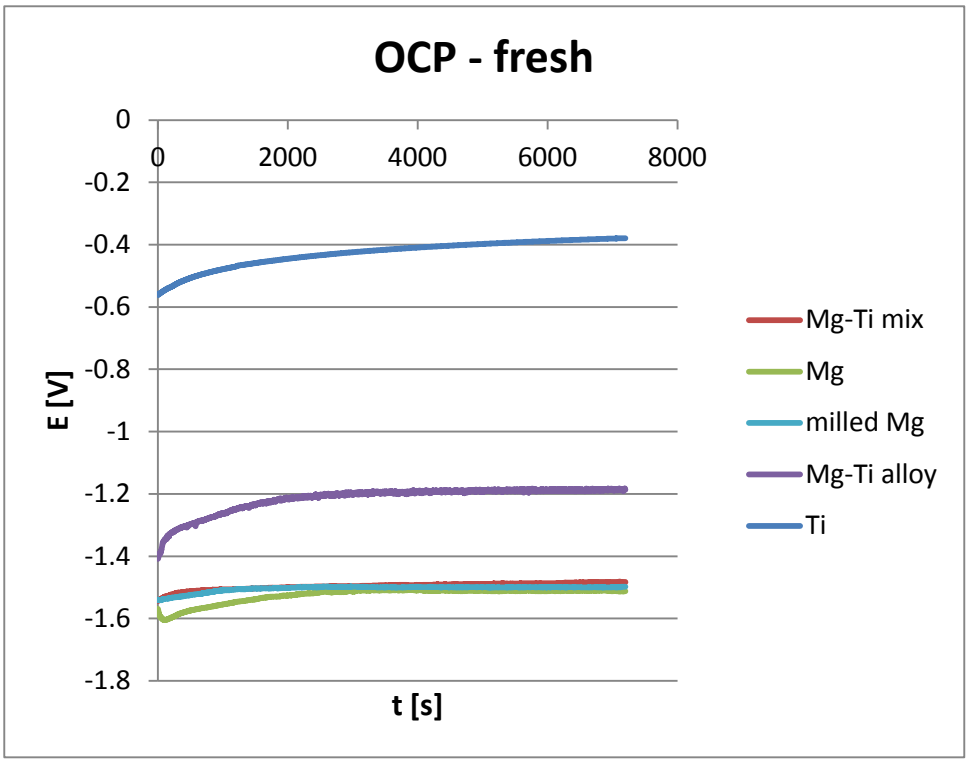

Figure 34: OCP scans of unmilled Mg powder, milled Mg powder, $Mg_{80}Ti_{20}$ mixture and alloy milled for 25 h.

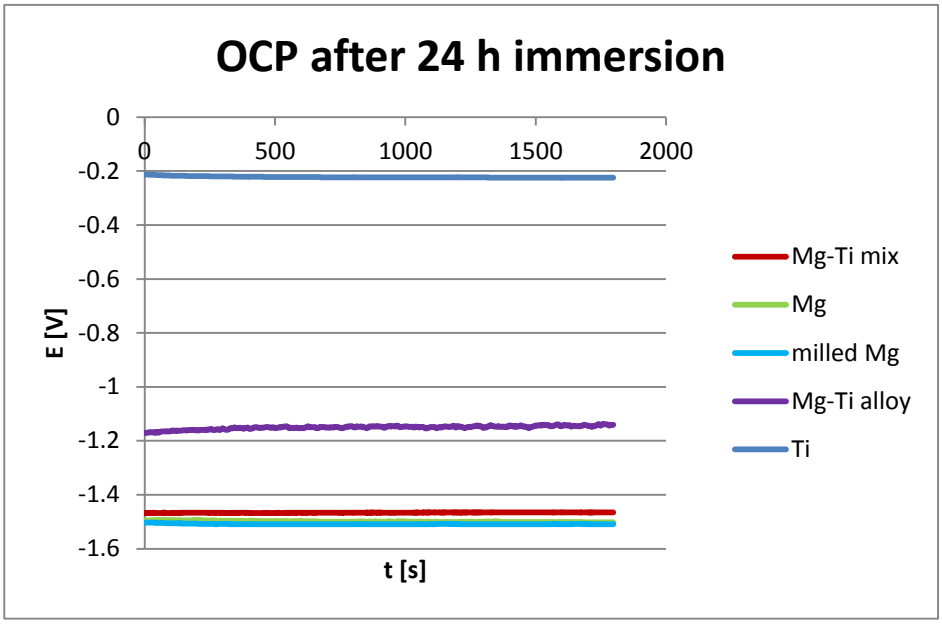

Figure 35: OCP of all samples after 24 h of immersion in the test solution.

The observation of an elevated potential for the Mg-Ti alloy is further confirmed in potentiodynamic polarization (PDP) scans (Figure 36). The plots of samples in their fresh state

and after 24 h of immersion does not differ significantly, so only the fresh state is presented here. The values for the OCP (Figure 37) and current density (Figure 38) at the OCP at both time points are compared.

PDP illustrates that not only is the potential of the alloy higher, its current density at the OCP is also lower than that of pure Mg. These two factors show that Mg-Ti alloy is less prone to corrosion due to its higher potential and corrodes more slowly than pure Mg because the current density is lower. Of all the samples tested, Ti has the highest potential and lowest current density at OCP, illustrating its superior corrosion resistance. In case of the pure Mg and mixture samples the potential does not differ much from each other, nor does it change with prolonged immersion time. However, it is much lower for both Ti and the alloy, which indicates that a protective layer forms on the surfaces of those samples over time and increases protection with prolonged exposure. At the same time the current density drops for the alloy, which further indicates that it is being protected against corrosion. The current density also decreases significantly for pure Mg, most likely owing to the precipitation of components from the test solution which cover the sample surface. In case of ball-milled Mg and the Mg-Ti mixture the current density goes up with immersion time, indicating that these samples suffer accelerated corrosion when immersed for longer times. When comparing the overall numbers it is clear that the current density of the alloy is lower than that of all samples except for Ti at any time point during the test, illustrating its superior corrosion resistance compared to pure Mg.

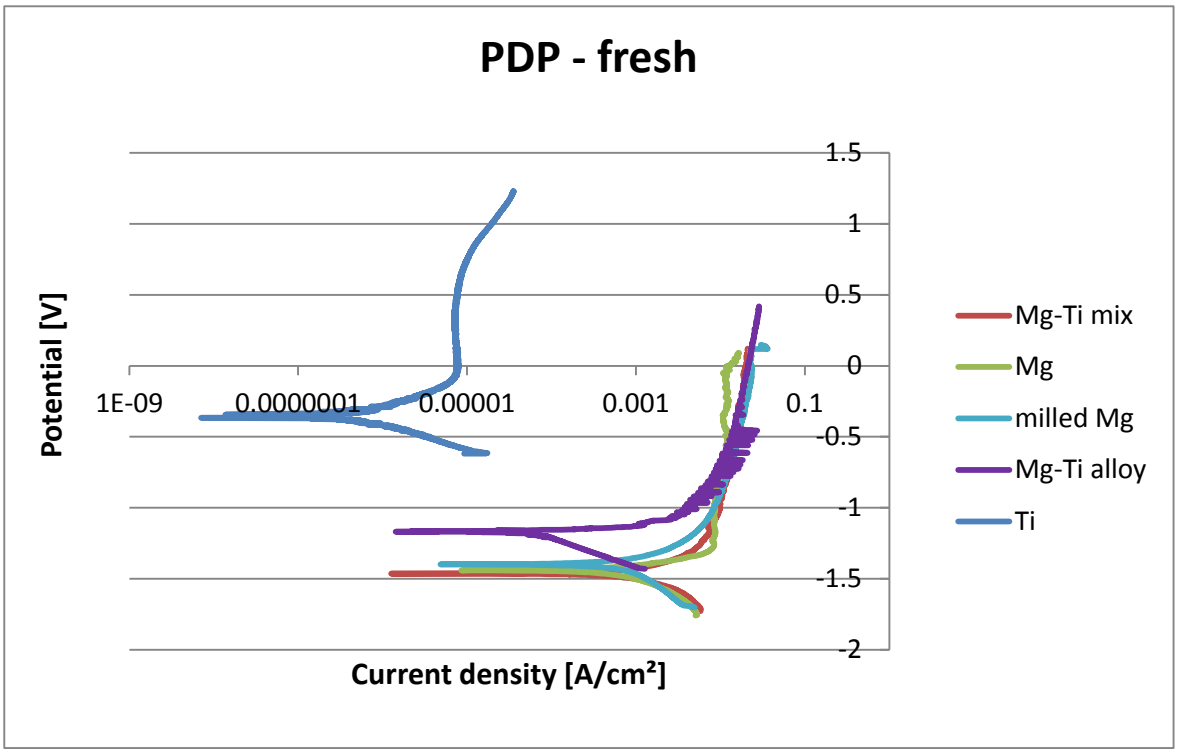

Figure 36: PDP of of unmilled Mg powder, milled Mg powder, Mg80Ti20 mixture and alloy milled for 25 h.

In the case of the alloy there are many jumps to higher currents in the anodic region. In the anodic region the slopes of all samples except unmilled magnesium are quite similar. Unmilled magnesium exhibits the steepest slope, which indicates a relative resistance to corrosion.

When comparing the shape of the PDP scans the alloy shows an asymmetry around the OCP: the slope in the anodic region is flatter than that of the other samples, while the cathodic part mostly resembles two rather straight lines instead of a curve as in the case of all other samples. Between the rather flat part of the anodic region right after OCP and the steep increase is a slight bump in the alloy sample. The alloyed sample starts out at an almost ten times lower current density than the other samples at the beginning of the PDP scan. The shapes of the PDP scans are very similar when comparing the same sample type in fresh condition and after 24 h immersion, so the graphs for the longer immersed samples are not shown here. Figure 37and Figure 38 show the changes in potential and current density recorded at OCP during the PDP scans of freshly immersed samples and those immersed for a day prior to testing. In the potential diagram it is clearly visible that the pure magnesium samples and the mixture have comparable potentials, but the alloy's potential is significantly higher. The OCP of ball-milled

magnesium drops slightly after one day of immersion, while the potential of all other samples increases on the second day. The increase in potential during OCP could be due to the deposition of minerals from Hanks' solution on the sample surface. The OCP difference between the fresh and pre-corroded Mg-Ti mixtures are hardly discernable. The OCP of the alloy is increased by a higher amount than untreated magnesium. The biggest difference is found in the titanium sample, which also has the highest potentials at both time points. The current density of titanium on both the fresh and pre-corroded samples are so low that they do not show up in the collective diagram (Figure 38). Among the fresh samples the current density is highest for the unmilled magnesium sample, followed by the mixture, then the milled magnesium, and the alloy. Although the current density of the unmilled magnesium sample drop drastically after 24 h of immersion, the current density increases for the milled magnesium sample and the mixture. This suggests that the protective layer on untreated magnesium grows stronger or thicker to better protect the material over time, whereas the surface layers on the milled sample and the mixture are weakened with increasing exposure time. The alloy experiences a slight drop in current density on the second test day, which means that its corrosion protection mechanism is already very effective soon after immersion and does not change much with prolonged exposure to the test solution. The alloy has significantly lower current densities on both test days compared to any pure magnesium samples and the mixture.

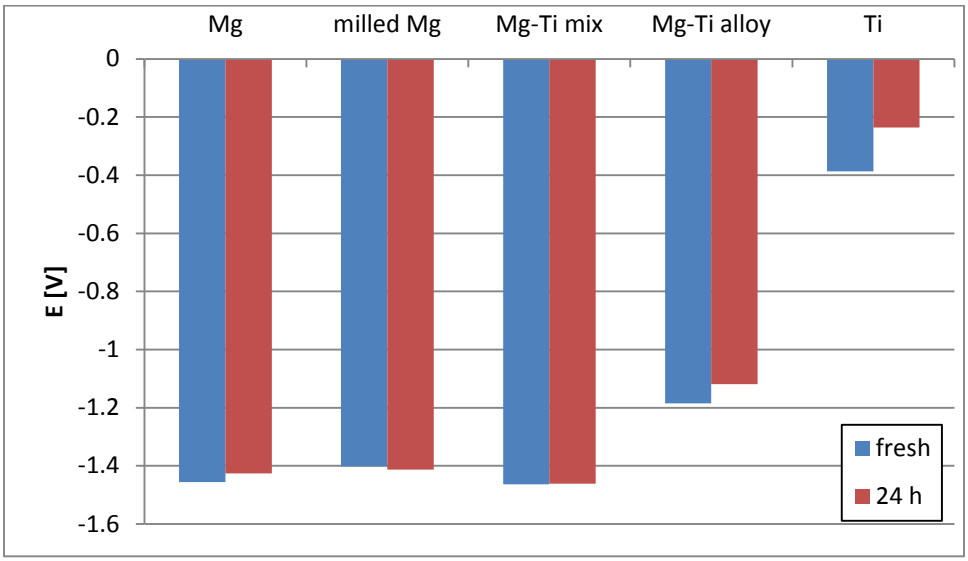

Figure 37: Potential at OCP on fresh samples compared to samples corroded for 24 h.

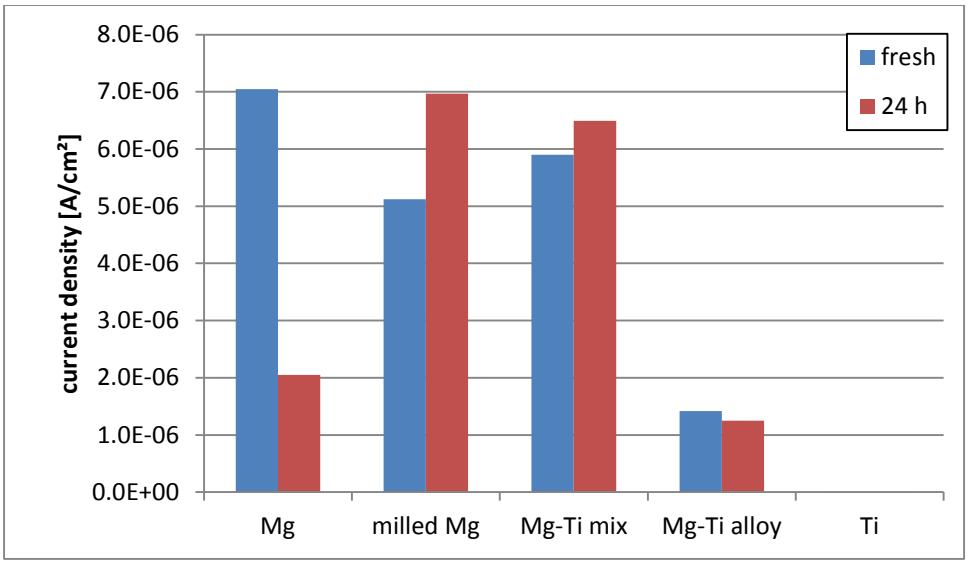

Figure 38: Current density at OCP on fresh samples compared to samples corroded for 24 h.

In the Nyquist plots obtained from EIS measurements it is immediately evident that the low-frequency loop of the alloy is much larger for those of the pure magnesium samples and the Mg-Ti mixture (Figure 39). The size of this loop is related to the corrosion resistance in that a larger diameter indicates superior corrosion resistance[27]. However, the loop of the alloy is very noisy. The Mg-Ti mixture and milled Mg do not show much noise at the same frequencies.

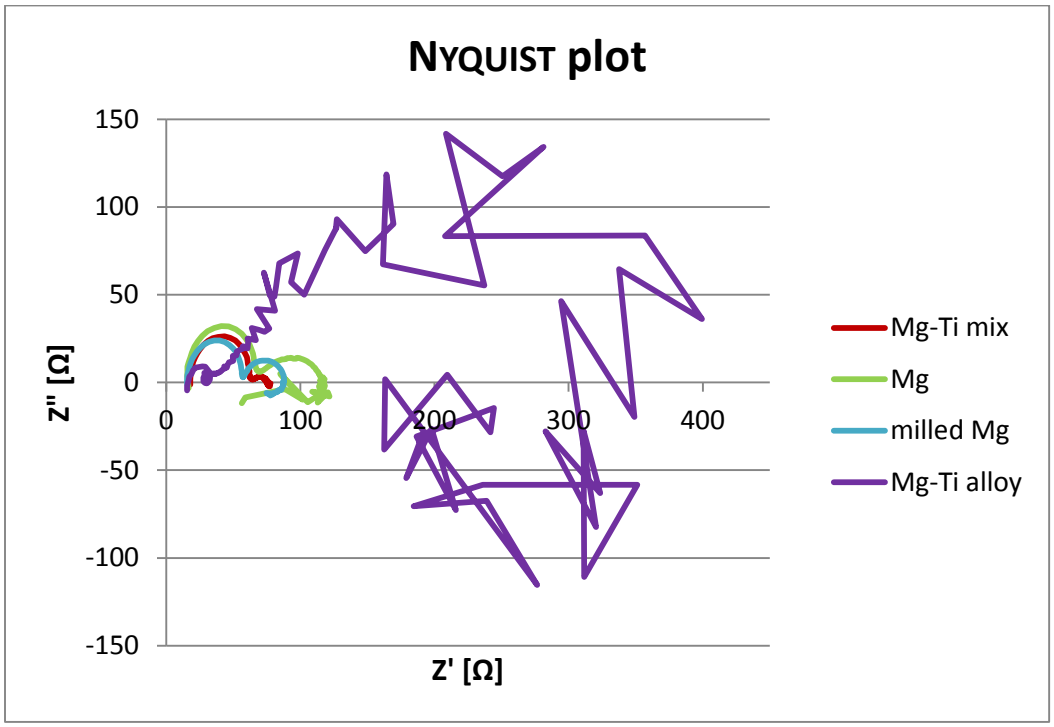

Figure 39: EIS of fresh samples containing magnesium.

When comparing the Nyquist plot of unmilled magnesium in the fresh state and after immersion in the test solution for 24 h a difference in the shape of the loops can be observed (Figure 40). The fresh loop is oval rather than round and has a noisy piece at its end. The positions of the loops are shifted.

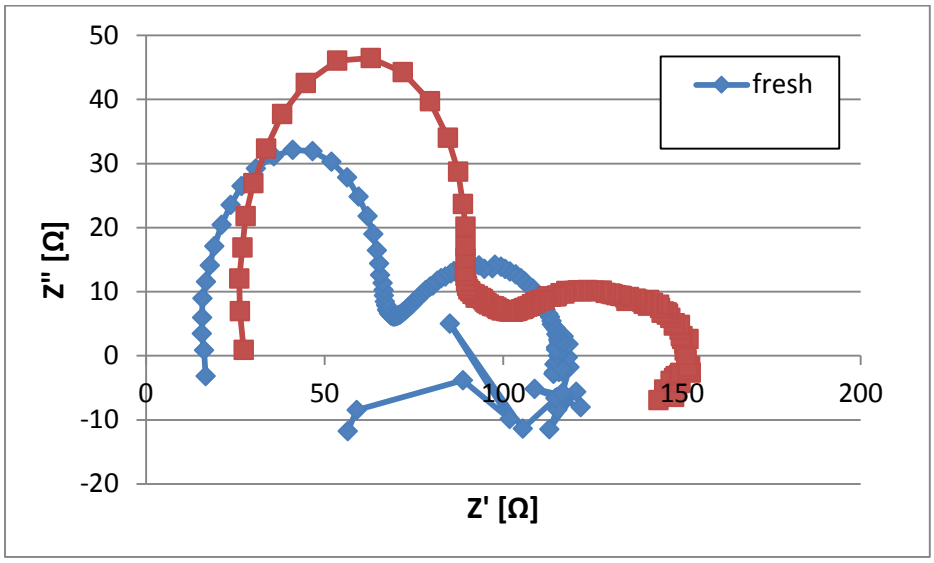

Figure 40: Nyquist plot of unmilled magnesium samples.

A similar effect is seen for ball-milled magnesium (Figure 41). In addition the size of the loop has increased after the sample was exposed to the corrosive solution for one day.

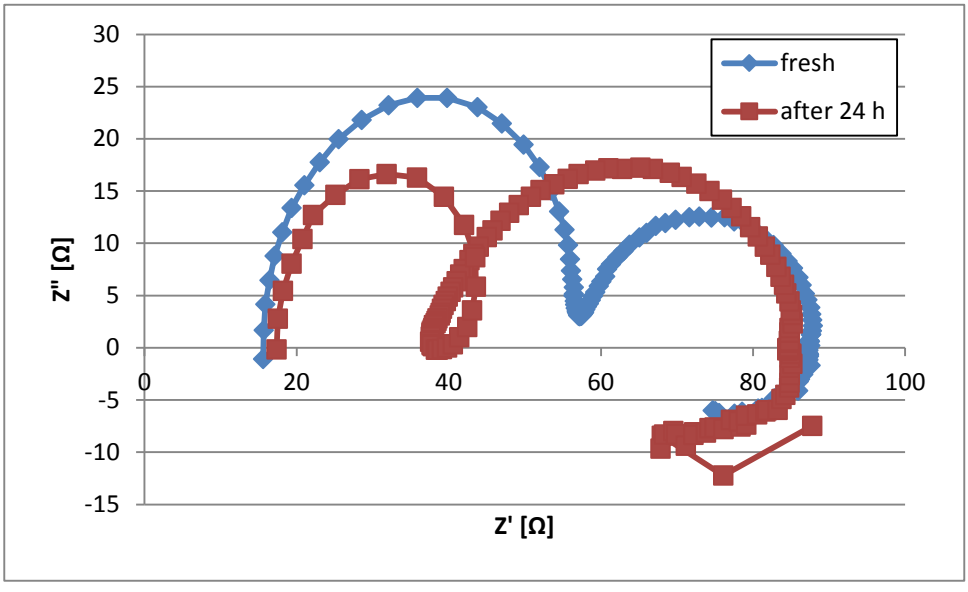

Figure 41: Nyquist plot of milled magnesium samples.

The mixture of magnesium and titanium shifts to much lower impedance values after prolonged immersion in Hanks' solution (Figure 42). In addition, the loop after 24 h of immersion is smaller than when tested after only a brief contact with the test solution.

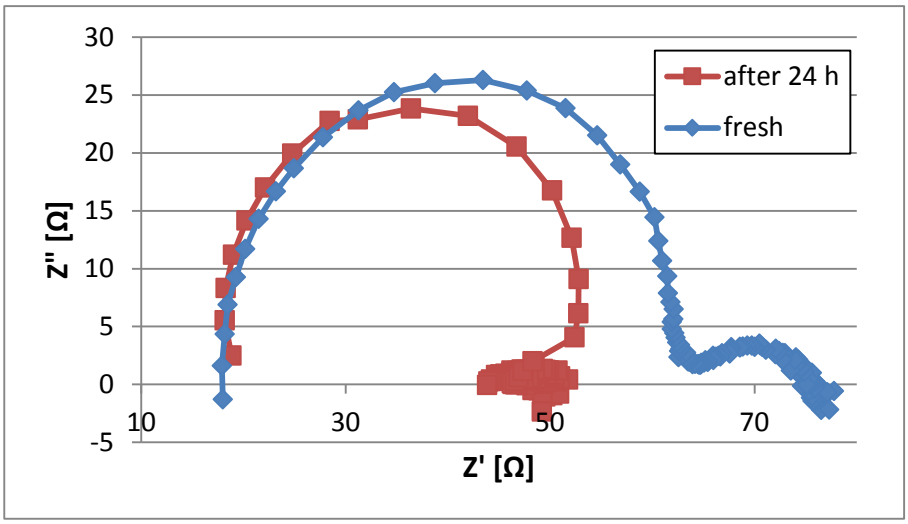

Figure 42: Nyquist plot of Mg-Ti mixture samples.

The alloy sample has the largest loop of all magnesium containing samples in the fresh state. It even grows slightly bigger in diameter after one day of immersion in the test solution (Figure 43). In the fresh state the low frequency loop goes deep into the inductive regime. The noisy response in the low frequency regime implicates that the sample is instable, i.e., undergoing active corrosion, according to Kirkland et al.[77].

After 24 h of immersion the low frequency loop of the titanium sample increases compared to the fresh state (Figure 44), indicating that the oxide layer has grown in the meantime to provide even better protection.

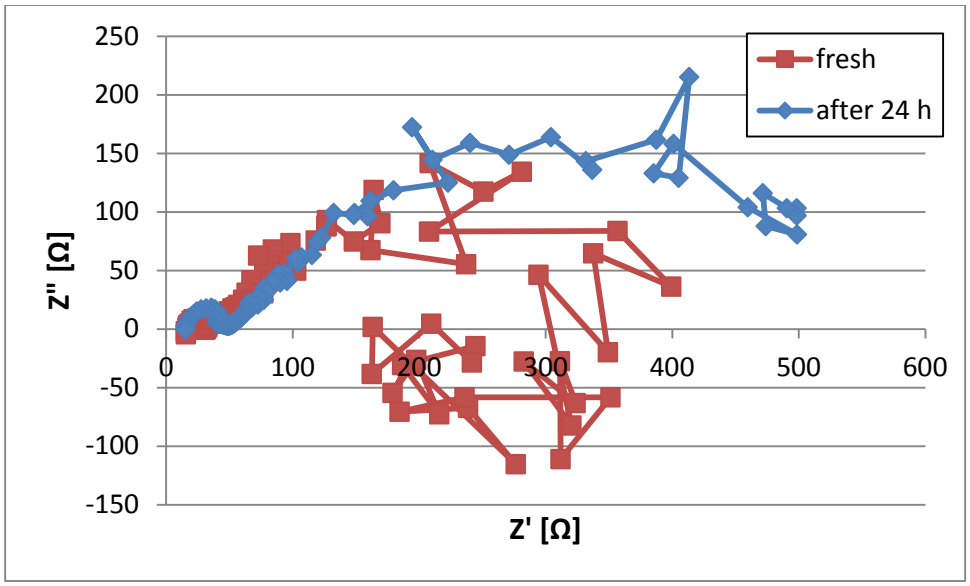

Figure 43: Nyquist plot of alloy samples.

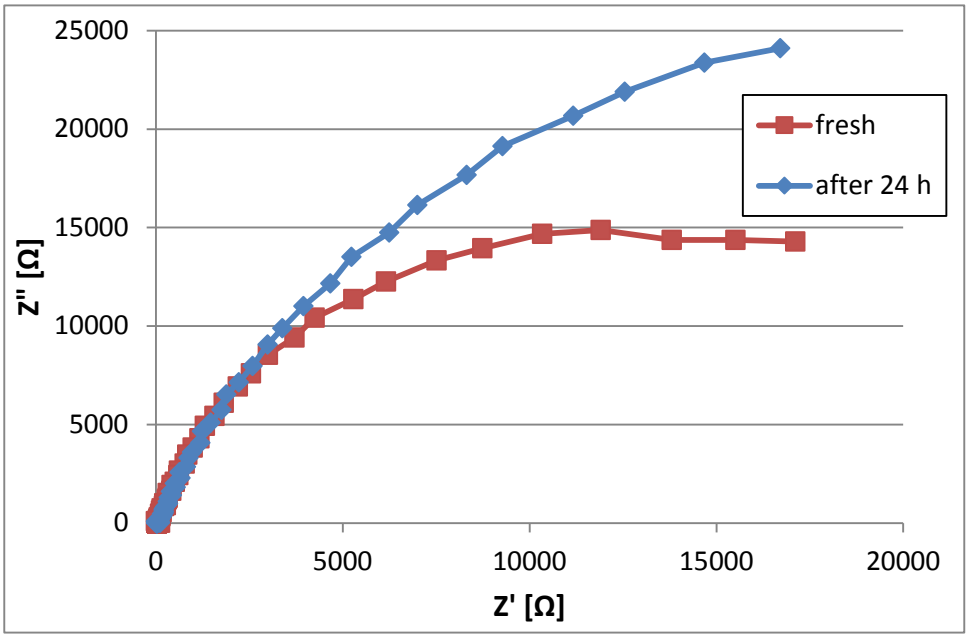

Figure 44: Nyquist plot of titanium foil.

The diameter of the loops observed in the Nyquist plots is directly related to the resistance of the material. The average resistance values of at least three samples of each composition and immersion time are presented in Figure 44. The resistance is closely linked to the corrosion resistance of the samples. As expected, titanium has by far the highest resistance and its resistance increases over time, indicating that the oxide layer on the surface is becoming thicker

and improving to shield the underlying metal from corrosion. The alloy resistance is the second highest measured in this study. It is orders of magnitude lower than that of titanium, but still significantly higher than the resistance of pure magnesium and the mixture. The alloy's resistance also increases with prolong immersion, similar to titanium. It improves its corrosion resistance within the 24 h of immersion. This fits well with the observation from the hydrogen evolution experiments where the corrosion rate of the alloy decreases over time. Although much lower than the alloy and titanium, the resistance of pure magnesium also increases within one day of immersion in Hanks' Solution. When ball-milled, the resistance of magnesium was found to decreases slightly compared to the unprocessed state. Milled magnesium also shows no significant change in resistance with increased exposure to the test solution. The physical mixture of Mg and Ti shows the lowest resistance of all tested samples. In this case the resistance even decreases after one day in the test solution. Due to galvanic coupling between the magnesium and titanium particles no stable protective layer seems to be able to form. Even worse, the protection that was still present from the naturally occurring surface oxides of the particles that form in air shortly after immersion into the test solution is weakened over time.

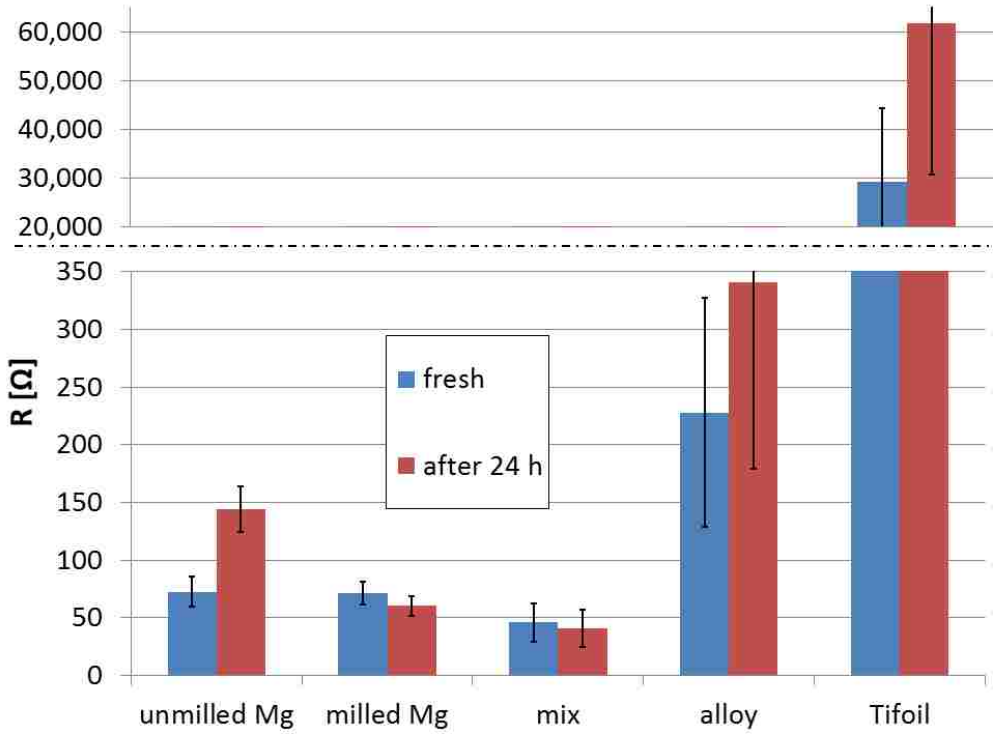

Figure 45: Averaged resistance values of different samples in their fresh state and after immersion in the corrosion test solution for 24 h. Error bars represent standard derivation.

The findings for ball-milled magnesium presented here are in contradiction to several reports in the literature. It has been reported that ball milling alone improves the corrosion resistance of magnesium[50], but this effect was not observable here. Grosjean et al. reported improved corrosion resistance of magnesium after ball milling and attributed it to an increased number of surface defects and grain boundaries where a protective magnesium hydroxide layer could be formed more easily[24]. However, it should be pointed out that the test solution used in the cited study was 1 M KOH solution with pH=14 [24], which is by far less aggressive on magnesium because of the high pH that stabilizes the hydroxide layer forming on the surface of magnesium in aqueous solutions. The study by Grosjean et al cannot, therefore, be compared with corrosion tests at physiological pH in a test solution which has many more corrosive and protective species. Grosjean's group also ran the same experiments in 0.3 M borate buffer solution with pH=8.4, which provides more active corrosion conditions[24]. In this environment the potential of the milled magnesium is shifted to more positive values as well, but the corrosion current is almost unchanged by milling in this test solution and the polarization resistance only changes slightly[24]. The group suggests that the cathodic reduction of water is controlling the corrosion of magnesium in borate solution and is not affected by ball milling[24]. Another big difference between Grosjean's test solutions and Hanks' solution is the presence of chloride ions, which are known to decrease the corrosion resistance by converting the magnesium hydroxide layer protecting the underlying magnesium into easily dissolvable magnesium chloride, reducing the protective function[27]. The effects of the chloride ions may be more impactful in milled magnesium with its strained lattice and many surface defects and grain boundaries, which offer many more sites for chloride ion attack than coarse-grained magnesium. The effectiveness of ball-milled for improving the corrosion resistance of magnesium is therefore dependent on the test solution and not a universal feature. It cannot explain the improved corrosion resistance of the Mg-Ti alloy, as the OCP is not improved by ball-milling and hardly changed compared to unmilled magnesium. Similarly, no improvement in current density was observed through ball-milling of Mg alone.

The presence of titanium does not improve the corrosion resistance. The Mg-Ti mixture and the alloy contain the same amount of titanium, yet their corrosion behaviors are very different. Adding titanium to magnesium in the form of a physical mixture reduces the corrosion resistance dramatically through the creation of a galvanic couple, as is obvious from the EIS

measurements. However, the presence of titanium in the alloy has a beneficial effect. Alloying Mg with Ti via ball-milling not only increases the open circuit potential, but also increases the diameter of the second loop observed during electrochemical impedance spectroscopy, which is related to the corrosion resistance. It can be concluded that the alloy gains its corrosion resistance from a decrease in the corrosion potential and a more effective corrosion protection layer forming on the surface. Xu et al. credit the improved corrosion resistance of their samples to a passivating film formed by a mixture of stable TiO_2 and MgO on the sample surfaces[39]. This is another logical explanation for the improved corrosion resistance of the alloy. The adjoining titanium oxide could help stabilize the magnesium oxide in its vicinity. In that case it would be a pure size effect and the difference between the physical mixture and the alloy that matters is a finer dispersion of the titanium atoms in the magnesium matrix.

This corrosion protection layer surely benefits from the presence of titanium oxide, but that alone does not explain the big improvement. Titanium oxide is likely also present in the physical mixture of magnesium and titanium, but it does not significantly improve the corrosion resistance. The increased potential probably plays an important role, which is an effect of alloying. Similarly, alloying may influence the oxide formation of the Mg-Ti alloy in contact with corrosive media.

Although the alloy's loop is much smaller than that of titanium, it is significantly larger than that of pure magnesium. This finding suggests that a corrosion protection layer forms on the alloy, slowing down its corrosion, but not stopping it completely, as in the case of titanium.

Figure 46: Sample surfaces before (far left) and after electrochemical corrosion experiments. Note the black surface on the alloy.

The surfaces of the sample pellets (Figure 46) look very different after the corrosion experiments. Surface features do not differ with short or long exposure to Hanks' Solution. The

surface of samples made of pure Mg (milled and unmilled) flakes off after 24 h. A similar effect can be observed for Mg-Ti mixtures and alloys, but in their case the material comes off in smaller particles. The most striking feature is the color of the corroded surface: pure magnesium samples have a white film on the surface, the mixture is dark gray (white + black), while the alloy surface turns black. Blackening of the surface was also observed by Brett et al. on their Mg-Si-Ti alloy samples[38] and by Xu et al. on magnetron sputtered Mg-Ti thin films[39]. Brett et al. attributed the black color to the formation of oxides[38].

The white corrosion products could be $Mg(OH)_2$, MgO, or other ionic compounds formed with the anions present in the test solution. The black color on the surface of the alloy could indicate the formation of Ti_2O_3, as TiO_2 is white and TiO resembles bronze with its golden color. However, Ti_2O_3 is formed at very high temperatures, so it's not likely to form under the conditions experienced in these experiments. It has been reported that titania changes color from white to black upon hydrogenation, which introduces disorder into the material[129]. This is a much more likely explanation for the black corrosion layer formed on the alloy, as Mg-Ti alloys were investigated as hydrogen storage materials[128,41]. In XRD spectra the white and black titania look identical, but the black TiO_2 shows a broader O1s peak in XPS[129].

Conclusion

The electrochemical behavior of pure, untreated Mg, ball-milled Mg, and the Mg-Ti mixture differ only slightly. Electrochemically ball-milling pure Mg does not have much of an effect in Hanks' solution. In contrast, the alloy behaves very differently. Features of improved corrosion resistance, i.e., higher potential and lower current density were only found for Ti and the Mg-Ti alloy, not for the physical mixture that represents the same composition as the alloy or ball-milled Mg. This means that the protective mechanism is not solely due to the titanium content or processing by ball-milling alone, but that an alloy has to be formed to achieve improved corrosion resistance. The electrochemical observation of a higher corrosion resistance of the alloy compared to pure magnesium and Mg-Ti mixtures further confirms the superior corrosion resistance of Mg-Ti alloys compared to pure magnesium observed in hydrogen evolution experiments.

Now that the improved corrosion resistance of Mg-Ti alloy has been proven in vitro, in vivo measurements can be conducted to check whether the corrosion protection mechanism also works there.

X-ray photoelectron spectroscopy analysis

Introduction

The alloying effect of titanium in magnesium is readily visible in XRD and the effects of alloying on the material are also evident in corrosion experiments. The influence of alloying on the electronic state might give a valuable insight on why and how alloying magnesium with titanium improves its corrosion resistance so drastically.

X-ray photoelectron spectroscopy (XPS) probes the electronic state of materials and can be used to determine bonding types. My hypothesis was that alloying magnesium with titanium could change the electronic structure of magnesium and/or titanium.

Jensen et al. investigated magnetron sputtered $Mg_{80}Ti_{20}$ thin films by XPS[130]. When comparing their experimental results to density functional theory (DFT) calculations for samples with the same composition, they found that the density of states (DOS) is strongly dependent on the state of the Ti, meaning whether it's randomly distributed or forms nano-clusters[130]. When comparing the DOS from the simulation with the XPS experiments the DOS matched that of the nano-cluster case, thus concluding that Ti is not truly randomly distributed in Mg-Ti, but stays in small clusters[130]. According to the DFT calculation Ti has only one dominant peak at the Fermi level when quasi-randomly distributed[130]. However, when Ti atoms are allowed to cluster together two peaks appear, one on each side of the Fermi level[130]. Ti's d-orbital is accredited for the majority of contribution to the total DOS[130]. When looking at the DOS even in small clusters Ti resembles elemental Ti, whereas isolated Ti looks very different[130]. Thus even forming small clusters is energetically more favorable for Ti, bringing it close to its bulk state[130]. Jensen's observation of nanoclusters fits well with a report by Liang and Schulz[25] that during ball milling not all of the titanium dissolves in magnesium, but some stays behind in elemental form. For the case of Mg hardly any difference can be seen between the nano cluster and quasi-random version[130]. Isolated Ti atoms sitting in a matrix of Mg attract charge from Mg, which causes the peak to center at 0 eV[130]. Ti-Ti bonds however bind electrons more tightly and their peaks fall below 0 eV[130]. The difference between a single titanium atom and clusters of a few titanium atoms embedded in a magnesium matrix is large in the group's simulations[130].

Jensen's group found that even in UHV the samples oxidized, so the presented Mg XPS scan contains a feature typical of MgO in addition to the elemental Mg peak[130]. XPS 2p scans of both Mg and Ti are shown in their paper to represent the valence spectrum[130].

Although XPS data for sputtered[130] and vapor deposited[131] thin film Mg-Ti alloys have been reported by several research groups, only Ti 2p[130]or Ti 1s and Auger line[131] scans were shown. This is especially astonishing since Jensen et al. concluded from their density functional theory calculations that several orbitals in titanium are affected by the alloying process[46]: The titanium atoms in immediate contact with magnesium have s-states that are very similar to those of magnesium, while the titanium atoms in the middle of the nanoclusters retain the states of elemental titanium[46]. The p- and d-states of titanium are affected as well[46]. Proximity to titanium also shifts the magnesium p-states, according to simulation results[46].

Experimental details

Samples were prepared by compressing Mg-Ti alloy powders in different compositions (10, 20, and 40 at.-%) milled for 25 h each and at different stages of ball milling at a fixed composition of 20 at.-% (0, 6, 12, 25, and 50 h of milling) into discs, that were mounted on the sample holder with spring clips. X-ray photoelectron spectroscopy (XPS) was performed with a K-alpha (Thermo Scientific). Prior to scanning the sample surfaces were ion etched inside the XPS chamber for 1800 s to remove airborne particles and the oxide layer that forms on both magnesium and titanium upon contact with air. XPS scans were taking with the flood gun running to minimize charging. The x-ray spot size was 400 µm. Scans were taking with energy step sizes of 0.1 eV and pass energies of 50 eV. The dwell time was set to 50 ms. 25 scans were taken of the magnesium states and 50 scans of titanium states to obtain sufficiently strong signals despite the low titanium concentration.

Results and discussion

In this study, the XPS spectra of ball-milled Mg-Ti alloys were compared with that of a physical mixture of magnesium and titanium, which represents the starting materials before the mechanical alloying process. Alloys with various milling times (6, 12, 25, and 50 h) were

compared to the unmilled physical mixture. The influence on composition was also investigated by comparing alloys with 10, 20, and 40 at.-% titanium which were all milled for 25 h.

Mg1s scans show the same peaks for all investigated compositions (10, 20, and 40 at.-% titanium) after 25 h of milling (Figure 47). There is a sloping shoulder on the low binding energy side of the peaks. This asymmetric peak shape stems from the close proximity of the peaks of elemental magnesium and magnesium oxide (MgO) in the scanned region. All sampled Mg2s spectra seem to be composed of two peaks, although the database only lists a single peak in that region for magnesium, which coincides with the stronger peak position. No possible impurities could be matched to the extra peak. However, as those two peaks appear in elemental magnesium in the unmilled sample, they must be inherent to elemental magnesium, possibly interference peaks. The Mg2p spectra match those presented by Jensen et al.[130]. The most prominent peak corresponds to elemental magnesium, while the weaker one tagged on the high binding energy side indicates the presence of MgO. The detected MgO peaks in the Mg2p and Mg1s spectra underline the presence of magnesium oxide throughout the powder particles. Magnesium oxide is present in the bulk of the samples because the oxide layer formed on the precursor material in air is worked into the bulk of the particles during ball milling. The magnesium Auger lines do not show any anomalies.

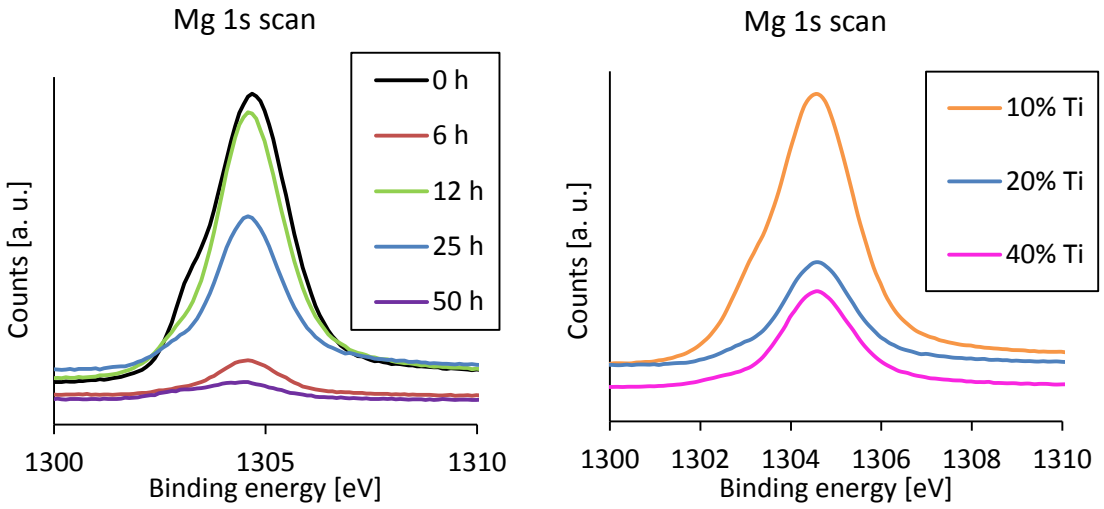

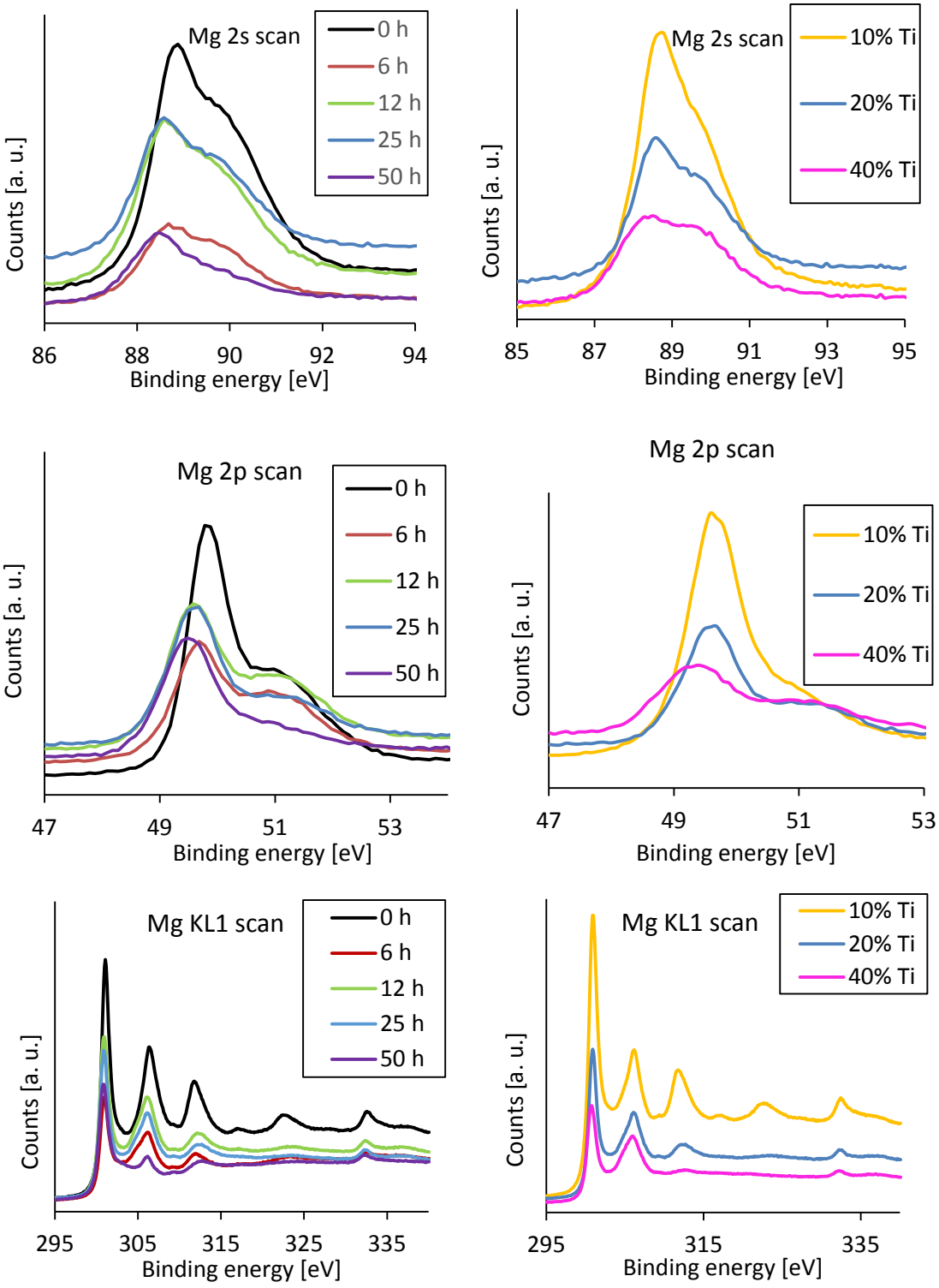

Figure 47: XPS Mg scans of all electronic states that can be probed. Comparison of photoelectron lines after milling 20 at.-% titanium containing Mg-Ti mixtures for different times (left) and after milling for 25 h for different titanium contents (right).

The Ti2p peaks (Figure 48) observed in this study closely resemble those reported by Jensen et al.[130] Both peaks in the sampled spectrum correspond to elemental Ti2p peaks. No TiO_2 peak is discernible. Ti Auger lines exhibit the TiTLM3 peak around 1103 eV, however, they have a small second peak attached to the regular peak on the low binding energy side.

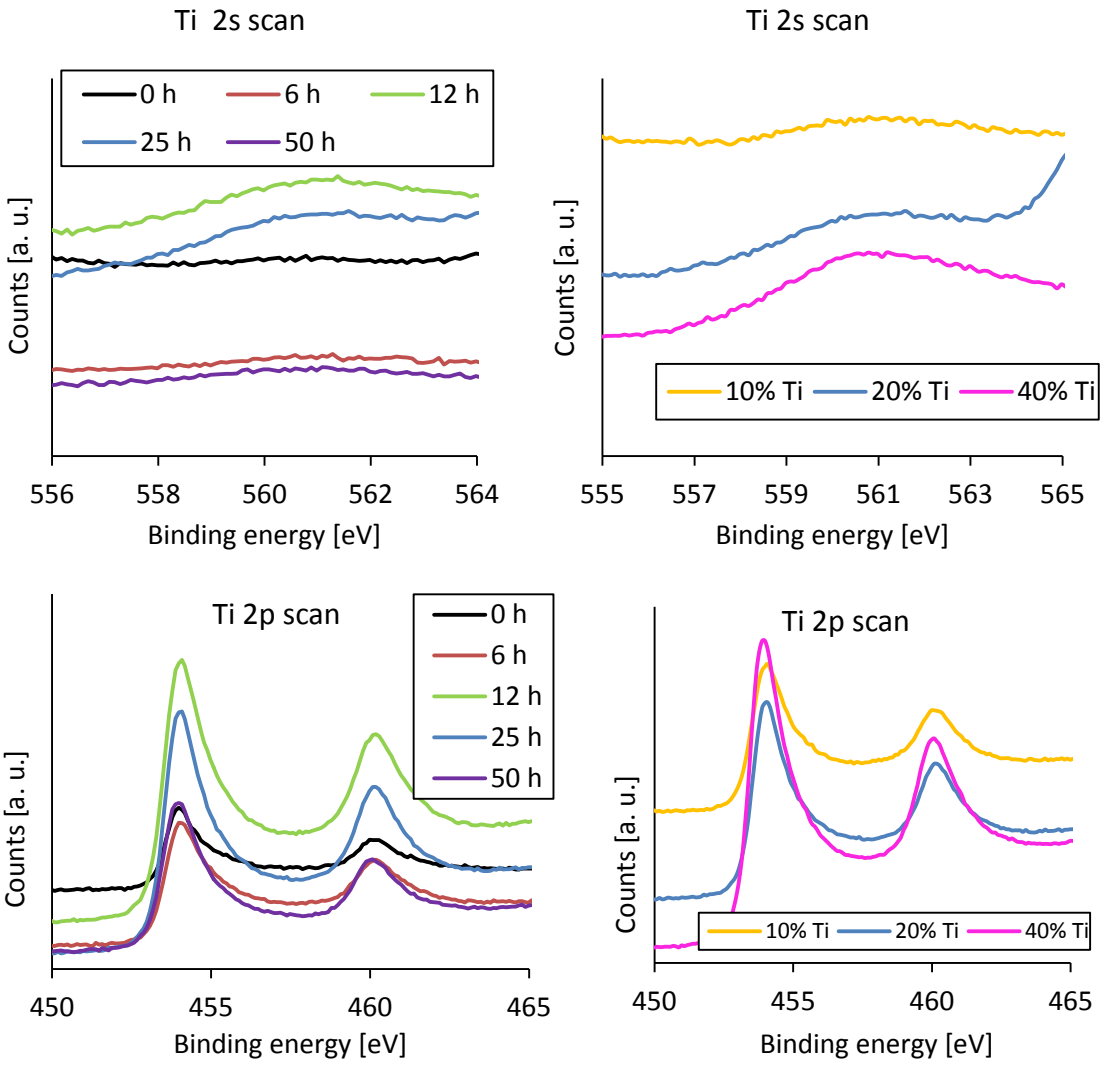

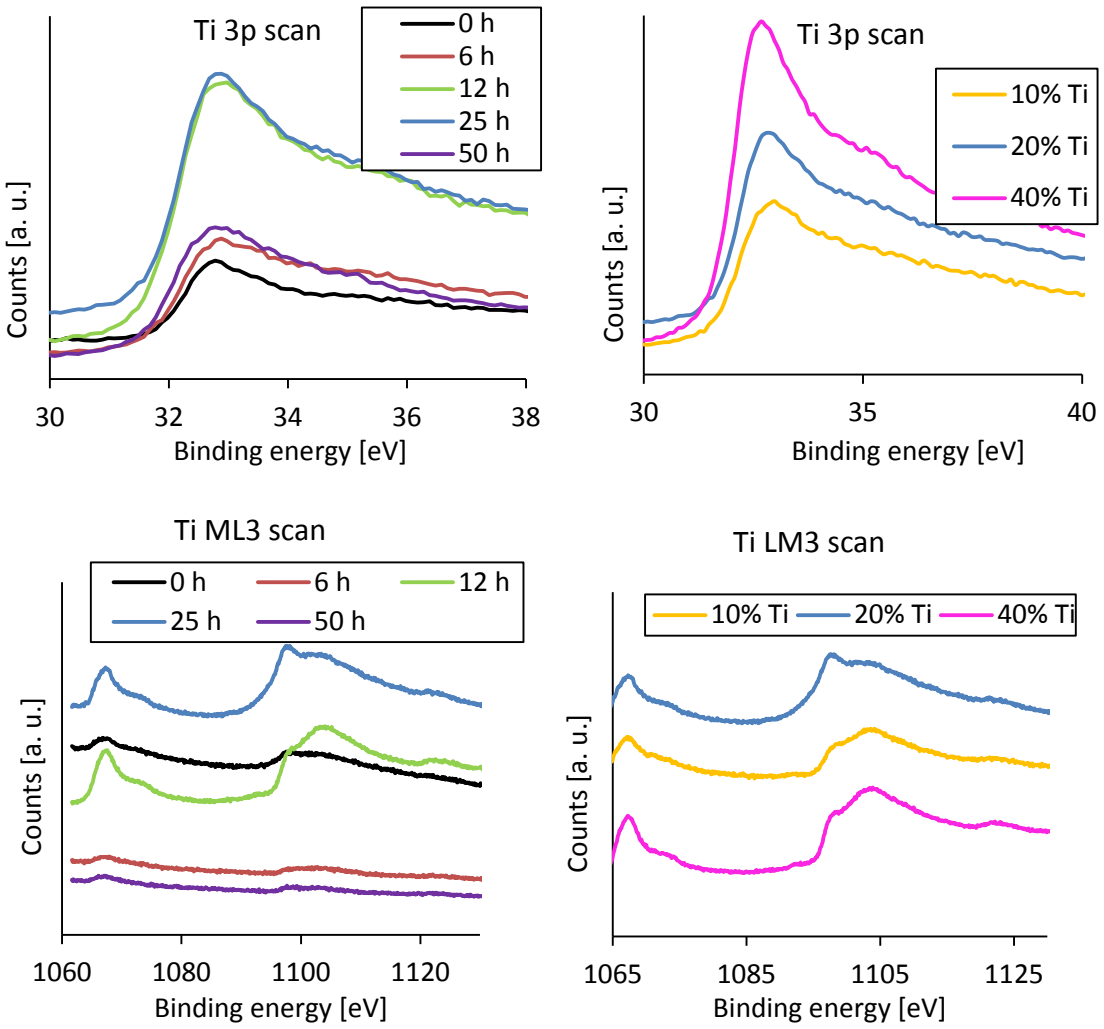

Figure 48: XPS Ti scans. Comparison of photoelectron lines after milling 20 at.-% titanium containing Mg-Ti mixtures for different times (left) and after milling for 25 h for different titanium contents (right).

The Mg and Ti 2p scans presented here correspond well with those published by Jensen et al.: The Ti 2p scan shows 2 elemental Ti peaks. Mg2p has a strong elemental Mg peak with a smaller MgO peak wedged onto it. These structures can be seen in both the physical mixture and the ball-milled Mg-Ti sample.

Although no differences could be found in most spectra, the Ti3s scans show very different peak structures: For Ti3s one peak is observed for the physical mixture of magnesium and titanium powders as expected, but after milling a second peak emerged right next to the original peak. The peak observed in the pure mixture is an interference peak stemming from magnesium,

according to a personal discussion with Dr. Brian R. Strohmeier from ThermoFisher. He explained that the extra peak observed in the Ti3s scan range is a plasmon loss peak belonging to Mg2p, which appears on the higher binding energy side than the real peak.

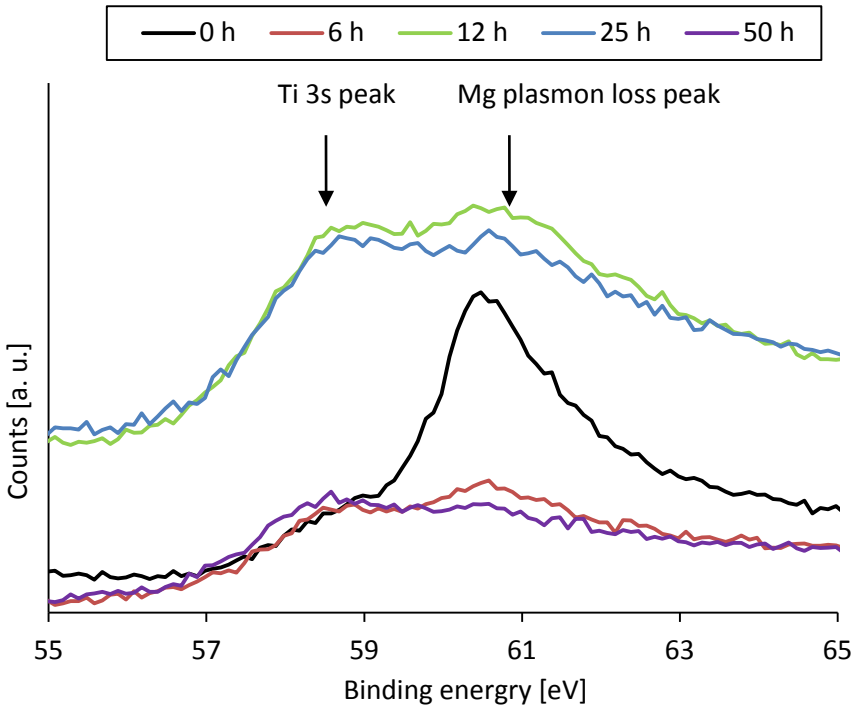

Figure 49: Comparison of Ti3s photoelectron lines after different milling durations. All samples contain 80 at.-% magnesium and 20 at.-% titanium.

Jensen et al. have reported that the electronic structure of their sputtered Mg-Ti alloys did not show any difference from the recorded standard spectra for pure Mg and Ti[130]. The effect of mechanical alloying on the electronic structure may be too low to be picked up, although theoretical calculations by Jensen et al. suggest a charge transfer from Mg to Ti[46]. Another possible explanation is that the oxygen present in the sample might have a bigger impact on the electronic structure than the effect of alloying, so that it is not visible. Additionally, Mg only has orbitals and p orbitals, so that the electrons are fairly close to the nucleus. In such a constellation weak ionization may not easily be detected because of the strong force of the nucleus on the electrons due to their close proximity. The d orbitals in Ti are more easily affected because they are further away from the nucleus, but cannot be probed with XPS.

P, d, and f orbital peaks experience spin-orbit splitting when ionized[132]. Variations in the elemental binding energies can be used to identify the chemical state of the material[132].

XPS spectra of Mg1s, Mg2s, Mg2p, Ti2s, Ti3s, Ti2p, and Ti3p photoelectron lines as well as Auger lines for both elements (MgKL1 and TiLM3) can be obtained. Although changes in the electronic structure are observed in simulations, they might not be as visible in experiments. It is possible that the changes are too subtle to be visible in XPS scans or the number of titanium atoms in immediate vicinity to magnesium is too small to show an effect. Alternatively, the present MgO could be overpowering the more subtle changes due to the presence of titanium. Jensen et al. argued that their cluster model explains why Mg-Ti PVD alloys do not have an improved corrosion resistance compared to magnesium[46]. This observation is in stark contrast with the corrosion tests presented in this work. Therefore, cluster formation may not happen when mechanically alloying magnesium with titanium. Although there are indications for pure titanium remaining after ball-milling in XRD scans and metallographic sections, the corrosion resistance is greatly improved through alloying. The material obtained by milling magnesium and titanium could be an alloy with pure titanium dispersed in it.

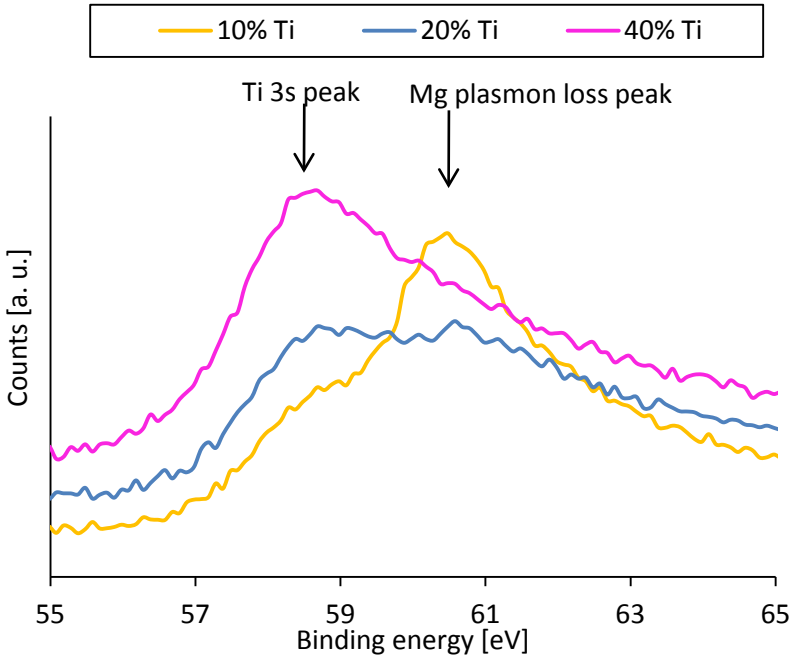

Figure 50: Comparison of Ti3s photoelectron lines after milling for 25 h for different titanium contents.

Conclusion

According to XPS measurements the process of mechanical alloying does not alter the electronic structure of Mg and Ti, at least not to a measurable extent. The spectra look identical before and after milling for all investigated compositions (10 - 35 at.-% Ti) and milling times (0 - 50h). However, simulations indicate that a charge transfer happens within the alloy[130]. This charge transfer may be too weak to be picked up by XPS. Therefore, XPS is not a helpful technique to study the alloying effect of titanium on magnesium.

Cytocompatibility of Mg-Ti alloy

After demonstrating improved corrosion resistance of Mg-Ti alloy compared to pure magnesium, the next step is to check the alloy's cytotoxicity. For a gross assessment of cytotoxicity animal cells were used. The cytotoxicity tests were run on supernatants from incubating the tested materials in cell culturing medium to check whether ions given off by the samples have a toxic effect on the cells. Supernatant preparation also offers a way to check for the concentration and type of ions released from the material. As it has been shown that the popular MTT stain is not a good choice for working with magnesium samples[115], therefore staining methods were selected in which the stain never comes into contact with magnesium-containing solutions.

It is well known that all metals corrode in physiological environments[21]. Metallic ions can have harmful effects on cells and can be toxic in sufficiently high doses[21]. The negative effects may be either elicited directly by the ions, or complexes they form with organic matter (e.g., proteins), salts formed from the ions, or metal oxides[21]. The presence of magnesium ions has been shown to be beneficial to cells in certain doses[19]. Rapid corrosion of magnesium in contrast had cyto- and genotoxic effects on cells[31]. Several researchers have established cytotoxicity levels for titanium ions with different cell lines[102,106].

Experimental details:

Sample fabrication

Pure magnesium samples were made from -325 mesh pure Mg powder (99.8 %, AlphaAesar). Mg-Ti alloy containing 20 at.-% titanium was fabricated by high-energy ball milling for 25 h in a SPEX 8000D mixer/mill with a ball-to-powder mass ratio of 16:1. The starting reagents Mg (same as pure magnesium sample) and titanium powder (-325 mesh, 99.5 % (metals basis), AlphaAesar) were measured and filled into the milling vial (stainless steel vial and ball set, both SPEX) in an argon filled glove box to avoid oxygen contamination during milling. Pure magnesium was processed in the same way for reference of the effect of ball milling alone on the corrosion resistance. After milling the vials were opened in air.

Supernatant preparation

The sample powders were compressed at over 10t in a ½" die (resulting stress: over 789.4 MPa). The pellets were then coated in epoxy (Buehler) and both sides ground up to 4000 paper to expose a defined surface area to the solution. Finally, some excess epoxy was cut off around the samples to make them fit into 50 mL centrifuge tubes. The samples were sterilized by UV radiation for 1 h on each side. To make supernatant, the samples were immersed into 15 mL alpha modification of Minimum Essential Medium (αMEM; HyClone Laboratories, Inc. by Thermo Scientific) supplemented with10 % fetal bovine serum (FBS; Atlanta biologicals) for 1 day and 1 week in centrifuge tubes. During immersion the centrifuge tubes with the solution were kept in an incubator with 5% CO_2 at 37°C on a shaker plate to mimick body temperature and avoid concentration gradients that could affect the corrosion rate. The centrifuge tube caps were only screwed on loosely to allow CO_2 in to keep the buffer active. After taking out the sample pellets the pH was measured with an accumet BASIC AB15 pH meter (Fisher Scientific). The solution was filtered first with filter paper to remove any particles that may have come off the samples during corrosion and then sterile filtered with a 0.22 µm sterile PES syringe filter (TISCH Scientific). The exposed surface was 2 x 126.68 mm^2 = 253.36 mm^2. With 15 mL of solution, this results in a surface to volume ratio of 16.9 mm^2/mL.

To check the effect of elevated pH and the presence of Mg/Ti ions by themselves on the pH indicator (phenol red) in αMEM separately, additional supernatants were prepared with a piece of titanium foil (0.89 mm thick, 99.7% (metals basis), AlfaAesar) in regular medium and in medium with a starting pH of 9 incubated for one week. Another supernatant was prepared from a physical mixture of magnesium and titanium particles compressed into a disk to distinguish the effects of the presence of magnesium and titanium from that of the alloy that was also incubated with αMEM for one week.

Cell culturing

Pre-osteoblastic mouse cells of the MC3T3-E1 cell line (ATCC CRL-2593) were cultured in αMEM + 10% FBS in an incubator at 37°C with 5% CO_2in a humidified atmosphere. When nearly confluent, the cells were harvested and seeded on 24 well plates with a density of 20,000 cells/well and let to attach over night. On the next day the medium used for seeding was removed and replaced by serial dilutions of the supernatant and fresh αMEM + 10% FBS for the control row. The exact well plate layout is depicted in Figure 51. The cells were exposed to the

supernatant and serial dilutions of it for 24 h. Prior to staining the medium was removed and all well plates washed with 500 µL calcium-free phosphate buffered saline (PBS) twice to remove any residual medium to avoid side reactions with the dye before the stain was added.

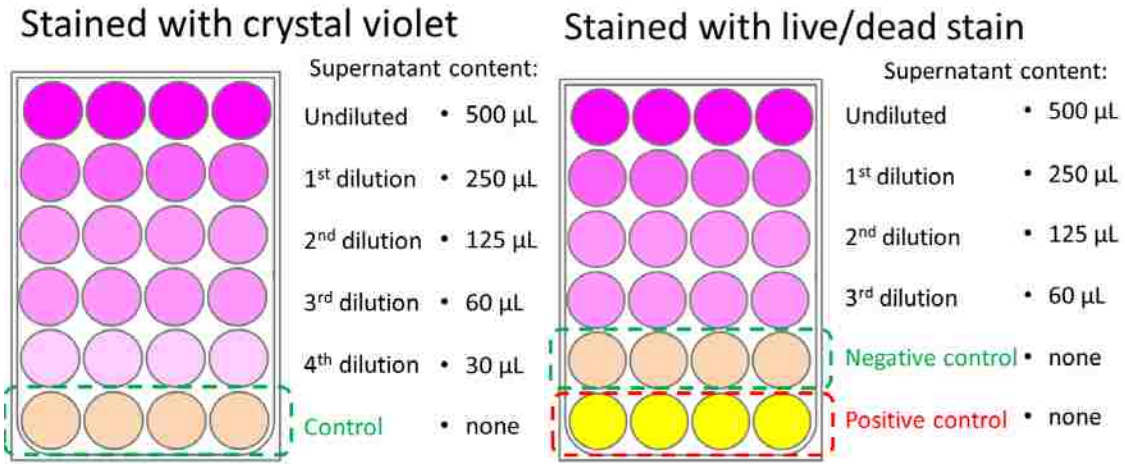

Figure 51: Experimental layout for the cytotoxicity tests. The balance of the sample solution to 500 µL was αMEM + 10% FBS.

Method for crystal violet staining

Crystal violet (C.I. 42555; Basic Violet3 by Sigma Chemical Co., C25H30ClN3) was dissolved in de-ionized water to yield a 0.1 % solution. 250 µL of the crystal violet solution was added to each well. The stain was removed again after 15 min. and the wells were rinsed twice with 500 µL de-ionized water each to remove excess stain. Finally, 500 µL ethanol was filled into each well to elute the stain. The well plates were shaken for 2 h while the ethanol dissolved the stain. Absorbance was read in a well plate reader (SynergyMx by BioTek controlled by reading software Gen5 2.00) at a wavelength of 595 nm.

Method for live/dead staining

The cells in the positive control row were killed by replacing the cell culturing medium with 70% methanol and exposing them to the alcohol for 40 min. before the medium of the other wells was removed to prepare for staining. Calcein AM and ethidiumhomodimer (EthD-1) (LIVE/DEAD Viability/Cytotoxicity Kit, Life Technologies) were dissolved together in sterile PBS at concentrations of 1:2,000 and 1:500 respectively, according to the manufacturer's protocol. All cells were stained with a 1:1 mixture of pure PBS and staining solution and incubated for 30-45 min. Fluorescence was read from the bottom as an area scan with a 5x5 point grid with a well plate reader (SynergyMx by BioTekcontrolled by reading software Gen5 2.00). The excitation

wavelengths were 485 nm (calcein AM) and 528 nm (EthD-1). Fluorescence was read at 530 and 617 nm, respectively. The average of the calcein AM fluorescence signal from the negative control was set to represent 100% live cells and the average EthD-1 response from the dead cell control represents 100% dead cells. Conversely, the EthD-1 signal from the negative control group and the calcein AM fluorescence from the positive control can be regarded as the background fluorescence level. In the graphs error bars represent standard deviations.

Ion concentration measurements

Inductively coupled plasma optical emission spectroscopy (ICP-OES) was used to determine the magnesium and titanium ion content in the cell culturing medium and the supernatants made from it. The sample solutions were digested with trace metals grade nitric acid to make sure no particles were left behind. A 1:10 dilution of the sample solutions was made with de-ionized water to be measured in a VARIAN Vista-Pro CCD Simultaneous ICP-OES machine. Calibration standards containing both magnesium and titanium ions in concentrations ranging from 0.01 to 100ppm were made with magnesium and titanium ICP standards (1000 µg/mL, ULTRAgrade Solution, Ultra Scientific).

Analysis

Outliers in the cytotoxicity experiments were identified with Dixon's Q test[133]. All values that satisfied the 95% confidence level[134] for a sample size of four were disregarded. One-way Analysis of Variance (ANOVA) with Tukey test was performed using GraphPadInStat version 3.05 for Windows 95, GraphPad Software, San Diego, California, USA.

Material characterization

To characterize the crystal structure after milling, x-ray diffraction (XRD) scans of all sample powders were taken with a Siemens D5000 x-ray diffractometer between 31.5 and 38° (Mg) / 41° (alloy) 2θ with a step size of 0.02° and a scan speed of 0.4 °/min. The compressed samples were again scanned after they had been used to make the supernatant in order to find out what the surface is comprised of. This scan was run from 20 to 100° with a step size 0.01°, speed 0.12°/min.

To narrow down the list of possible phases to identify from XRD scans, x-ray photoelectron spectroscopy (XPS) was conducted with a K-alpha x-ray photoelectron spectrometer system(Thermo Scientific). The sample surface was ion-milled for 600 s with 3000 eV ion energy,

high current prior to data acquisition. The flood gun was turned on during measurements to minimize charging. For survey scans 25 scans with dwell times of 10 ms were ran at a pass energy of 200 eV and with energy step size 1 eV. The binding energy was scanned from -10 to 1350 eV. More detailed scans of individual elements (Mg, Ti, O) were run with pass energy 50 eV, 50 scans, dwell time 50 ms, energy step size 0.1 eV. Again, the binding energy was scanned.

Results & Discussion

After 24 h of immersion in cell culturing medium white spots become visible on the surface of the untreated magnesium sample (Figure 52a). The amount of white surface products further increases with prolonged exposure so that after one week in the solution almost all of the surface is covered in it (Figure 52c). At the same time the sample can be seen to expand on the two exposed sides that are not confined by the epoxy (Figure 52b). Originally, the sample was 6.5 mm high, after one corrosion in the medium for one day it has expanded to a thickness of 10.5 mm, which is an increase of 62 %. After one week one side of the sample has expanded tremendously (Figure 52d). Before corrosion this sample was 8.2 mm thick, during corrosion it expanded to about 18 mm, which is more than double the original thickness or an increase in thickness by over 120 %.

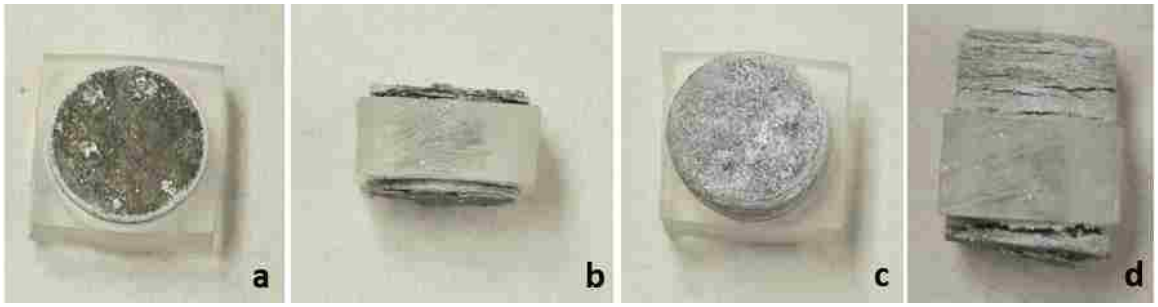

Figure 52: Untreated magnesium sample after immersion in cell culturing medium. White spots are formed on the surface after just one day of immersion (a). By the time one week has gone by the whole surface in covered in a white layer (b). The sample also expands on the two exposed sides, already noticeable after one day (c) and very pronounced after one week (d). One side expanded more than the other.

In contrast, the ball-milled magnesium sample shows mainly grey spots on its surface after one day of corrosion in medium (Figure 53a). Some areas on the surface even still look metallic. On

one side white corrosion products are formed inside pits in addition to the dark grey and metallic areas (Figure 53b). Within one week the entire sample surface becomes covered in an uneven, thick layer of white crystals (Figure 53c).

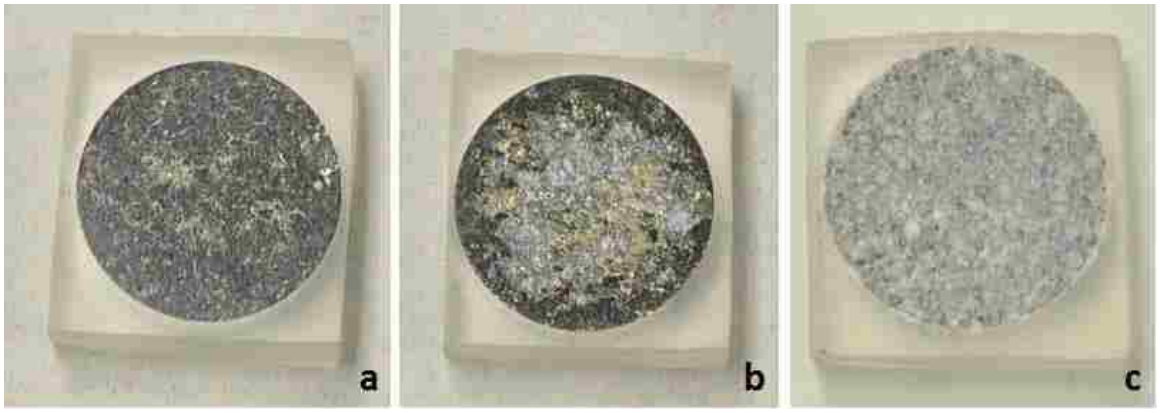

Figure 53: Milled magnesium samples after making supernatant. The sample immersed for 24 h still has shiny metallic spots although the majority of the surface is covered in dark grey layers (a). On one side there is also a large portion of white surface products in pits formed on the surface (b). After one week the sample is encrusted in a thick layer of salt crystals (c).

The alloy surface turned black upon exposure to the medium (Figure 54a), similar to what was observed for corrosion in Hanks' solution. A few tiny pits can be observed, but they appear to be much smaller than in the case of the white pits on the ball-milled magnesium sample. The surface remains very smooth overall. The optical impression already suggests that different corrosion products form on the surface of those two materials. After one week a white layer has formed on top of the black surface. Very thin and faint on one side (Figure 54b), thick and opaque on the other (Figure 54c). The pits have grown larger and deeper as well. Pitting is especially severe on the white side. Hydrogenation of titania introduces disorder into the lattice that turns the usually white titania black[129]. This effect, however, showed no difference between hydrogenated and natural titania in the XRD spectra published by Chen et al. [129], who experimented with hydrogenated titania nanocrystals. As Mg-Ti alloys were first researched as a hydrogen storage materials, it is easily imaginable that the hydrogen generated during the corrosion of magnesium would be stored in titanium oxide formed on the surface of the alloy.

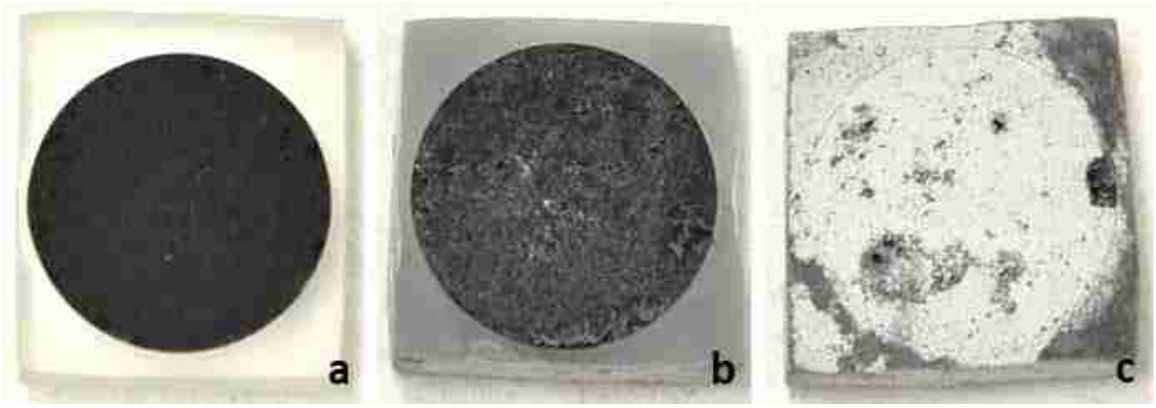

Figure 54: Alloy samples after incubation in supernatant. After 24 h of exposure to the medium the alloy surface is black (a). After one week a white layer has formed on top, thin on one side (b) and very thick, completely opaque on the other (c). Chunks are missing from the white surface and to a much lesser degree from the blacker side.

XPS detected N, P, Ca, Na, Mg, Ca, O, Cl, C (second most prominent peak) and O (most prominent peak) for unmilled magnesium that was in the supernatant solution for a week (Figure 55).

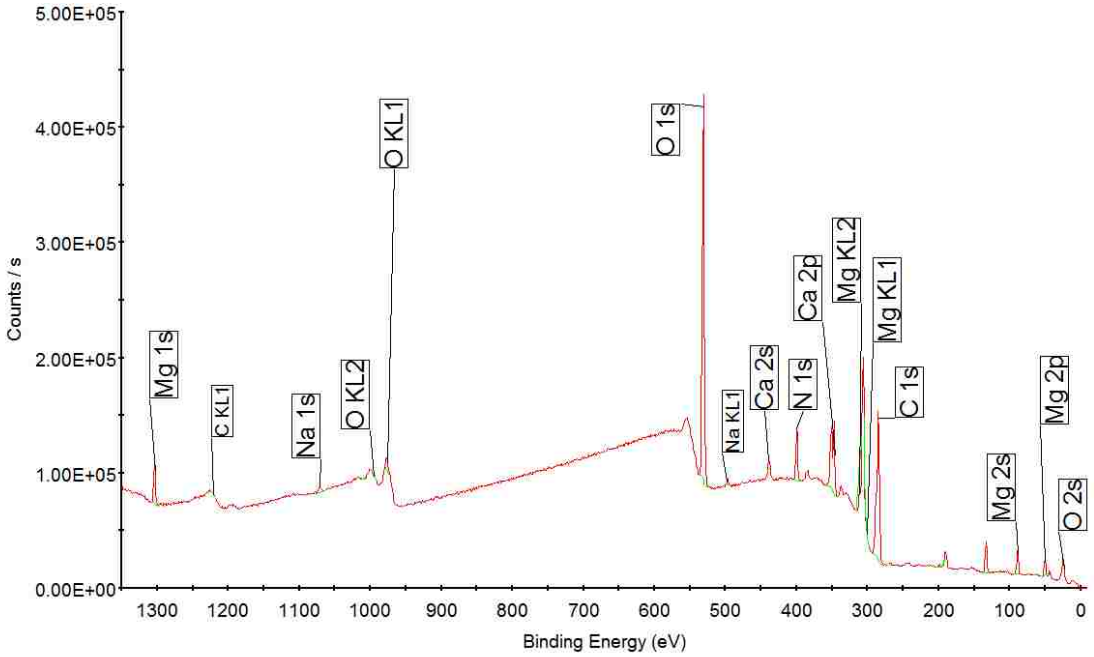

Figure 55: XPS survey scan of the unmilled magnesium sample surface after one week of immersion in cell culturing medium.

In the ball-milled sample immersed for a week, C and O also take the place of most and second most prominent peaks, respectively. No Na was detected, but Mg, N, Ca, P were present.

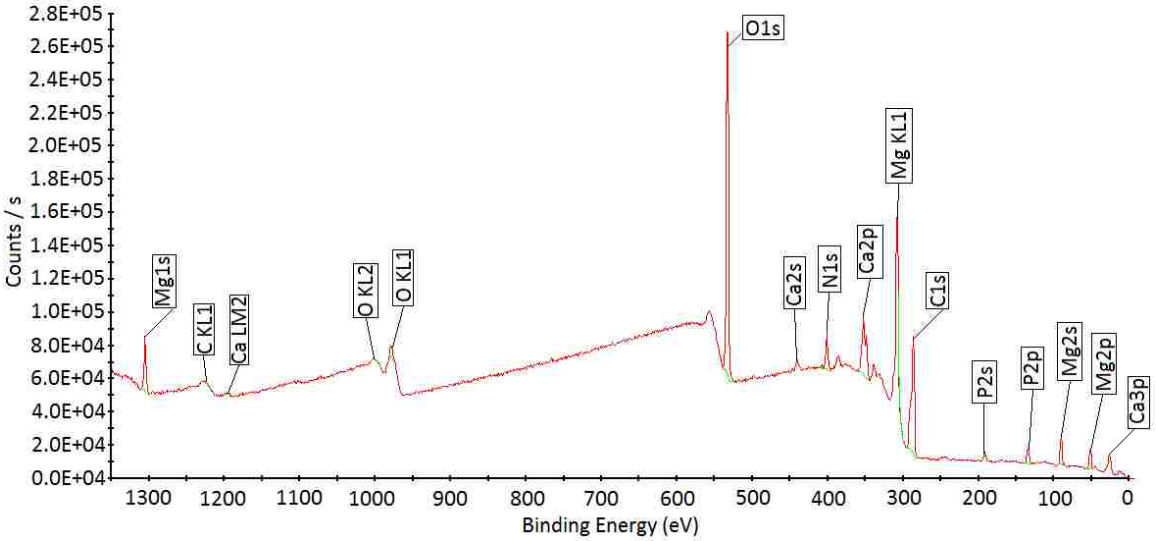

Figure 56: XPS survey scan of the ball-milled magnesium sample surface after one week of immersion in cell culturing medium.

On the black surface of the alloy Ca, N, P were detected in addition to Mg. The by far most prominent peak is C. A sizable O peak is also observed. A weak Ti2p signal was detected, with the peak mainly comprised of TiO_2.

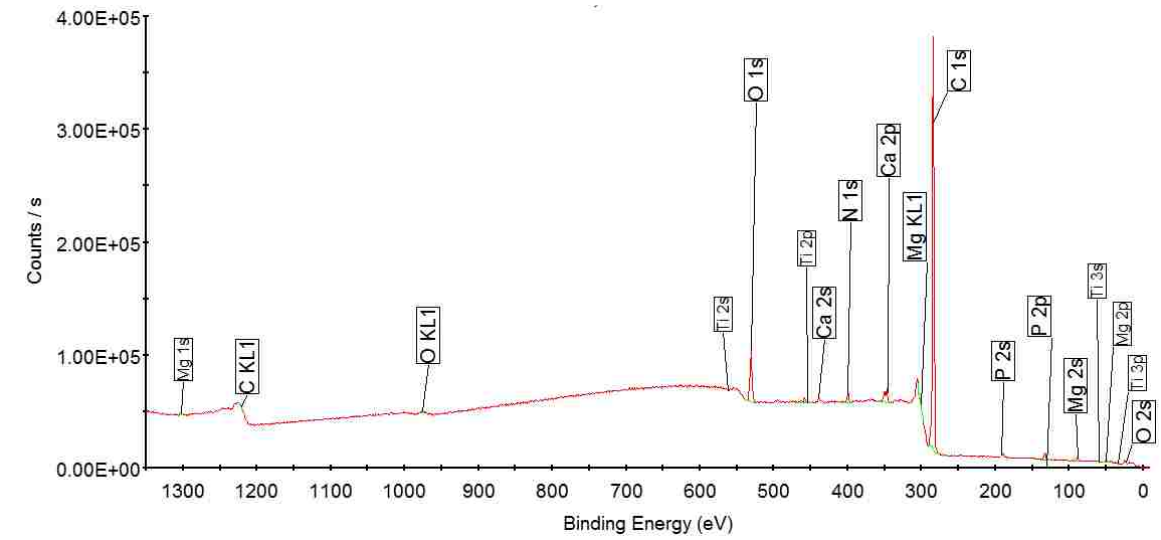

Figure 57: XPS survey scan of the black side of the alloy sample after corrosion for one day.

On the white alloy surface the C and O peaks are still the most prominent features. In addition, a very weak Ca peak can be found in the survey scan. Mg peaks are also very small and Ti cannot even be detected. This indicates that the thick white layer may be primarily made up of C and O and is so thick that it shields the underlying material.

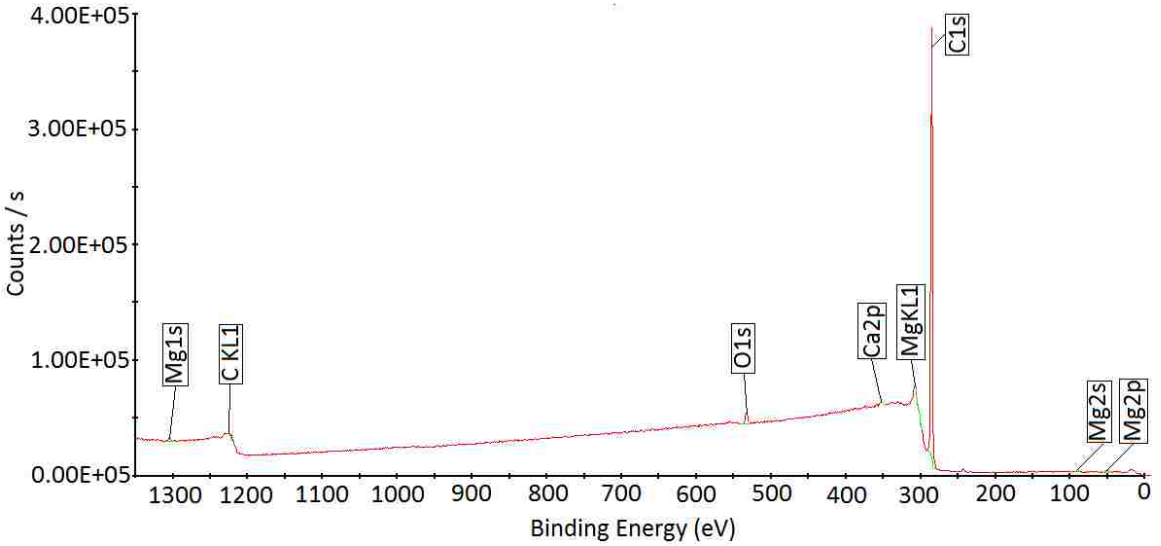

Figure 58: XPS survey scan of the white side of the alloy sample after corrosion.

As the XRD graph of the as-fabricated sample powders shows, milling magnesium decreases the intensity and increases the full width at half maximum (FWHM), while the peak positions remain constant (Figure 60). The dotted lines indicate the peak positions for pure magnesium. When alloying magnesium with titanium the peaks shift towards higher angles because the lattice

parameters decrease when titanium is incorporated into the magnesium lattice. At the same time the intensity is further decreased drastically.

When comparing the Mg1s and Mg2p scans of the samples, most peaks have contributions of both elemental and oxide peaks (Figure 59). While the Mg1s peak of unmilled magnesium lies between the peak positions for elemental and oxidized magnesium, the peak of milled magnesium coincides exactly with the MgO peak position. Thus, the surface of milled magnesium consists mainly of MgO and that of unmilled magnesium contains both metallic and oxidized magnesium. The Mg2p peak of unmilled magnesium is made up of elemental and oxide contributions, but its closer to the elemental peak position. In the case of milled magnesium the Mg2p peak is also comprised of oxide and elemental parts, in this case almost equal. The alloy's Mg2p peak matches with the elemental magnesium position.

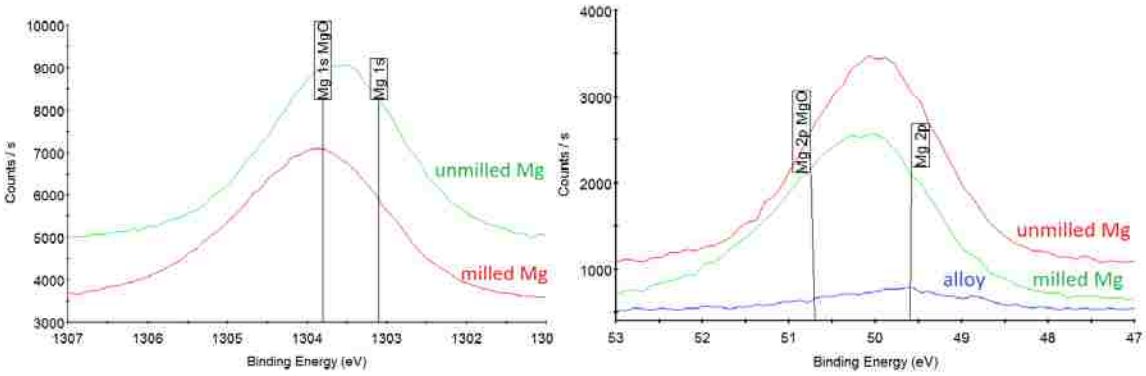

Figure 59: Comparison of Mg 1s and 2p scans of several samples. The alloy's Mg1s peak was too weak to be detectable. In both graphs the MgO position is on the left and the elemental peak on the right.

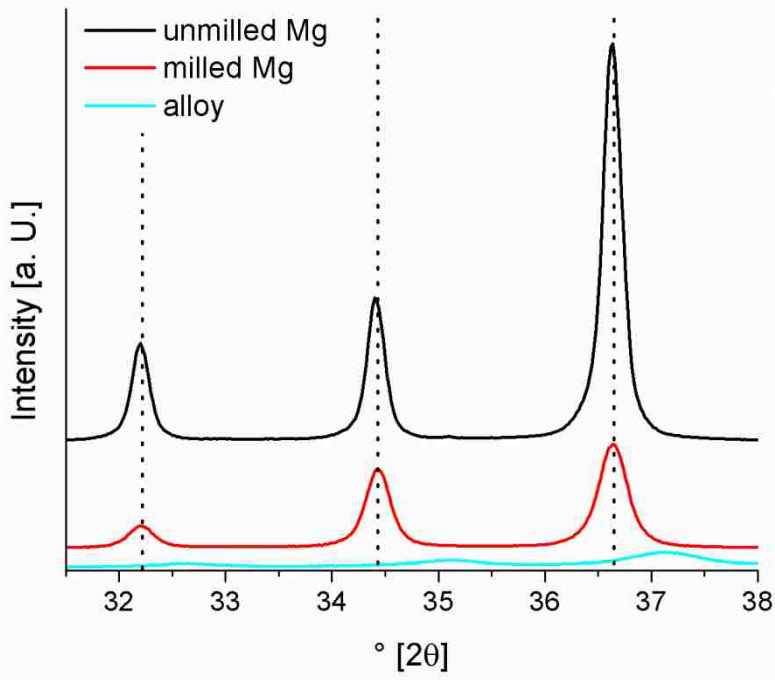

Figure 60: XRD graphs of all sample compositions used. The dotted lines denote the peak positions for Mg according to the powder diffraction file (PDF).

The corroded milled magnesium and alloy samples show mainly the original material´s peaks after one day immersion. After one day of corrosion the XRD graph of the alloy sample still only shows the original alloy peaks, although the intensity has decreases slightly (Figure 61). In the milled magnesium XRD the original magnesium peaks are the main features. A slight bump around 43° corresponds to magnesium oxide. For the unmilled magnesium, the original magnesium peaks are still visible, but have weakened significantly in intensity. Peaks of newly formed phases on the surface are much stronger than the original features on this sample.

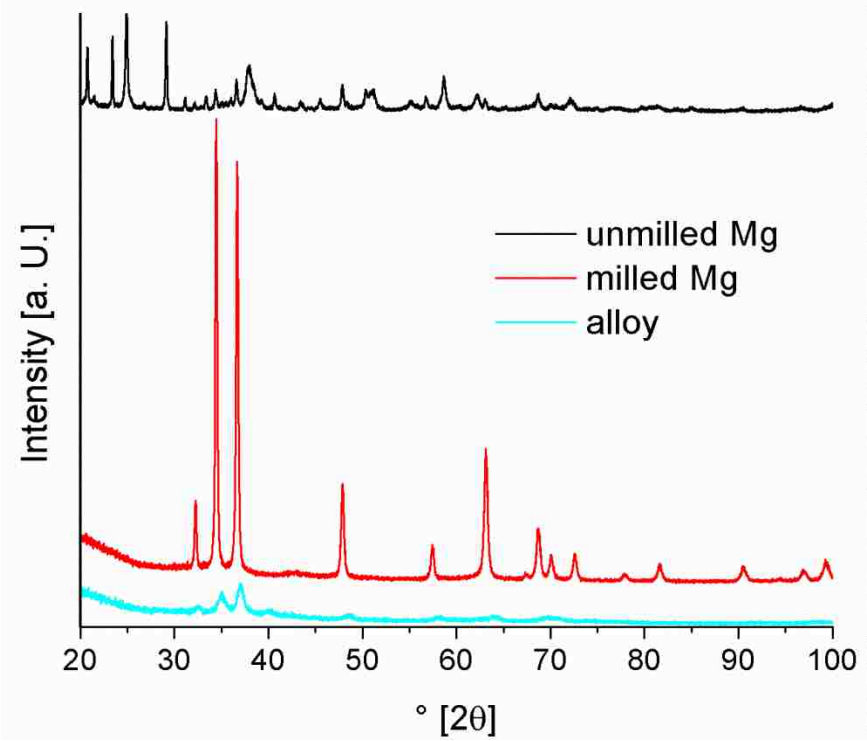

Figure 61: XRD graphs of samples corroded for 24 h.

After one week of exposure to the corrosive solution the original magnesium peaks in the unmilled magnesium sample have become even weaker (Figure 62). At the same time some of the peaks corresponding to the surface layer formed during degradation have grown stronger because more of the material has formed on the sample, as can be seen on the photos of the sample after corrosion. The magnesium peaks of the ball-milled sample are now also joined by strong peaks that must correspond to the corrosion layer on the surface. Many of the extra peaks in both magnesium samples are in the same position, indicating that they share at least most of the same products formed on the surface. In the alloy samples the original peaks are largely overshadowed by the corrosion products formed on the surface. The low counts and broad peaks make identifying the phases difficult, but they coincide with the positions for titanium oxides, mixed Mg-Ti oxides, and magnesium oxides. The white alloy side has also peaks that can partly matched to $MgCaH_{3.72}$, $CaCO_3$*6 H_2O, $Mg_3Ca(CO_3)_4$, and $Mg_5(CO_3)_4(OH)_2$*5 H_2O. One possible explanation for the low counts and broad peaks is that incorporating hydrogen into titanium oxide causes lattice distortions[129]. The low counts and washed out peaks could also be caused by proteins and other organic substances from the medium that accumulated on the surface. This organic matter may not be arranged orderly and thus won't contribute to XRD

peaks but dampen the signal derived from inorganic matter underneath and among it. This would explain the large amount of C and O found by XPS and the peaks observed by XRD. The peaks found on the corroded magnesium samples are likely inorganic salts present in the solution. Possible matches are $MgCO_3$*3 H_2O, $CaCO_3$, $Mg(OH)_2$, $Mg_2CO_3(OH)_2$*0.5 H_2O, $Mg_2PO_4(OH)$, $Mg_2P_2O_7$, $Mg_2(OH)_3Cl$*4 H_2O, and other salts. The surface composition of pure magnesium and alloy samples is thus very different. The products formed on the alloy surface may help protect the material against corrosion. XRD graphs of corroded unmilled magnesium samples of both time points are very similar, just the intensity of some peaks has increased greatly after one week of corrosion. Cell culturing medium is a very complex solution containing not only inorganic salts but a multitude of organic components, including proteins. This makes it hard to identify corrosion products formed on the surface because there are so many possibilities.

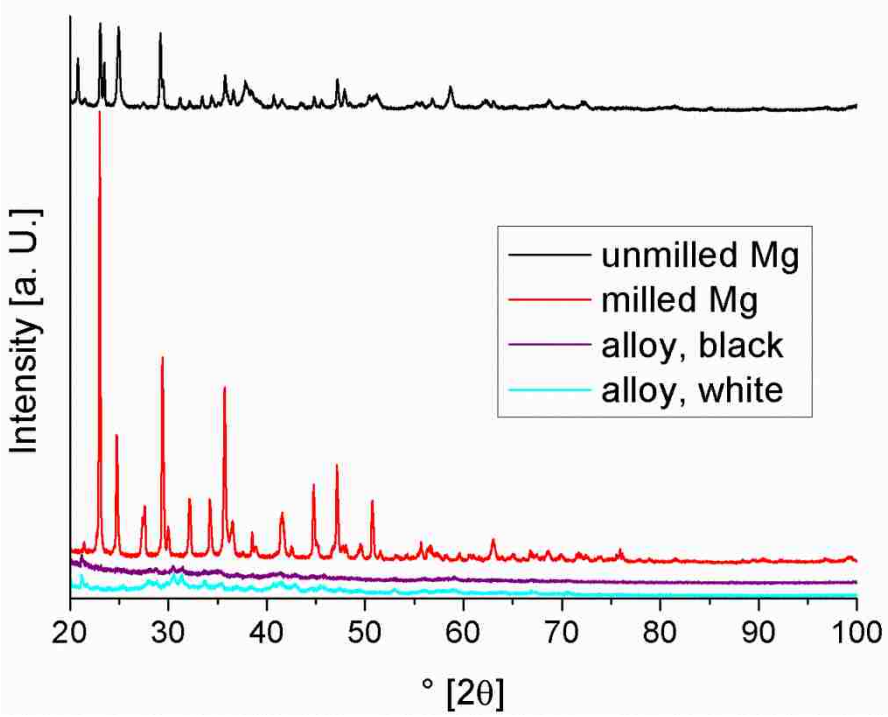

Figure 62: XRD graphs of the 1 week supernatant samples after corrosion.

After one day of incubation the pH of the medium has risen for all samples (Table 1). The pH difference between ball-milled magnesium and the alloy is small, but there is a marked difference between those two samples and untreated magnesium. The magnesium pH rose by the largest amount, which fits the observation of most severe corrosion on the untreated

magnesium sample. The lower pH of ball-milled magnesium is reflected in the still rather salmon pink color of the supernatant, that changed the least from the original orange color (Figure 63). With significantly increased pH the solution in which pure magnesium was immersed turned bright pink. The Mg-Ti solution paled, compared to the other two. After one week the differences have leveled out and both magnesium supernatants are intensely pink, corresponding to an increased pH in a comparable range. At this timepoint the pH for the untreated magnesium sample is the lowest. However, since the values are very close together, this could be well within the error margin.

Table 5: pH values of supernatant after different incubation times for all samples.

Sample	After 24 h	After 1 week
Untreated Mg	8.19	8.08
Ball-milled Mg	7.78	8.11
Mg-Tialloy	7.84	8.12

Interestingly, in untreated magnesium supernatant the pH falls from the 24 h to the 1 week timepoint. This phenomenon could mean that magnesium corrodes very actively within the first 24 h of immersion, so that the buffer is not reacting fast enough to keep the pH down. The buffer capacity depends on the concentration of buffer in solution. As CO_2 is supplied during incubation, the carbonate buffer can be replenished. However, the cap on the centrifuge vial was screwed on loosely, so that the gas is not instantaneously in contact with the solution. As the gas flows into the centrifuge tube over time the pH is lowered, explaining the lower pH after one week of immersion.

Although the pH values of all three samples are very similar, the Mg-Ti supernatant lost its color so this effect is not due to pH change. To investigate what causes the pH indicator to lose its color additional supernatants were made for the purpose of studying the color change during incubation for 1 week. A piece of titanium foil and a physical mixture of magnesium and titanium in the same composition as the alloy were used for comparison.

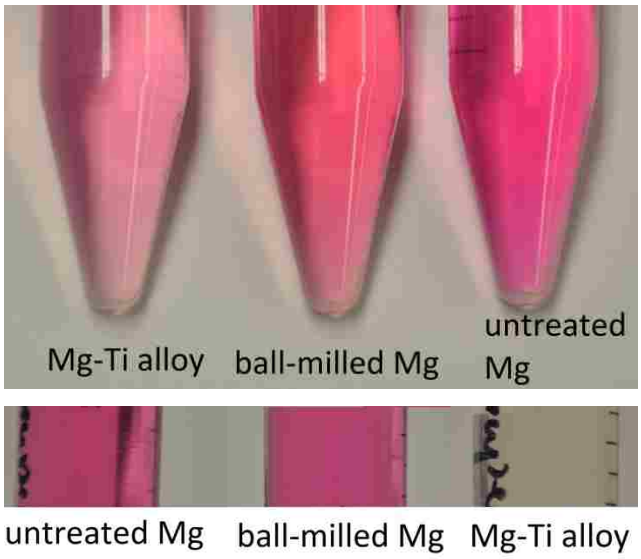

Figure 63: Supernatant color after incubating the samples for 24 h (left) and 1 week (right).

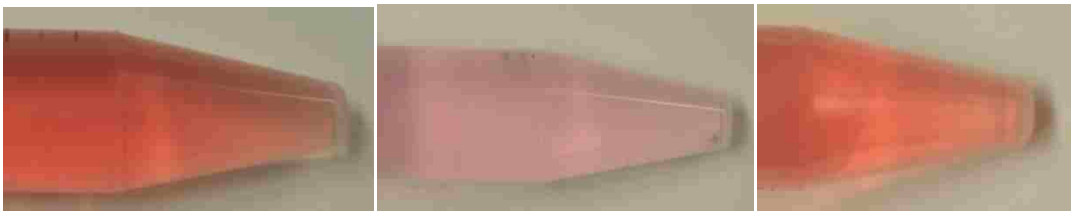

Figure 64: Supernatants with Ti foil (left), Mg-Ti mixture (middle), and Ti foil in supernatant with a pH of 9 (right) after one week of incubation. Ti by itself does not change the color of the phenol red in the cell culturing medium even at elevated pH values, but when Mg is mixed with it a slight decolorization is observed.

When incubating a piece of titanium foil in αMEM + 10% FBS for one week, the color of the solution does not change at all (Figure 64), which indicates that the pH value does not change. The solution does not pale or completely lose color as observed for Mg-Ti alloy incubated for one week. Thus, the presence of elemental titanium alone does not de-color phenol red. To double-check whether a heightened pH drives the effect a piece of titanium foil was incubated in supernatant with its pH adjusted to 9 before the start of the experiment. Judging from the pH indicator color the pH returned back to the original color of the cell culturing medium, indicating that the pH has significantly been reduced with steady supply of CO_2 inside the incubator. Either the pH was too low to elicit the reaction or pH does not affect the color changing reaction. An influence of the pH value can therefore not be ruled out, but is likely not the major driving force for de-coloration of phenol red in the presence of titanium.

With a pellet of a physical mixture of Mg and Ti compressed, the solution (Figure 64, middle) pales noticeably over the course of one week, but does not lose its color completely. The pH of the supernatant after incubation for a week was 8.22, thus comparable to that of pure magnesium. The pH alone therefore cannot be responsible for the color loss, as the pH indicator becomes colorless at pH > 14. It could be an effect of the combination of Mg and Ti in the solution together, e.g., Mg ions in the presence of titanium. TiO_2 might act as a catalyst for a magnesium ion based reaction that does not take place without the presence of titanium and changes the color of phenol red. A possible mechanism could be complexing of phenol red with magnesium, changing the structure of the molecule and altering its color.

αMEM contains 97.67 mg/L $MgSO_4$ according to the manufacturer, which is equivalent to 19.73 mg/L of magnesium. ICP measured a magnesium concentration of 19.8 µg/mL in αMEM + 10 FBS. ICP-OES measurements (Figure 65) showed the lowest magnesium ion concentration for ball-milled magnesium after 24 h of immersion (442 ppm), followed by pure magnesium (529 ppm). The values for the alloy are the highest (709 ppm). When incubating the samples in the medium for one week the alloy again shows the highest magnesium concentration of 1544 ppm. The second highest concentration (1459 ppm) is found in the ball-milled magnesium case and the pure magnesium sample has the lowest magnesium ion count (1142 ppm). The titanium ion concentration found in case of the alloy sample is 2 ppm after 24 h and 1 ppm after one week. It was interesting to notice that titanium ions were found in the solution after corrosion. This means that titanium does corrode as well or comes off the sample during magnesium corrosion. If Ti would not corrode a concentration of zero would be expected. If titanium was corroding with the same pace as magnesium (i.e., 1 atom of titanium for every 4 atoms of magnesium) the concentration would be expected to be 177.25 mg/L after 24 h and 386 mg/L after a week of immersion. As the solution was filtered before ICP no big solid pieces of titanium could have accidentally picked up, but only titanium ions or particles smaller than 0.22 µm in size (mesh size of the filter). Apparently titanium does corrode alongside magnesium or is released from the material as surrounding magnesium is dissolved, just at a much slower pace than the magnesium dissolution rate. Cadosch et al. reported that precursors of human osteoclasts can grow and differentiate into mature cells on titanium[78]. As such they actively corrode away the material and take it up[78]. During this process the metal ions might be released into the surrounding tissue or blood circulation[78]. This report together with the results obtained in this study indicate that even titanium, considered fairly bioinert, will most likely be removed from

the implantation site. Mg-Ti thus might be a fully biodegradable material that might be suitable for biodegradable implants if it proves to be biocompatible.

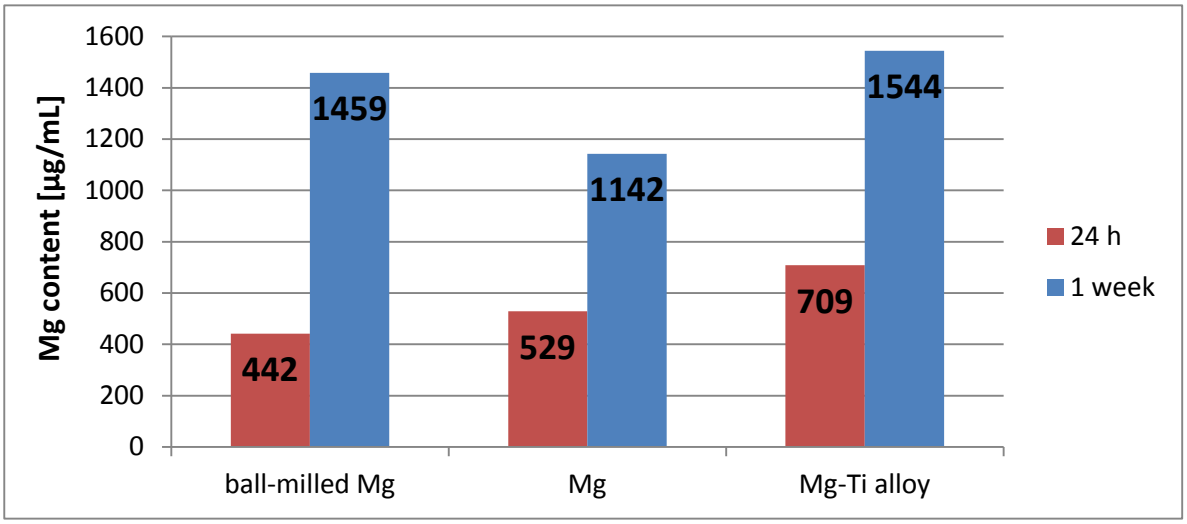

Figure 65: Total magnesium content in the supernatants after incubation for 24 h and 1 week as measured by ICP-OES.

It comes as a surprise to find that the magnesium ion concentration is the highest for the alloy sample, after it showed much better corrosion resistance in both the hydrogen evolution test as well as the electrochemical scans presented in previous chapters. However, those corrosion tests were carried out in Hanks' Solution. There is a possibility that the corrosion mechanisms in cell culturing medium are slightly changed due to the addition of proteins. The presence of proteins, e.g., albumin, can have a drastic effect on the corrosion rate of metals[135,136]. Proteins adhere to almost all solid surfaces in vivo[137]. Proteins for example reduce the influence of the pH on the corrosion behavior of titanium alloys[137]. Proteins affect the corrosion behavior of some metals, but they can accelerate or slow down corrosion, depending on their role in the corrosive environment[137]. Another question is where the magnesium ions go after corroding from the metal sample. A rather thick white corrosion layer was observed on the pure magnesium samples, whereas the alloy sample seems to be largely free from deposits, except for one side of the sample immersed for one week. Magnesium ions might have been incorporated into this corrosion layer and thus do not show up in the solution itself. Large crystals were observed to form in the one week supernatants, which were insoluble even when heating the solution up to 37°C. Although great care was taken to shake them up when collecting supernatant for cell experiments or ICP, there is likely a certain difference in the amount that was picked up. It can

clearly be seen from photos taken after the cell experiments that the amount of crystals varies in different wells (Figure 68). Taking into account these factors, the magnesium ion concentration measured by ICP may not accurately reflect the true corrosion rate of the samples, but there is a clear trend that more ions are in the solution with increased incubation time. This finding could explain the formation of crystals in the one week supernatant as excess magnesium that causes the precipitation of Mg-containing salts. The solubility of salts is also pH-dependent and the increased pH after one week might also play a role, although it is surely not the only reason because the pH of the magnesium supernatant after 24 h is even higher, but no crystals were observed in this case.

There are two possible ways where titanium ions could come from: Either titanium atoms turn into ions after the surrounding magnesium atoms have corroded away, leaving them exposed to the solution or small particles containing titanium or titanium clusters, smaller than 0.22 µm so that they fit through the sterile filter, become dissolved during digestion in preparation for ICP. In either case, titanium is liberated from the sample, so that probably no titanium mesh is formed after the magnesium has corroded away. This finding indicates that even after sintering titanium will probably come off the material under corrosive conditions, including in vivo. The titanium will also go away from the material and not stay behind by itself.

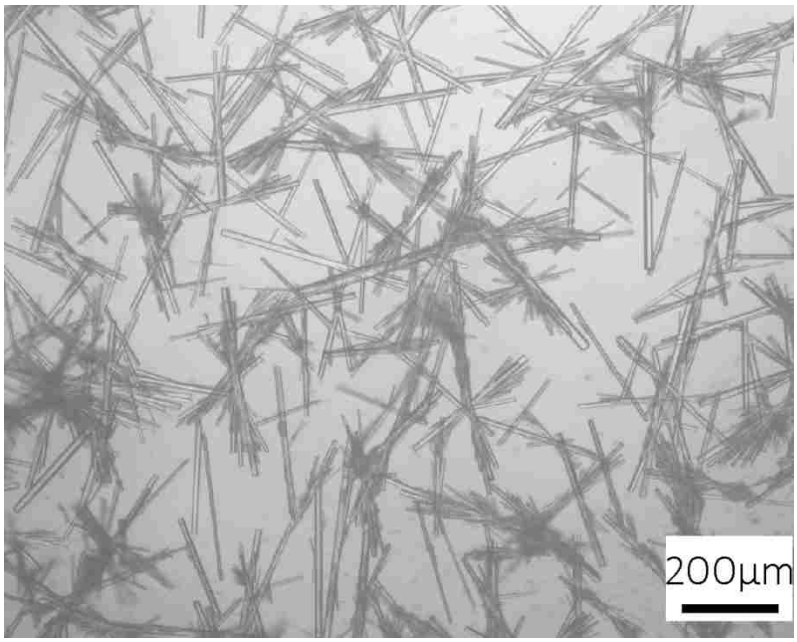

Figure 66: Needle-shaped crystals observed in undiluted 1 week supernatant after 24 h of incubation with cells.

Incubation of one week supernatants with cells for 24 h caused needle-like crystals in the undiluted supernatants (Figure 66). Very similar structures have been reported by other groups before, e.g., in a study on Mg-Ag alloys by Tie et al.[22] and an investigation on the cytotoxicity of degrading magnesium on human bone tumor cells by Wang et al.[105]. A possible explanation for the formation of crystals in these supernatants is the high ion content paired with a high pH. The precipitation of some salts is pH-dependent. As the supernatants were sterile filtered prior to the cell tests the crystals must have formed after filtering because in their size they would not have fit through the filter. There is, however, an indication that crystals already formed before filtering. There was more resistance to pushing the 1 week supernatants through the sterile filter than the 24 h supernatants although all solutions appeared clear and without debris to the naked eye. Though not observed before, the 1 week untreated magnesium supernatant contains small white particles after thawing. Those particles could be the same as observed after incubation with cells. Freezing could further accelerate precipitation. The particles do not dissolve after heating the solution up to 37°C prior to exposing the cells to it, but no crystals were observed after 24 h of incubation with the cells.

The supernatant solutions were freshly made at the time the crystal violet experiments were carried out. To store the supernatant solutions until the live/dead assays were run, the solutions were frozen. After thawing white precipitates (Figure 67) were observed in the 1 week supernatants, which are presumably the crystals observed after incubating the supernatants with cells.

Figure 67: On the far left is the unmilled magnesium supernatant prepared for 24 h. No white crystals can be seen at the bottom of the centrifuge tube, which is representative for all 24 h supernatant solutions. To its right is the 1 week unmilled magnesium supernatant, in which white crystals have accumulated at the tip of the centrifuge tube. The right image shows the crystals in the alloy supernatant (left) and milled magnesium supernatant (right), both incubated for 1 week.

Figure 68: Particles in wells after adding the supernatant. As an example the undiluted and 1st dilution wells of the 1 week supernatant of the alloy sample is shown. From the 2nd dilution on, no particles were observable by naked eye.

The crystal particles can clearly be seen in the undiluted and 1st dilution wells of all 1 week supernatants (Figure 68). The amount of crystals per well varies, depending on how many crystals were taken up with the pipette while transferring the solution into the wells. Although the crystals can be evenly distributed in the centrifuge tube through vortexing for a short time, they begin to settle as soon as the tube is taken off the vortexer. The crystals did not dissolve during incubation with cells.

From the color of the solutions it can be seen that the supernatants retain their original pH even after incubation for one day, i.e., the cells are indeed exposed to the measured pH values. However, those values are not expected to negatively influence the cells. Slightly higher pH has even been found to have a positive impact on the activity of human osteoblasts[138]. Patients with respiratory alkalosis show an increased rate of fracture healing[139].
In the magnesium samples it is obvious that the pH of the supernatants incubated for one week is higher than that after just one day. With serial dilutions the pH drops towards the value of fresh medium.

Figure 69: Alloy supernatants after 24 h exposure to cells. On the left the supernatant prepared for 24 h and on the right the 1 week supernatant.

Figure 70: Unmilled magnesium supernatants after 24 h exposure to cells. On the left the supernatant prepared for 24 h and on the right the 1 week supernatant.

Figure 71: Milled magnesium supernatants after 24 h exposure to cells. On the left the supernatant prepared for 24 h and on the right the 1 week supernatant.

The gross cytotoxicity of supernatants made from untreated and ball-milled magnesium was compared to that obtained with a Mg-Ti alloy containing 20 at.-% Ti. The alloy is compared to pure magnesium because magnesium is considered to be biocompatible. When treating the cells with the 24 h supernatant and staining with crystal violet a concentration-dependent detrimental effect is observed for all samples (Figure 72). For untreated Mg supernatant incubated for 24 h in the crystal violet stained experiments the differences between the undiluted supernatant and the third ($p < 0.05$) and fourth ($p < 0.001$) dilutions as well as the control row ($p< 0.01$) are significant. There is also a significant difference between the first and fourth dilutions with $p < 0.05$.Within the ball-milled magnesium supernatant experiments only the undiluted and first dilution differ from the control group ($p < 0.5$). For the alloy, there is only a significant difference between the undiluted supernatant and the fourth dilution ($p<0.5$). At all concentrations, however, the highest intensities are observed for the alloy supernatant. When comparing the three supernatants to each other, in the undiluted supernatant no significant difference was found between the unmilled and milled magnesium or ball-milled magnesium vs. alloy. Unmilled magnesium compared to the alloy is significantly different, though ($p<0.05$). The

first dilution comparison yielded $p<0.001$ for unmilled magnesium vs. ball-milled magnesium and ball-milled magnesium vs. alloy. The difference between unmilled magnesium and the alloy is smaller ($p< 0.01$).

From the 2nd dilution on the same number of cells than in the control group or more are found for this treatment. For ball-milled magnesium the cell count stays below that of the control group for all tested concentrations and in the case of untreated magnesium it takes four dilutions to overcome toxic effects on the cells. No significant difference between all three samples is found in the 2ndand 4thdilution.

With the one week supernatant no differences between the dilutions and control group can be observed and ANOVA confirms that no significant differences were found among the dilutions for both the alloy and ball-milled magnesium. When comparing the different dilution steps among the three supernatants no significant differences are found between the two magnesium samples as well as in the comparison of ball-milled magnesium and the alloy for all dilutions. From the first dilution on the number of cells is comparable to that of the control group, so that no toxic effects are detected with this experimental method. The results obtained for the treatment undiluted supernatant are to be treated with caution, since large crystals (Figure 66) were observed to form inside the wells during incubation. These crystals were extremely stable and did not dissolve during staining, so that the crystals might have taken up stain in addition to the cells and falsified the result. The crystals likely formed due to a high ion content in the supernatant stemming from the long exposure of the corroding samples to the test solution. Overall, Mg-Ti alloy shows better cytocompatibility in supernatant form after 24 h and is not more cytotoxic than pure magnesium after a week according to the crystal violet staining experiments.

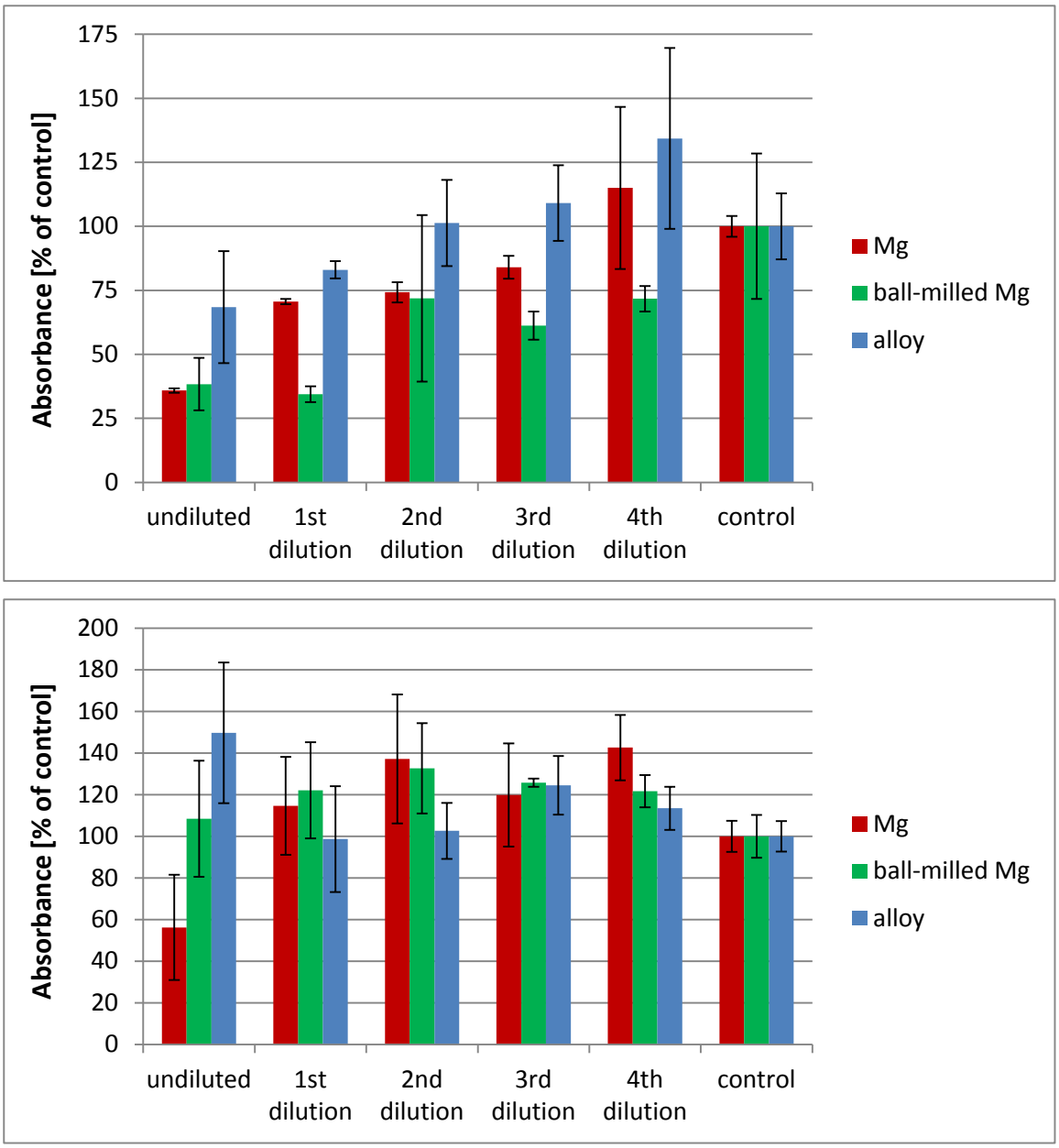

Figure 72: Result of the supernatant cytotoxicity test stained with crystal violet, 24 h supernatant of top, 1 week supernatant on bottom.

Crystal violet staining works based on reduced growth rates when cells are exposed to toxic substances[140]. Differences in growth rates are determined by colorimetric assessment of the stained cells[140]. Although crystal violet is a simple and reproducible cytotoxicity assay[141], it has limitations: It is a protein-based, non-specific staining method that stains all adherent cells, regardless of whether they are alive or dead[140]. Variations in cell numbers can therefore only arise if the cells in one treatment die early during the exposure time while the cells in less toxic

solutions multiply during the incubation time. Alternatively, dead cells can be found to be rounded up at the end of the experiment and easily wash off during the washings before staining. Any adhering dead cells will stay behind and be stained, so crystal violet only gives vague information about cytotoxicity. Live/dead staining gives a more detailed assessment of cytotoxicity.

In contrast to the crystal violet staining experiment, the intensity readings for live cells with 24 h supernatants (Figure 73) are very uniform and vary hardly between undiluted and diluted supernatant or the live control. Statistically there are no significant differences between the living cells in the undiluted supernatant and subsequent dilutions and the live control for the pure magnesium samples. The difference between undiluted supernatant and the first dilution of the 24 h alloy sample is not significant, but the difference to the second and fourth dilutions ($p<0.05$) and third dilution as well as the live control ($p<0.01$) is. Among the dilutions and compared to the live control no significant difference was found. When comparing the dead cells within each sample, there are only significant differences ($p<0.001$) of supernatant containing and live control cells in comparison to dead control for all samples.

With undiluted one week supernatants only a small fraction of the cells survives the day of incubation (Figure 74) and no significant difference between all three tested supernatants is found. This is in stark contrast to the results obtained with 24 h supernatants and the differences between the supernatants for 24 h and 1 week among each sample composition were significant ($p<0.001$). But from the first dilution of the one week supernatant on the cytotoxicity declines abruptly and the pure magnesium samples reach over 50% compared to the control, while the alloy response is even comparable to the live control, exceeding the 100% mark. Despite the large variation in numbers, statistically there is no significant difference between the pure magnesium samples or between unmilled magnesium and the alloy, but there is a significant difference between milled magnesium and the alloy ($p<0.001$). This relationship also holds true for the following dilutions.

The stained dead cell intensities of the undiluted supernatants after one week (Figure 74) show drastic differences comparing untreated magnesium to milled magnesium and the alloy ($p<0.001$). The difference between milled magnesium and the alloy is less extreme ($p<0.01$). Within each sample's supernatant treated wells there are no significant differences, nor when comparing them to the respective live controls.

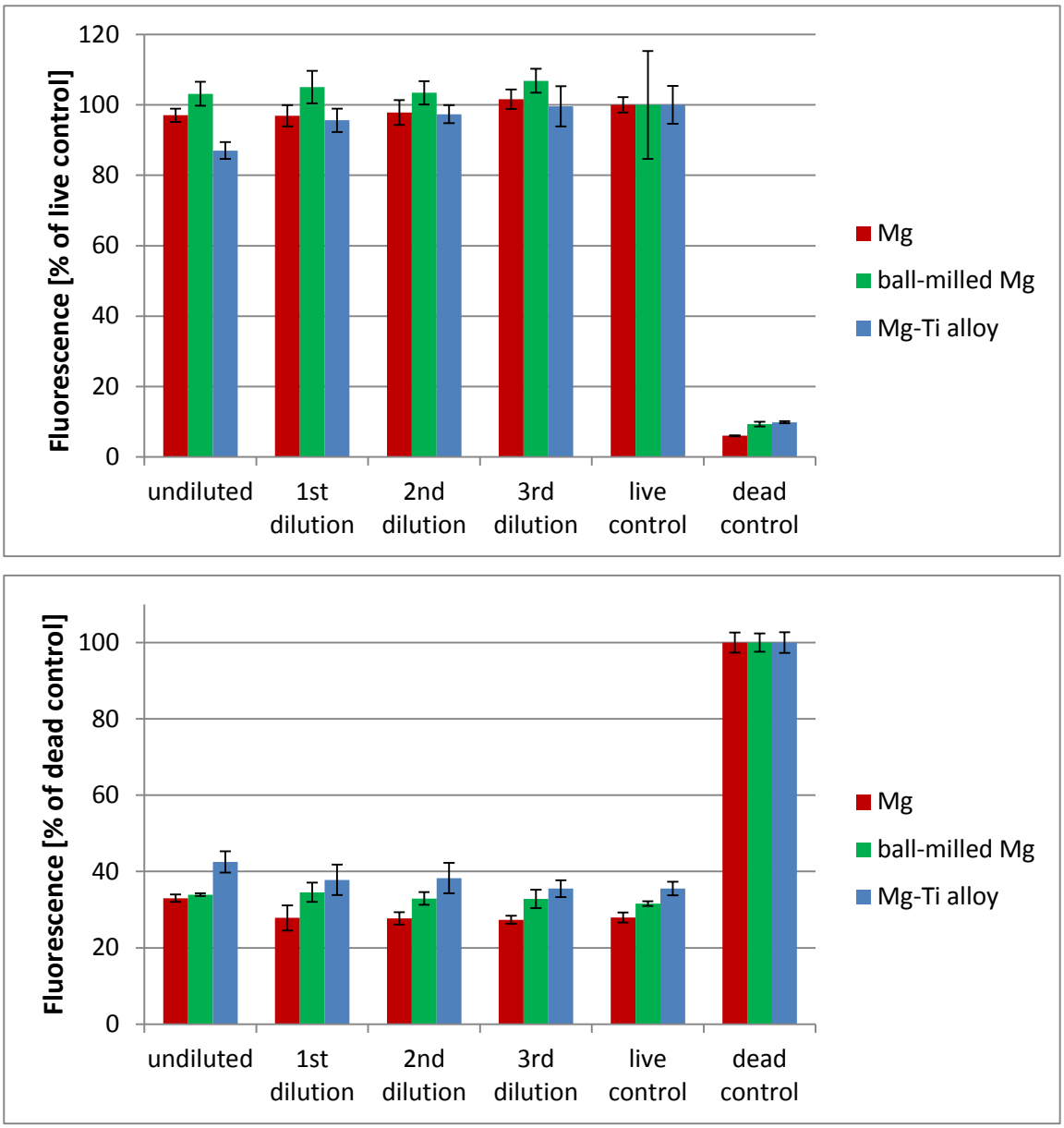

Figure 73: Result of the 24 h supernatant cytotoxicity test, living cells stained with calcein AM (top) and dead cells stained with EthD-1 (bottom).

Although the intensity from stained dead cells is the highest among all samples at all dilutions for the alloy with both time points and the differences compared to the pure magnesium samples are significant according to ANOVA, it should be noted that there is no significant difference between the supernatant containing wells and the live control. This means that the amount of dead cells when exposed to supernatant is similar to that obtained by culturing the cells without the influence of supernatant. It can therefore be regarded as background.

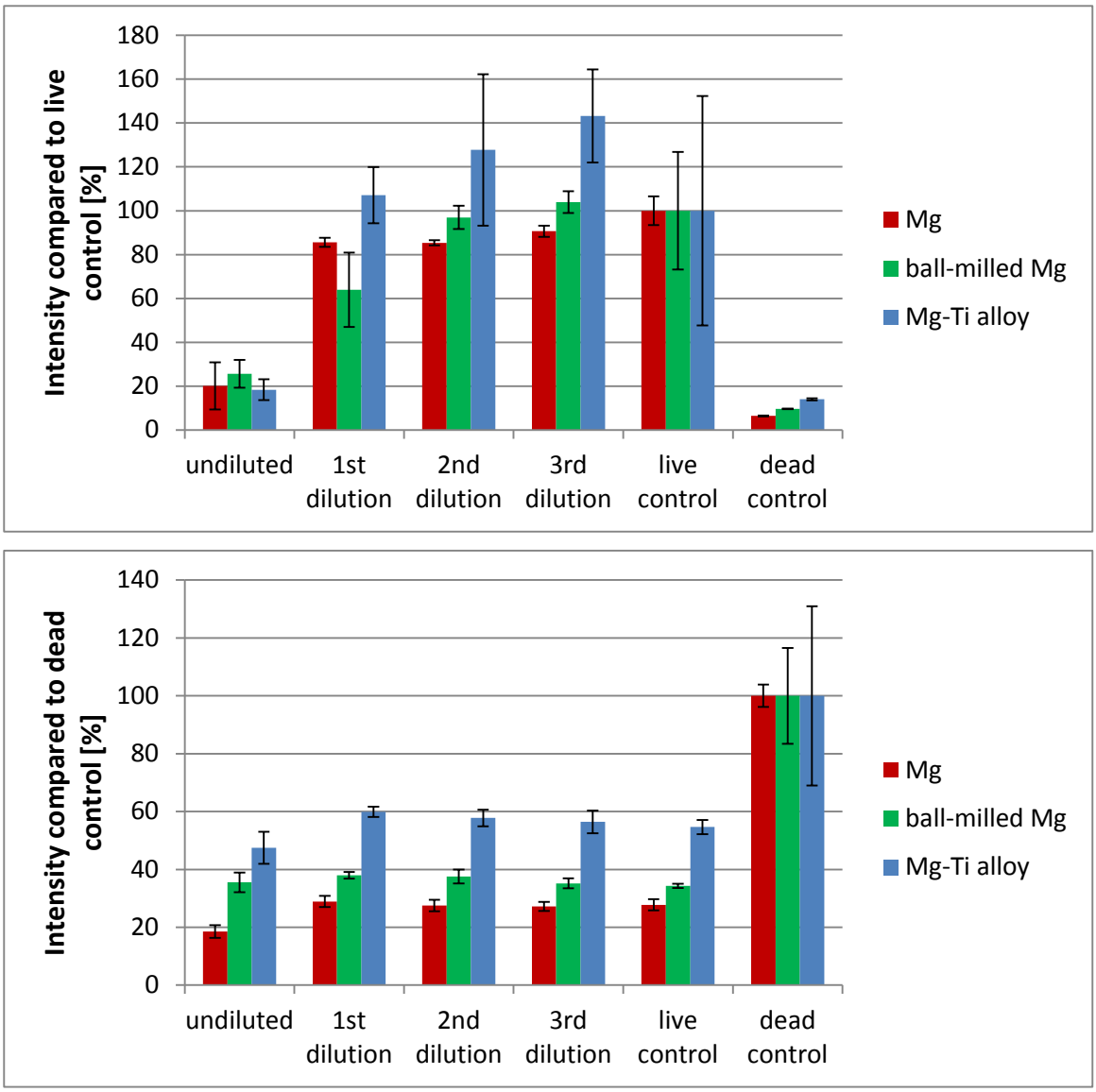

Figure 74: 1 week supernatant results, living cells stained with calcein AM (top) and dead cells stained with EthD-1 (bottom).

The one week supernatants are clearly extremes that are unlikely to occur in the body where body fluids will ensure at least some removal of ions and mediation of pH changes at the implantation site. When an implant is placed into the body, this results in a wound site. Plenty of blood flushes by the implant, which can reduce the pH and lower the ion concentration that rises due to corrosion of the implant material. Once the wound is healed, the implant is surrounded by newly grown tissue that also contains blood vessels[8]. The steady supply and exchange of nutrients and transport of waste products can also take excessive magnesium and other ions with it, bringing the implant site closer to a physiologically normal condition. The

buffers in body fluids and the flow of the body fluids past the implantation site can neutralize the increasing pH of corroding surfaces.[20]

It was found that a magnesium ion concentration of 96 - 153 mg/L promotes cell proliferation[103]. The observed growth of osteoblast cells was faster than the control grown in just medium[103]. Magnesium ion concentrations of 505-374 mg/L showed a decrease to 28-73% in viability in comparison to the control[103]. Comparing these numbers to the 24 h crystal violet stained experiments shows a similar result for the undiluted supernatants: with magnesium ion concentrations of over 440 mg/L the staining fluorescence is greatly reduced, indicating that there is less metabolic activity of the cells. However, it would then be expected that from the second dilution on the cells should thrive better than the untreated control, which is not the case. Only at the fourth dilution the fluorescence of the supernatant-treated cells is higher that of the control. Stronger fluorescence means more cells or more metabolic activity of the existing cells. Both indicate a higher biological activity of the cells. The differences in numbers observed here compared to the report in the literature[103] could be due to a different kind of cells used for the experiments, but the trend is the same: a slightly increased magnesium ion concentration boosts the cells' metabolic activity. In the live/dead stained 24 h experiment all cells treated with supernatants seemed to thrive, despite the high magnesium ion concentration. A link to the magnesium concentration in this case could explain the slightly lower fluorescence for the alloy supernatant as the highest magnesium ion concentrations were found in the alloy supernatants. In the 1 week live/dead stained experiments the intensity of the live stain is decreased significantly for the undiluted supernatants, which is in accordance with the dose-dependent viability. In this case the cell viability as expressed by stain intensity recovers by reducing the amount of ions in half in the first dilution for all three samples, although the alloy's magnesium ion concentration in that case should still be well above 700 mg/L, which is expected to decrease the viability. Despite the high ion concentration the cells with the alloy supernatant reach over 100% intensity in the first dilution. Pichler et al. linked reduced viability to an increase in pH instead of high ion concentrations[19]. In this study, however, there is a stronger link between cell viability indicated by fluorescence and ion concentration rather than increased pH. If the pH was mainly responsible for reduced cell activity, the undiluted supernatant of the unmilled magnesium sample incubated for 24 h should show the lowest cell activity through fluorescence, even lower than the supernatants of all samples incubated for one week, but that is not the case.

Conclusion

Judging from the cytotoxicity results presented here, in supernatant form Mg-Ti alloy containing 20% of titanium is no more cytotoxic than pure magnesium to pre-osteoblastic mouse cells. Detecting titanium in the supernatants suggests that against common perceptions titanium may not stay behind forming a porous network when the magnesium atoms in the alloy dissolve during corrosion. Mg-Ti alloys might indeed truly biodegradable. Granted, it should be investigated what the local and systemic effect of titanium ions or particles released from the material into surrounding tissues and the body would be, but this is beyond the scope of this work.

Influence of the incorporation of pure magnesium and alloy particles on the degradation of PLGA

Introduction

Using Mg and Mg-Ti particles as reinforcement for Poly(D, L-lactide-co-glycolide) (PLGA) was explored as an alternative to bulk applications. This project is motivated by the shortcomings of PLGA, which is already used as a biodegradable material, for example, for drug release. When degrading in the body, PLGA decreases the pH in its vicinity, which is harmful to the surrounding cells exposed to the acidic degradation by-products[117]. By incorporating magnesium or Mg-Ti alloy into PLGA it is hoped to stabilize the pH and thus make the material more biocompatible. Furthermore, the degradation characteristics can be altered by adding other components to PLGA. Lastly, PLGA has low strength, which is unsuitable for load bearing applications. By incorporating metallic particles of higher strength the mechanical properties of PLGA-metal particle composite can be improved for wider range of biomedical applications.

In the degradation studies the effects of magnesium being present in the solution vs. being incorporated into the polymer were separated and the effect of a rising pH of the solution due to magnesium corrosion alone without the presence of magnesium ions was mimicked by initially starting the test with an elevated pH.

Experimental details

Sample preparation

PLGA with a D, L lactide:glycolide ratio of 50:50 and polycarboxylated end groups from DURECT Corp. (USA) was used for all samples. This version was chosen because it's known to be the fastest degrading variety to keep experimental times short. Mg-Ti alloy with a titanium content of 20 at.-% was fabricated by high-energy ball milling for 25 h in a SPEX mixer/mill. Stainless steel vials were filled with the precursor powder (magnesium 99.8%, titanium 99.5 % (metals basis), both -325 mesh, AlfaAesar) in the desired composition and sealed inside an argon filled glove box to avoid oxygen contamination. Details can be found in previous chapters.

Samples were fabricated by heating PLGA chunks up in a teflon petri dish, adding the enforcing component for composites, and mixing thoroughly to fuse the PLGA particles together and obtain a uniform sample. For the composites either pure magnesium (99.8%,-325 mesh, AlfaAesar) or Mg-20 at.-% Ti alloy were added in an amount equivalent to 20 wt.- of the PLGA matrix. This is equivalent to 13 V-% magnesium and 11 V-% alloy. The resulting mixture was pressed into a metal die with ¼" diameter at 70°C with a pressure of 1 t (resulting stress = 309.65 MPa) for 10 min. Oil was used as a lubricant to ease removal of the samples from the dies. Any oil residues were removed by briefly cleaning the samples with ethanol on a piece of KimWipe.

Degradation studies

To distinguish the effects of raised pH and increased Mg ion concentration in the solution on the degradation behavior of PLGA, pure PLGA samples were tested in solution with raised pH (pH=9) and with the same amount of magnesium as in the composites added to the solution. This was to find out whether magnesium has to be inside the polymer to alter the degradation behavior. All sample/test solution combinations are listed in Table 1.

Samples were incubated in 20 mL Hanks' Solution(composition in appendix) mixed with de-ionized water filtered through a Millipore Milli-Q (resistivity = 18 MΩ/cm) at 37°C on shaker tables to keep the test solution in motion and thus reduce pH or concentration gradients. Samples were taken out and their weight and the pH of the solution were measured after 3, 7, and 14 days. For the 2 week degradation study the test solution was replaced after 1 week. Before weighing the samples were rinsed with distilled water and ethanol and lyophilized for two days. The experiments were carried out in triplicates.

Table 6: Sample matrix.

Pure PLGA	Pure PLGA	Pure PLGA + external Mg	PLGA-Mg composite	PLGA-alloy composite
pH = 7.4	pH = 9	pH = 7.4	pH = 7.4	pH = 7.4

Measuring mechanical properties

Compression tests were carried out on the pillar-shaped PLGA samples (pure and composites) on an MTS 810 Material Test System with a 1,000 kN load cell. Crosshead speed was 0.1 mm/s.

Freshly fabricated and corroded samples were tested to evaluate the change of mechanical properties over time. Three samples were tested for each composition. Young's modulus was calculated from the resulting stress-strain curve.

Gel Permeation Chromatography (GPC)

Fresh samples as well as samples after each degradation time point were tested. Two samples of each composition/treatment were selected. For the measurement a small piece of each sample was dissolved in tetrahydrofuran (THF) with butylated hydroxytoluene (BHT) at a concentration of 5 - 10 mg/mL. The solution was filtered with a 0.45 µm filter to remove any remaining solid pieces.

The polymeric chain lengths of the samples were measured with a Shimadzu Prominence LC-20 AB HPLC system with a Waters 2410 refractive index detector attached. 300 x 7.5 mm PLgel 3 µm mixed-E column (PolymerLaboratories) and 300 x 7.8 mm Waters Styragel HR-1 and HR-2 columns connected in series were used for separation. Polystyrene standards (PolymerLaboratories) in the molecular range of 500 - 20,000 Da with tetrahydrofuran as eluent served for the linear range of calibration for molecular weight determination.

Pycnometry

The volumes of magnesium powders and alloy particles were measured in a micromeritics AccuPyc 1330 with ultra high purity helium (Scott Gross Co, Lexington KY). 10 cm^3 filtered sample cups were used. Prior to pycnometry the samples' weight was measured inside the sample cups so that the density of the materials can be calculated. Three samples each were measured.

Results and Discussion

The test solution without any samples will slowly increase its pH, so it was measured separately to obtain a pH change baseline (Figure 75). Pure PLGA first increases the solution's pH, but it drops in the long run. Even when started at a high pH of 9 the pH became increasingly acidic over the course of the experiment. In both the samples with external and incorporated Mg the pH initially rose to very high values and then dropped. This rise in pH is likely to be detrimental to cells as well as the large acidic drop. The PLGA/Mg-Ti composite made the pH of the test

solution rise over time as well, but the increase was moderate and the overall change was the smallest of all tested samples. It also remained at pH levels that could very well be tolerated by e.g., bone cells. The slow corrosion rate of Mg-Ti alloy has a positive effect on the pH balance of degrading PLGA and effectively cancels out the acidity of the polymer degradation products. This finding demonstrates that Mg-Ti alloy particles could be used to regulate the pH of degrading PLGA.

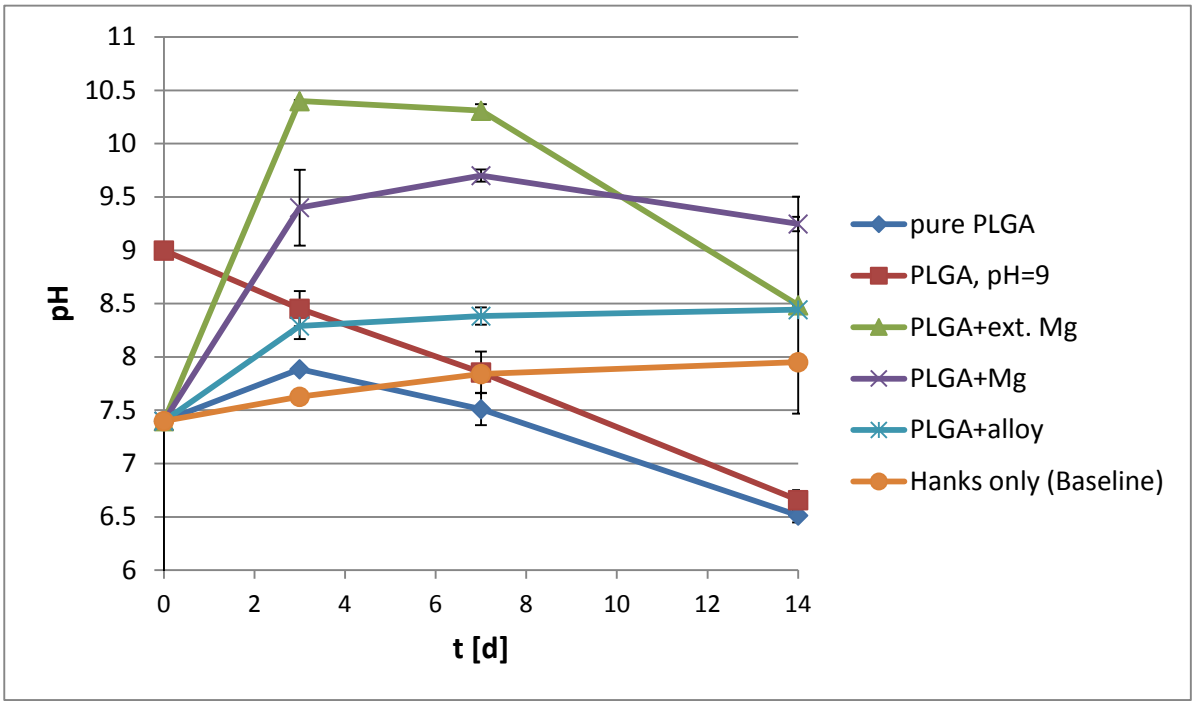

Figure 75: pH change of the test solution with composites and pure PLGA samples within two weeks in Hanks' Solution. The pH change of Hanks' Solution without any samples is presented to serve as a baseline.

It was found that the weight loss was also altered by incorporating metallic particles to the polymer (Figure 76). The biggest weight loss was observed for PLGA/Mg composites, most likely due to the rapid corrosion of magnesium particles inside the matrix. Pure PLGA samples in solutions with high pH values, i.e., pH = 9 or with Mg in the solution showed weight gain, which is due to the deposition of salts from the test solution onto the sample surface. The solubility of the salts in the fluid is pH-dependent and it is well-known that precipitation occurs at elevated pH. After an initial weight gain, pure PLGA keeps loosing mass. The PLGA/Mg-Ti composite alternates between mass gain and mass loss. These variations may be due to experimental

inaccuracies. Overall, the PLGA/alloy composites maintain their weight well over the course of the experiment.

During the degradation PLGA the pH of the test solution dropped continuously over the test period of 30 days in a study by Yoo et al. [116]. This trend fits well with the observation here that the pH of the test solutions drop over time when PLGA degrades in them. In the case of magnesium powder mixed into the solution the pH initially rises, which is expected due to the magnesium corrosion in the solution. However, even the pH of PLGA tested in regular Hanks' solution with a starting pH of 7.4 initially increased slightly. In contrast to Yoo´s experiments[116] Wu et al. observed a steady increase in pH when degrading their pure PLGA baseline sample in Hanks´ Solution[122].

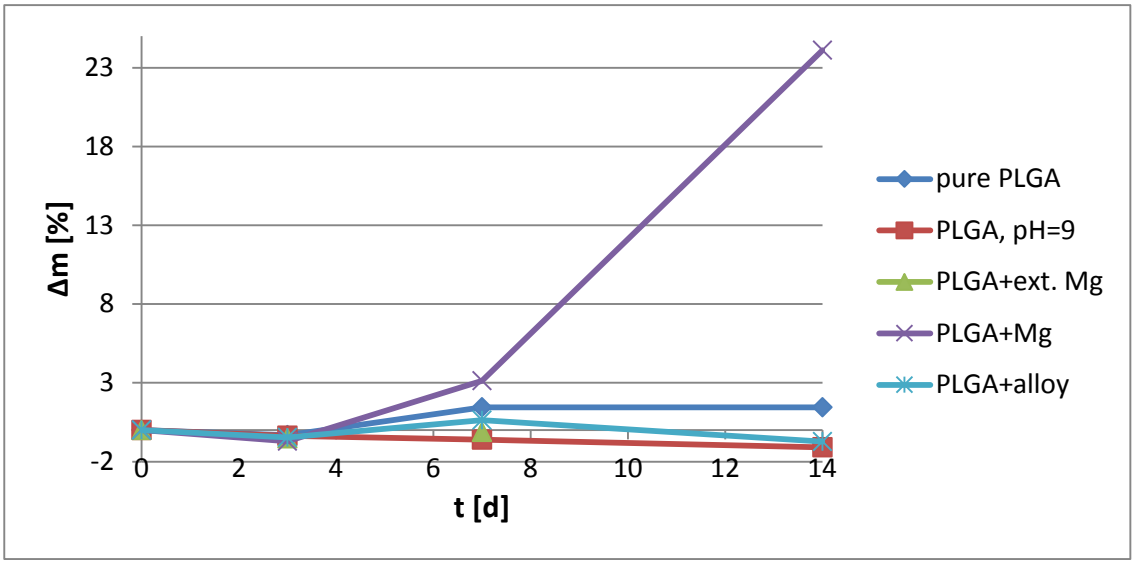

Figure 76: Weight change of samples during degradation in Hanks' Solution. Negative values indicate weight gain.

All samples start out with similar molecular weights (Figure 77). As immersion time increases the molecular weight decreases. Most samples show a steeper slope between 3 and 7 days, but the PLGA/Mg samples' chain length decreases almost linearly. At the same time the PLGA/Mg samples reach the highest pH in their test solutions. In contrast, the pure PLGA sample with magnesium mixed into the test solution has the lowest molecular weight after one week, although its test solution pH was even higher than that of the PLGA/Mg sample. The molecular weight of the PLGA/alloy composites is slightly higher than that of pure PLGA at all time points.

The curves for pH=9 and external magnesium solution differ hardly at all. To keep the molecular weight the highest, incorporating magnesium into the polymer works best. However, this brings about very large pH changes. Although not quite as effective as magnesium in maintaining the molecular weight, alloy composites would still be a good choice considering their pH change profile.

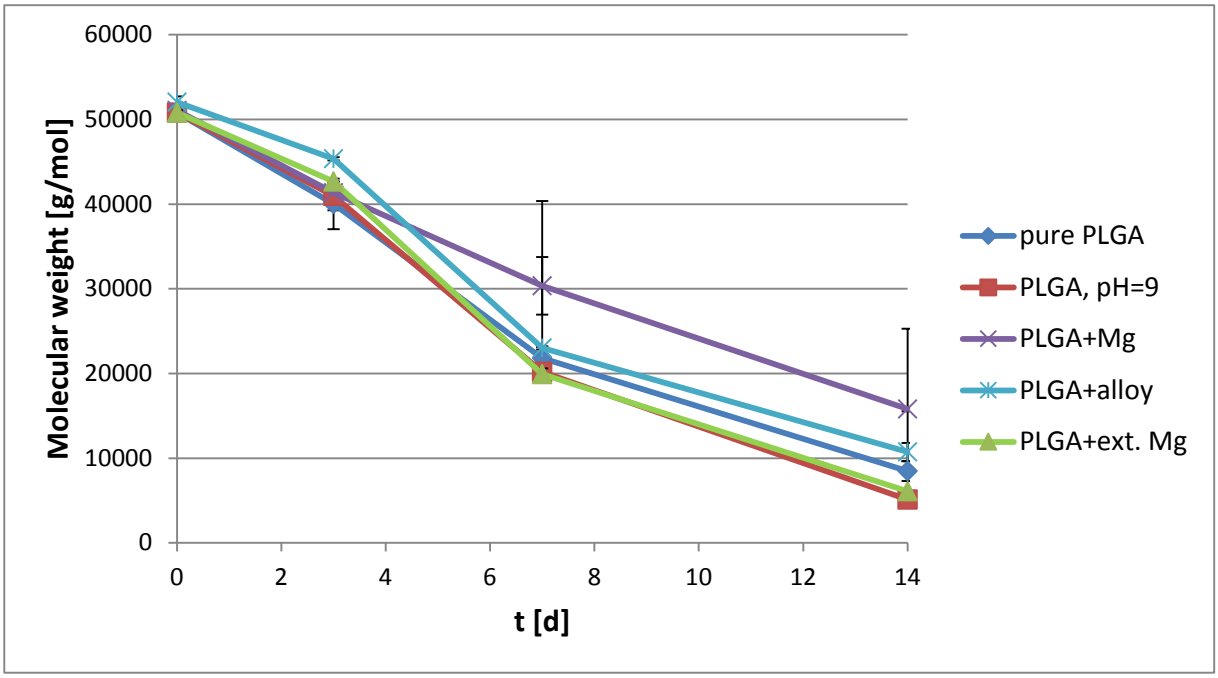

Figure 77: Change in molecular weight during the degradation study.

As expected, the composites' Young's modulus is higher than that of pure PLGA (Figure 78). The elastic modulus when incorporating alloy particles is higher than that with magnesium in undegraded samples as well as at any time during the degradation experiment. The Young's modulus of both composites drops sharply after just 3 days of degradation. At this time point the PLGA samples degraded in solution with a pH of 9 have the highest moduli. The samples in test solution with pH=9 continue their slope to day 7, while for the other samples the slope between day 3 and 7 is less steep than in the first part. It comes as a big surprise to see the composites' elastic modulus drop so sharply after they seemed to be more resistant to degradation judging from the molecular weight measurements.

Yoo et al. observed that PLGA degraded slower in Phosphate Buffered Saline (PBS) with higher pH than in an acidic environment[116]. At the endpoint of the experiments presented here that is also true for almost all samples, except for the PLGA sample degraded in the solution with

magnesium powder added to it. This sample's pH was always higher than that of the alloy test solution until the last time point, yet the final molecular weight is lower that of most samples, including those who corroded under more acidic conditions. It has been observed that PLGA degraded faster when it had magnesium incorporated and a larger amount of added magnesium alloy lead to higher corrosion rates[122], but there is no report through which mechanism it accelerated. This is opposite to what was found here: When magnesium or alloy is incorporated into PLGA it retains a higher molecular weight compared to pure PLGA.

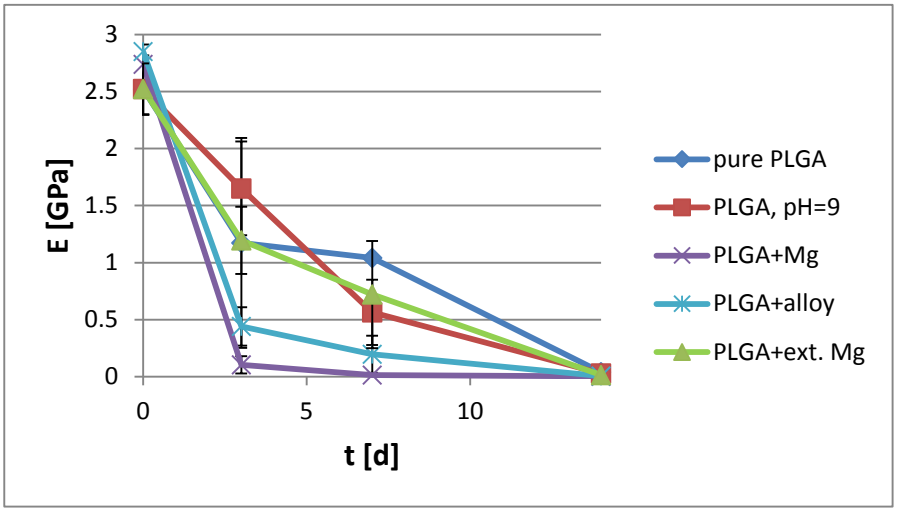

Figure 78: Change in Young's modulus with increasing degradation time.

No big difference in the stress-strain curves can be seen when comparing undegraded pure PLGA and composites with both magnesium and alloy (Figure 79). Incorporating metal into the polymer thus does not improve the ultimate compression strength. The PLGA reinforced with AZ31 alloy fibers fabricated by Wu et al. had an increased ultimate tensile strength and elongation compared to pure PLGA[122]. That no difference in strength or elongation was detected here could be due to the shape of the metallic particles or because the samples were loaded in compressive, not tensile mode.

The as-fabricated samples (Figure 80) have a well-defined geometry and smooth outer surfaces. The pure PLGA sample is transparent. The composites have a metallic sheen from the embedded particles. From optical inspection the particles are uniformly distributed throughout the sample.

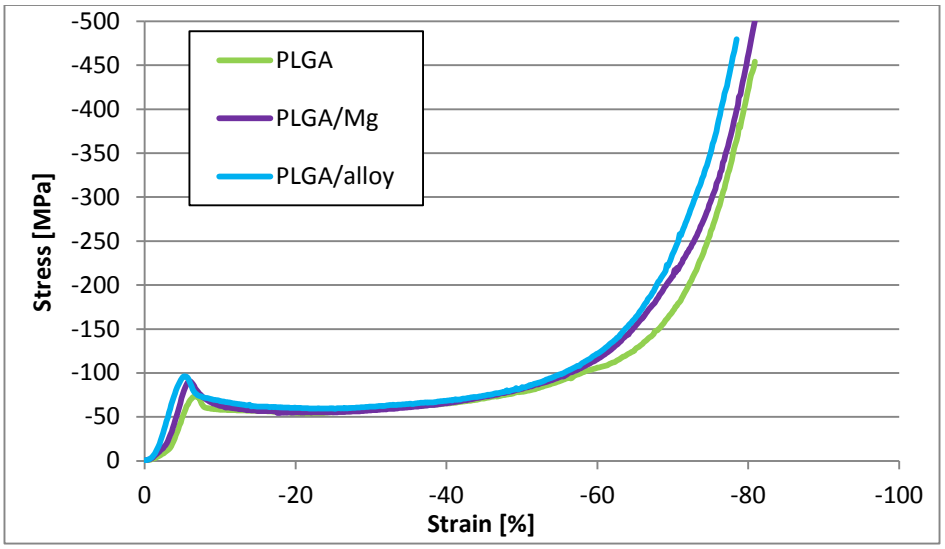

Figure 79: Stress-strain curves for pure PLGA samples compared with PLGA-Mg composites.

Figure 80: Samples of all compositions as fabricated.

After three days in Hanks' Solution the PLGA sample's surface becomes rough and it becomes translucent (Figure 81). The PLGA sample immersed into test solution with magnesium powder mixed into it looks similar, but additionally has magnesium particles pressed into its surface in some spots. The sample degraded at pH = 9 has its surface covered in a white precipitation layer. The salts from the test solution probably precipitated due to the high pH. The magnesium inside the PLGA/Mg composite has visible corroded and the sample turned a lighter shade of grey with white spots mixed in. The sample bloated visibly and small pores can be seen to have formed on the outer surfaces. The alloy composite also expanded and is a little lighter in color than the as-fabricated sample, but no pores can be seen with the naked eye.

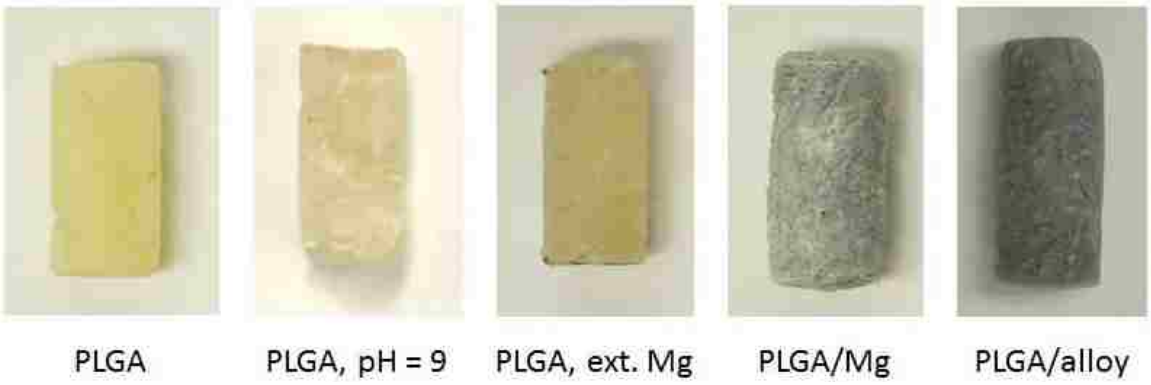

Figure 81: Samples after 3 days of degradation in Hanks' Solution.

After one week in the test solution all three pure PLGA samples are coated with a thick white layer on the majority of the sample surfaces (Figure 82). The samples also deformed slightly. The magnesium composite expanded even further and large cracks are visible in addition to the pores. The composite with alloy particles has become lighter in color than at the three day mark and also expanded more. Small pores can be detected on the surface at this point, but there are fewer than on the PLGA/Mg samples on day three.

Figure 82: Samples after one week of degradation.

At the end of the experiment the PLGA samples are obviously deformed (Figure 83). They became so soft during the long immersion in the test solution that they had lost their original shape and molded into the tip shape of the centrifuge tubes they were kept in during degradation studies. The PLGA samples stuck to the centrifuge tube and had to be scraped off. They also felt very sticky when touched. The white coating on the PLGA samples is missing in some areas on the samples, either from attaching to the centrifuge tube they degraded in or from extreme deformation that flaked off some of the precipitation. The composites expanded further and are now also completely covered in a white surface layer. The magnesium

composite has pores in many different sizes. The alloy composite now also has larger pores on the surface. The pore size after two weeks of immersion in the test solution is roughly comparable to those on the magnesium composite after one week. However, the alloy does not show the large cracks that accompany the pores in the magnesium composites after one week.

Figure 83: Samples after two weeks of degradation in Hanks' Solution.

During degradation the sample geometries change. The PLGA/Mg composites and the PLGA samples in the solution with magnesium powder mixed in increase their length almost linearly throughout the whole degradation process. All samples increase in length within the first week of immersion, but the PLGA sample in the test solution with pH = 9 decreases in length after that. The pure PLGA sample in regular Hanks' Solution hardly changes its length between one and two weeks of immersion. The alloy composite increases its length close to linearly in the first week, then the length jumps up faster in the last week of the test. After two weeks, the composites have increased their length significantly and to a similar extend. The smallest change in length is experienced by the PLGA sample tested in the high pH solution, probably due to severe deformation during the second half of the test, as indicated by the sample photo after the completed test (Figure 83). The length change of the PLGA sample tested in solution with magnesium powder falls in between that of the composites and pure PLGA.

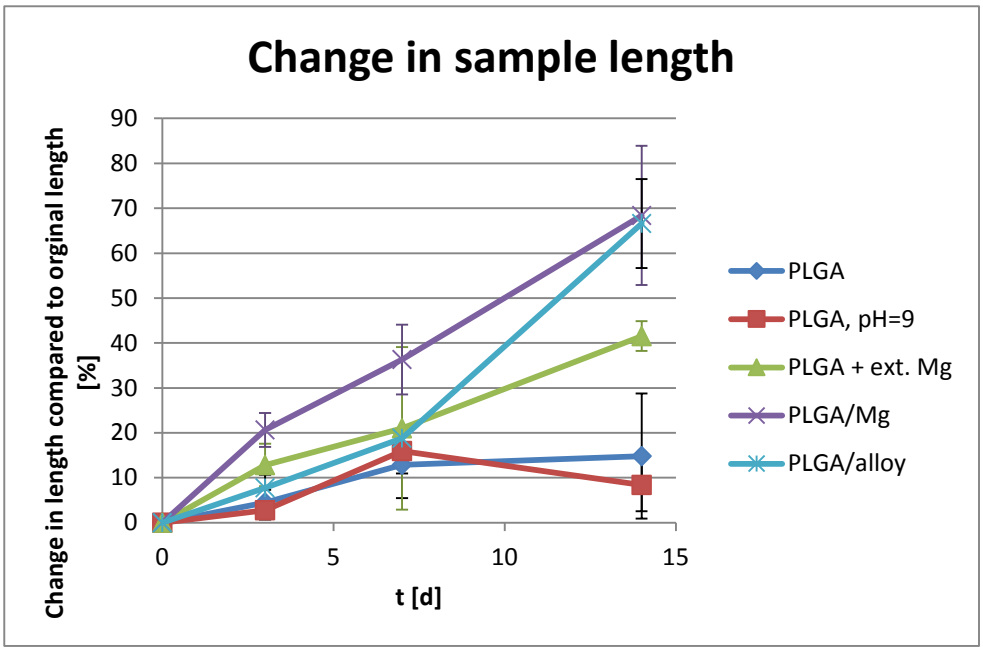

Figure 84: Change in sample length over degradation time.

The samples also all increase their diameters during degradation (Figure 85). Similar to the change in length, the biggest changes are experienced by the magnesium composite, followed by the alloy composite. The diameter changes very little for the pure PLGA samples within the first week of immersion and slightly more for the alloy composite. The diameter changes of the pure PLGA samples are very similar at all time points. The diameter of the alloy composites changes rapidly in the second week of the test. The change in diameter of the magnesium composite is very different from that of all other samples: The initial change within three days is very large, after that the slope of the changes decreases slightly.

The composite samples swelled up during degradation and increased in volume by forming pores. Swelling was slower in composites with the alloy compared to those with magnesium. This effect can explain the large drop in Young's modulus observed for the composites. Another indication that the composites don't get weaker per se is the high molecular weight they retain compared to PLGA samples while the elastic modulus drops drastically. The Young's modulus in this case may not be an accurate measure of the degradation rate as it is influenced by the swelling of the composites that does not appear to the same extent in the pure PLGA samples and occurs at different rates in composites with magnesium and alloy particles.

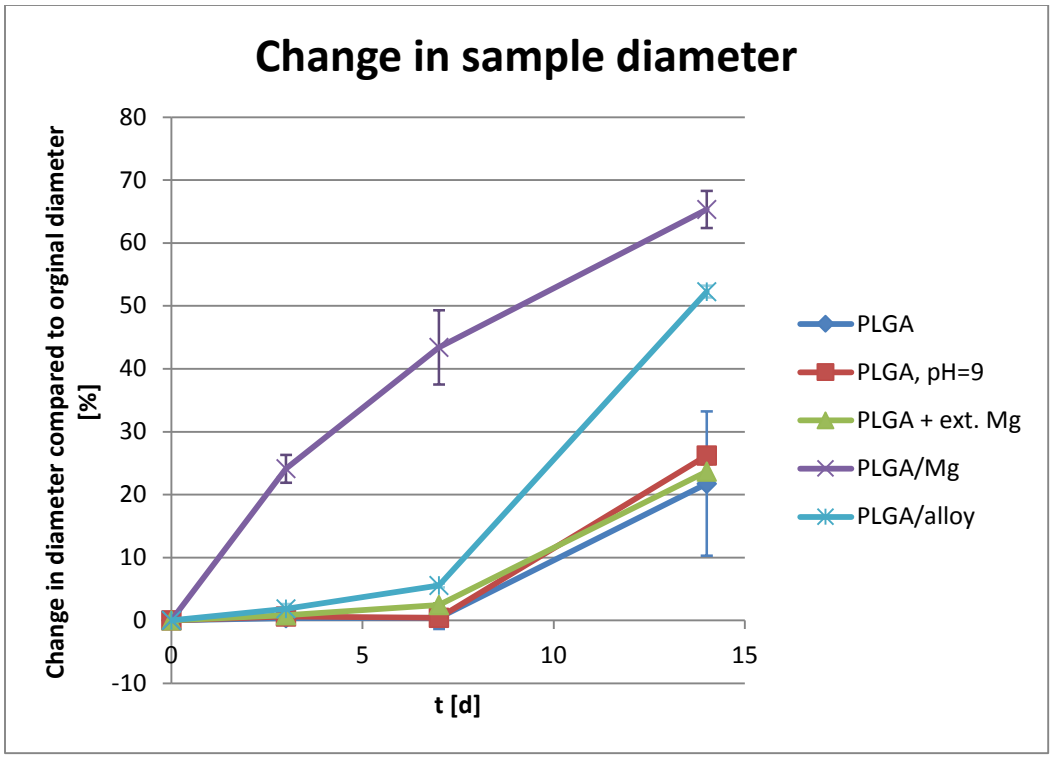

Figure 85: Diameter changes with degradation time.

Increasing the Mg ion concentration in the test solution had similar effects on the degradation rate as starting out with a high pH, so it can be assumed that the effect of magnesium in the solution is brought about by a rising pH and not the presence of magnesium ions. In contrast, there is a big difference in the degradation behavior between magnesium composites and pure PLGA samples tested in solution with magnesium powder. The magnesium composites lost significantly more weight, but retained their molecular weight better than PLGA samples degraded in the presence of magnesium ions. The swelling behavior also differed markedly when the magnesium is incorporated into the polymer. Thus, these effects are not purely due to the presence of magnesium ions but only elicited when forming a composite with the PLGA. It is hypothesized that the pores form at sites where the metallic particles corroded. Since the pores are much larger than individual particles it is not just a matter of particles leaving behind holes after having been dissolved. It was observed that the samples start to float in the test solution after swelling up, i.e., after forming pores. This indicates that the samples have decreased their density, which cannot be explained through the mass loss of polymer and metal. Instead, the pores may be caused by local accumulation of hydrogen bubbles formed during the degradation of the metals. The gas is trapped inside the porous structure, buoying the samples. As

degradation progresses, holes may combine together to form larger voids when the polymer in between them is degraded, thus growing bigger. This hypothesis is in accordance with the observation that the composites containing fast degrading magnesium show pores earlier and have bigger pores than composites containing the alloy, which corrodes more slowly and thus produces less hydrogen.

Estimation of Young's modulus from PLGA/alloy composite modulus

Although the Young's modulus of the alloy cannot be calculated from the Young's modulus of the composites, it does provide a hallmark for estimating the elastic modulus. The Voigt model is not suitable for a polymer/metal composite, as it assumes that the strain experienced by both components is the same. This is clearly not the case when deforming a soft polymeric matrix with comparatively stiff metallic particles embedded into it. The Reuss model (Eq. 2), assuming that the stress experienced by both components is the same, works much better for this case. Unfortunately, the Reuss model is very sensitive to the data put into it, so backcalculating the modulus of the alloy from the measured composite modulus results in huge errors and even negative results, which are clearly not reasonable. It must therefore be assumed that it's not possible to obtain the alloy's modulus in a useful range of error from either of those two models from the composite modulus. However, with the Reuss model an assumed Young's modulus can be validated.

$E = \Sigma E_i V_i$ Voigt average (12)

$1/E = \Sigma V_i/E_i$ Reuss average (13)

With:

E: Young's modulus of the composite

E_i: Young's modulus of the individual phases in the composite

V_i: volume fractions of the individual phases in the composite

To estimate the modulus of the alloy the Voigt model (Eq. 1) works best as it can be seen as a mixture of two metals that would experience the same strain when deformed side by side. The alloy contains 20 at.-% titanium, which is equivalent to 33 wt.-%. With the theoretical densities of magnesium (1.74 g/cm³) and titanium (4.5 g/cm³) the volume fractions of magnesium (85.8

vol.-%) and titanium (14.2 vol.-%) can be determined. Taking into account the theoretical elastic moduli of magnesium (44 GPa) and titanium (116 GPa), the Voigt model predicts a Young's modulus of 54 GPa for the alloy as a mixture of both magnesium and titanium.

Using this theoretical Young's modulus of the alloy and the modulus of PLGA determined earlier, the theoretical modulus of the PLGA/alloy composite can be calculated. The density of PLGA is known from the dimensions and weights of the undegraded pure PLGA samples. The density of $Mg_{80}Ti_{20}$ alloy was determined by pycnometry. As the weight of the PLGA and alloy used to make a composite are known as well, the predicted Young's modulus of the composite with the theoretical modulus of the alloy according to the Reuss model is 2.81 GPa, which is fairly close to the experimental average of 2.85 GPa. It can therefore be assumed that 54 GPa is a reasonable estimate for the alloy modulus.

Conclusion

PLGA samples degraded faster in test solution with higher initial pH and magnesium powder mixed into the test solution, both probably catalyzed by the high pH of the test solution. Incorporating metal particles into PLGA slowed down the degradation process judging from the changes in molecular weight. However, in other regards there is a big difference between the magnesium and alloy composites. When alloy particles are incorporated into PLGA the pH is much better maintained within a physiologically tolerable range avoiding damage to the surrounding tissue through acidification in its vicinity. Incorporating Mg-Ti particles into PLGA maintains the overall weight better than in the case of incorporating pure magnesium or pure PLGA. The swelling of the composites during degradation could open up new strategies for drug delivery profiles. Comparing the swelling behavior of the two composites it depends on the corrosion rate of the material. By incorporating metals with different corrosion rates into PLGA the swelling can be controlled to match different application requirements. The pore formation offers the potential for tissue ingrowth.

4. CONCLUSION & OUTLOOK

Mg-Ti alloys show improved corrosion resistance compared to pure magnesium in simulated physiological conditions and the elicited cytotoxicity was not higher than that of pure magnesium. It was clearly demonstrated that the improved corrosion resistance is a result of alloying magnesium with titanium, not due to the processing treatment or or the presence of Ti alone. The decreased cytotoxicity is likely coupled to the slower corrosion rate. By forming composites of Mg/PLGA or Mg-Ti/PLGA, the degradation rate of commonly used PLGA can be tuned for implant and drug delivery applications. Based on these findings Mg-Ti alloys are promising biodegradable materials for several biomedical applications.

Thus, Mg-Ti alloys should be further explored considering that many properties of Mg-Ti alloys have not been thoroughly investigated yet (e.g., mechanical properties). Working with Mg-Ti alloys is challenging due to their metastable nature, but as new, alternative techniques become available and are further developed the task consolidating them to full density will become feasible.

Consolidation by SPS should be further explored to check whether full density can be achieved with a modified set of parameters. As there are limitations to SPS for scaling up alternative non-equilibrium consolidation methods are worth exploring in parallel. When high-quality consolidated samples can be fabricated reliably in sufficient quantity weight loss measurements in vivo or in vitro should be conducted to determine the exact corrosion rate of Mg-Ti alloys with different titanium contents. Electrochemical studies on alloys with varying compositions will help better understand the effect of alloying and the residual titanium particles within the alloy matrix. Consolidated samples will further be useful to determine the mechanical properties of the alloys in quasistatic and dynamic tests. The mutual influence of cyclic loading and corrosion is important to know to determine whether the material could hold up to the loads during fracture healing.

More detailed cell studies that go beyond gross cytotoxicity assessments are needed before eventually the material can be tested in vivo to find out how exactly the material behaves in the body and whether there are any harmful effects associated with the degradation in the body. By varying the metal particle content or alloy composition the properties of the PLGA composites

could be fine-tuned to be suitable for different applications. By incorporating actual drugs into the composites their release profile could be determined to check for possible applications.

APPENDIX

Hanks' Balanced Salt Solution

Hanks' Balanced Salt Solution (HBSS) is a simulated body fluid containing all the physiological inorganic salts at concentrations similar to those in the human body[77]. It does not mimic all available compositions in different implant sites, but is not implant site specific[77]. HBSS is the most commonly used test solution for in vitro magnesium corrosion tests, therefore making it easy to compare results across the literature[77]. It does not include proteins and is thus less complex than actual body fluids.

Table 7: Composition of HANKS' Balanced Salt Solution

Component	Concentration [g/L]
NaCl	8
KCl	0.4
$CaCl_2 \cdot 2\ H_2O$	0.1858
$NaHCO_3$	0.35
$C_6H_6O_6$(glucose)	1
$MgSO_4 \cdot 7\ H_2O$	0.2
KH_2PO_4	0.09
Na_2HPO_4	0.03

The constituents are dissolved in de-ionized water and the pH is adjusted to 7.4.

REFERENCES

1 John M. Flynn, Lael M. Luedtke, Theodore J. Ganley, Judy Dawson, Richard S. Davidson, John P. Dormans, Malcolm L. Ecker, John R. Gregg, B. David Horn, and Denis S. Drummond, *Comparison of Titanium Elastic Nails with Traction and a Spica Cast to Treat Femoral Fractures in Children*. (2004).

2 M. Sherif El-Eskandarany, *MECHANICAL ALLOYING FOR FABRICATION OF ADVANCED ENGINEERING MATERIALS*. (NOYES PUBLICATIONS, WILLIAM ANDREW PUBLISHING, Norwich, New York, U.S.A., 2001).

3 R. C. Zeng, W. Dietzel, F. Witte, N. Hort, and C. Blawert, "Progress and challenge for magnesium alloys as biomaterials," Adv. Eng. Mater. **10** (8), B3-B14 (2008).

4 V. P. Mantripragada, B. Lecka-Czernik, N. A. Ebraheim, and A. C. Jayasuriya, "An overview of recent advances in designing orthopedic and craniofacial implants," J. Biomed. Mater. Res. Part A **101** (11), 3349-3364 (2013).

5 A. F. Mavrogenis, R. Dimitriou, J. Parvizi, and G. C. Babis, "Biology of implant osseointegration," J. Musculoskelet. Neuronal Interact. **9** (2), 61-71 (2009).

6 Y. F. Ding, C. E. Wen, P. Hodgson, and Y. C. Li, "Effects of alloying elements on the corrosion behavior and biocompatibility of biodegradable magnesium alloys: a review," J. Mat. Chem. B **2** (14), 1912-1933 (2014).

7 M. P. Staiger, A. M. Pietak, J. Huadmai, and G. Dias, "Magnesium and its alloys as orthopedic biomaterials: A review," Biomaterials **27** (9), 1728-1734 (2006).

8 J. Park and R.S. Lakes, "Biomaterials – An Introduction", (Springer, 2007).

9 G. L. Song, "Control of biodegradation of biocompatable magnesium alloys," Corrosion Science **49** (4), 1696-1701 (2007).

10 B. Zberg, P. J. Uggowitzer, and J. F. Loffler, "MgZnCa glasses without clinically observable hydrogen evolution for biodegradable implants," Nature Materials **8** (11), 887-891 (2009).

11 P. Erne, M. Schier, and T. J. Resink, "The road to bioabsorbable stents: Reaching clinical reality?," Cardiovasc. Interv. Radiol. **29** (1), 11-16 (2006).

12 Larry L. Cunningham Richard H. Haug, M. Todd Brandt, "Plates, Screws, and Children: Their Relationship in Craniomaxillofacial Trauma," Journal of Long-Term Effects of Medical Implants **13** (4), 271-287 (2003).

13 F. Witte, H. Ulrich, M. Rudert, and E. Willbold, "Biodegradable magnesium scaffolds: Part I: Appropriate inflammatory response," J. Biomed. Mater. Res. Part A **81A** (3), 748-756 (2007).

14 D. Williams, "The Essential Materials Paradigms for Regenerative Medicine," Jom **63** (4), 51-55 (2011).

15 M. A. Woodruff, C. Lange, J. Reichert, A. Berner, F. L. Chen, P. Fratzl, J. T. Schantz, and D. W. Hutmacher, "Bone tissue engineering: from bench to bedside," Mater. Today **15** (10), 430-435 (2012).

16 A. K. Srivastava, C. T. Mehlman, E. J. Wall, and T. T. Do, "Elastic stable intramedullary nailing of tibial shaft fractures in children," J. Pediatr. Orthop. **28** (2), 152-158 (2008).

17 J. B. Hunter, "The titanium elastic nail," A O Dialogue, 8 (1999).

18 D. Furlan, Z. Pogorelic, M. Biocic, I. Juric, D. Budimir, J. Todoric, T. Susnjar, D. Todoric, J. Mestrovic, and K. P. Milunovic, "ELASTIC STABLE INTRAMEDULLARY NAILING FOR PEDIATRIC LONG BONE FRACTURES: EXPERIENCE WITH 175 FRACTURES," Scand. J. Surg. **100** (3), 208-215 (2011).

19 K. Pichler, T. Kraus, E. Martinelli, P. Sadoghi, G. Musumeci, P. J. Uggowitzer, and A. M. Weinberg, "Cellular reactions to biodegradable magnesium alloys on human growth plate chondrocytes and osteoblasts," Int. Orthop. **38** (4), 881-889 (2014).

20 Y. H. Yun, Z. Y. Dong, N. Lee, Y. J. Liu, D. C. Xue, X. F. Guo, J. Kuhlmann, A. Doepke, H. B. Halsall, W. Heineman, S. Sundaramurthy, M. J. Schulz, Z. Z. Yin, V. Shanov, D. Hurd, P. Nagy, W. F. Li, and C. Fox, "Revolutionizing biodegradable metals," Mater. Today **12** (10), 22-32 (2009).

21 F. Witte, T. Calliess, and H. Windhagen, "Biodegradable synthetic implant materials. Clinical applications and immunological aspects," Orthopade **37** (2), 125-130 (2008).

22 D. Tie, F. Feyerabend, W. D. Muller, R. Schade, K. Liefeith, K. U. Kainer, and R. Willumeit, "ANTIBACTERIAL BIODEGRADABLE Mg-Ag ALLOYS," Eur. Cells Mater. **25**, 284-298 (2013).

23 D. A. Puleo and A. Nanci, "Understanding and controlling the bone-implant interface," Biomaterials **20** (23-24), 2311-2321 (1999).

24 M. H. Grosjean, M. Zidoune, L. Roue, J. Huot, and R. Schulz, "Effect of ball milling on the corrosion resistance of magnesium in aqueous media," Electrochim. Acta **49** (15), 2461-2470 (2004).

25 G. Liang and R. Schulz, "Synthesis of Mg-Ti alloy by mechanical alloying," J. Mater. Sci. **38** (6), 1179-1184 (2003).

26 Q. M. Peng, K. Li, Z. S. Han, E. D. Wang, Z. G. Xu, R. P. Liu, and Y. J. Tian, "Degradable magnesium-based implant materials with anti-inflammatory activity," J. Biomed. Mater. Res. Part A **101A** (7), 1898-1906 (2013).

27 F. Rosalbino, S. De Negri, G. Scavino, and A. Saccone, "Microstructure and in vitro degradation performance of Mg-Zn-Mn alloys for biomedical application," J. Biomed. Mater. Res. Part A **101A** (3), 704-711 (2013).

28 M. V. Manuel and N. Hort, "Magnesium: An Essential Nutrient for a Good Biomaterial," Jom **63** (4), 99-99 (2011).

29 R. J. Elin, "MAGNESIUM - THE 5TH BUT FORGOTTEN ELECTROLYTE," American Journal of Clinical Pathology **102** (5), 616-622 (1994).

30 B. Homayun and A. Afshar, "Microstructure, mechanical properties, corrosion behavior and cytotoxicity of Mg-Zn-Al-Ca alloys as biodegradable materials," J. Alloy. Compd. **607**, 1-10 (2014).

31 A. L. Di Virgilio, M. Reigosa, and M. F. L. de Mele, "Biocompatibility of magnesium particles evaluated by in vitro cytotoxicity and genotoxicity assays," Journal of Biomedical Materials Research Part B-Applied Biomaterials **99B** (1), 111-119 (2011).

32 B. Predel and O. Madelung (ed.), *Landolt-Börnstein, Group IV Physical Chemistry - Phase Equilibria, Crystallographic and Thermodynamic Data of Binary Alloys, Volume 5 - Electronic Materials and Semiconductors*. (Springer, 1998).

33 J. G. Zheng, P. G. Partridge, J. W. Steeds, D. M. J. Wilkes, and C. M. WardClose, "Microstructure of vapour quenched Ti-29 wt% Mg alloy solid solution," J. Mater. Sci. **32** (12), 3089-3099 (1997).

34 D. M. J. Wilkes, P. S. Goodwin, C. M. WardClose, K. Bagnall, and J. Steeds, "Solid solution of Mg in Ti by mechanical alloying," Mater. Lett. **27** (1-2), 47-52 (1996).

35 K. Asano, H. Enoki, and E. Akiba, "Synthesis process of Mg-Ti BCC alloys by means of ball milling," J. Alloy. Compd. **486** (1-2), 115-123 (2009).

36 T. Haruna, D. Motoya, Y. Nakagawa, N. Yamashita, and T. Oishi, "Corrosion Resistance of Titanium-Magnesium Alloy in Weak Acid Solution Containing Fluoride Ions," Mater. Trans. **54** (2), 143-148 (2013).

37 Y.- T. Cheng, M. W. Verbrugge, M. P. Balogh, D. E. Rodak, and M. Lukitsch, US Patent No. 7,651,732 (January 26 2010).
38 C. M. A. Brett, L. Dias, B. Trindade, R. Fischer, and S. Mies, "Characterisation by EIS of ternary Mg alloys synthesised by mechanical alloying," Electrochim. Acta **51** (8-9), 1752-1760 (2006).
39 Z. Xu, G.-L. Song, and D. Haddad, "Corrosion Performance of Mg-Ti Alloys Synthesized By Magnetron Sputtering," Magnesium Technology 2011, 611-615 (2011).
40 K. Asano, H. Enoki, and E. Akiba, "Synthesis of HCP, FCC and BCC structure alloys in the Mg-Ti binary system by means of ball milling," J. Alloy. Compd. **480** (2), 558-563 (2009).
41 W. P. Kalisvaart and P. H. L. Notten, "Mechanical alloying and electrochemical hydrogen storage of Mg-based systems," J. Mater. Res. **23** (8), 2179-2187 (2008).
42 K. Maweja, M. Phasha, and N. van der Berg, "Microstructure and crystal structure of an equimolar Mg-Ti alloy processed by Simoloyer high-energy ball mill," Powder Technology **199** (3), 256-263 (2010).
43 P. Perez, G. Garces, and P. Adeva, "Influence of titanium volume fraction on the mechanical properties of Mg-Ti composites," Int. J. Mater. Res. **100** (3), 366-369 (2009).
44 Z. Esen, B. Dikici, O. Duygulu, and A. F. Dericioglu, "Titanium-magnesium based composites: Mechanical properties and in-vitro corrosion response in Ringer's solution," Mater. Sci. Eng. A-Struct. Mater. Prop. Microstruct. Process. **573**, 119-126 (2013).
45 Q. Shen, L. M. Zhang, H. Tan, and F. Q. Jing, "Preparation of Mg-Ti system alloy and FGM with density gradient by spark plasma sintering technique," J. Wuhan Univ. Technol.-Mat. Sci. Edit. **19** (1), 58-60 (2004).
46 I. J. T. Jensen, S. Diplas, and O. M. Lovvik, "Density functional calculations of Ti nanoclusters in the metastable Mg-Ti system," Phys. Rev. B **82** (17) (2010).
47 C. C. Koch (ed.), "Nanostructured Materials: Processing, Properties, and Applications", (William Andrew Publishing, 2007).
48 C. Suryanarayana, "Mechanical alloying and milling," Progress in Materials Science **46** (1-2), 1-184 (2001).
49 J. S. Benjamin, "DISPERSION STRENGTHENED SUPERALLOYS BY MECHANICAL ALLOYING," Metallurgical Transactions **1** (10), 2943-& (1970).
50 M. Zidoune, M. H. Grosjean, L. Roue, J. Huot, and R. Schulz, "Comparative study on the corrosion behavior of milled and unmilled magnesium by electrochemical impedance spectroscopy," Corrosion Science **46** (12), 3041-3055 (2004).
51 J. Huot, G. Liang, and R. Schulz, "Mechanically alloyed metal hydride systems," Appl. Phys. A-Mater. Sci. Process. **72** (2), 187-195 (2001).
52 C. S. Bonifacio, T. B. Holland, and K. van Benthem, "Evidence of surface cleaning during electric field assisted sintering," Scr. Mater. **69** (11-12), 769-772 (2013).
53 M. Ishiyama, presented at the Powder Metallurgy World Congress, Kyoto, Japan, 1993 (unpublished).
54 S. H. Risbud and Y. H. Han, "Preface and historical perspective on spark plasma sintering," Scr. Mater. **69** (2), 105-106 (2013).
55 Z. H. Zhang, Z. F. Liu, J. F. Lu, X. B. Shen, F. C. Wang, and Y. D. Wang, "The sintering mechanism in spark plasma sintering - Proof of the occurrence of spark discharge," Scr. Mater. **81**, 56-59 (2014).
56 F. M. Zhang, M. Reich, O. Kessler, and E. Burkel, "The potential of rapid cooling spark plasma sintering for metallic materials," Mater. Today **16** (5), 192-197 (2013).
57 Robert Aalund, "Spark Plasma Sintering", (2008).

58 F. M. Zhang, A. Weidmann, J. B. Nebe, U. Beck, and E. Burkel, "Preparation, microstructures, mechanical properties, and cytocompatibility of TiMn alloys for biomedical applications," Journal of Biomedical Materials Research Part B-Applied Biomaterials **94B** (2), 406-413 (2010).
59 F. M. Zhang, J. Shen, and J. F. Sun, "The effect of phosphorus additions on densification, grain growth and properties of nanocrystalline WC-Co composites," J. Alloy. Compd. **385** (1-2), 96-103 (2004).
60 M. Omori, "Sintering, consolidation, reaction and crystal growth by the spark plasma system (SPS)," Mater. Sci. Eng. A-Struct. Mater. Prop. Microstruct. Process. **287** (2), 183-188 (2000).
61 Y. W. Gu, K. A. Khor, and P. Cheang, "Bone-like apatite layer formation on hydroxyapatite prepared by spark plasma sintering (SPS)," Biomaterials **25** (18), 4127-4134 (2004).
62 M. Nygren and Z. J. Shen, "On the preparation of bio-, nano- and structural ceramics and composites by spark plasma sintering," Solid State Sci. **5** (1), 125-131 (2003).
63 R. Sivakumar, S. Q. Guo, T. Nishimura, and Y. Kagawa, "Thermal conductivity in multi-wall carbon nanotube/silica-based nanocomposites," Scr. Mater. **56** (4), 265-268 (2007).
64 F. Watari, A. Yokoyama, M. Omori, T. Hirai, H. Kondo, M. Uo, and T. Kawasaki, "Biocompatibility of materials and development to functionally graded implant for bio-medical application," Compos. Sci. Technol. **64** (6), 893-908 (2004).
65 F. M. Zhang, E. Otterstein, and E. Burkel, "Spark Plasma Sintering, Microstructures, and Mechanical Properties of Macroporous Titanium Foams," Adv. Eng. Mater. **12** (9), 863-872 (2010).
66 F. M. Zhang, M. Adam, F. Ahmed, E. Otterstein, and E. Burkel, "Pulsed electric field induced diamond synthesis from carbon nanotubes with solvent catalysts," Diam. Relat. Mat. **20** (5-6), 853-858 (2011).
67 M. Pozuelo, C. Melnyk, W. H. Kao, and J. M. Yang, "Cryomilling and spark plasma sintering of nanocrystalline magnesium-based alloy," J. Mater. Res. **26** (7), 904-911 (2011).
68 Lech Pawlowski, *The Science and Engineering of Thermal Spray Coatings*. (Wiley, 2008), 2nd edition ed.
69 Z. A. Munir, U. Anselmi-Tamburini, and M. Ohyanagi, "The effect of electric field and pressure on the synthesis and consolidation of materials: A review of the spark plasma sintering method," J. Mater. Sci. **41** (3), 763-777 (2006).
70 M. Nygren and Z. Shen, "Spark plasma sintering: Possibilities and limitations", in *Euro Ceramics Viii, Pts 1-3*, edited by H. Mandal and L. Ovecoglu (Trans Tech Publications Ltd, Zurich-Uetikon, 2004), Vol. 264-268, pp. 719-724.
71 T. B. Holland, U. Anselmi-Tamburini, and A. K. Mukherjee, "Electric fields and the future of scalability in spark plasma sintering," Scr. Mater. **69** (2), 117-121 (2013).
72 U. Anselmi-Tamburini, J. E. Garay, and Z. A. Munir, "Fast low-temperature consolidation of bulk nanometric ceramic materials," Scr. Mater. **54** (5), 823-828 (2006).
73 K. Morsi, A. El-Desouky, B. Johnson, A. Mar, and S. Lanka, "Spark plasma extrusion (SPE): Prospects and potential," Scr. Mater. **61** (4), 395-398 (2009).
74 H. Danninger M. Dlapka, C. Gierl, B. Lindqvist, "Sinterhärten – eine spezielle Wärmebehandlung für pulvermetallurgische Präzisionsteile," HTM Journal of Heat Treatment and Materials **67** (3), 223-231 (2012).

75 M. S. Yurlova, V. D. Demenyuk, L. Y. Lebedeva, D. V. Dudina, E. G. Grigoryev, and E. A. Olevsky, "Electric pulse consolidation: an alternative to spark plasma sintering," J. Mater. Sci. **49** (3), 952-985 (2014).
76 G. Song, A. Atrens, D. Stjohn, J. Nairn, and Y. Li, "The electrochemical corrosion of pure magnesium in 1 N NaCl," Corrosion Science **39** (5), 855-875 (1997).
77 N. T. Kirkland, N. Birbilis, and M. P. Staiger, "Assessing the corrosion of biodegradable magnesium implants: A critical review of current methodologies and their limitations," Acta Biomater. **8** (3), 925-936 (2012).
78 D. Cadosch, M. S. Al-Mushaiqri, O. P. Gautschi, J. Meagher, H. P. Simmen, and L. Filgueira, "Biocorrosion and uptake of titanium by human osteoclasts," J. Biomed. Mater. Res. Part A **95A** (4), 1004-1010 (2010).
79 Shaylin Shadanbaz Jemimah Walker, Nicholas T. Kirkland, Edward Stace, Tim Woodfield, Mark P. Staiger, George J. Dias, "Magnesium alloys: Predicting *in vivo* corrosion with *in vitro* immersion testing," Journal of Biomedical Materials Research B: Applied Biomaterials **100B** (4), 1134-1141 (2012).
80 G. L. Song, "Control of biodegradation of biocompatable magnesium alloys," Corrosion Science **49**, 1696–1701 (2007).
81 G. Song, A. Atrens, and D. StJohn "An Hydrogen Evolution Method for the Estimation of the Corrosion Rate of Magnesium Alloys," Magnesium Technology 2001, 255 – 262 (2001).
82 Y. Wang, S. Z. Qiao, and X. Wang, "Electrochemical hydrogen storage properties of ball-milled NdMg12 alloy with Ni powders," Int. J. Hydrog. Energy **33** (3), 1023-1027 (2008).
83 Princeton Applied Research, "Basics of Electrochemicala Impedance Spectroscopy".
84 H. S. Han, Y. Y. Kim, Y. C. Kim, S. Y. Cho, P. R. Cha, H. K. Seok, and S. J. Yang, "Bone formation within the vicinity of biodegradable magnesium alloy implant in a rat femur model," Met. Mater.-Int. **18** (2), 243-247 (2012).
85 I. Johnson, K. Akari, and H. N. Liu, "Nanostructured hydroxyapatite/poly(lactic-co-glycolic acid) composite coating for controlling magnesium degradation in simulated body fluid," Nanotechnology **24** (37) (2013).
86 K. Y. Chiu, M. H. Wong, F. T. Cheng, and H. C. Man, "Characterization and corrosion studies of fluoride conversion coating on degradable Mg implants," Surf. Coat. Technol. **202** (3), 590-598 (2007).
87 Z. Pu, G. L. Song, S. Yang, J. C. Outeiro, O. W. Dillon, D. A. Puleo, and I. S. Jawahir, "Grain refined and basal textured surface produced by burnishing for improved corrosion performance of AZ31B Mg alloy," Corrosion Science **57**, 192-201 (2012).
88 P. K. Bowen, J. Drelich, and J. Goldman, "Zinc Exhibits Ideal Physiological Corrosion Behavior for Bioabsorbable Stents," Adv. Mater. **25** (18), 2577-2582 (2013).
89 K. A. Khalil, E. S. M. Sherif, and A. A. Almajid, "Corrosion Passivation in Simulated Body Fluid of Magnesium/Hydroxyapatite Nanocomposites Sintered by High Frequency Induction Heating," Int. J. Electrochem. Sci. **6** (12), 6184-6199 (2011).
90 M. I. Jamesh, G. S. Wu, Y. Zhao, D. R. McKenzie, M. M. M. Bilek, and P. K. Chu, "Effects of zirconium and oxygen plasma ion implantation on the corrosion behavior of ZK60 Mg alloy in simulated body fluids," Corrosion Science **82**, 7-26 (2014).
91 R. Z. Xu, X. B. Yang, X. M. Zhang, M. Wang, P. H. Li, Y. Zhao, G. S. Wu, and P. K. Chu, "Effects of carbon dioxide plasma immersion ion implantation on the electrochemical properties of AZ31 magnesium alloy in physiological environment," Appl. Surf. Sci. **286**, 257-260 (2013).

92 F. Chen, H. Zhou, S. Cai, F. X. Lv, and C. M. Li, "Corrosion resistance properties of AZ31 magnesium alloy after Ti ion implantation," Rare Metals **26** (2), 142-146 (2007).
93 R. Z. Xu, G. S. Wu, X. B. Yang, T. Hu, Q. Y. Lu, and P. K. Chu, "Controllable degradation of biomedical magnesium by chromium and oxygen dual ion implantation," Mater. Lett. **65** (14), 2171-2173 (2011).
94 C. C. Ribeiro, I. Gibson, and M. A. Barbosa, "The uptake of titanium ions by hydroxyapatite particles - structural changes and possible mechanisms," Biomaterials **27** (9), 1749-1761 (2006).
95 K. Pichler, S. Fischerauer, P. Ferlic, E. Martinelli, H. P. Brezinsek, P. J. Uggowitzer, J. F. Loffler, and A. M. Weinberg, "Immunological Response to Biodegradable Magnesium Implants," Jom **66** (4), 573-579 (2014).
96 B. Liu and Y. F. Zheng, "Effects of alloying elements (Mn, Co, Al, W, Sn, B, C and S) on biodegradability and in vitro biocompatibility of pure iron," Acta Biomater. **7** (3), 1407-1420 (2011).
97 H. Hermawan, D. Dube, and D. Mantovani, "Degradable metallic biomaterials: Design and development of Fe-Mn alloys for stents," J. Biomed. Mater. Res. Part A **93A** (1), 1-11 (2010).
98 B. Wegener, B. Sievers, S. Utzschneider, P. Muller, V. Jansson, S. Rossler, B. Nies, G. Stephani, B. Kieback, and P. Quadbeck, "Microstructure, cytotoxicity and corrosion of powder-metallurgical iron alloys for biodegradable bone replacement materials," Mater. Sci. Eng. B-Adv. Funct. Solid-State Mater. **176** (20), 1789-1796 (2011).
99 R. Orinakova, A. Orinak, L. M. Buckova, M. Giretova, L. Medvecky, E. Labbanczova, M. Kupkova, M. Hrubovcakova, and K. Koval, "Iron Based Degradable Foam Structures for Potential Orthopedic Applications," Int. J. Electrochem. Sci. **8** (12), 12451-12465 (2013).
100 P. P. Mueller, S. Arnold, M. Badar, D. Bormann, F. W. Bach, A. Drynda, A. Meyer-Lindenberg, H. Hauser, and M. Peuster, "Histological and molecular evaluation of iron as degradable medical implant material in a murine animal model," J. Biomed. Mater. Res. Part A **100A** (11), 2881-2889 (2012).
101 X. N. Gu, Y. F. Zheng, Y. Cheng, S. P. Zhong, and T. F. Xi, "In vitro corrosion and biocompatibility of binary magnesium alloys," Biomaterials **30** (4), 484-498 (2009).
102 D. A. Puleo and W. W. Huh, "ACUTE TOXICITY OF METAL-IONS IN CULTURES OF OSTEOGENIC CELLS DERIVED FROM BONE-MARROW STROMAL CELLS," J. Appl. Biomater. **6** (2), 109-116 (1995).
103 Li-Ying Qiao Jia-Cheng Gao, Ren-Long Xin, "Effect of Mg 2+ concentration on biocompatibility of pure magnesium," Front. Mater. Sci. China **4** (2), 126-131 (2010).
104 Y. Zhang, L. Ren, M. Li, X. Lin, H. F. Zhao, and K. Yang, "Preliminary Study on Cytotoxic Effect of Biodegradation of Magnesium on Cancer Cells," J. Mater. Sci. Technol. **28** (9), 769-772 (2012).
105 Q. Wang, S. Jin, X. Lin, Y. Zhang, L. Ren, and K. Yang, "Cytotoxic Effects of Biodegradation of Pure Mg and MAO-Mg on Tumor Cells of MG63 and KB," J. Mater. Sci. Technol. **30** (5), 487-492 (2014).
106 Y. Li, C. Wong, J. Xiong, P. Hodgson, and C. Wen, "Cytotoxicity of Titanium and Titanium Alloying Elements," J. Dent. Res. **89** (5), 493-497 (2010).
107 M. Zaidi, J. Kerby, C. L. H. Huang, Asmt Alam, H. Rathod, T. J. Chambers, and B. S. Moonga, "DIVALENT-CATIONS MIMIC THE INHIBITORY EFFECT OF EXTRACELLULAR IONIZED CALCIUM ON BONE-RESORPTION BY ISOLATED RAT OSTEOCLASTS - FURTHER EVIDENCE FOR A CALCIUM RECEPTOR," J. Cell. Physiol. **149** (3), 422-427 (1991).

108 V. S. Shankar, C. M. R. Bax, Asmt Alam, B. E. Bax, C. L. H. Huang, and M. Zaidi, "THE OSTEOCLAST CA-2+ RECEPTOR IS HIGHLY SENSITIVE TO ACTIVATION BY TRANSITION-METAL CATIONS," Biochem. Biophys. Res. Commun. **187** (2), 913-918 (1992).
109 V. S. Shankar, Asmt Alam, C. M. R. Bax, B. E. Bax, M. Pazianas, C. L. H. Huang, and M. Zaidi, "ACTIVATION AND INACTIVATION OF THE OSTEOCLAST CA-2+ RECEPTOR BY THE TRIVALENT CATION, LA-3+," Biochem. Biophys. Res. Commun. **187** (2), 907-912 (1992).
110 K. G. Nichols and D. A. Puleo, "Effect of metal ions on the formation and function of osteoclastic cells in vitro," J. Biomed. Mater. Res. **35** (2), 265-271 (1997).
111 G. J. Thompson and D. A. Puleo, "EFFECTS OF SUBLETHAL METAL-ION CONCENTRATIONS ON OSTEOGENIC CELLS DERIVED FROM BONE-MARROW STROMAL CELLS," J. Appl. Biomater. **6** (4), 249-258 (1995).
112 G. J. Thompson and D. A. Puleo, "Ti-6Al-4V ion solution inhibition of osteogenic cell phenotype as a function of differentiation timecourse in vitro," Biomaterials **17** (20), 1949-1954 (1996).
113 J. X. Wang, G. Q. Zhou, C. Y. Chen, H. W. Yu, T. C. Wang, Y. M. Ma, G. Jia, Y. X. Gao, B. Li, J. Sun, Y. F. Li, F. Jiao, Y. L. Zhao, and Z. F. Chai, "Acute toxicity and biodistribution of different sized titanium dioxide particles in mice after oral administration," Toxicol. Lett. **168** (2), 176-185 (2007).
114 C. M. Sayes, R. Wahi, P. A. Kurian, Y. P. Liu, J. L. West, K. D. Ausman, D. B. Warheit, and V. L. Colvin, "Correlating nanoscale titania structure with toxicity: A cytotoxicity and inflammatory response study with human dermal fibroblasts and human lung epithelial cells," Toxicol. Sci. **92** (1), 174-185 (2006).
115 J. Fischer, M. H. Prosenc, M. Wolff, N. Hort, R. Willumeit, and F. Feyerabend, "Interference of magnesium corrosion with tetrazolium-based cytotoxicity assays," Acta Biomater. **6** (5), 1813-1823 (2010).
116 J. Y. Yoo, J. M. Kim, K. S. Seo, Y. K. Jeong, H. B. Lee, and G. Khang, "Characterization of degradation behavior for PLGA in various pH condition by simple liquid chromatography method," Bio-Med. Mater. Eng. **15** (4), 279-288 (2005).
117 D. H. Kohn, M. Sarmadi, J. I. Helman, and P. H. Krebsbach, "Effects of pH on human bone marrow stromal cells in vitro: Implications for tissue engineering of bone," J. Biomed. Mater. Res. **60** (2), 292-299 (2002).
118 H. W. Lee, S. H. Seo, C. H. Kum, B. J. Park, Y. K. Joung, T. I. Son, and D. K. Han, "Fabrication and characteristics of anti-inflammatory magnesium hydroxide incorporated PLGA scaffolds formed with various porogen materials," Macromol. Res. **22** (2), 210-218 (2014).
119 J. Y. Wu, X. Lu, L. L. Tan, B. C. Zhang, and K. Yang, "Effect of hydrion evolution by polylactic-co-glycolic acid coating on degradation rate of pure iron," Journal of Biomedical Materials Research Part B-Applied Biomaterials **101** (7), 1222-1232 (2013).
120 P. I. Chang, "POLYMER IMPLANT MATERIALS WITH IMPROVED X-RAY OPACITY AND BIOCOMPATIBILITY," Biomaterials **2** (3), 151-155 (1981).
121 M. Ngiam, S. S. Liao, A. J. Patil, Z. Y. Cheng, C. K. Chan, and S. Ramakrishna, "The fabrication of nano-hydroxyapatite on PLGA and PLGA/collagen nanofibrous composite scaffolds and their effects in osteoblastic behavior for bone tissue engineering," Bone **45** (1), 4-16 (2009);Z. L. Mou, L. J. Zhao, Q. A. Zhang, J. Zhang, and Z. Q. Zhang, "Preparation of porous PLGA/HA/collagen scaffolds with supercritical CO2 and application in osteoblast cell culture," J. Supercrit. Fluids **58** (3), 398-406 (2011).

122 Y. H. Wu, N. Li, Y. Cheng, Y. F. Zheng, and Y. Han, "In vitro Study on Biodegradable AZ31 Magnesium Alloy Fibers Reinforced PLGA Composite," J. Mater. Sci. Technol. **29** (6), 545-550 (2013).
123 B. D. Cullity and S. R. Stock, *Elements of X-ray diffraction*. (Prentice Hall, 2001), 3rd ed.
124 *ASM Handbook Vol. 14B Metalworking: Sheet Forming*. (ASM International, 2006).
125 ASM International Handbook Committee, *Metals Handbook*. (1990), 10 ed.
126 J. Huot, G. Liang, S. Boily, A. Van Neste, and R. Schulz, "Structural study and hydrogen sorption kinetics of ball-milled magnesium hydride," J. Alloy. Compd. **293**, 495-500 (1999).
127 R. A. H. Niessen and P. H. L. Notten, "Electrochemical hydrogen storage characteristics of thin film Mg (X, X = Sc, Ti, V, Cr) compounds," Electrochem. Solid State Lett. **8** (10), A534-A538 (2005).
128 K. Asano, H. Enoki, and E. Akiba, "Synthesis of Mg-Ti FCC hydrides from Mg-Ti BCC alloys," J. Alloy. Compd. **478** (1-2), 117-120 (2009).
129 X. B. Chen, L. Liu, P. Y. Yu, and S. S. Mao, "Increasing Solar Absorption for Photocatalysis with Black Hydrogenated Titanium Dioxide Nanocrystals," Science **331** (6018), 746-750 (2011).
130 I. J. T. Jensen, O. M. Lovvik, H. Schreuders, B. Dam, and S. Diplas, "Combined XPS and first principle study of metastable Mg-Ti thin films," Surf. Interface Anal. **44** (8), 986-988 (2012).
131 T. Mitchell, S. Diplas, P. Tsakiropoulos, J. F. Watts, and J. A. D. Matthew, "Study of alloying behaviour in metastable Mg-Ti solid solutions using Auger parameter measurements and charge-transfer calculations," Philosophical Magazine a-Physics of Condensed Matter Structure Defects and Mechanical Properties **82** (4), 841-855 (2002).
132 William F. Stickle John F. Moulder, Peter E. Sobol, Kenneth D. Bomben, *Handbook of X-ray Photoelectron Spectroscopy*. (Perkin-Elmer Corporation, Eden Prairie, Minnesota, 1992).
133 R. B. Dean and W. J. Dixon, "SIMPLIFIED STATISTICS FOR SMALL NUMBERS OF OBSERVATIONS," Anal. Chem. **23** (4), 636-638 (1951).
134 D. B. Rorabacher, "STATISTICAL TREATMENT FOR REJECTION OF DEVIANT VALUES - CRITICAL-VALUES OF DIXON Q PARAMETER AND RELATED SUBRANGE RATIOS AT THE 95-PERCENT CONFIDENCE LEVEL," Anal. Chem. **63** (2), 139-146 (1991).
135 A. Yamamoto and S. Hiromoto, "Effect of inorganic salts, amino acids and proteins on the degradation of pure magnesium in vitro," Mater. Sci. Eng. C-Biomimetic Supramol. Syst. **29** (5), 1559-1568 (2009).
136 N. T. Kirkland, J. Lespagnol, N. Birbilis, and M. P. Staiger, "A survey of bio-corrosion rates of magnesium alloys," Corrosion Science **52** (2), 287-291 (2010).
137 M. A. Khan, R. L. Williams, and D. F. Williams, "The corrosion behaviour of Ti-6Al-4V, Ti-6Al-7Nb and Ti-13Nb-13Zr in protein solutions," Biomaterials **20** (7), 631-637 (1999).
138 K. K. Kaysinger and W. K. Ramp, "Extracellular pH modulates the activity of cultured human osteoblasts," J. Cell. Biochem. **68** (1), 83-89 (1998).
139 R. J. Newman, M. H. Stone, and S. K. Mukherjee, "ACCELERATED FRACTURE UNION IN ASSOCIATION WITH SEVERE HEAD-INJURY," Injury-Int. J. Care Inj. **18** (4), 241-246 (1987).
140 K. Chiba, K. Kawakami, and K. Tohyama, "Simultaneous evaluation of cell viability by neutral red, MTT and crystal violet staining assays of the same cells," Toxicol. Vitro **12** (3), 251-258 (1998).

141 K. Saotome, H. Morita, and M. Umeda, "CYTOTOXICITY TEST WITH SIMPLIFIED CRYSTAL VIOLET STAINING METHOD USING MICROTITRE PLATES AND ITS APPLICATION TO INJECTION-DRUGS," Toxicol. Vitro **3** (4), 317-321 (1989).

VITA

Ilona Hoffmann

Born in Wittlich, Germany

Education

2010 – 2014: PhD Candidate, Materials Science and Engineering, University of Kentucky, Lexington KY

2004 – 2010: University of Karlsruhe (now KIT), Germany: Diploma in Mechanical Engineering with major in Materials Science and Engineering. Thesis topic: "Magnesium-Titanium: a Biocompatible, Biodegradable, Mechanically-Matched Material for Temporary Implants"

Professional memberships

University of Kentucky Materials Research Society chapter (president for academic year 2011/12)

University of Kentucky Society for Biomaterials chapter (secretary for academic year 2011/12)

Publications

Ilona Hoffmann, Yang-Tse Cheng, David A. Puleo, Guangling Song, Richard A. Waldo, *Mg-Ti: A Possible Biodegradable, Biocompatible, Mechanically Matched Material for Temporary Implants*, Mater. Res. Soc. Symp. Proc. Vol. 1301 (2011). DOI: 10.1557/opl.2011.566

Presentations

Ilona Hoffmann, Yang-Tse Cheng, David A. Puleo, Guangling Song, Richard A. Waldo, *Mg-Ti: A Possible Biodegradable, Biocompatible, Mechanically Matched Material for Temporary Implants*, Materials Research Society Fall Meeting, Boston (MA), 2010

Ilona Hoffmann, David A. Puleo, Yang-Tse Cheng, *Magnesium-Titanium Alloys for Biodegradable Implants*, Materials Science & Technology 2011 Conference, Columbus (OH), 2011

Ilona Hoffmann, Yang-Tse Cheng, David A. Puleo, Making the Impossible – Synthesis and Processing of Non-Equilibrium Materials, Center for Advanced Materials, University of Kentucky, Lexington (KY), 2012

Ilona Hoffmann, David A. Puleo, Yang-Tse Cheng, *Corrosion Behavior of Mg_xTi_{1-x} Alloys Fabricated by Mechanical Alloying and Compaction Methods*, Materials Science & Technology 2012 Conference, Pittsburgh (PA),2012

Ilona Hoffmann, *Non-equilibrium Processing*, 3rd International Forum on Sustainable Manufacturing – Products, Processes and Systems, University of Kentucky, 2013

Fellowships

Halcomb Fellowship in Medicine and Engineering, academic years 2012/13 and 2013/14

Harrison D. Brailsford Graduate Fellowship, academic year 2011/12